Forschungsbericht 2025-20

Gust-Induced Amplitude Effects in Transonic Flow

Diliana Friedewald

Deutsches Zentrum für Luft- und Raumfahrt
Institut für Aeroelastik
Göttingen

DLR Deutsches Zentrum für Luft- und Raumfahrt

Forschungsbericht 2025-20

Gust-Induced Amplitude Effects in Transonic Flow

Diliana Friedewald

Deutsches Zentrum für Luft- und Raumfahrt
Institut für Aeroelastik
Göttingen

161 Seiten
110 Bilder
13 Tabellen
127 Literaturstellen

Deutsches Zentrum
DLR für Luft- und Raumfahrt

Herausgeber:

Deutsches Zentrum
für Luft- und Raumfahrt e. V.
Wissenschaftliche Information
Linder Höhe
D-51147 Köln

ISSN 1434-8454
ISRN DLR-FB-2025-20
Erscheinungsjahr 2025
DOI: 10.57676/t8jn-aj61

Instationär nichtlineare Aerodynamik, Transsonische Strömung, Anregungen großer Amplitude, Böen, Lasten, Auftrieb, Ablösung, URANS, FSI

Diliana FRIEDEWALD
DLR, Institut für Aeroelastik, Göttingen

Böen-Induzierte Amplitudeneffekte in Transsonischer Strömung
Technische Universität Braunschweig

Die Auslegung einer Transportflugzeugkonfiguration bedarf u. a. Böenlastrechnungen für eine optimale Strukturdimensionierung. In der vorliegenden Arbeit wird der Einfluss einer instationär nichtlinearen aerodynamischen Modellierung im Vergleich zu einer zeitlinearisierten aerodynamischen Modellierung auf die Berechnung von Böenantworten in verschiedenen transsonischen Strömungen untersucht. Die Antworten werden dabei auf Basis der instationären Reynolds-gemittelten Navier-Stokes Gleichungen (URANS) im Zeitbereich sowohl für eine 2D-Profilkonfiguration, als auch für eine Transportflugzeugkonfiguration berechnet.

Es zeigt sich, dass es drei grundlegend verschiedene nichtlineare Antworttypen gibt, die entweder einen geringeren, einen höheren oder einen gleichbleibenden maximalen Auftriebsbeiwert im Vergleich zu den zeitlinearisierten Berechnungen ergeben. Diese nichtlinearen Antworttypen können jeweils auf spezifische Veränderungen im instationären Strömungsfeld zurückgeführt werden. Die Analysen lassen weiterhin vermuten, dass die stationäre Auftriebspolare, bzw. der konkrete Verlauf des stationären Auftriebsderivatives, als Indikator für das Auftreten des jeweiligen Antworttyps dienen könnte.

Die beobachteten nichtlinearen Effekte aus rein aerodynamischen Simulationen finden sich auch für aeroelastische Simulationen in der Analyse des Flügelwurzelbiegemoments wieder.

unsteady nonlinear aerodynamics, transonic flow, large-amplitude excitation, gust, loads, lift, separation, URANS, FSI

(Published in english)

Diliana FRIEDEWALD
German Aerospace Center (DLR), Institute of Aeroelasticity, Göttingen

Gust-Induced Amplitude Effects in Transonic Flow

Technical University Braunschweig

The design of a transport aircraft configuration requires, among others, gust load computations for optimal structural sizing. The present work analyzes the influence of an unsteady nonlinear aerodynamic modeling in comparison to a time-linearized aerodynamic modeling on the computation of transonic gust responses. The time-domain simulations are based on the unsteady Reynolds-averaged Navier-Stokes equations (URANS) and are carried out for an airfoil configuration as well as for a transport aircraft configuration.

Based on the investigations, three types of nonlinear lift responses are identified, that lead to either a lower, higher or similar peak lift value compared to a time-linearized computation. Each of these types is caused by specific changes in the unsteady flow field. Moreover, the results indicate that the steady lift polar, or more specifically, the distinct trend of the lift curve slope, might serve as an indicator for the occurrence of the respective response type.

The reported nonlinear effects from purely aerodynamic simulations can also be found for aeroelastic simulations in the analysis of the wing root bending moment.

Gust-Induced Amplitude Effects in Transonic Flow

Von der Fakultät für Maschinenbau
der Technischen Universität Braunschweig

zur Erlangung der Würde
einer Doktor-Ingenieurin (Dr.-Ing.)
genehmigte Dissertation

von:	Diliana Friedewald
geboren in:	Schwerin

eingereicht am:	13.03.2025
mündliche Prüfung am:	18.06.2025

Vorsitz:	Prof. Dr.-Ing. Sebastian Heimbs
Gutachter:	Prof. Dr.-Ing. Lorenz Tichy
Gutachter:	Prof. Dr.-Ing. David E. Rival

2025

Abstract

The design of a transport aircraft configuration requires a variety of load computations for optimal structural sizing. Certification specifications demand, e.g., the computation of gust encounters with different amplitudes at transonic cruise speeds. Due to the large number of necessary computations, frequency-based methods are state-of-the-art in an industrial context. However, these time-linearized methods are strictly valid only for excitations with very small amplitudes. In order to enable an accurate load prediction also for large-amplitude excitations, computed results are partially corrected, e.g., on the basis of wind tunnel data. For optimizing an aircraft's sizing even further and more automated, a more accurate, i.e., unsteady nonlinear, load prediction for excitations with large amplitudes is required.

The present work analyzes the influence of an unsteady nonlinear aerodynamic modeling in comparison to a time-linearized aerodynamic modeling on the computation of transonic gust responses. The time-domain simulations are based on the unsteady Reynolds-averaged Navier-Stokes equations (URANS) and are carried out for an airfoil configuration as well as for a transport aircraft configuration. Sinusoidal, as well as "1-cos" gusts, are used for the excitation. Gust lengths and gust amplitudes are varied. Gust encounters take place under different transonic steady conditions, in order to assess the influence of the steady base flow field. Finally, the impact of the observed aerodynamic nonlinearities is analyzed also for a flexible model of the transport aircraft configuration.

Based on these investigations, three types of nonlinear lift responses are identified:

- Nonlinear lift responses of type A lead to a lower peak lift coefficient prediction than time-linearized computations. Shock-induced flow separation dominates the unsteady flow here.
- Nonlinear lift responses of type B correspond to higher peak lift values than the prediction by the time-linearized method. These responses involve a significant topological change in the flow field without significant separation.
- Nonlinear lift responses of type C mark the transition between types A and B and correspond to comparable peak lift values for time-linearized and nonlinear computations, even though the underlying unsteady flows differ fundamentally.

The results indicate that the steady lift polar, or more specifically, the distinct trend of the lift curve slope, might serve as an indicator for the occurrence of the respective response type: If the steady angle of attack is lower than the angle of attack at which the maximum of the lift curve slope is expected, the time-linearized method might underestimate or overestimate the actually occurring, nonlinear maximum value. If the steady angle of attack is larger, only conservative loads can be expected using the time-linearized method.

Zusammenfassung

Die Auslegung einer Transportflugzeugkonfiguration bedarf einer Vielzahl an Lastenrechnungen für eine optimale Strukturdimensionierung. Die Zulassungsvorschriften verlangen dabei unter anderem die Berechnung von Böen mit verschiedenen Amplituden bei transsonischen Reiseflugeschwindigkeiten. Um die Vielzahl an Böenlastberechnungen durchführen zu können, werden im industriellen Kontext standardmäßig frequenzbasierte Verfahren eingesetzt. Diese zeitlinearisierten Methoden sind streng genommen jedoch nur bei sehr kleinen instationären Störungen gültig. Für eine möglichst genaue Lastvorhersage auch bei großen Amplituden werden die berechneten Ergebnisse daher bspw. auf der Basis von Messdaten aus Windkanalversuchen korrigiert. Um die Strukturdimensionierung jedoch weitergehend und möglichst automatisiert zu optimieren, sind genauere, d.h. instationär nichtlineare, Lastberechnungen bei Anregungen mit großen Amplituden notwendig.

In der vorliegenden Arbeit wird deshalb der Einfluss einer instationär nichtlinearen aerodynamischen Modellierung im Vergleich zu einer zeitlinearisierten aerodynamischen Modellierung auf die Berechnung von Böenantworten in verschiedenen transsonischen Strömungen untersucht. Die Antworten werden dabei auf Basis der instationären Reynoldsgemittelten Navier-Stokes Gleichungen (URANS) im Zeitbereich sowohl für eine 2D-Profilkonfiguration, als auch für eine Transportflugzeugkonfiguration berechnet. Sinusförmige Böen wie auch "1-cos"-Böen werden zur Anregung genutzt, Böenamplituden und Böenlängen werden jeweils über einen weiten Wertebereich variiert. Die Böentreffer erfolgen bei verschiedenen Strömungszuständen, um auch den Einfluss der stationären Grundströmung zu analysieren. Die Auswirkungen der beobachteten aerodynamischen Nichtlinearitäten werden abschließend auch für ein flexibles Modell der Transportflugzeugkonfiguration untersucht.

Es zeigt sich, dass es bezogen auf den maximal auftretenden Auftriebsbeiwert drei grundlegend verschiedene nichtlineare Antworttypen gibt:

- Nichtlineare Auftriebsantworten des Typs A führen nichtlinear gerechnet zu einem geringeren maximalen Auftriebsbeiwert als die zeitlinearisierte Berechnung. Der Grund dafür sind starke stoß-induzierte Strömungsablösungen, die die instationäre Strömung dominieren.
- Nichtlineare Auftriebsantworten des Typs B ergeben einen höheren Maximalwert als die zeitlinearisierte Methode vorhersagt. Diese Art der Antworten tritt für Strömungen auf, die durch die externe Anregung eine signifikante topologische Änderung des Strömungsfeldes, jedoch ohne signifikante Strömungsablösung, erfahren.

– Nichtlineare Auftriebsantworten des Typs C kennzeichnen den Übergang zwischen Typ A und B und resultieren in vergleichbaren Werten für den maximalen Auftriebsbeiwert, obwohl sich die instationären Strömungsfelder grundlegend voneinander unterscheiden.

Die Analysen lassen vermuten, dass die stationäre Auftriebspolare, bzw. der konkrete Verlauf des stationären Auftriebsderivatives, als Indikator für das Auftreten des jeweiligen Antworttyps dienen könnte. Ist der stationäre Anstellwinkel kleiner als der Winkel, bei dem das Maximum des stationären Auftriebsderivatives zu erwarten ist, kann die zeitlinearisierte Methode den tatsächlich auftretenden, nichtlinearen Maximalwert über- oder unterschätzen. Ist der stationäre Anstellwinkel größer, sind vermutlich ausschließlich konservative Lastvorhersagen mit den zeitlinearisierten Verfahren zu erwarten.

Acknowledgements / Danksagungen

Für die wissenschaftliche Betreuung der vorliegenden Dissertation möchte ich Herrn Prof. Dr. Lorenz Tichy herzlich danken. Ich bedanke mich für kritische Fragen, eine immer konstruktive Gesprächsatmosphäre und für das ausnahmslose Vertrauen in meine Arbeit, welches ich in den vergangenen Jahren entgegengebracht bekommen habe. Herrn Prof. Dr. David Rival danke ich für die Bereitschaft, als Gutachter für diese Arbeit zur Verfügung zu stehen und Herrn Prof. Dr. Sebastian Heimbs für die Bereitschaft, den Vorsitz der Prüfungskommission zu übernehmen.

Die vorliegende Arbeit entstand während meiner Tätigkeit als wissenschaftliche Mitarbeiterin am Institut für Aeroelastik des Deutschen Zentrums für Luft- und Raumfahrt in Göttingen. Daher möchte ich meinem Abteilungsleiter, Herrn Prof. Dr. Holger Hennings, herzlich dafür danken, dass er mir stets den Freiraum ermöglicht hat, den ich in den unterschiedlichen Arbeitsphasen benötigt habe. Vielen Dank für Ihre Unterstützung, vor allem auch in der letzten Phase der Arbeit, und die Ermunterung dazu, immer auch über den wissenschaftlichen Tellerrand hinaus zu blicken.

Die angenehme Arbeitsatmosphäre am Institut und speziell der sehr kollegiale Austausch haben es mir ermöglicht, die vorliegende Arbeit so zu schreiben, wie sie nun ist. Ob zu Diskussionen zum „Großen Ganzen", zu fachlichen Details, zu IT-Fragen oder zum Korrekturlesen der Arbeit – auf der Suche nach Diskussions- und Ansprechpartnern standen eure Türen immer offen: Christoph, Michael, David, Guido, Sebastian, Kris, Marc, Jens, Jens, Christopher, Olli, Johannes, Anne, Vega, Markus, Arne, Yves, Urte und Heike – DANKE!

In fast jedem Ratgeber zum Thema „Promotion" wird betont, wie wichtig auch eine ausgewogene Work-Life-Balance sei, um die Dissertation über die Zielgerade bringen zu können. Mit zwei Kindern zu Hause brauchte ich mir glücklicherweise um den „Life"-Anteil wenig Sorgen zu machen - er passierte von ganz allein. Dass ich trotzdem ausreichend Zeit und Kraft für den „Work"-Anteil zur Verfügung hatte, verdanke ich meiner Familie und meinen Freunden in nah und fern. DANKE – für eure fortwährende Unterstützung im Hintergrund, für die Motivation auf den letzten Metern und auch für eine garantierte Abwechslung auf die angenehmste Art und Weise!

Göttingen, im März 2025 Diliana Friedewald

Contents

List of Symbols

α_G	=	gust-induced angle of attack, deg
α_{Heave}	=	angle of attack due to heave mode, deg
α_{Pitch}	=	angle of attack due to pitch mode, deg
α_0	=	steady angle of attack, deg
$\widehat{\alpha}_G$	=	amplitude of gust-induced angle of attack, deg
c	=	chord length, m
c_{fx}	=	x-component of skin friction coefficient
C_L	=	lift coefficient
C^n_{L,α_G}	=	n-th harmonic of the lift's frequency response function, deg^{-1}
$C_{L,0}$	=	steady lift coefficient
ΔC_L	=	unsteady increment of the lift coefficient
ΔC_L^{Max}	=	maximum unsteady increment of the lift coefficient
$\Delta C_L^{Max,Lin}$	=	maximum increment of the time-linearized lift coefficient
δC_L^{Max}	=	relative difference in maximum incremental lift
c_{MAC}	=	length of the mean aerodynamic chord, m
C_{My}	=	pitching moment coefficient
c_p	=	pressure coefficient
$c_{p,crit}$	=	critical pressure coefficient
dt	=	time step size, s
f	=	frequency, Hz
H	=	gust-gradient distance, m
k_{Gust}	=	reduced frequency of the gust
l_{ref}	=	Reynolds reference length, m
L_G	=	gust length, m
m^{Lin}	=	effective linear lift curve slope, 1/deg
m^{NL}	=	effective nonlinear lift curve slope, 1/deg
Ma	=	Mach number
ndt	=	number of time steps
q_3	=	modal coordinate of heave mode
q_5	=	modal coordinate of pitch mode
Re	=	Reynolds number
t	=	time, s
T	=	period, s
τ	=	nondimensional time

τ_G	=	significant point in nondimensional time related to the gust velocity
τ_L	=	significant point in nondimensional time related to the lift coefficient
$\Delta\tau$	=	nondimensional time step size
U_∞	=	free-stream velocity, m/s
W_G	=	vertical gust velocity, m/s
$\widehat{W}_G$	=	amplitude of gust velocity, m/s
$\widetilde{W}_G$	=	normalized gust velocity, m/s
x	=	x-coordinate, m
x_S	=	shock position, m
x_S^{Max}	=	maximum shock position, m
y	=	y-coordinate, m
z	=	z-coordinate, m

Abbreviations

AIAA	=	American Institute of Aeronautics and Astronautics
CFD	=	Computational Fluid Dynamics
CS	=	Certification Specification
DFT	=	Discrete Fourier Transform
DLM	=	Doublet-Lattice Method
DLR	=	Deutsches Zentrum für Luft- und Raumfahrt (German Aerospace Center)
DPW	=	Drag Prediction Workshop
DNS	=	Direct Numerical Simulation
DNW	=	Deutsch-Niederländische Windkanäle (German-Dutch Wind tunnels)
DSV	=	Dynamic Stall Vortex
EAS	=	Equivalent Airspeed
FRF	=	Frequency Response Function
FSI	=	Fluid-Structure Interaction
HALE	=	High-Altitude Long-Endurance
HTP	=	Horizontal Tail Plane
LE	=	Leading Edge
LES	=	Large-Eddy Simulation
LFD	=	Linear Frequency Domain
NACA	=	National Advisory Committee for Aeronautics
NASA	=	National Aeronautics and Space Administration
NL	=	Nonlinear
RANS	=	Reynolds-Averaged Navier-Stokes
RSM	=	Reynolds-Stress Model
SAO	=	Spalart-Allmaras, Original
SOB	=	Side-Of-Body [separation]
SPP	=	Steps Per Period
SST	=	Shear-Stress Transport
TE	=	Trailing Edge
TWG	=	Transonic Wind tunnel Göttingen
URANS	=	Unsteady Reynolds-Averaged Navier-Stokes

1 Introduction

1.1 Motivation

The European Commission has set the ambitious goal of reducing the net emissions of greenhouse gases down to the value of zero by the year 2050, making Europe the first climate-neutral continent on earth ("European Green Deal" [1]). To reach this goal, the energy requirements of future aircraft need to be halved. Therefore, aircraft design needs to be further optimized to the limits of what is physically possible while maintaining the necessary safety factors prescribed by the regulations.

Optimizing aircraft sizing to obtain the lowest structural mass is one possibility for directly reducing fuel consumption. The concept of the so-called "Energy-efficient aircraft" is, e.g., addressed in the current aviation strategy of the German Aerospace Center (DLR) [2]. Identifying potential structural savings demands a more accurate knowledge of an aircraft's peak loads than available today [3].

The "Certification Specifications for Large Aeroplanes" (CS-25) [4] define the scope of load computations that need to be carried out to design and certify a new transport aircraft configuration. Among others, maneuver, ground, and gust load computations must be considered. Discrete "1-cos" gust encounters must be computed with various gust lengths and small to large gust amplitudes to prove the structural stability of all aircraft components. Especially the estimation of peak internal loads is crucial for an appropriate structural sizing [5]. However, the certification specifications do not specify which level of physical modeling accuracy needs to be satisfied by the numerical methods. On the one hand, load analysis needs to be conservative with respect to the certification. On the other hand, aircraft manufacturers want to ensure that the aircraft does not become unnecessarily heavy. These two main requirements need to be balanced for a proper load computation and hence define the choice of an appropriate computational method. A recent study shows the influence that a nonlinear aerodynamic modeling has on the computation of internal (gust) loads on an aircraft configuration with a high aspect ratio wing [6]. Dynamic CFD-based gust loads show a considerable effect on the sizing loads of the wing, especially for the transonic cruise load case. A potential-theory-based method predicts significantly lower internal loads here.

Since the 1970s, potential-theory-based methods have been used as cornerstones in aerodynamic modeling in the aircraft industry, where one of them is the unsteady linear Doublet-Lattice method (DLM) [7]. Though the method does not include effects of viscosity, recompression shocks, or the wing thickness, its low computational cost and its robustness lead to a key role in an aircraft's design and certification process for several

decades. Moreover, at least some of the method's deficiencies can be eliminated easily using one of numerous DLM-corrections [8–15]. While increasing accuracy, the short computational time is preserved, which is of paramount importance during an industrial design process.

Lately, the increase in computational power has facilitated the application of the so-called linear frequency domain (LFD) solvers [16] in industry [17, 18]. They solve the time-linearized Reynolds-averaged Navier-Stokes (RANS) equations and include additional physical effects compared to the DLM, such as nonlinearities of the steady base flow which are introduced, e.g., by a transonic flow field. Still, the results of these time-linearized methods are independent of the excitation amplitude, which makes them physically correct only for excitations with very small amplitudes. Computed results are therefore corrected, e.g., on the basis of measurement data from wind tunnel tests, in order to enable an accurate load prediction.

However, the demand for a more lightweight aircraft structure increases the need for an improved prediction accuracy for large-amplitude excitations [3]. Today's standard computational fluid dynamics (CFD) solvers, based on the unsteady RANS (URANS) equations, incorporate unsteady nonlinear aerodynamic effects, but seem prohibitive for an industrial application with respect to computational time and robustness. Moreover, since appropriate numerical methods in combination with sufficiently increased computational power only became available in the last decade, there is only little investigated on the influence of an unsteady nonlinear aerodynamic modeling in transonic flows up to the present day. Recent publications indicate a significant impact on computed peak loads when unsteady nonlinear aerodynamic methods instead of time-linearized methods are used [6, 19–21]. However, comprehensive studies on the underlying aerodynamic effects are missing. Experimental data does not seem to be available at all, to the best of the author's knowledge. Therefore, the current thesis will analyze the impact of an unsteady nonlinear aerodynamic modeling in transonic flows for large-amplitude gust excitations and identify nonlinear effects in aerodynamic and aeroelastic gust responses.

1.2 Hypotheses

Large-amplitude gust encounters introduce nonlinear effects in the resulting responses [6, 19, 20, 22, 23]. The current understanding, and therefore the **main hypothesis of this work**, is that these nonlinear effects mainly result from unsteady shock-induced flow separation. It is assumed that this flow separation leads to an early breakdown in the lift's response to a gust and, therefore, to a lower value for the maximum lift when nonlinear instead of time-linearized methods are used for the computations. This hypothesis will

be scrutinized in this work, together with the following additional hypotheses, to get a deeper insight:

- **A.** Unsteady nonlinear effects get stronger with increasing Mach number and decreasing excitation frequency.
- **B.** Similar basic nonlinear aerodynamic effects can be observed for a two-dimensional airfoil and a transport aircraft configuration.
- **C.** Specific aerodynamic stages for the response of the lift coefficient over time can be identified for a discrete gust encounter of a transport aircraft configuration.
- **D.** For a large-amplitude gust encounter of a two-dimensional airfoil in transonic flow, the maximum dynamic lift might result in larger values than the maximum static lift, implying a dynamic overshoot.
- **E.** The difference between time-linearized and nonlinear peak lift response is larger for purely aerodynamic simulations than for fluid-structure coupled simulations.
- **F.** The "critical gust length" depends on the excitation amplitude.

For context on the hypotheses, see Chapter 2, "Fundamentals and State-of-the-Art".

1.3 Objectives and Overview of this Thesis

This thesis will give insight into governing physical effects that arise when unsteady nonlinear aerodynamic models are used for the computation of large-amplitude gust responses. It gives orientation on steady base flow conditions and levels of excitation that might lead to specific nonlinear effects in the responses.

For this purpose, the thesis is structured as follows: Chapter 2 introduces the physical background of steady and unsteady aerodynamics that is necessary to interpret the final results. Different computational methods for unsteady aerodynamics are described, and the basics of gust analysis in the context of aircraft design are explained. In this chapter, the technical principles are explained, as well as the relevant current state-of-the-art, which provides the context for the above-mentioned hypotheses.

Chapter 3 presents the basic fluid mechanics equations together with details on the different turbulence models that are used. Moreover, the aeroelastic equations of motion are introduced, as well as the force summation method for the calculation of the final internal loads. Gust signals are described that are used for the excitation of the respective flow fields. Then, the numerical framework is introduced, which is used for the unsteady aerodynamic and aeroelastic computations. Finally, details are given on the post-processing of the responses.

Chapter 4 introduces models and test cases for the configurations considered: the two-

dimensional airfoil ”RAE2822” and the transport aircraft configuration ”NASA Common Research Model (CRM)”.

Chapter 5 and Chapter 6 introduce the results of the computations and an in-depth analysis of observed nonlinear effects. The main hypothesis and the additional hypotheses A – D will be investigated in Chapter 5. Purely aerodynamic results are analyzed with a first focus on monofrequent excitations of the flow field and the corresponding responses for the airfoil and the transport aircraft configuration. Basic nonlinear aerodynamic effects in the global lift response are worked out, and their connection to specific features in the steady and unsteady pressure distribution is shown. The aerodynamic responses to discrete, i.e., broadband, ”1-cos” gusts are subsequently analyzed for the same nonlinear aerodynamic effects and specific stages in the nonlinear lift response are derived.

Aeroelastic gust responses are treated in Chapter 6, investigating hypotheses E and F. Unsteady nonlinear responses of the wing root bending moment and corresponding critical gust lengths are analyzed. Differences and analogies between aerodynamic and aeroelastic lift responses conclude this chapter.

Chapter 7 summarizes the main findings and the responses to the hypotheses. It relates the findings to the current state-of-the-art. A final assessment of the findings from this work, including the implications for future work, is formulated in Chapter 8.

Additional information is presented in the Appendices A and B.

Remark
Note that some of the results are already published in the following two journal publications:

- [24] Friedewald, D.: Numerical Simulations on Unsteady Nonlinear Transonic Airfoil Flow. Aerospace, Vol. 8, No. 1, Art. 7, 2021, `https://doi.org/10.3390/aerospace8010007`
- [25] Friedewald, D.: Large-Amplitude Gusts on the NASA Common Research Model. Journal of Aircraft, Vol. 60, No. 6, pp. 1901–1916, 2023, `https://doi.org/10.2514/1.C037198`

2 Fundamentals and State-of-the-Art

This chapter introduces the fundamentals of steady and unsteady aerodynamics that are relevant to understand the following work. Different computational methods for unsteady aerodynamics are described together with their ability to model different physical effects. Finally, some background information on the computation of gusts in the context of aircraft design is presented.

2.1 Steady Aerodynamics

Airfoil Flow

This section first gathers the fundamentals for steady airfoil flows as it forms the basis for the investigations in this thesis. Trends from common aerodynamic textbooks, such as Anderson [26], Leishman [27], or Vos and Farokhi [28], are illustrated below using steady RANS-based simulation results of a NACA0012 at fully turbulent conditions for a Reynolds number of $Re = 6.5 \times 10^6$. Steady lift polars and lift curve slopes for different Mach numbers are shown in Fig. 2.1 and typical polar trends can be observed: Increasing the Mach number of the flow decreases the steady maximum lift C_L^{Max} and increases the lift curve slope $\partial C_L/\partial\alpha$ in the linear part of the polar. Independently of the Mach number, there is a linear range of the lift polar at low angles of attack, followed by a nonlinear range at higher steady angles of attack. The lower the Mach number, the bigger the linear angle-of-attack range. For low Mach numbers, the linear lift curve slope can be approximated reasonably well by $\partial C_L/\partial\alpha \approx 2\pi/\beta$, which corresponds to the slope for incompressible flow, 2π, multiplied by Glauert's compressibility correction

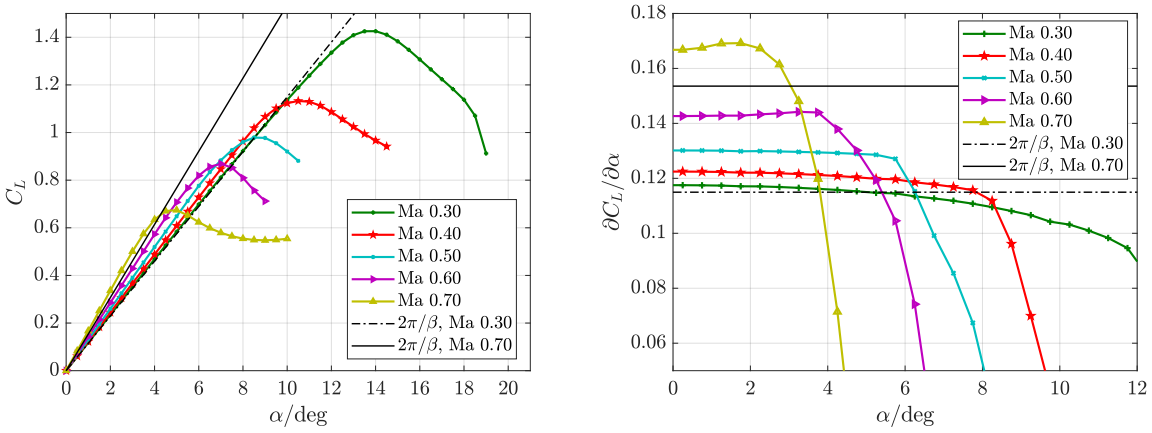

(a) Lift polars **(b)** Lift slopes

Fig. 2.1: Exemplary steady lift data for a NACA0012 airfoil

factor $1/\beta = 1/\sqrt{1 - Ma^2}$ [29], where Ma denotes the Mach number. For higher Mach numbers, however, this approximation does not agree well anymore due to viscous effects, compare the curves, e.g., for Mach 0.70.

Linear and nonlinear parts of the lift polar can be attributed to different flow fields, which are illustrated exemplarily in Fig. 2.2 and Fig. 2.3 for the NACA0012 at Mach 0.70. At lower angles of attack, the flow is fully subsonic, i.e. the minimum pressure is below the critical pressure value and, hence, Mach < 1 in the flow field ($\alpha = 0.5$ deg). Moreover, the flow is completely attached. With an increasing angle of attack, the flow is accelerated on the upper side of the airfoil, and supersonic velocities are locally reached, which are terminated by a recompression shock ($\alpha = 2.0$ deg). Transonic flow conditions have developed, however, the flow is still fully attached. The shock position shifts downstream with a further increasing angle of attack, shock strength grows, and shock-induced separation finally starts to occur ($\alpha = 4.0$ deg). The flow can reattach at moderate angles of attack, as only a small separation bubble is present downstream of the shock. With

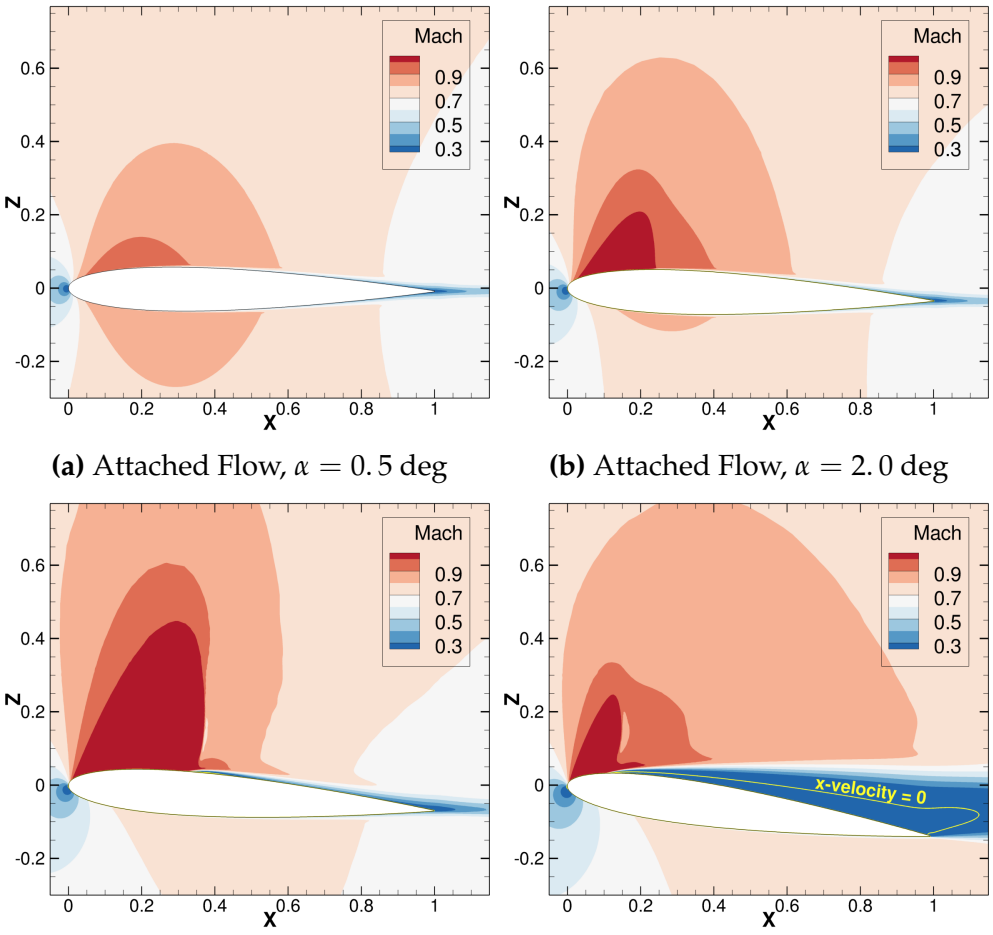

(a) Attached Flow, $\alpha = 0.5$ deg

(b) Attached Flow, $\alpha = 2.0$ deg

(c) Pre-Stall, $\alpha = 4.0$ deg

(d) Stall, $\alpha = 8.0$ deg

Fig. 2.2: Flow fields for a NACA0012 at Mach 0.70

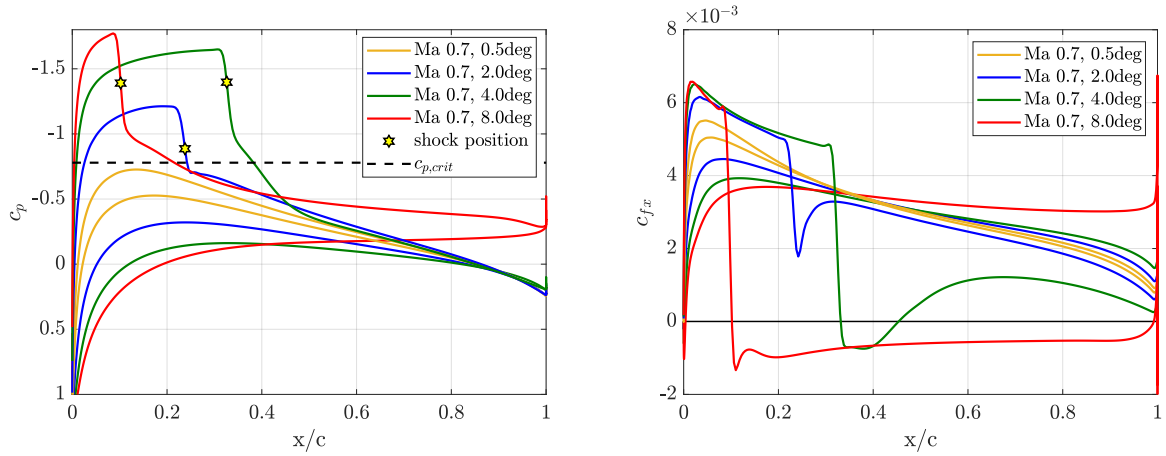

(a) Pressure coefficients with detected shocks **(b)** Skin friction coefficients

Fig. 2.3: Surface pressure and skin friction distribution for a NACA0012 at Mach 0.70

further increasing angle of attack, the size of the separation bubble grows until, at some point, the shock position starts to shift upstream again. At slightly higher angles of attack, first, the maximum steady lift is reached and second, the flow becomes fully separated behind the shock. A significant decrease of the lift can be observed. At this point, the flow is fully stalled ($\alpha = 8.0$ deg). It can be expected, that the linearity of the lift polar is lost, when recompression shocks are developed, as can, e.g., be derived by data from Nitzsche et al. [30].

In the surface solutions of the simulations, a shock is detected if the pressure coefficient on the surface of the airfoil is lower than the isentropic critical pressure value $c_{p,crit}$, i.e., the local Mach number is higher than 1.0. In this case, the x-position of the maximum pressure gradient is defined to be the shock position. Separation is detected if the x-component of the skin friction vector c_{fx} is lower than zero.

Fig. 2.4 illustrates shock formation and separation patterns for different Mach numbers. It becomes clear that shock-induced separation dominates for Mach 0.70 and does also

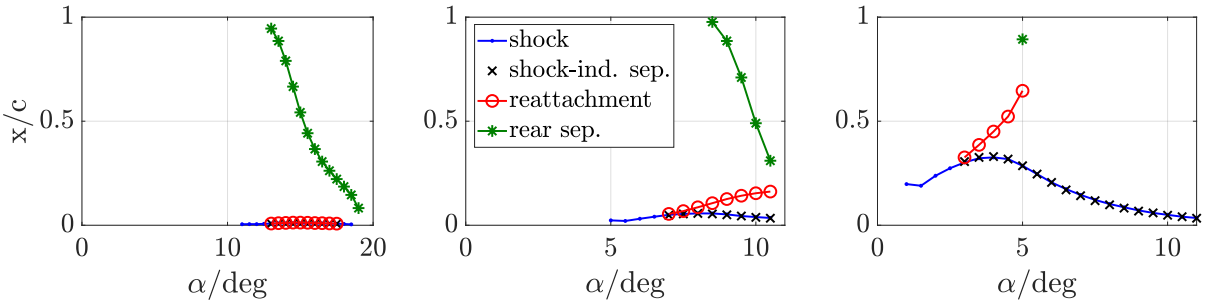

(a) Mach 0.30 **(b)** Mach 0.50 **(c)** Mach 0.70

Fig. 2.4: Formation of shocks and separation patterns for a NACA0012 at $Re = 6.5 \times 10^6$

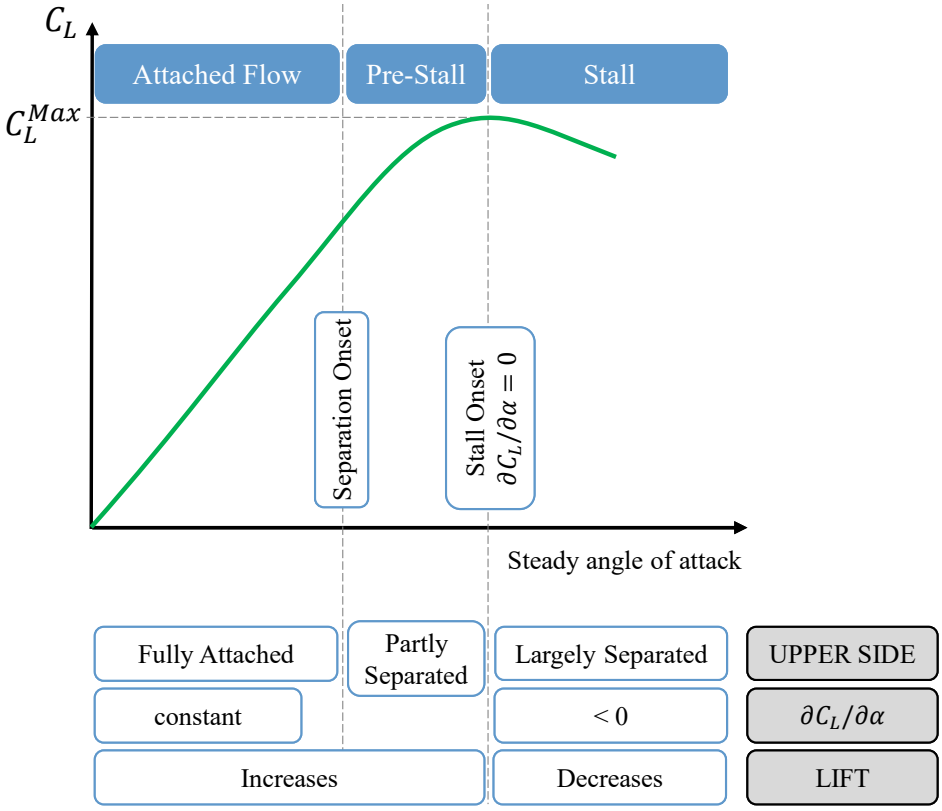

Fig. 2.5: Classification of steady airfoil flow

exist for Mach 0.30. For the latter, however, trailing edge separation is the dominating separation mechanism for these specific conditions. Moreover, the supersonic region only develops in a very narrow region close to the leading edge (x/c < 2%) and does not shift significantly further downstream. For Mach numbers in between, e.g., Mach 0.50, both types of separation play a significant role. Note that the specific separation behavior differs depending on the airfoil and the flow conditions. Various stall types are defined in literature [28, 31, 32].

For medium to high Mach numbers, the shock position shifts downstream with increasing angle of attack, but only up to a certain point. For larger angles of attack, a so-called "inverse shock motion" is established, i.e., the shock shifts upstream with increasing angle of attack. This behavior was observed in experiments by Pearcey in 1959 [33] and, e.g., by McDevitt and Okuno in 1985 [34]. This range of increasingly upstream shock positions is often associated with the range of potential shock buffet [30, 34], i.e., a global aerodynamic instability [35–37].

Finally, Fig. 2.5 summarizes the current understanding of the general properties for steady airfoil flow as described above. In this work, three stages in an airfoil's lift polar are distinguished: Attached Flow, Pre-Stall, and Stall.

Flow on Transport Aircraft Configurations

The general physical trends that are described above for airfoil configurations also apply to the wings of transport aircraft configurations. However, the additional spanwise component of the flow introduces a smearing of the local effects so that the trends in the resulting global forces and coefficients are smoothened compared to the two-dimensional cases.

The series of AIAA's Drag Prediction Workshop in the last two decades shows a significant increase in the modeling quality of RANS-based CFD solvers in the past decades, when it comes to the prediction of aircraft configurations at cruise flight conditions [38, 39]. Already in the 2010s, the aircraft industry states that "CFD is widely developed for the cruise design regime" [40]. However, it "still faces essential challenges towards the borders of the flight envelope" [40]. Flow conditions including significant flow separation, still pose a major challenge in the predictive capabilities of full aircraft configurations [41].

Among other things, the extent of a potentially existing side-of-body (SOB) separation at the wing-fuselage junction is under discussion, as various publications show [42–45]. This SOB can be very large in numerical simulations under certain conditions, but it is probably overestimated. Reliable experimental data to validate the numerical models for this effect hardly exist so far.

2.2 Unsteady Nonlinear Aerodynamics

Subsonic Flow

Unsteady nonlinear effects in subsonic flows are investigated intensively since the end of the 1960s. The term "dynamic stall" is closely connected with the rotary-wing community. It describes "an unsteady aerodynamic phenomenon resulting from the combination of high angles of attack and a rapid angle of attack change of a lifting surface during which the flow separates" [46]. This phenomenon has already been known for a relatively long time, but is still not entirely understood, as there are too many influencing variables. Among others, McCroskey et al. [32], Leishman [27], Choudhry et al. [47] and Gardner et al. [46] provide a comprehensive overview of this topic. The term "dynamic overshoot" is often used in the field of helicopter dynamic stall [32] and describes a dynamic exceeding of the steady maximum lift. Related physical mechanisms are discussed in detail in Ericsson and Reding [48]: dynamic effects lead to a more stable boundary layer, and so the onset of flow separation is delayed. In consequence, the instantaneous dynamic lift can reach higher values than the static maximum. Additionally, a leading-edge vortex ("Dy-

namic Stall Vortex", DSV) might occur, so the dynamic maximum lift might be increased even more.

For subsonic flows, this correlation seems to be generally accepted. For shock-induced dynamic stall, which occurs at higher Mach numbers, the DSV seems to play a secondary role if any at all: Based on wind tunnel tests, Liiva [49] showed, that the occurrence of a recompression shock changes the unsteady flow dynamics fundamentally compared to subsonic flows. There is no sudden separation at the leading edge, but separation takes place behind the recompression shock. Visbal [50] confirms these findings, stating that for high Mach numbers, the "dynamic stall process is controlled by the shock/boundary-layer interaction rather than by the formation of a leading-edge vortex". There seems to be a consensus, however, that the effect of the Mach number on the process of dynamic stall is not well understood and requires more investigation [47, 51]. Especially the existence of dynamic overshoots in transonic flow is not yet sufficiently investigated. One of the very early dynamic stall publications is even questioning their existence [52].

At the end of the 2010s, Mallik and Raveh [22] report RANS-based gust responses in subsonic flows at low and high angles of attack for a NACA0012 airfoil and a High-Altitude Long-Endurance (HALE) configuration. They point out the importance of the steady-state flow field: at high angles of attack (i.e., close to the onset of steady stall conditions) short gusts can induce significantly higher loads than at lower angles of attack due to the formation of a DSV. By adding a very flexible structural model, the authors observe that the effect for the peak responses might be reversed if the first elastic mode interacts with the flow separation and the arising DSV.

Though physics-based empirical models exist for the prediction of unsteady nonlinear subsonic flow (so-called "Dynamic Stall models", e.g. [53–55]) it seems to be an open question if such models for large-amplitude excitations can be developed in a general formulation also for unsteady nonlinear transonic flows. A theoretical framework based on physical correlations is currently not available for this type of flow.

Transonic Flow, Early Findings

A comprehensive overview of unsteady linear transonic aerodynamics on different airfoils is given by Tijdeman in 1977 [56]. Based on experiments on a thin, conventional NACA64A006 airfoil with harmonic flap oscillations and a supercritical pitching NLR7301 airfoil he categorized three basic types of unsteady shock motion and identified the shock strength as the key parameter in the dynamic system. It is emphasized that an oscillating recompression shock does not imply an unsteady nonlinear response per se, as all unsteady responses resulted in a linear behavior. Pitching amplitudes up to 0.5 deg at Mach 0.70 were tested.

In 1981, Dowell et al. [57] showed first numerical results on amplitude nonlinearities in unsteady transonic airfoil flows using LTRAN2 (low frequency, transonic small disturbance procedure). Numerical solutions were evaluated for a pitching NACA64A006 airfoil at several transonic Mach numbers. One of the findings was a frequency- and amplitude-dependent boundary between linear and nonlinear aerodynamic behavior with the term ”nonlinear” referring to a 5% deviation from the linear pitching moment derivative. It was shown that this boundary corresponds to a motion of the computed recompression shock of about 5% over the airfoil’s chord. Moreover, it was found that nonlinear effects decrease with increasing excitation frequency and that the inflow Mach number changes the linear/nonlinear boundary.

McCroskey summarizes the main findings from numerical and experimental studies at the beginning of the 1980s [58] and illustrates different ”unsteady flow regimes for a transonic airfoil”. The range of nonlinear responses is expected for low to medium excitation frequencies, where possibly large shock motions occur. Once the shock motion is small enough, only linear responses are triggered. McCroskey suggests using different numerical methods for different frequency ranges to compute responses as accurately as necessary but at the same time as fast as possible.

Besides these early findings, deeper insight into unsteady nonlinear transonic flow could not be expected at that time since neither experimental data nor reliable numerical data were available. More accurate analysis and prediction of unsteady transonic flows required more mature numerical methods together with an increase in computational power.

Transonic Flow, Modern Literature

Numerical studies on amplitude effects in transonic flows are a rather young field of research: It took until the 2010s that studies based on URANS simulations emerged, which dealt with transonic large-amplitude gust excitations, see [6, 19–21, 23, 59, 60]. Most of these studies focus on the resulting loads and only marginally on the aerodynamics involved. Mainly complex three-dimensional aeroelastic configurations are analyzed during ”1-cos” gust encounters, probably since the CS-25 demands these broadband excitations. There seems to be a consensus that responses to long ”1-cos” gusts are more affected by amplitude effects than responses to short gusts.

High-fidelity gust encounter simulations, including structural coupling and flight mechanics modeling are carried out by Reimer et al. [21]. It is shown that the purely aerodynamic response leads to the highest peak loads, whereas the integration of additional disciplines leads to a loads reduction in any case. Moreover, the applied DLM-based pro-

cess produces higher loads than the CFD-based process, emphasizing the importance of viscous effects in transonic and subsonic flows.

A quasi-steady doublet-lattice correction method is applied to gust encounter simulations by Friedewald et al. [23]. A swept wing and a rigid transport aircraft configuration are subjected to "1-cos" gusts of different lengths and amplitudes. It is found that the normalized peak lift coefficient decreases with increasing excitation amplitude, corresponding to a significantly altered frequency response spectrum. The nonlinear responses are induced by flow separation, whose effects cannot be modeled by the doublet-lattice correction.

Amplitude effects on an aeroelastic transport aircraft configuration are investigated by Kaiser et al. [19]. The data suggest that there seems to be no clear trend concerning the peak load estimation for this configuration: Depending on gust length and amplitude, the application of a nonlinear aerodynamic method can either lead to a decrease or an increase in the computed peak loads in comparison to a time-linearized method. It is shown that both minimum and maximum wing bending moments are affected, as well as the computed torsional moments. It remains an open question what causes these different trends and to what extent this can be generalized. However, there are indications that the correct modeling of the shock motion plays an important role in the computation of large-amplitude excitations and that this motion cannot be correctly modeled using the LFD [19, 59]. URANS-based time-marching methods produce superior results here.

The influence of different turbulence models on large-amplitude gust responses is studied by Feldwisch [20]. Though their different separation characteristics affect the range of responses for the excited structural frequencies, general trends with respect to peak load prediction are comparable between the models.

Experiments on Large-Amplitude Gust Encounters in Transonic Flows

Experimental data for gust responses in subsonic and transonic flow only seems to be available for small-amplitude excitations, as the literature survey from 2017 by Lancelot et al. [61] shows. Between 1966 and 2017, 21 different gust generators have been built worldwide, where only five of them operate in transonic conditions. An additional setup for transonic gust studies was recently published [62]. All of the experiments show the same characteristics: None of the built gust generators significantly exceeds gust-induced angles of attack of more than one degree. Moreover, the implementation of a distinct gust velocity profile in the wind tunnel seems to be a major challenge, independently of the gust generator concept.

2.3 Computational Methods for Unsteady Aerodynamics

One of the first analytical solution for the flow around a harmonically oscillating airfoil was found by Theodorsen and Mutchler [63], who solved this problem for an inviscid, incompressible two-dimensional flow under the assumption of small disturbances. Their frequency-domain approach can be transformed into time-domain, resulting in the formulations established by Wagner [64] for responses to a step change in the angle of attack. A decade later, Küssner [65] and Sears [66, 67] formulated analytical solutions for responses to harmonic gust disturbances in time- and frequency-domain, respectively. Still, these are valid only for the assumptions of inviscid and incompressible thin-airfoil flow and small disturbances.

Generally speaking, in these simplified types of flows, unsteady effects cause an amplitude reduction and a phase lag of the response compared to their quasi-steady counterparts for low- to moderate excitation frequencies. Besides the frequency of the excitation, only the type of motion (e.g., heave or pitch) or the external disturbance (e.g., gust) influences the response.

An important parameter in the description of unsteady aerodynamics is the so-called "reduced frequency" k, which serves as a dimensionless quantity and is defined as follows

$$k = \frac{2\pi f \, l_{ref}}{U_\infty}. \tag{2.1}$$

The freestream velocity is denoted by U_∞, the excitation frequency by f, and a characteristic length of the configuration by l_{ref}. Note that some publications use only half of the characteristic length for the definition of the reduced frequency, which is not the case in this work.

For realistic flow conditions during flight, however, effects of compressibility and viscosity must be taken into account, as well as the realistic geometry, including the exact airfoil shape. With increasing physical insight, mathematical knowledge, and computational power, a variety of computational methods for fluid dynamics have been developed over the last century. In the 1970s, e.g. the Doublet-Lattice method (DLM) was developed [7, 68], and facilitated the computation of unsteady three-dimensional compressible flows. Though the geometric representation of the lifting surfaces in this panel method is still very simple, and viscosity is not taken into account, the method computes responses to harmonic excitations very fast, robust, and at the same time reasonably accurate for subsonic flows. Furthermore, since it is a method based on potential theory, it is capable of predicting only time-linearized responses. Naturally, this method has its deficiencies when it comes to the prediction of transonic or even separated flows. Numerous DLM-correction methods [8–15] based on experimental or numerical data were

developed to overcome these shortcomings, however, none of them can fully eliminate them.

Since the 1990s, solvers based on RANS-equations emerged, which can model the effects of viscosity and compressibility and are therefore well-suited for the computation of transonic flows at complex configurations. Linear and nonlinear steady and unsteady phenomena can be modeled with these type of solvers. Their biggest disadvantage is the need for large computational power. For this reason, unsteady time-marching computations on a larger scale have only been feasible since the 2010s. However, this improved model fidelity now provides physical insight complementary to experimental data from wind tunnel tests. Consequently, modern aircraft design includes numerous steady and unsteady numerical calculations in addition to conventional wind tunnel tests. Due to the increased confidence in these methods, it is even considered to reduce the number of flight tests during the certification process and replace them with numerical simulations [69].

From a modeling perspective, the conditions of a fully attached flow can be satisfactorily modeled using a steady RANS approach. Different turbulence models result in almost identical solutions for the linear part of the polar. Differences only start to occur with the onset of flow separation, see e.g. [30], and none of the models is exclusively superior. However, unsteady RANS simulations seem to be capable of capturing main flow features of unsteady separated flows, as comparative studies to more expensive numerical approaches show [70,71]. Especially the turbulence model of Spalart and Allmaras [72] is widely used in aircraft aerodynamics. Though it is based on only one equation for turbulent closure, it predicts the flow physics at the design point of a typical transport aircraft configuration with good agreement to experimental data [38]. Even in off-design conditions, it reproduces some of the main features of transonic separated flows in reasonable agreement to experiments [36]. Though validation data for large-amplitude excitations in transonic flow is missing, wind tunnel data for small-amplitude gust responses can be used to validate numerical methods within the given scope. This was, e.g., done successfully for a gust experiment in the transonic wind tunnel Göttingen (DNW-TWG) by Neumann and Mai [73]. Steady and unsteady features of the flow are well captured, though it needed a complex numerical setup.

Striving for reduced computational costs while keeping the effects of steady nonlinearities as, e.g., recompression shocks, linear frequency domain (LFD) solvers matured in the 2010s, that allow solving the time-linearized RANS equations for their first harmonic small-disturbance solution. These solvers are applied, e.g., for CFD-based flutter computations [74], or the prediction of gust loads [19,75,76]. They even start to replace potential-

theory-based load computations in the industrial context [17] due to their increase in accuracy but comparably short computational times. Moreover, these solvers are quite robust, especially in comparison to URANS-based time-marching methods. However, due to their time-linearized formulation these solvers have their shortcomings when it comes to the computation of responses to large-amplitude excitations. Kaiser et al. [19] show that the unsteady motion of the transonic recompression shock and the changes in shock strength are not modeled correctly for large-amplitude responses.

Summing up, numerical simulations have reached a status in the last decade that allows for conducting "numerical experiments": reliable and accurate methods are available to gain physical insight in phenomena, which might be difficult to obtain under wind tunnel or flight test conditions.

2.4 Gusts for Aircraft Design

General Background

Gusts are atmospheric motions that induce a disturbed velocity field. As a result, they cause altered aerodynamics and, thus, altered loads on the aircraft. The aircraft's response to a gust results in a compensatory flight dynamics motion, as well as in altered stresses and strains in the structure. The first NACA report from 1915 already addresses this topic and describes an analytical approach to calculating any gust loads on the aircraft [77]. Since then, there has been a continuous development of the certification regulations, both in the definition of gusts, as well as in the models and methods used to calculate the loads. Detailed descriptions of the relevant history can be found in Donely (1949) [78], Houbolt (1973) [79], Etkin (1981) [80], Hoblit (1988) [5], Murrow et al. (1989) [81], Barnes (1990) [82], and Fuller (1995 and 1997) [83, 84]. The current requirements for calculating gust loads on transport aircraft were established in the year 1996 [84]. At the same time, the regulations of the European and American certification authorities were harmonized [82]. The current certification specifications for large transport aircraft distinguish between two types of atmospheric disturbances: discrete gust design criteria are listed in CS 25.341 (a) and continuous turbulence design criteria are described in CS 25.341 (b). For both types, internal loads and stresses need to be computed, taking into account all relevant disciplines: flight dynamics, structural dynamics, unsteady aerodynamics, and, if existent, also control system dynamics. Active control systems are standard in modern transport aircraft, including systems for gust load reduction, see [85, 86] for more detailed information on this topic.

Discrete Gust Encounters as demanded by CS-25

In this thesis, the focus is on discrete gust encounters as one possibility of atmospheric disturbances. The respective "Certification Specifications for Large Aeroplanes" (CS-25) demand that a "sufficient number of gust gradient distances" is considered for the certification of a transport aircraft configuration, see CS 25.341 "Gust and turbulence loads" [4]. The discrete gust profile that needs to be considered has a "1-cos" shape and the actual gust velocity W_G is defined by

$$W_G(x) = \begin{cases} \frac{\widehat{W}_G}{2}\left(1 - \cos\left(\pi H^{-1} t U_\infty\right)\right) & \text{for } 0 \leq t \leq (2H/U_\infty) \\ 0 & \text{else.} \end{cases} \tag{2.2}$$

The gust gradient H corresponds to half the gust length, L_G, and it is defined in parallel to the airplane's flight path. It ranges between 9 m and at least 107 m. Longer gust gradients are requested if $12.5 \cdot c_{MAC} > 107.0$ m. However, no specific reference value for the maximum gust gradient is given that needs to be covered beyond $H = 107.0$ m.

The amplitude of the gust velocity $\widehat{W}_G$ (in "Equivalent Airspeed", EAS) is calculated by

$$\widehat{W}_G = U_{ref} F_g \left(\frac{H}{107}\right)^{1/6} \tag{2.3}$$

with H in m.

The reference velocity U_{ref} is prescribed in EAS by CS-25 [4] and depends on the altitude and the selected design velocity, see Fig. 2.6. The different design speeds of an aircraft are described by V_B as design speed for maximum gust intensity, V_C as design cruise speed, and V_D as design dive speed [4]. The flight profile alleviation factor, F_g, varies linearly between 0 and 1, depending on the aircraft's weight, its maximum operating altitude, and the flight altitude. Table 2.1 highlights typical aircraft data following Jenkins [87],

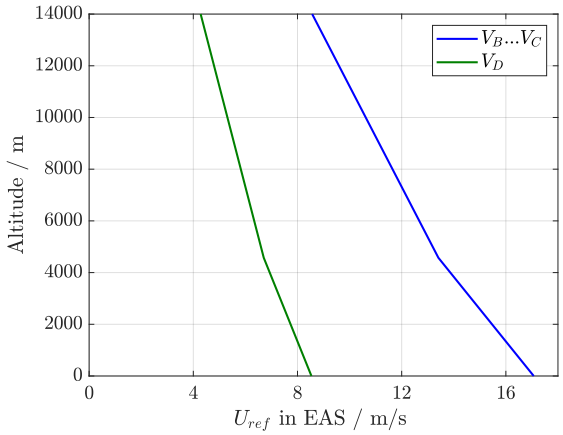

Fig. 2.6: Reference gust velocity U_{ref}

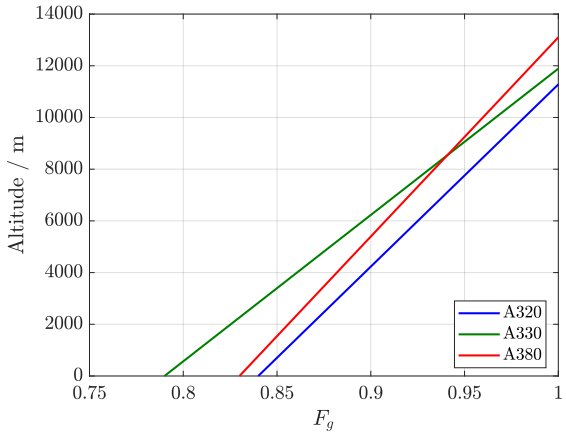

Fig. 2.7: Flight profile alleviation factor F_g

Table 2.1: Dimensions and weights for different Airbus aircraft [87]

Airbus aircraft	A320	A330	A380
c_{MAC}	4. 29 m	7. 26 m	12. 02 m
max. operating altitude	11 280 m	11 890 m	13 100 m
max. landing weight	64 500 kg	177 190 kg	381 000 kg
max. zero fuel weight	60 500 kg	165 142 kg	356 000 kg
max. take-off weight	73 500 kg	230 000 kg	540 000 kg
F_g at sea level	0.84	0.79	0.83

allowing the determination of the specific factor F_g. Results for three exemplary aircraft types, representing a short, medium and long range aircraft, are shown in Fig. 2.7. The CS-25 demand the computation of vertical and lateral gusts. In this thesis, only vertical gusts are considered.

Gathering the above real-world aircraft data, typical gust lengths and amplitudes can be derived, which serve as an orientation for the parameter space that is investigated in this thesis. Typical gust lengths result in $L_G/c_{MAC} \approx 1.5$ to $L_G/c_{MAC} \approx 50$. Maximal certification-relevant gust amplitudes at an altitude of 10 km are in the order of $\widehat{W}_G \approx 15.0$ m/s in true air speed (TAS).

Critical Gust Length in Aeroelastic Responses

In a time-linearized and purely aerodynamic system, it can be expected that larger excitation amplitudes lead to higher peak lift values. Similarly, longer gusts induce higher peak lift values than shorter gusts. These effects can be observed in the time-linearized aerodynamic results, independently of the configuration or flow condition considered. There is no restoring mechanism in a linear aerodynamic system as long as the steady base flow corresponds to attached flow conditions. For a fluid-structure coupled system, however, the time-linearized responses show decreasing peak values for gusts beyond a certain length as the structural forces counteract the aerodynamic forces. This effect is mainly caused by the reaction of the rigid-body modes of the aircraft to the gust excitation, as described in Hoblit [5]. The gust length for maximum peak forces or moments is usually referred to as ”critical gust”, ”tuned gust”, or ”worst-case gust”. It is a key parameter during the load computation in aircraft design.

Due to the complexity of the aeroelastic system, it is not straightforward to estimate the critical gust length for a specific quantity of interest, not even for a time-linearized sys-

tem. Several methods exist to predict critical gust lengths for a given configuration at specific flight conditions, e.g., [88–90]. Ideally, these methods aim for the smallest possible number of computations. In an industrial context, a Monte Carlo search seems to be common practice [88].

One of the simplest methods to estimate a critical load factor for a specific aircraft design is the so-called "Pratt method" [91], which is also applied for the certification of smaller aircraft configurations in CS-23 [92]. It assumes a single critical gust length of $L_G = 25\,c_{MAC}$, which is a value that can be tracked back to in-flight measurements on aircraft configurations by the NACA (National Advisory Committee for Aeronautics) in the 1940s [78]. Flomenhoft recapitulates in 1994: "[It is] based on oscillograph recordings of gust loads, from which it was noted by the NACA that the maximum gust loads in the records tended to rise to a peak in 10 chord lengths traveled." [93]. While in the 1940s, the gust's shape was assumed to be triangular, and the critical gust length was assumed to be ten chord lengths, the gust model was changed to a "more rational discrete gust" [93] in the 1950s: An equivalent 12.5-chord gust gradient (gust length of $L_G = 25\,c_{MAC}$) exchanged the 10-chord linear ramp for the critical analysis. Historical details can be found in the reviews by Murrow, Pratt, and Houbolt [81] and Fuller [83].

3 Methods and Tools

The first part of this chapter addresses the field of fluid mechanics and introduces the basic sets of equations, followed by a description of the fluid-structure coupled, i.e., aeroelastic, system. Applied gust signals are defined, and the framework for the numerical simulations is described. The chapter ends with some details on the post-processing of the response signals.

3.1 Fundamental Equations of Fluid Mechanics

In this section, the fundamental equations of fluid mechanics are examined as they are presented in [94, 95]. All fluid mechanics equations of motion are based on the principle of conservation. Mass, momentum, and energy properties are considered in a closed control volume. All kinds of flow can then be characterized by the transport of these variables over the boundaries of the specific control volume (flux), the impact of internal and external forces on the control volume, and any additional sources and sinks. Convective fluxes are proportional to the flow velocity, diffusive fluxes depend on a specific gradient. In the following, the conservation equations will be written in their differential form for three-dimensional cartesian coordinates, i.e. the indices i and j equal 1,2,3 and Einstein's summation convention is valid.

Mass conservation

The formulation of the mass conservation leads to

$$\frac{\partial \rho}{\partial t} + \frac{\partial \left(\rho u_i\right)}{\partial x_i} = 0, \tag{3.1}$$

with the density ρ, the time t, the velocity vector $u_i = (u_1,u_2,u_3) = (u,v,w)$ and the cartesian coordinates $x_i = (x_1,x_2,x_3) = (x,y,z)$. In a closed control volume without any sources or sinks, mass can neither be developed nor destroyed.

Momentum conservation

The conservation of momentum in the absence of any body- or volume forces (such as, e.g., gravitational forces or centrifugal forces) can be formulated as

$$\frac{\partial(\rho u_i)}{\partial t} + \frac{\partial(\rho u_i u_j)}{\partial x_j} = \frac{\partial \tau_{ij}}{\partial x_j} - \frac{\partial p}{\partial x_i}. \tag{3.2}$$

The aerodynamic forces that are considered in this thesis arise either from pressures p or from (viscous) shear stresses τ acting on a specific surface. Therefore, the total stress tensor σ_{ij} results in

$$\sigma_{ij} = -p\delta_{ij} + \tau_{ij}, \tag{3.3}$$

with δ_{ij} as Kronecker delta. Due to the conservation of angular momentum, the stress tensor is assumed to be symmetric $\sigma = \sigma^T$. Moreover, for a Newtonian fluid, the viscous stresses are proportional to the strain rate, with the dynamic viscosity μ as the proportionality factor

$$\tau_{ij} = 2\mu S_{ij} - \frac{2}{3}\mu \frac{\partial u_j}{\partial x_j}\delta_{ij}. \tag{3.4}$$

The tensor of the strain rate S_{ij} takes the form

$$S_{ij} = \frac{1}{2}\left(\frac{\partial u_i}{\partial x_j} - \frac{\partial u_j}{\partial x_i}\right). \tag{3.5}$$

Conservation of Energy

The total energy E is calculated by the sum of the inner energy e and the kinetic energy of the fluid

$$E = e + \frac{|u_i|^2}{2}. \tag{3.6}$$

In the absence of any heat sources, the conservation of the total energy E can be formulated as

$$\frac{\partial \rho E}{\partial t} + \frac{\partial(\rho u_j H)}{\partial x_j} = \frac{\partial(u_i \tau_{ij})}{\partial x_j} + \frac{\partial}{\partial x_j}\left(k\frac{\partial T}{\partial x_j}\right), \tag{3.7}$$

with the thermal conductivity coefficient k and the absolute static temperature T. The total enthalpy H is defined by

$$H = E + \frac{p}{\rho} = h + \frac{|u_i|^2}{2} \tag{3.8}$$

with h as the inner enthalpy. Additionally to the five Navier-Stokes equations (3.1), (3.2), (3.7), two thermodynamic equations are needed to solve for the seven unknown flow field variables ρ, u, v, w, E, p and T. Both equations are based on the assumption of an ideal gas: the equation of state

$$p = \rho R T \tag{3.9}$$

and the definition of the inner energy

$$e = c_v T. \tag{3.10}$$

The specific gas constant for air is $R = 287.05 \frac{J}{kg\,K}$ and c_v denotes the heat capacity at constant volume (isochoric condition).

3.2 Turbulence Modeling: RANS approach

Having introduced the fundamental equations of fluid mechanics, the focus shall now be on the modeling of turbulent flows, for which different approaches exist, such as the

Direct Numerical Simulation (DNS) or the Large-Eddy Simulation (LES), see e.g. [94]. For most of the practical applications, knowledge of the time-averaged values of the different flow variables are sufficient. Hence, the currently most widespread approach is based on turbulence modeling using the RANS equations. The difficulty of this approach is the appropriate formulation of the unknown Reynolds stresses, as will be shown later on.

Reynolds averaging

Following the theory of Reynolds, every flow variable (such as the pressure p) can be split up into a time-averaged value $\overline{p}$ and a fluctuation p' about it

$$p(x_i,t) = \overline{p}(x_i) + p'(x_i,t). \tag{3.11}$$

The mean values for statistically steady flow are defined as

$$\overline{p}(x_i) = \lim_{T\to\infty} \frac{1}{T} \int_t^{t+T} p(x_i,t)\, dt \tag{3.12}$$

where t denotes the time and T the averaging interval, see Fig. 3.1(a). For statistically unsteady flow, time-averaging can not be applied, but an ensemble average needs to be used

$$\overline{p}(x_i,t) = \lim_{N\to\infty} \frac{1}{N} \sum_{n=1}^{N} p_n(x_i,t), \tag{3.13}$$

with N as the number of repetitions, see Fig. 3.1(b). N needs to be large enough in order to eliminate the influence of the turbulent fluctuations.

Favre averaging

For flows without a constant density throughout the flow field a density-weighted averaging (Favre averaging) should be carried out for some of the flow quantities instead of a Reynolds averaging. The Favre decomposition, e.g., for the flow velocity, consists of a

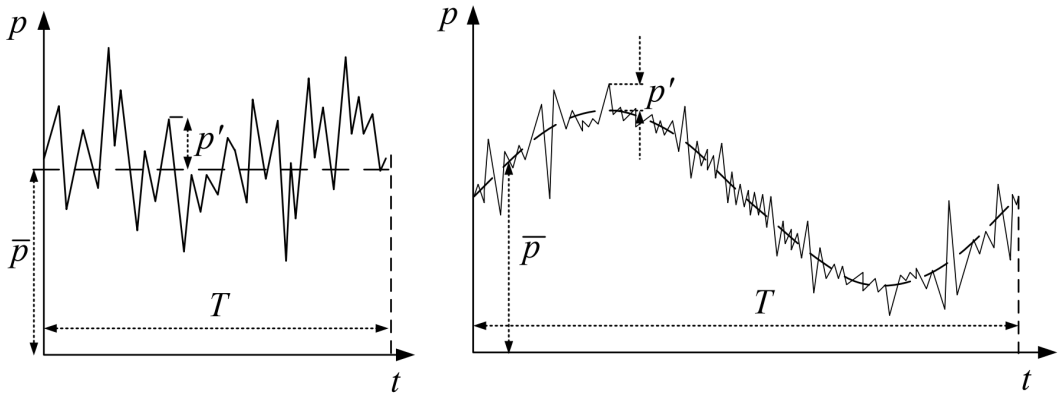

(a) Time averaging for steady flow **(b)** Ensemble averaging for unsteady flow

Fig. 3.1: Averaging for steady and unsteady flow [94]

mean value $\widetilde{u}_i$ and a fluctuation u_i''

$$u_i = \widetilde{u}_i + u_i''. \tag{3.14}$$

The mean value is defined by

$$\widetilde{u}_i = \frac{1}{\overline{\rho}} \lim_{T\to\infty} \frac{1}{T} \int_t^{t+T} \rho u_i \, dt = \frac{\overline{\rho u_i}}{\overline{\rho}}, \tag{3.15}$$

with the Reynolds averaged density $\overline{\rho}$. What is different compared to the Reynolds averaging, is that the following mean value vanishes

$$\overline{\rho u_i''} = 0. \tag{3.16}$$

Favre- and Reynolds-averaged Navier-Stokes equations

For applying the Navier-Stokes equations to compressible flows, usually Reynolds-averaging is used to calculate the flow variables of density and pressure. All other variables are decomposed using Favre averaging [94]. After the appropriate decompositions, the final equations read

– Favre- and Reynolds-averaged conservation of mass

$$\frac{\partial \overline{\rho}}{\partial t} + \frac{\partial \overline{\rho}\widetilde{u}_i}{\partial x_i} = 0 \tag{3.17}$$

– Favre- and Reynolds-averaged conservation of momentum

$$\frac{\partial \overline{\rho}\widetilde{u}_i}{\partial t} + \frac{\partial \overline{\rho}\widetilde{u}_i\widetilde{u}_j}{\partial x_j} = -\frac{\partial \overline{p}}{\partial x_i} + \frac{\partial \left(\widetilde{\tau}_{ij} - \overline{\rho}\widetilde{u_i''u_j''}\right)}{\partial x_j} \tag{3.18}$$

– Favre- and Reynolds-averaged conservation of energy

$$\frac{\partial \overline{\rho}\widetilde{E}}{\partial t} + \frac{\partial \overline{\rho}\widetilde{u}_j\widetilde{H}}{\partial x_j} = \frac{\partial}{\partial x_j}\left(k\frac{\partial \widetilde{T}}{\partial x_j} - \overline{\rho}\widetilde{u_j''h''} + \widetilde{\tau u_i''} - \overline{\rho}\widetilde{u_j''K}\right) + \frac{\partial}{\partial x_j}\left[\widetilde{u}_i\left(\widetilde{\tau}_{ij} - \overline{\rho}\widetilde{u_i''u_j''}\right)\right] \tag{3.19}$$

Note: The Favre- and Reynolds-Averaged Navier-Stokes equations are often only referred to as RANS equations. Though this notation is incomplete, it is used throughout this thesis for reasons of consistency with other literature.

The equations above introduce an important term $\tau_{ij}^F = -\overline{\rho}\widetilde{u_i''u_j''}$, which is called the Favre-averaged Reynolds-stress tensor. It comprises six additional unknowns, which can, e.g., be modeled on the basis of the eddy-viscosity hypothesis or which can be solved for directly using so-called Reynolds-stress models. Both approaches are shortly described below.

Eddy-Viscosity hypothesis

Currently established turbulence models are based on the linear eddy-viscosity hypothesis introduced by Boussinesq. It is assumed that turbulent shear stresses are linearly proportional to the Reynolds-averaged strain-rate tensor $\widetilde{S}$. Analogously to the definition of the shear stresses τ_{ij}, equation (3.4), the Favre-averaged Reynolds-stress tensor can be expressed as

$$\tau_{ij}^{F} = -\overline{\rho}\widetilde{u_i'' u_j''} = 2\mu_T \widetilde{S}_{ij} - \frac{2}{3}\mu_T \frac{\partial u_k}{\partial x_k}\delta_{ij} - \frac{2}{3}\overline{\rho}\widetilde{K}\delta_{ij}, \tag{3.20}$$

In order to be consistent with the definition of the turbulent kinetic energy K, the term $-\frac{2}{3}\overline{\rho}\widetilde{K}\delta_{ij}$ needs to be introduced additionally. The corresponding Favre-average reads

$$\overline{\rho}\widetilde{K} = \frac{1}{2}\overline{\rho}\widetilde{u_i'' u_i''}. \tag{3.21}$$

The eddy-viscosity μ_T defines the factor of proportionality. It is not a physical property of the fluid but depends on local flow conditions and history effects. The eddy-viscosity is also needed for the definition of the turbulent transport of heat

$$\overline{\rho}\widetilde{u_j'' h''} = -k_T \frac{\partial \widetilde{T}}{\partial x_j} \tag{3.22}$$

with the turbulent thermal conductivity coefficient k_T

$$k_T = c_p \frac{\mu_T}{\mathrm{Pr}_T}. \tag{3.23}$$

Pr_T is the turbulent Prandtl number.

In this thesis, only fully turbulent computations are shown, therefore $\mu = \mu_T$. The definition of the appropriate viscosity μ_T is the task of the corresponding turbulence model. Models based on the eddy-viscosity hypothesis offer a good cost-benefit-ratio: they are relatively easy to implement, quite fast in their computations, and offer sufficient accuracy for many engineering applications. More details on the specific formulations of the different models can be found in the literature, e.g. [94, 95]. In this thesis, two turbulence models based on the eddy-viscosity hypothesis are applied:

- One-Equation model "Spalart-Allmaras" in Original formulation (SAO): The model of Spalart and Allmaras [72] was developed on an empirical basis. The eddy-viscosity is defined by only one additional transport equation. The model was developed for aerodynamic applications. It leads to good results, especially for attached flow and it might predict the separation onset earlier than other turbulence models while offering low computational cost and a robust convergence behavior [38]. Moreover, the requirements for the resolution of the boundary layer on the computational mesh are less strict than for other turbulence models [96].

– Two-Equation model "Menter Shear Stress Transport" (Menter SST): The turbulence model Menter SST [97] uses the K-ω model from Wilcox in the near-wall regions and blends over to the K-ϵ model with increasing wall distance. Additionally, Menter introduced a modification for the "Shear Stress Transport", which can be applied to all two-equation turbulence models. The SST modification should improve results especially for cases with negative pressure gradients [94,96]. It limits the maximum shear stresses and so influences separation onset and the flow further downstream.

Differential Reynolds-stress models (RSM)

Reynolds-stress models are a comparably young family of turbulence models, whose development and first implementation into the DLR TAU-Code [98] was in the 2000s. These models solve transport equations for each individual stress component and an additional length scale. They prove to show superior results especially for corner flows on three-dimensional configurations, e.g., at the wing-body juncture [43–45]. However, due to the increased number of equations, Reynolds-stress models tend to demand more computational time and are not as robust in their convergence behavior compared to simpler models. For the computations in this thesis, a differential Reynolds-stress model, with formulations by Speziale-Sarkar-Gatski and Launder-Reece-Rodi (SSG/LRR) in combination with the ln-omega approach is used as described in [44].

3.3 Aeroelastic Equations of Motion and Internal Loads

The aeroelastic equations of motion can be expressed as the equilibrium between inertial, elastic, and aerodynamic forces

$$M_{gg}\ddot{x}_g(t) + Kx_g(t) = P_g^{Aero}(t), \tag{3.24}$$

while damping forces are neglected here. M is the mass matrix, K the stiffness matrix, P^{Aero} correspond to the aerodynamic loads and $x(t)$ describe the dynamic displacements. The index g denotes the structural node-set. The displacements can be expressed in terms of structural mode shapes Φ by modal reduction, and so significantly reduce the number of degrees of freedom for this system

$$x_g(t) \approx \Phi_{gh} q(t). \tag{3.25}$$

The index h describes the modal basis. The vector $q(t)$ denotes the modal coordinates and describes the time-varying motion of each mode. Aerodynamic forces f_a can be mapped via a spline matrix H from the aerodynamic to the structural coordinates

$$P_g^{Aero}(t) = H_{ga} f_a(t). \tag{3.26}$$

The final system of equations to be solved results in

$$M_{hh}\ddot{q}(t) + K_{hh}q(t) = \Phi_{gh}^{T} H_{ga} f_a(t). \tag{3.27}$$

The internal loads (sometimes also called section loads), L_c, act on the structure and are therefore necessary quantities of interest during the design of an aircraft. They are computed as the difference between aerodynamic and inertial loads using, e.g., the Force Summation Method [99]

$$\Delta L_c(t) = T_{cg}\left(H_{ga} f_a(t) - M_{gg}\Phi_{gh}\ddot{q}(t)\right), \tag{3.28}$$

where the matrix T integrates the loads on specific monitoring stations of the structural model, such as the load's reference axes. Note that the resulting loads ΔL_c represent the unsteady load increments, as only dynamic displacements and forces around the steady state are used in the previous equations.

3.4 Gust Signals

In this thesis, the responses to monofrequent and broadband gusts are computed. The equations for both types of excitation are listed below as they are used in the simulations.

Sinusoidal Gust Signals

In the first part of this thesis, a sinusoidal gust velocity is used for the excitation of the flow field, see Fig. 3.2. Responses to various gust lengths L_G and gust amplitudes $\widehat{W}_G$ are then analyzed for their nonlinear content. The vertical gust velocity $W_G(t,x)$ is defined by

$$W_G(t,x) = \widehat{W}_G \cdot \sin\left(\omega_G\, t + \phi_G(x)\right) \tag{3.29}$$

$$= \widehat{W}_G \cdot \sin\left(\frac{2\pi}{L_G}\left(U_\infty t + x_{ref} - x\right)\right) \tag{3.30}$$

with U_∞ being the freestream velocity of the flow, and ω_G and ϕ_G correspond to the angular gust velocity and the phase shift of the gust. x_{ref} defines the initial phase shift in space respectively, see Fig. 3.2. The gust length L_G can be directly transferred to the reduced frequency of the gust, k_{Gust}, using the following relation

$$k_{Gust} = \frac{\omega_G l_{ref}}{U_\infty} = \frac{2\pi l_{ref}}{L_G}. \tag{3.31}$$

Discrete "1-cos" Gust Signals

In the second part of the thesis, discrete "1-cos" gusts are used for the excitation of the aerodynamic and the aeroelastic system. The certification specifications require their

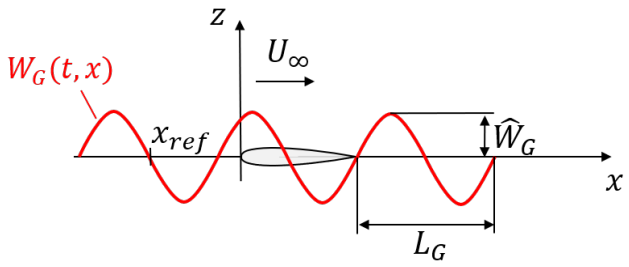

Fig. 3.2: Sketch of a sinusoidal gust that is used for the excitation of the flow

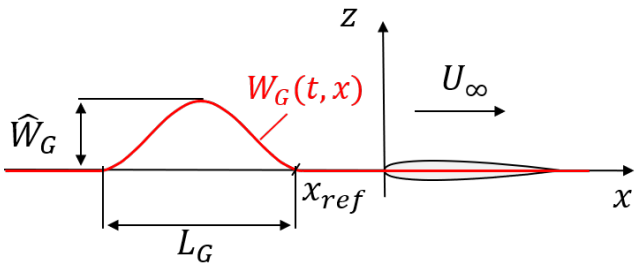

Fig. 3.3: Sketch of a discrete gust that is used for the excitation of the flow

computation, as already described in Chapter 2.4. The equation for the corresponding gust velocity W_G is again described below, but in a slightly different notation. Relevant variables are depicted in Fig. 3.3,

$$W_G(x) = \begin{cases} \frac{\widehat{W}_G}{2}\left(1 - \cos\left(\frac{2\pi}{L_G}\left(U_\infty t + x_{ref} - x\right)\right)\right) & \text{for } x_{ref} \leq x \leq x_{ref} + L_G \\ 0 & \text{else.} \end{cases} \tag{3.32}$$

The "1-cos" gust differs from the sinusoidal gust as it excites a broad frequency spectrum instead of a single frequency. Whereas a long gust excites mainly low frequencies but with a high magnitude, a shorter gust with the same amplitude in the time-domain excites a broader spectrum with a lower magnitude, compare Fig. 3.4.

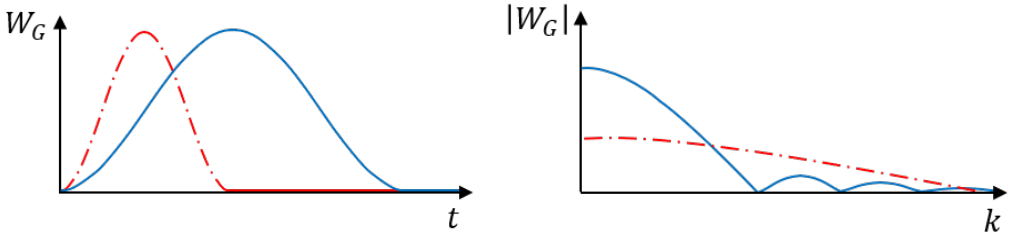

(a) Time signals **(b)** Magnitude in frequency domain

Fig. 3.4: Sketch of long (solid) and short (dashed) discrete gust excitations

3.5 Numerical Framework

3.5.1 CFD Solver TAU

Fluid dynamic simulations are carried out using the DLR TAU-Code [100, 101], which is a Finite-Volume URANS solver. The fluxes are spatially discretized by applying a central scheme. The solution is marched to a steady state using a local time stepping scheme [102] with a first-order implicit lower-upper symmetric Gauss-Seidel (LU-SGS) scheme. A multigrid algorithm with a 3-level V-cycle is used for all computations to improve convergence. The dual time stepping algorithm of Jameson [103] with second-order backward-differencing scheme is applied for the unsteady gust calculations. Moreover, the Arbitrary Lagrangian-Eulerian (ALE) formulation [104] is implemented and allows for deforming grids.

The Spalart-Allmaras one-equation turbulence model in its original formulation (SAO) [72] is used for turbulent closure. It proves to be a robust model with a good convergence behavior, which is a prerequisite for the computation of large databases. For validation purposes, some cases are re-computed using different turbulence models: results for the airfoil configuration are simulated additionally using the model of Menter SST, whereas the aircraft configuration is simulated additionally using a differential Reynolds-stress model.

3.5.2 FSForcedMotion

All gust encounter simulations are computed in the FlowSimulator framework [105], which enables efficient and parallel multidisciplinary computations. The in-house tool ”FSForcedMotion” is applied for the definition and control of aerodynamic and aeroelastic unsteady simulations [75].

Gusts are modeled using the field velocity method, which was introduced in the 1990s by Singh, Parameswaran, and Baeder [106, 107]. In this approach, the gust velocities are prescribed as grid velocities that vary with time and so the influence of a lifting surface on the gust is omitted. However, it proves to show accurate results compared to a resolved gust approach for gusts that are longer than two times the mean aerodynamic chord [108] and it can be easily implemented into most CFD codes. It exploits the velocity-related terms of existing grid deformation methods and is therefore widely in use today in several flow solvers [109–111].

For the fluid-structure-coupled simulations in this thesis, aerodynamic forces are computed using the computational fluid dynamics approach described above. A finite num-

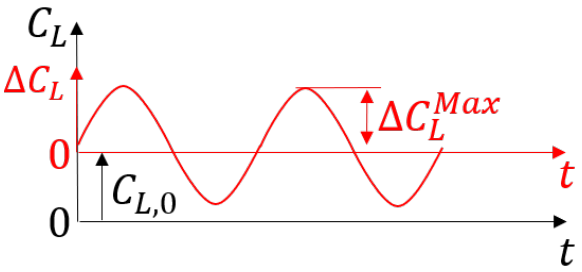

Fig. 3.5: Variables of the lift response

ber of natural eigenmodes represents the structural modal. Heave and pitch modes are also included as rigid-body modes to account for basic flight mechanic properties.

For time integration of the aeroelastic governing equations, the Newmark-β method [112] is used. The predictor step predicts the generalized displacements based on extrapolated generalized aerodynamic forces. These displacements are mapped onto the aerodynamic surface grid and the aerodynamic forces are computed for each time step. These forces are then used to update the displacements in a corrector step. Radial basis functions are used to propagate the surface deformation into the volume mesh [113].

3.6 Post-Processing of the Time- and Frequency-Domain Data

This section introduces some details on the post-processing of the global lift coefficient as the main focus of the final analysis is based on this variable. However, all other variables are subject to identical routines.

All gust computations are initiated based on converged steady-state solutions. The unsteady lift increment $\Delta C_L(t,\widehat{W}_G)$, see Fig. 3.5, is defined by

$$\Delta C_L(t,\widehat{W}_G) = C_L(t,\widehat{W}_G) - C_L(t,\widehat{W}_G = 0), \tag{3.33}$$

to account for numerical inaccuracies that might result from time integration. Building this difference is essential to enable highly accurate analyses, especially for small excitation amplitudes. The numerical settings for the unsteady computations of $C_L(t,\widehat{W}_G = 0)$ must therefore be precisely matched to the respective gust computations in order to eliminate the numerical errors.

For an evaluation of the system behavior, an amplitude-dependent Frequency Response Function (FRF) of the lift, C_{L,α_G}, can be defined using the Discrete Fourier Transform (DFT) such that

$$C_{L,\alpha_G}(k,\widehat{W}_G) = \frac{DFT\left(\Delta C_L(t,\widehat{W}_G)\right)}{DFT\left(\alpha_G(t,\widehat{W}_G)\right)}. \tag{3.34}$$

Note that in case of a purely harmonic excitation, only the very last period of each of the computed time signals is used for the DFT in order to neglect the transient behavior. The time history of the gust-induced angle of attack $\alpha_G(t) = \arctan\left(W_G(t)/U_\infty\right)$ at $x = y = z = 0$ forms the input to the system. Thus, in case of purely sinusoidal gust excitations, the input signal has only one harmonic component. For the output signal, complex-valued Fourier coefficients are computed for all harmonic responses. Superscript numbers on the variables denote the respective number of the harmonics, such that e.g. C^1_{L,α_G} and C^2_{L,α_G} denote the first and the second harmonic Fourier coefficients of the FRF.

Responses for the lowest gust amplitude computed, $\widehat{W}_G = 10^{-6}$ m/s, are considered as unsteady linear responses, and their computed first harmonic of the FRF will be taken as the time-linearized reference value $C^{Lin}_{L,\alpha_G}(k_{Gust}) \approx C_{L,\alpha_G}(k_{Gust}, \widehat{W}_G = 10^{-6}\,\mathrm{m/s})$.

Most of the subsequent analyses refer to the maximum lift increment. The incremental, time-linearized maximum lift value for each gust can be calculated using the value of the first harmonic and the gust amplitude

$$\Delta C_L^{Max,Lin}(k_{Gust}, \widehat{W}_G) = |C^{Lin}_{L,\alpha_G}(k_{Gust})| \cdot \widehat{\alpha}_G(\widehat{W}_G). \tag{3.35}$$

Another variable used for analyzing the unsteady data is defined as the "effective slope", m^{NL},

$$m^{NL}(k_{Gust}, \widehat{W}_G) = \frac{\Delta C_L^{Max}(k_{Gust}, \widehat{W}_G)}{\widehat{\alpha}_G(\widehat{W}_G)}, \tag{3.36}$$

and it is illustrated in Fig. 3.6. It approaches the magnitude of the first harmonic response in the linear case, i.e. $m^{Lin} = |C^{Lin}_{L,\alpha_G}|$. Note, however, that the nonlinear effective slope m^{NL} increasingly deviates from the magnitude of the first harmonic response with increasing nonlinear response effects.

Finally, the relative difference in the maximum incremental lift, δC_L^{Max}, is defined as

$$\delta C_L^{Max}(k_{Gust}, \widehat{W}_G) = \frac{\Delta C_L^{Max} - \Delta C_L^{Max,Lin}}{\Delta C_L^{Max,Lin}} \cdot 100\%. \tag{3.37}$$

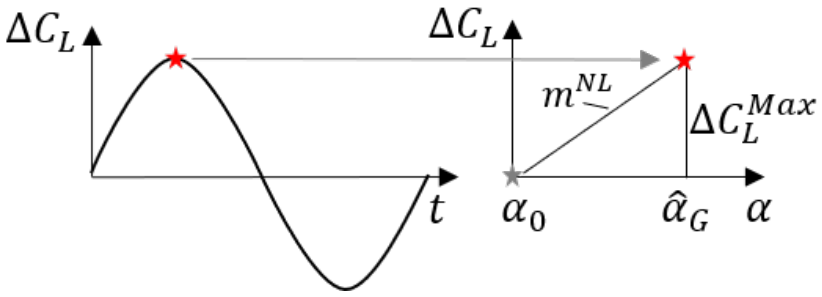

Fig. 3.6: Effective slope m^{NL}

4 Models, Test Cases and Numerical Settings

This chapter introduces models, as well as test cases, and specific numerical settings, that are used for the numerical simulations in Chapters 5 and 6.

4.1 RAE2822 airfoil

Configuration

The RAE2822 airfoil was designed and extensively tested in wind tunnels during the 1970s [114]. The design condition is at Mach 0.66 at an angle of attack of $\alpha = 1.06$ deg, where the airfoil shows a subsonic rooftop-type pressure distribution with rear-loading [114]. At higher Mach numbers, it develops transonic pressure distributions that are similar to the ones from typical supercritical airfoils. The RAE2822 airfoil has a maximum thickness of 12.1% and is widely used for the validation of turbulence models in transonic flow conditions [96,115,116]. It is chosen for the basic test cases in this thesis as it is a well-known airfoil and shows comparable flow features to airfoils from transonic transport aircraft configurations.

CFD mesh

The results for the RAE2822 airfoil are presented for a CFD mesh with about 240.000 nodes, depicted in Fig. 4.1. The upper and lower surfaces of the airfoil are discretized with 300 cells each. The cell size on the central part of the airfoil is about $x/c = 0.004$, whereas the leading edge has a finer spacing. It is a hybrid mesh which consists of quadrilateral cells in the vicinity and the wake of the airfoil, see Fig. 4.1(b) and Fig. 4.1(c), and triangular cells in the remaining parts of the mesh. The farfield extends to a distance of 100 chords

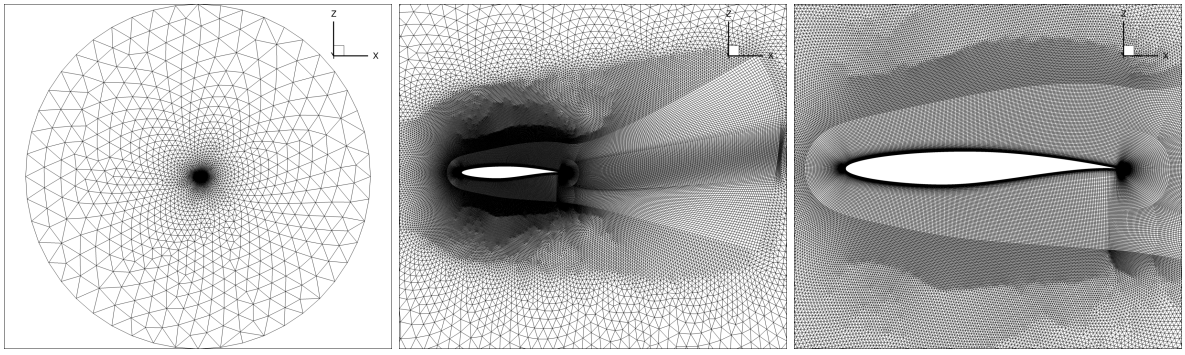

(a) Far-field mesh **(b)** Quads in the near-field and the wake **(c)** Close-up of the near-field mesh

Fig. 4.1: Hybrid CFD mesh for the RAE2822 airfoil with about 240.000 nodes

Table 4.1: Gust velocities and gust-induced angles of attack at Mach 0.70

$\widehat{W}_G$ / m/s	1×10^{-6}	0.1	1.0	3.0	5.0	7.5	10.0	12.5	15.0
$\widehat{\alpha}_G$ / deg	2.5×10^{-7}	0.025	0.25	0.74	1.24	1.85	2.47	3.09	3.70

in every direction from the airfoil, see Fig. 4.1(a). A wall-resolved approach is used, and the distances of the first off-body grid nodes satisfy $y^+(1) < 1.0$. A grid sensitivity study is shown in Appendix A.1 and demonstrates the validity of the current mesh.

Monofrequent Gust Test Cases

The Reynolds number for these test cases corresponds to $Re = 6.5 \times 10^6$ and is based on the reference chord length of $l_{ref} = c = 1.0$ m. Gust encounters are simulated at four different transonic Mach numbers: Mach 0.66, Mach 0.68, Mach 0.70, and Mach 0.72, each at a steady angle of attack of $\alpha_0 = 3.0$ deg.

In order to analyze basic aerodynamic effects, gust encounters on this airfoil configuration are performed using sinusoidal gust excitations as defined in Chapter 3.4. Gust lengths vary between $L_G = 2.5$ m and $L_G = 125.5$ m, see Table 4.3. The smallest simulated gust amplitude is as low as $\widehat{W}_G = 1 \times 10^{-6}$ m/s in order to guarantee a linear gust response, see Appendix A.3. Gust amplitudes are increased up to $\widehat{W}_G = 15.0$ m/s, see Table 4.1.

The time step size differs slightly for each Mach number; see Table 4.2, for a constant nondimensional time step size of $\Delta\tau = dt/(c/U_\infty) = 0.0417$. The time step size is fixed for all simulated gust lengths at one single Mach number in order to resolve the same physical effects for each gust length. As a consequence, short gusts are simulated with fewer time steps per period (SPP) than long gusts; see Table 4.3. A convergence study for the time step size can be found in Appendix A.2. In any case, the applied CFL number is equal to 50. The number of total time steps (ndt) varies between 1200 and 15060.

Table 4.2: Time step size: $\Delta x = 4.17\%$c per time step for each Mach number

Mach	U_∞ / m/s	dt / s	Inner Iterations
0.66	218.65	1.91×10^{-4}	400
0.68	225.28	1.85×10^{-4}	400
0.70	231.90	1.80×10^{-4}	400
0.72	238.52	1.75×10^{-4}	400

Table 4.3: Numerical settings for different gust lengths, independent of the Mach number

L_G / m	k_{Gust}	SPP	nr. of Periods	ndt
2.5	2.51	60	20	1200
⋮	⋮	⋮	⋮	⋮
18.0	0.35	432	20	8640
21.0	0.30	504	10	5040
25.0	0.25	600	10	6000
31.5	0.20	756	10	7560
42.0	0.15	1008	10	10080
62.5	0.10	1500	5	7500
125.5	0.05	3012	5	15060

Based on the convergence of the mean lift response and the first and second harmonic response, it is decided to define three groups concerning the number of periods computed: shorter gusts are simulated for 20 periods, longer gusts are simulated for five periods and all gust lengths in between are simulated for ten periods; see Table 4.3.

4.2 NASA Common Research Model

Configuration

The NASA Common Research Model was developed in 2008 to provide the community with a freely available and state-of-the-art transonic aircraft model for experimental and numerical research [117, 118]. It became a standard test case, e.g., for the international AIAA CFD Drag Prediction Workshop (DPW)[1] series [38, 45, 119]. The geometry used in this work is taken from DPW-IV [42] and it is designed for a Mach number of 0.85, a steady lift coefficient $C_L = 0.50$ and a Reynolds number $Re = 40 \times 10^6$, with the reference length equal to the mean aerodynamic chord, i.e. $l_{ref} = c_{MAC} = 7.0$ m. Computations are carried out for the rigid, as well as for the flexible aircraft model. Note that a load control system is not included in the computations, i.e., all results are for the open-loop system.

CFD mesh

Hybrid CFD meshes are generated using the commercial grid generation tool CENTAUR™ (CentaurSoft) [120]. Three different mesh levels are set up, and a sensitivity study is reported in Appendix B.1. The medium-level grid is used for all computations

[1] https://aiaa-dpw.larc.nasa.gov, retrieved 24 August 2021

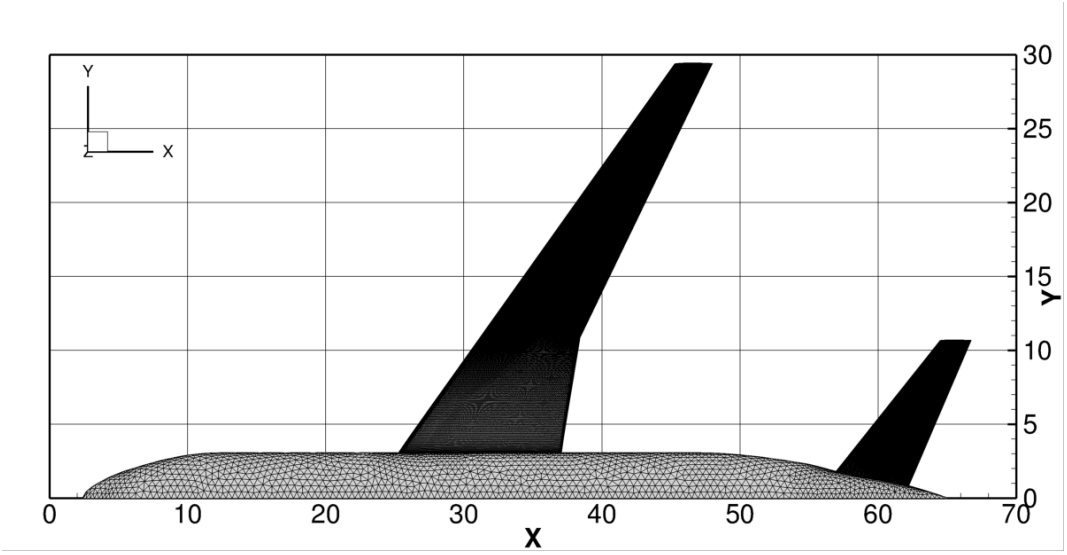

(a) Half-model of the aircraft configuration

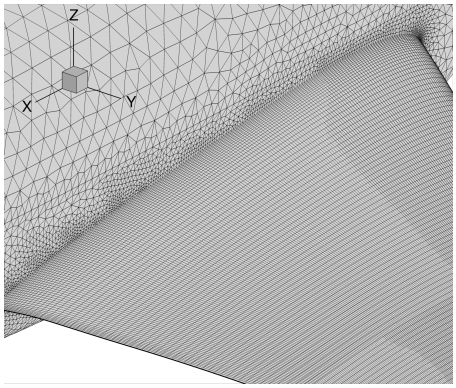

(b) Wing-body junction

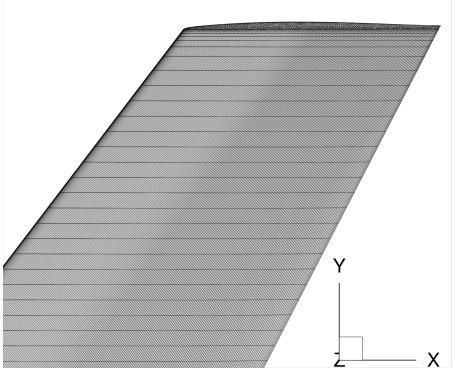

(c) Wing tip

Fig. 4.2: CFD mesh for the NASA Common Research Model

throughout the paper. It comprises 11 million mesh nodes with nearly 120 000 surface nodes; see Fig. 4.2. The wing is discretized using 200 points in the chord direction and 180 points in the spanwise direction. The horizontal tailplane is discretized with 150 chordwise and 100 spanwise nodes, respectively. A wall-resolved approach is applied, and the distances of the first off-body grid nodes all satisfy $y^+(1) < 1.0$.

FERMAT Structural Model

A structural model for the NASA CRM is defined by Klimmek [121] with the so-called "FERMAT model". The mass case C6 is used, which corresponds to the maximum take-off weight with MTOW $=$ 260.000 kg and a center of gravity position of $x = 33.68$ m. Rigid-body modes "heave" and "pitch" are considered in the computations, as well as the first five symmetric elastic modes, see Table 4.4. A sensitivity study concerning the number of mode shapes in the aeroelastic computations can be found in Appendix B.2.

Table 4.4: Considered mode shapes of the FERMAT model

Mode ID	Mode Description	Generalized Mass	Frequency / Hz
3	Heave	260 000 kg	-
5	Pitch	$25 \cdot 10^6$ kg·m^2	-
7	First Wing bending	1.0	1.065
11	Wing fore/aft	1.0	2.39
13	Second Wing bending	1.0	2.93
15	Fuselage vertical bending	1.0	3.04
17	Fuselage vertical bending and HTP bending	1.0	3.58

Test Cases for Sinusoidal and "1-cos" Gusts

Different types of gust encounters are simulated for the transport aircraft configuration. Sinusoidal gust simulations are carried out at three different Mach numbers: Mach 0.83, Mach 0.85, and Mach 0.87, each at a steady angle of attack of $\alpha_0 = 2.02$ deg. This angle of attack corresponds to the design lift coefficient of $C_L = 0.5$ at the design Mach number 0.85. The angle of attack is kept constant for all Mach numbers to allow for a proper aerodynamic parameter study. For the discrete gust encounters, computations at Mach 0.87 are omitted. Based on the findings of the sinusoidal gusts, it is assumed that there are no further new findings for Mach 0.87. For a proper resolution of the physical effects, a similar nondimensional time step size as for the airfoil computations is required: $\Delta\tau = 0.0466$, see Appendix B.4 for more details on that aspect.

For an investigation of basic aerodynamic effects, responses to sinusoidal gust excitations are computed with gust lengths that vary between 880.0 m and 18.0 m, see Table 4.5. Between three to eight periods are computed in order to get a converged mean value of the solution. Numerical details for the longest and the shortest gust at Mach 0.85 are listed in Table 4.6.

In addition to sinusoidal gusts, also discrete gust encounters are simulated for the NASA CRM, as this type of gust is relevant for the certification specifications. Therefore, "1-cos"

Table 4.5: Sinusoidal gusts: Gust lengths and corresponding reduced frequencies

L_G / m	880.0	440.0	293.0	220.0	147.0	110.0	88.0	...	18.0
k_{Gust}	0.05	0.10	0.15	0.20	0.30	0.40	0.50	...	2.40

Table 4.6: Sinusoidal gusts: Numerical settings for Mach 0.85 ($U_\infty = 250.99$ m/s) and a Reynolds number of 40×10^6

L_G / m	k_{Gust}	SPP	nr. of periods	ndt	dt / s	Inner Iterations
880.0	0.05	2640	3	7920	0.0013	100
18.0	2.4	54	8	432	0.0013	100

Table 4.7: Discrete gusts: Gust lengths and corresponding reduced frequencies; *only for aeroelastic computations.

L_G / m	420.0*	350.0*	280.0*	210.0	175.0	140.0	105.0	70.0	35.0
k_{Gust}	0.10*	0.13*	0.16*	0.21	0.25	0.31	0.42	0.63	1.26

Table 4.8: Gust velocities and gust-induced angles of attack for Mach 0.85

$\widehat{W}_G$ / m/s	1×10^{-6}	0.1	1.0	5.0	10.0	15.0	20.0
$\widehat{\alpha}_G$ / deg	2.3×10^{-7}	0.023	0.23	1.14	2.28	3.42	4.55

gusts are computed for the purely aerodynamic and also the flexible aircraft model. Simulated gust lengths and reduced frequencies are listed in Table 4.7. Note that three additional gust lengths are computed for the aeroelastic test cases. These rather long gusts (with respect to CS-25) are introduced to also discuss some effects of a nonlinear aerodynamic modeling on gust lengths beyond the current standard.

For both types of gust, sinusoidal and discrete, seven different gust amplitudes are simulated per gust length, see Table 4.8. Gust amplitudes vary between $\widehat{W}_G = 10^{-6}$ m/s and 20.0 m/s, which lead to gust-induced angles of attack between $\widehat{\alpha}_G = 2 \times 10^{-7}$ deg and $\widehat{\alpha}_G = 4.55$ deg, see Table 4.8. The smallest simulated gust amplitude guarantees a linear gust response, see Appendix B.3.

5 Aerodynamic Analysis

This chapter presents the results of the aerodynamic simulations. Responses to sinusoidal gusts are analyzed for a two-dimensional airfoil configuration, as well as for a transport aircraft configuration. Basic unsteady nonlinear aerodynamic effects are identified and connected to trends in the steady data. Then, the nonlinear effects of discrete gust encounters are investigated. The chronology of events during a discrete gust encounter is analyzed, where recurring aerodynamic stages in the responses are identified. A summary of the nonlinear aerodynamic effects forms the last part of this chapter.

5.1 Sinusoidal Gusts on the RAE2822 airfoil

5.1.1 Steady Polars

Steady polars for the RAE2822 are computed for four different Mach numbers: Mach 0.66, Mach 0.68, Mach 0.70 and Mach 0.72. Applied models are described in Chapter 4.1. Corresponding lift and moment polars are plotted in Fig. 5.1. All lift curves show typical results as described in Chapter 2.1: with an increase in the Mach number, the maximum lift decreases, but the linear lift curve slope increases. The linear range extends to larger angles of attack for lower Mach numbers. Pitching moment coefficients are referenced to the quarter-chord and show significantly stronger nonlinear trends than the lift coefficient. Local details such as shock position, and the extent of a separated flow region are more relevant here.

Gust encounter simulations are carried out at a steady angle of attack of $\alpha_0 = 3.0$ deg and attached transonic flow can be observed for all steady-state flows, see Fig. 5.2.

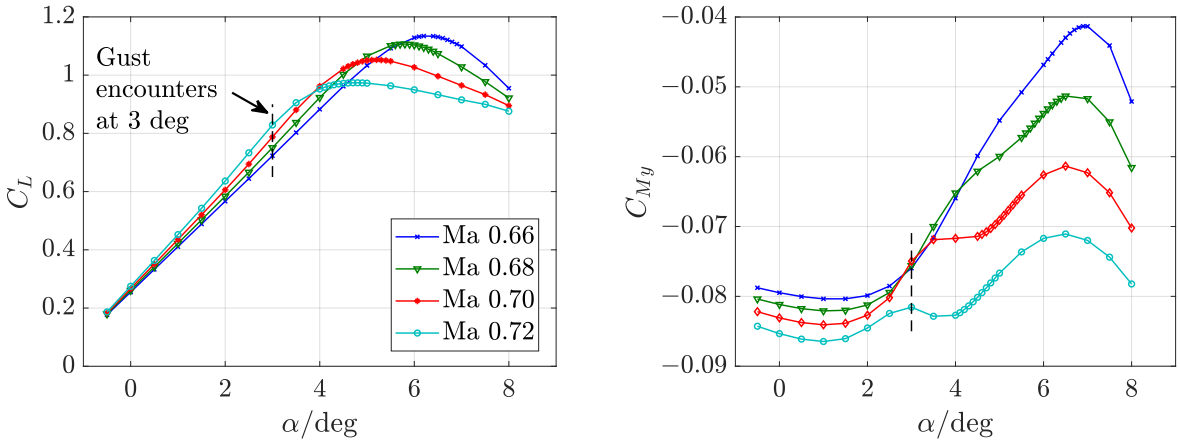

(a) Lift **(b)** Pitching moment

Fig. 5.1: Steady polars for the RAE2822 airfoil

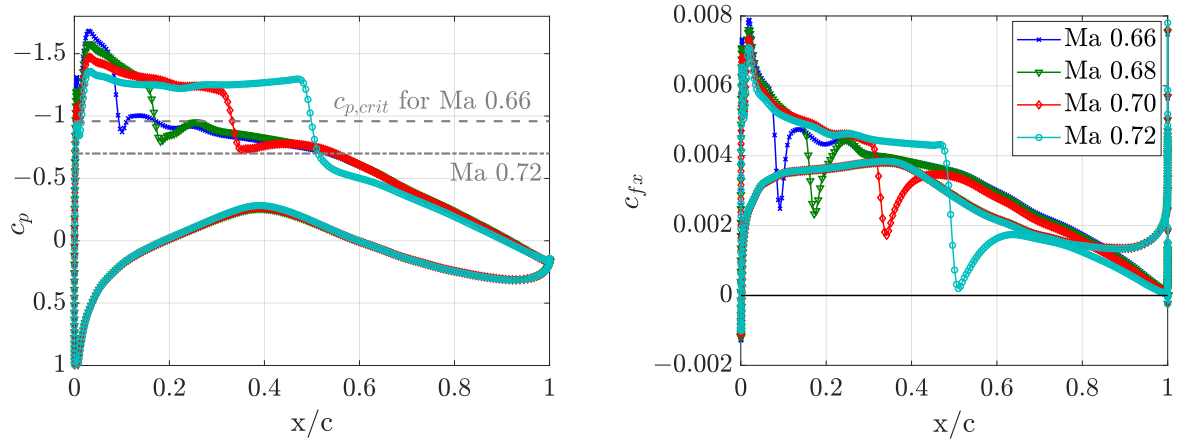

(a) Pressure coefficients **(b)** Skin friction coefficients

Fig. 5.2: Local coefficients for different Mach numbers at $\alpha_0 = 3.0$ deg

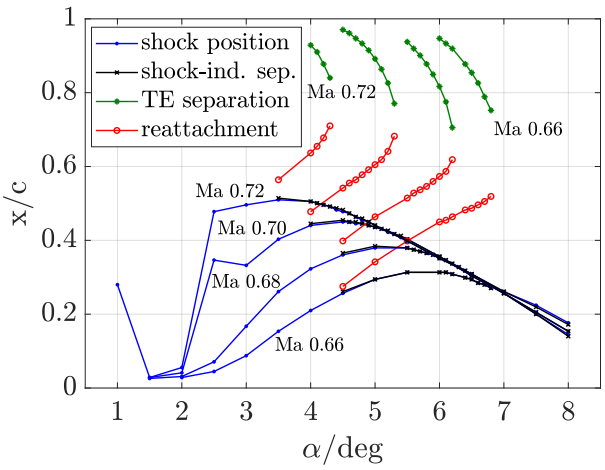

Fig. 5.3: Trends in separation and reattachment for the different Mach numbers

Fig. 5.3 summarizes shock motion, separation and reattachment behavior for this airfoil, as already discussed in Chapter 2.1. There is a rather large difference in the shock position for the different Mach numbers during the regular shock motion, whereas shock positions during inverse shock motion seem to be almost independent of the Mach number, and more depending on the steady angle of attack. For lower Mach numbers, the transition from fully attached to fully separated flow happens over a broader range of angles of attack than for higher Mach numbers.

Fig. 5.4 summarizes the characteristics of steady local and global trends for Mach 0.66 and Mach 0.70. In addition, labels show the respective angles of attack for the first shock occurrence, for separation onset and for maximum lift. Recall from Fig. 2.5 that these three stages are categorized in this work into (I) attached flow, (II) pre-stall flow, and (III) stalled flow.

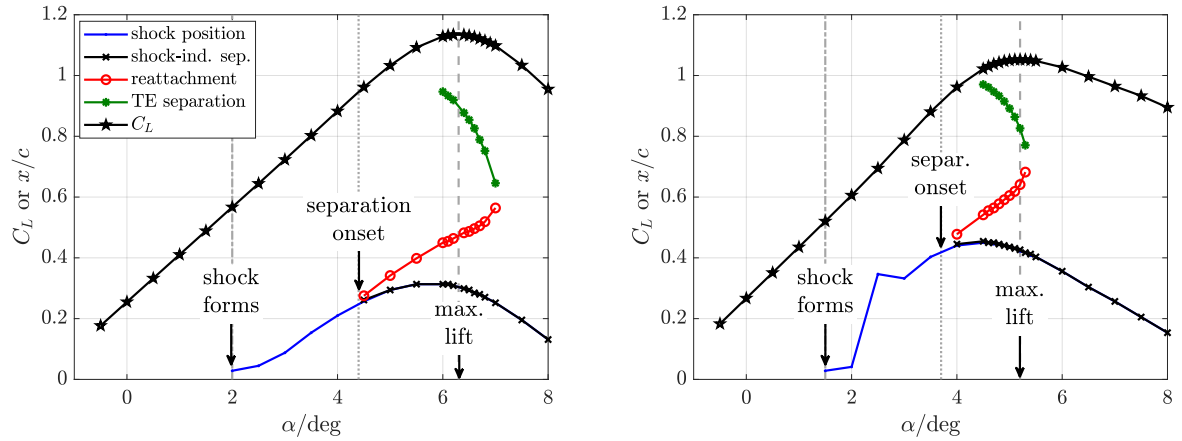

(a) Mach 0.66 **(b)** Mach 0.70

Fig. 5.4: Characteristics of steady airfoil flow

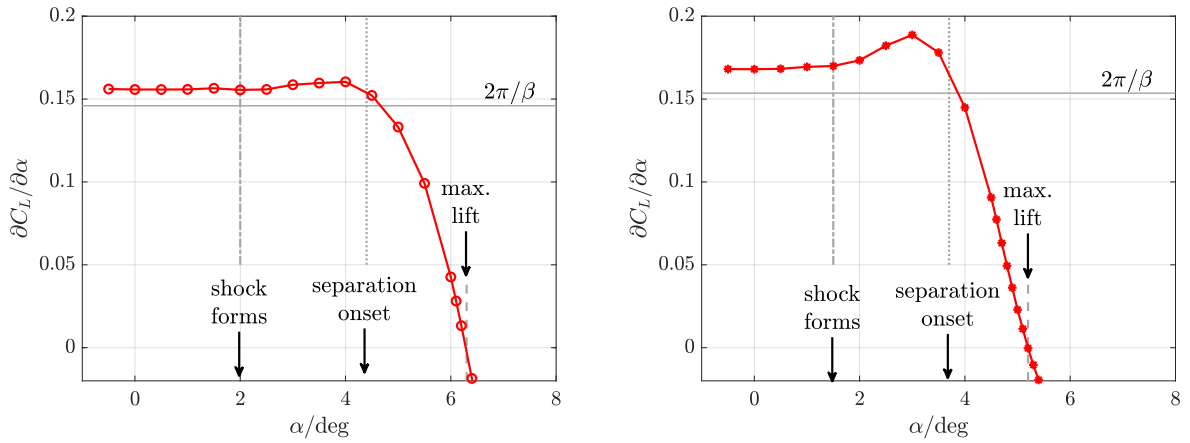

(a) Mach 0.66 **(b)** Mach 0.70

Fig. 5.5: Lift curve slopes

The results show that the range with attached flow can be divided further: Into a part with subsonic flow for lower angles of attack and a second part with transonic flow, which includes a recompression shock, for higher angles of attack.

From the corresponding lift curve slopes, Fig. 5.5, it is found that the range with subsonic flow corresponds to a nearly constant value of the lift curve slope. In the range with transonic flow conditions, the lift curve slope shows a nonlinear trend, which gets stronger with increasing Mach number. Just below the separation onset, the lift curve slope exhibits a maximum value and decreases significantly for higher angles of attack. Figures for Mach 0.68 and Mach 0.72 are listed in Appendix A.4 and reveal identical trends.

From these curves, it can be derived that the formation of the recompression shock introduces higher lift curve slopes than it can be expected from subsonic flow. Especially the

range with downstream shock positions shows the largest gradients in lift. As the maximum steady shock position occurs further downstream with increasing Mach number, the maximum lift curve slope is obtained for the highest Mach number considered.

5.1.2 Unsteady Nonlinear Responses

Gust encounters are simulated at a constant steady angle of attack of $\alpha_0 = 3.0$ deg for the different Mach numbers. Note that with each Mach number, the steady angle of attack for the gust encounter has a different position concerning the respective angle of attack where the peak of the lift curve slope occurs. Responses to monofrequent excitations are analyzed in the following.

Exemplarily, Fig. 5.6 shows lift and moment responses as a function of time for two different gust lengths and various amplitudes. The responses to both gust lengths are differently affected by the amplitude nonlinearities, compare, e.g. Fig. 5.6(a) and Fig. 5.6(b).

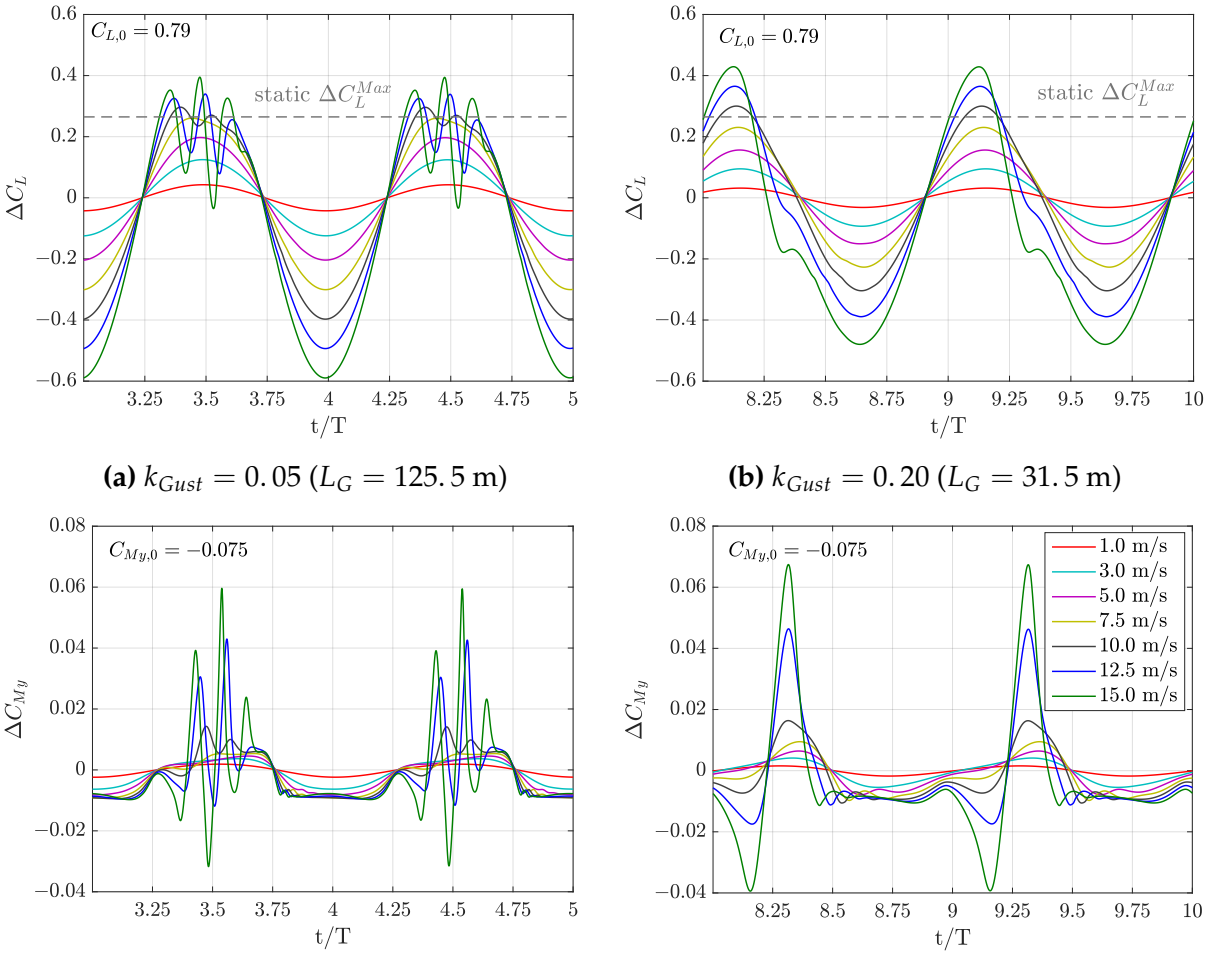

(a) $k_{Gust} = 0.05$ ($L_G = 125.5$ m)

(b) $k_{Gust} = 0.20$ ($L_G = 31.5$ m)

(c) $k_{Gust} = 0.05$ ($L_G = 125.5$ m)

(d) $k_{Gust} = 0.20$ ($L_G = 31.5$ m)

Fig. 5.6: Global coefficients for two gust lengths and various amplitudes at Mach 0.70

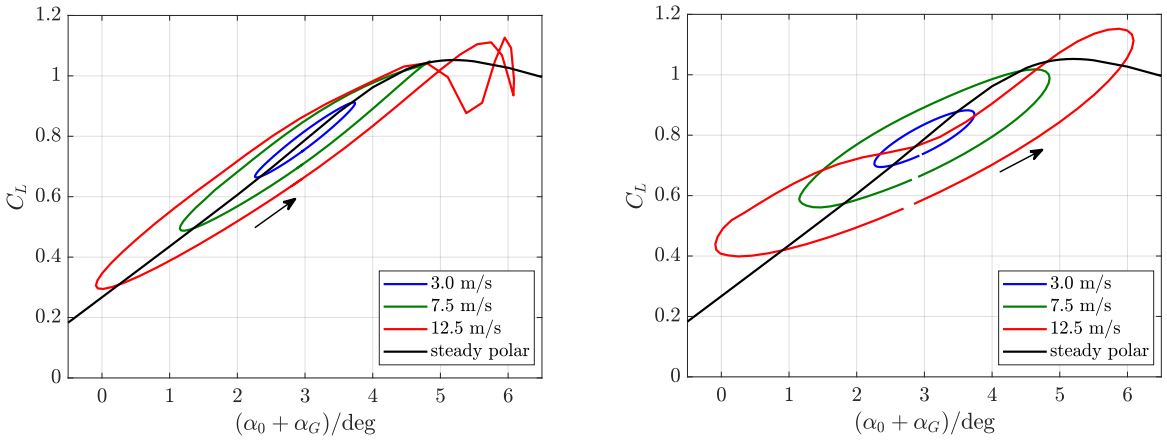

(a) $k_{Gust} = 0.05$ ($L_G = 125.5$ m) **(b)** $k_{Gust} = 0.20$ ($L_G = 31.5$ m)

Fig. 5.7: Lift over gust-induced angle of attack (referenced to the leading edge) at Mach 0.70 for different gust amplitudes $\widehat{W}_G$

They have in common, however, that an increase in the gust amplitude leads to stronger nonlinear effects in the responses. The response of the pitching moment is more affected by large amplitude excitations than the lift coefficient, as could already be expected from the steady trends.

It can be observed that nonlinear responses lead to an earlier breakdown of the lift compared to the linear counterparts. For both gust lengths, the first visible deviations from linearity are noticeable at about $\widehat{W}_G = 7.5$ m/s. The amplitude effects can be attributed to unsteady flow separation, as will be shown.

When lift responses are plotted versus gust-induced angle of attack instead of time, the plots resemble those known from subsonic "dynamic stall"-type flows, see e.g. [32]. Small-amplitude excitations induce responses with an elliptical shape which can be explained by a simple lag in the lift response compared to its quasi-steady solution, see Fig. 5.7. When the instantaneous angle of attack gets close to the value of the maximum steady lift, this elliptical shape gets deformed. For low excitation frequencies, i.e., long gusts, flow separation and lift breakdown might happen already on the increasing edge of the response, but only at an instantaneous value for the total angle of attack which is beyond the angle of attack for static maximum lift. The flow remains attached for higher angles of attack and allows for dynamic overshoots. The reattachment of the flow sets in at significantly lower angles of attack on the falling edge of the response and so typical stall hysteresis curves can be observed. For higher excitation frequencies, i.e., short gusts, deviations from the elliptical shape occur only at the falling edge of the response as the flow stays attached on the rising edge of the gust excitation. Moreover, the inclination of the ellipses decreases with increasing excitation frequency, which corresponds to a larger

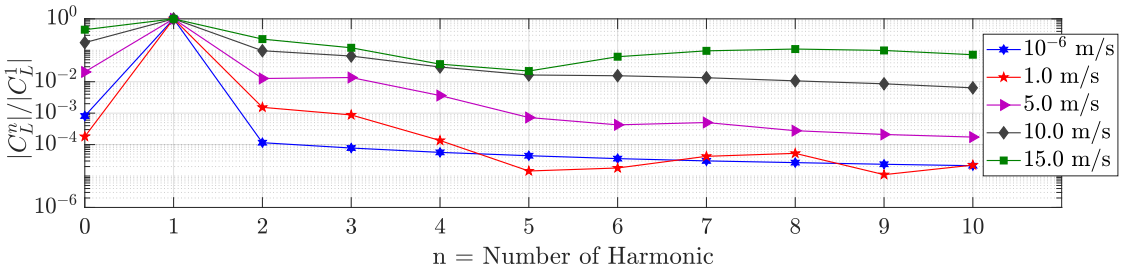

(a) $k_{Gust} = 0.05$ ($L_G = 125.5$ m)

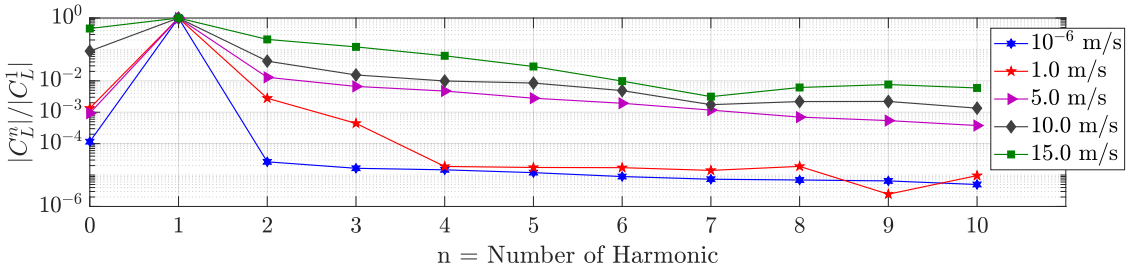

(b) $k_{Gust} = 0.20$ ($L_G = 31.5$ m)

Fig. 5.8: Normalized frequency content of the lift coefficient

lag in the responses. "Dynamic overshoots" can be observed for both gust lengths at $\widehat{W}_G = 12.5$ m/s, see Chapter 5.1.3 for more details.

The nonlinear trend in the time domain corresponds to an increased number of relevant higher harmonics. Fig. 5.8 illustrates the frequency content for both gust lengths and five amplitudes each. Larger gust amplitudes trigger higher harmonic content than smaller gust amplitudes. For the long gust with $\widehat{W}_G = 15$ m/s, even the 10th harmonic is only one order of magnitude lower than the first harmonic. For the shorter gust with $\widehat{W}_G = 15$ m/s, the 10th harmonic is at around 10^{-2} compared to the first harmonic. Taking a threshold of 10^{-3} for the higher harmonics [37], the gust amplitude needs to be lower than $\widehat{W}_G = 0.1$ m/s to obtain a linear response.

The harmonic content does not decrease monotonically with increasing higher harmonic. This might be an important aspect when reduced-order methods are applied that truncate behind a specific number of harmonics. Moreover, a growing mean value can be observed, which is plotted as 0th harmonic in Fig. 5.8. It reflects, that the nonlinear effects only occur on the positive part of the oscillating response.

Analysis of the First Harmonics

Current industrial practice involves frequency-based methods for load computations. Therefore, the impact of a nonlinear aerodynamic modeling on the first harmonic of the responses is analyzed in more detail here. Fig. 5.9 shows the complex-valued first har-

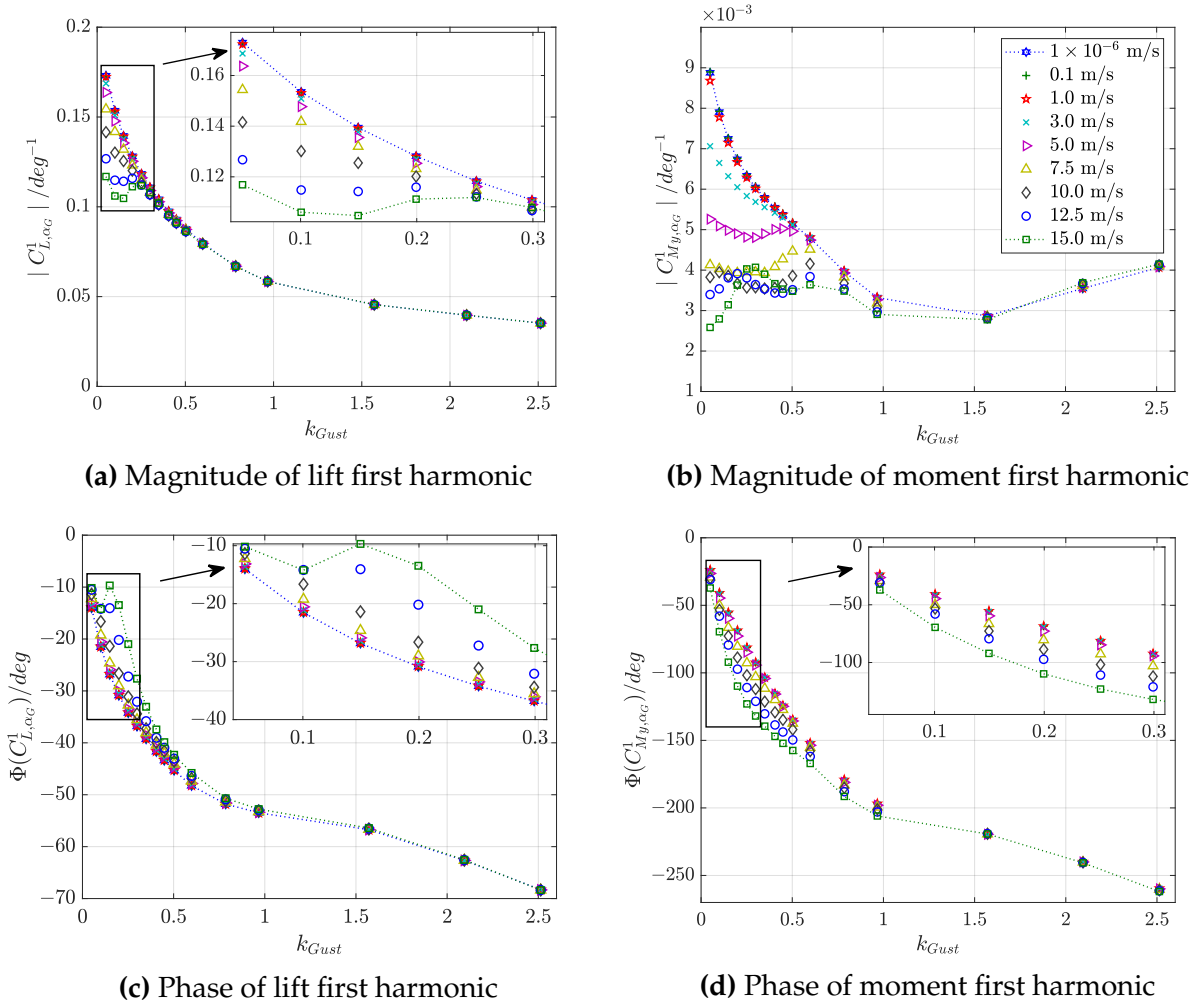

(a) Magnitude of lift first harmonic

(b) Magnitude of moment first harmonic

(c) Phase of lift first harmonic

(d) Phase of moment first harmonic

Fig. 5.9: First harmonic of lift and moment frequency response functions for all simulated excitations at Mach 0.70

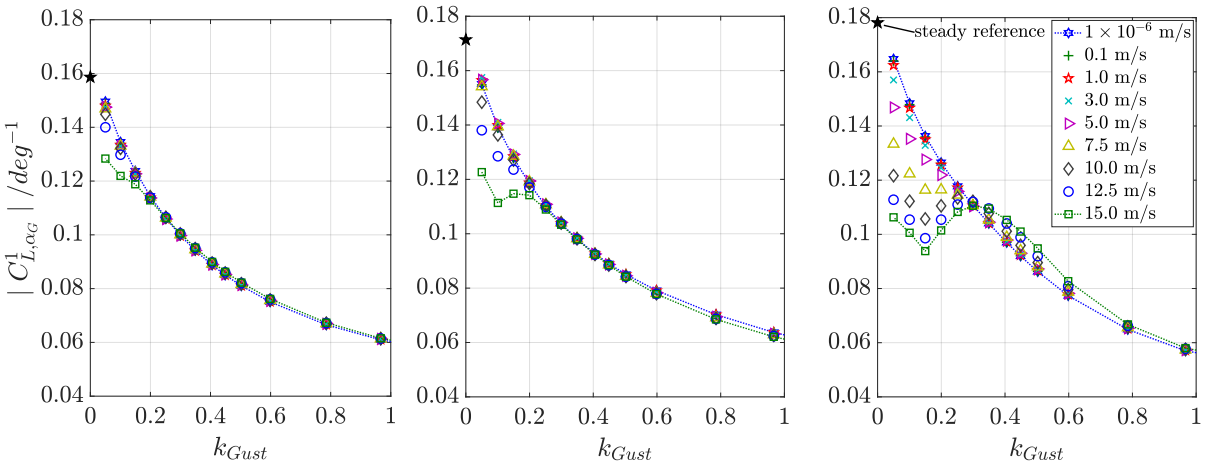

(a) Mach 0.66

(b) Mach 0.68

(c) Mach 0.72

Fig. 5.10: Magnitude of lift first harmonic. The black pentagram marks the steady reference value from the respective lift curve slope.

monic of lift and moment coefficients for all simulated gust encounters. Dotted lines mark both maximum and minimum gust amplitudes for better identification.

Identified trends from time-domain analysis are retrieved here: mainly large amplitude excitations at low frequencies lead to deviations from the linear response (dotted blue curve). The results in Figures 5.9 and 5.10 reveal that nonlinear responses can result in lower or higher first harmonics compared to the linear reference values. Large amplitudes affect the frequency response functions up to a particular limiting frequency, which strongly depends on the variable studied. There is a difference between lift and moment coefficient and magnitude and phase of the respective variable. For the gust test cases computed here, the limiting frequency for linear responses varies between $k_{Gust} = 0.30$ and $k_{Gust} = 1.5$.

Fig. 5.10 shows the effect of the underlying steady flow field on the first harmonic of the lift. The maximum gust amplitude of $\widehat{W}_G = 15.0$ m/s has only little effect on the responses for Mach 0.66, whereas at Mach 0.72, gust amplitudes of even $\widehat{W}_G = 1.0$ m/s deviate from the linear results. This emphasizes the significant effect of steady conditions onto the unsteady results [57]. The steady lift curve slopes $k_{Gust} = 0.0$ are also marked in the figures as a reference. It can well be recognized, that gust responses in the quasi-steady sense are identical to a change in the angle of attack.

Moreover, the sudden change of the trend for the larger amplitudes at Mach 0.72 and $k_{Gust} = 0.15$ might be a hint to an involvement of different concurrent unsteady effects. This "kink" can be observed with increasing intensity for all four Mach numbers. A similar hat-shaped response function can be observed for flows at buffet onset, i.e., in the vicinity of aerodynamic resonances [30,37,122]. This response function together with the oscillating lift coefficient in time-domain might indicate that large-amplitude excitations can also trigger fluid instabilities. The indicated oscillation in Fig. 5.6(a) has a duration of $t/T \approx 0.11$, and so corresponds to a reduced frequency of $k \approx 0.45$, which is in the typical range of reduced frequencies at buffet onset [37,122].

5.1.3 Maximum Lift Coefficient

This section focuses on the comparison between linear and nonlinear maximum peak lift values. Fig. 5.11 summarizes the incremental maximum unsteady lift for all computed gust encounters, $\Delta C_L^{Max} = max(\Delta C_L(t,\widehat{W}_G))$. General trends can be observed: the nonlinear lift maxima can result in larger or smaller peak values than the time-linearized reference values. It is also evident that dynamic overshoots can also occur in transonic flow. Responses to smaller gust amplitudes show a monotonic behavior with increasing frequency, which is an indication of the linearity of the responses. Large amplitudes de-

viate from the linear results in the range of lower frequencies but are almost on-spot for the higher frequencies. For reduced frequencies higher than 0.7, nonlinear effects vanish.

Comparing the nonlinearly computed maximum lift with the respective linear reference values (dash-dotted lines), first visible deviations occur at lift values that are significantly lower than the static maximum lift, for $\widehat{W}_G = 5.0\,\mathrm{m/s}$. The monotonic trend of the curves is lost when the static maximum lift is overshot for one of the frequencies. With increasing excitation amplitude, the overall maximum lift moves to higher frequencies. For the cases computed here, there is no saturation found in the maximum lift, but increasing the amplitude leads to higher and higher maximum values. Note that nonlinear responses can

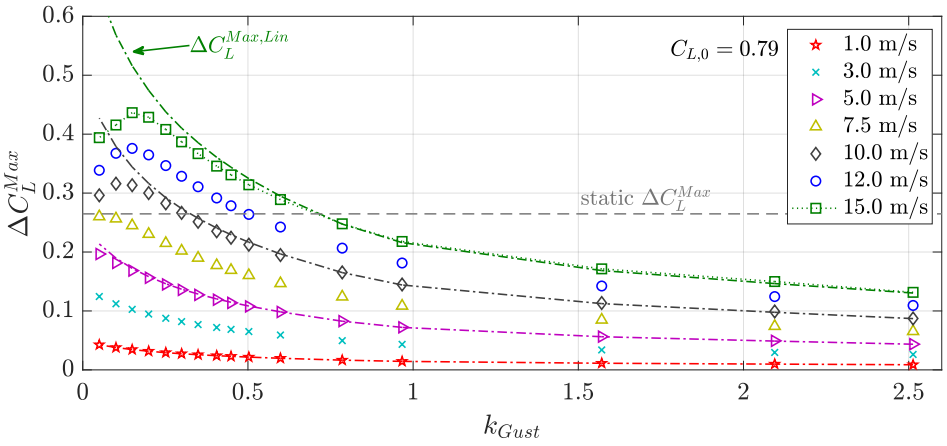

Fig. 5.11: Maximum lift increment during one period of excitation at Mach 0.70. (For a clearer presentation, the time-linearized curves are only included for every second excitation amplitude.)

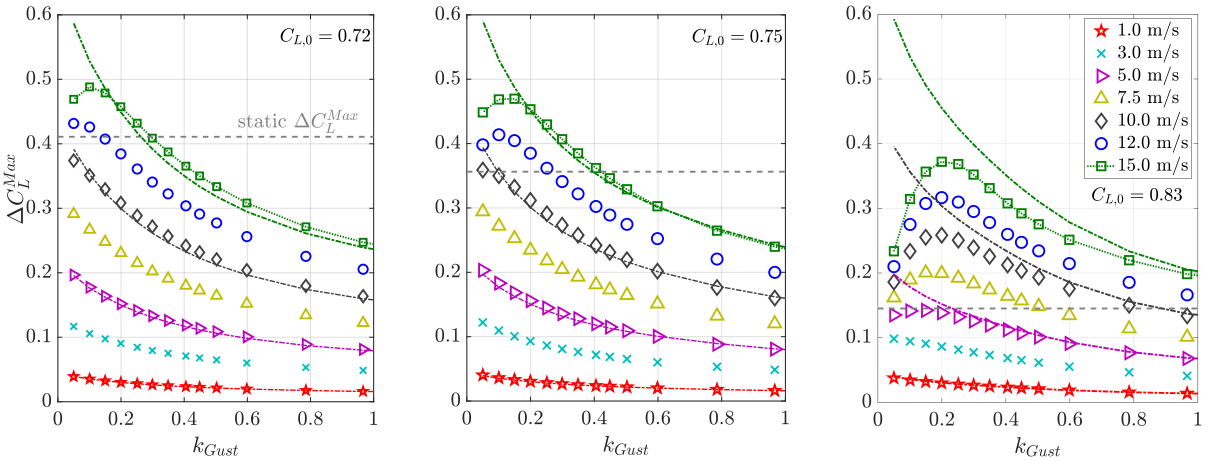

(a) Mach 0.66 **(b)** Mach 0.68 **(c)** Mach 0.72

Fig. 5.12: Maximum lift increment during one period of excitation.

already be recorded well below the static maximum lift is reached. However, in any case, a nonlinear response can be identified once the static maximum lift value is overshot.

Computations for different steady flow fields reveal that a reduction of the Mach number to Mach 0.66 and Mach 0.68 seems to trigger higher maximum lift values for the nonlinearly computed results compared to the linear ones, whereas an increase of the Mach number to Mach 0.72 seems to facilitate the opposite, see Fig. 5.12. This trend may be related to the different positions of the underlying steady flow in relation to the respective maximum of the lift curve slope. The lift curve slopes from Chapter 5.1.1 are summarized again in Fig. 5.13. For each of the Mach numbers, the steady angle of attack of $\alpha_0 = 3.0$ deg for the gust encounter has a different position in relation to the maximum of the curves. For the cases considered here, it is observed that the nonlinear method leads to higher maximum lift values than the time-linearized method if $\alpha_0 < \alpha\left((\partial C_L/\partial\alpha)^{Max}\right)$, see results for Mach 0.66 and Mach 0.68. Likewise, the time-linearized maximum lift exceeds its nonlinear counterpart if $\alpha_0 \geq \alpha\left((\partial C_L/\partial\alpha)^{Max}\right)$, see results for Mach 0.70 and Mach 0.72.

Analysis of Effective Slopes

From a quasi-steady perspective, pitching and gust excitation are equivalent. In the limit of an infinitely long gust, a gust is identical to a step change in the angle of attack. The results in this chapter suggest that the steady lift polar and its derivative can be taken as an indicator of the unsteady gust response behavior concerning the maximum lift prediction. The time-linearized method knows only a single derivative value, namely the one

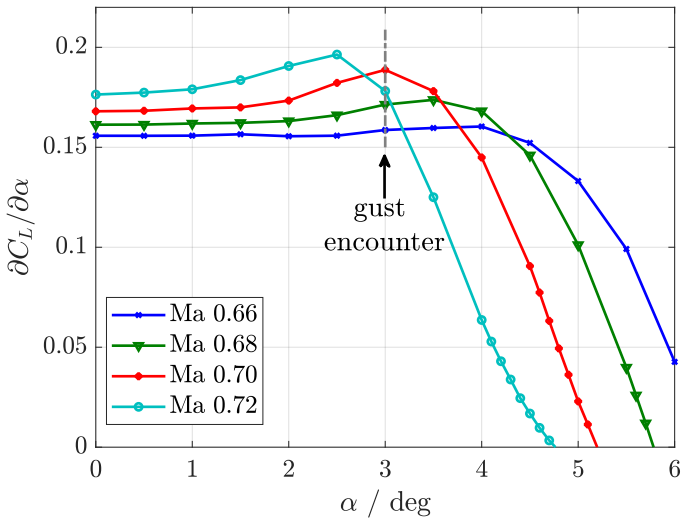

Fig. 5.13: Lift curve slopes with marked angle of attack for gust encounters

from the steady base flow. Hence, all computed responses are based on that value. The nonlinear method computes a new solution for every time step and evaluates the physics instantaneously. If the instantaneous flow field corresponds to a changed lift curve slope, this change is taken into account in the nonlinear calculation. As the steady data show, different topologies of the flow field (e.g., shock is present or not, separation is present or not) induce different lift curve slopes, which can be easily identified along the steady lift polar.

Fig. 5.14(a) shows a comparable evaluation of the effective slopes, m^{Lin} and m^{NL}, for the unsteady computations. For the nonlinear results, the same trends are present in the unsteady responses as can already be identified from the steady slope, though this happens to a different extent. With increasing excitation frequency, the trend of the steady slope is only stretched towards larger total induced angles of attack in the unsteady responses. So it seems that the unsteady effects only lead to a shift of the observed steady effects for the lift curve slopes towards higher angles of attack.

For example, at $k_{Gust} = 0.1$, first a slight increase and then a significant decrease in the slope m^{NL} can be observed in the computed parameter space, as it can also be observed for the steady slope. Since this long gust convects slowly over the airfoil, steady trends from the lift curve slope are reflected. For the medium frequencies, only an increase in the effective slopes can be observed in the computed angle of attack range. It can be assumed that larger gust amplitudes also lead to a decrease in the effective slope. The shortest gust with $k_{Gust} = 2.5$ results in linear responses, which is reflected in identical linear and nonlinear values. These gusts are simply too short to induce amplitude effects.

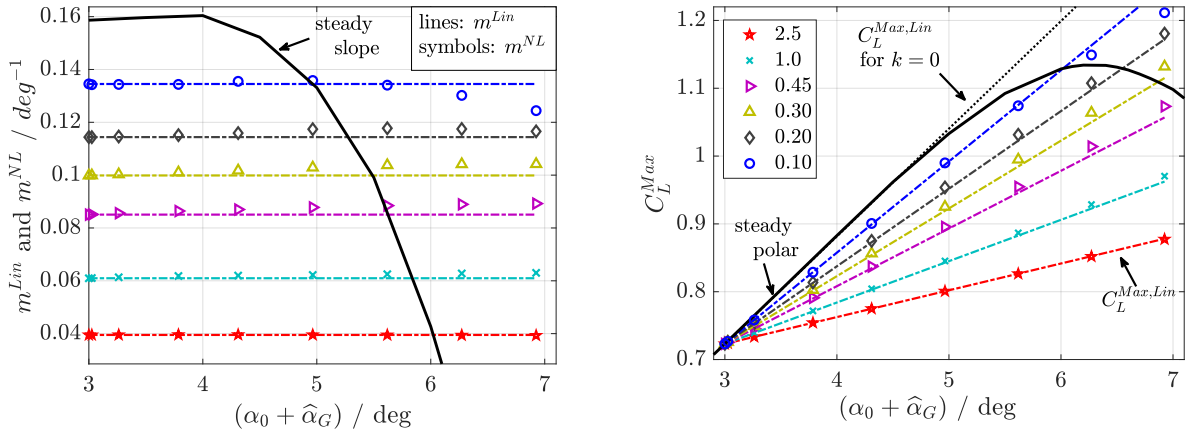

(a) Effective (linear and nonlinear) lift slopes

(b) Maximum gust-induced lift as a function of total induced angle of attack

Fig. 5.14: Time-linearized and nonlinear results for different reduced gust frequencies, k_{Gust}, at Mach 0.66 in comparison to steady data

Fig. 5.14(b) shows the values for the maximum unsteady (linear and nonlinear) lift coefficient together with the steady lift polar. The nonlinear computations result in higher lift coefficients than the time-linearized computation over the entire angle of attack range, which is connected to the higher effective slopes just discussed. For the longest gust ($k_{Gust} = 0.10$), flow separation sets in for higher amplitudes and the maximum lift coefficient breaks down, which, as already described, occurs with a slight delay compared to the steady data. Although the general qualitative trends of the steady and unsteady analyses are similar, the absolute values are strongly dependent on the excitation frequency. The data also suggest that the medium-length gusts amplify the increase in the slope caused by the nonlinear methods, which might occur due to the increased lag in the responses.

Fig. 5.15(a) shows evaluated data for Mach 0.70, where the steady angle of attack for the gust encounter is exactly at the angle of attack for the maximum steady lift curve slope. Consequently, the effective nonlinear slopes m^{NL} only show decreasing values with increasing induced angle of attack. The trend from the steady slope stretches towards larger induced angles of attack in the unsteady responses, as already observed for Mach 0.66. Again, this shift increases with increasing excitation frequency, i.e. decreasing gust length. The nonlinear maximum lift coefficients for the gust responses consequently result in identical or lower values than the time-linearized predictions, see Fig. 5.15(b). Nonlinear responses can not result in higher lift values than the time-linearized responses at this specific steady state.

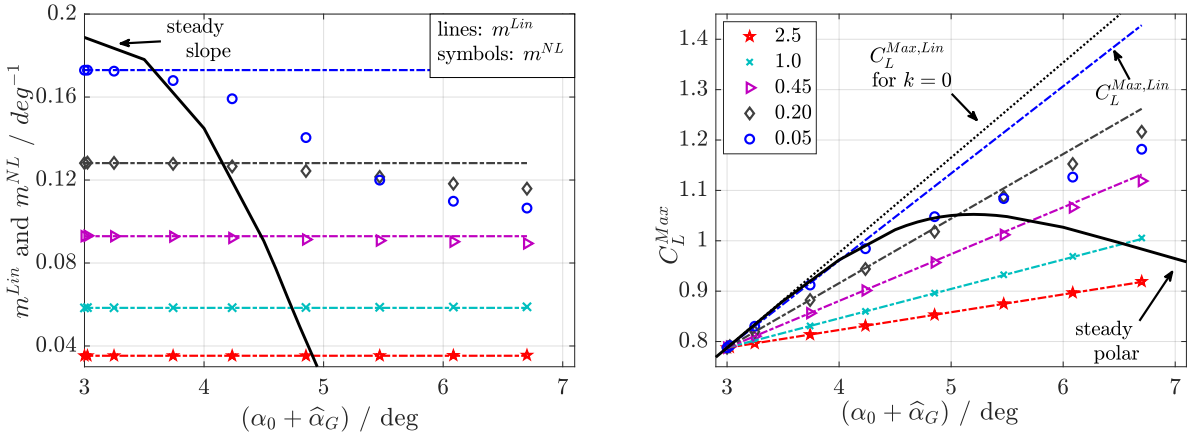

(a) Effective (linear and nonlinear) lift slopes

(b) Maximum gust-induced lift as a function of total induced angle of attack

Fig. 5.15: Time-linearized and nonlinear results for different reduced gust frequencies, k_{Gust}, at Mach 0.70 in comparison to steady data

Dynamic Overshoot

It is derived from the previous figures that low excitation frequencies in combination with large excitation amplitudes lead to an overshoot of the steady maximum value, independently of the Mach number. Note that a dynamic overshoot only seems to occur if the total induced angle of attack is larger than the angle of attack for the maximum steady lift coefficient, i.e. $(\alpha_0 + \widehat{\alpha}_G) > \alpha\left(C_L^{Max}\right)$, which is consistent with the findings for subsonic dynamic overshoots. However, whereas a delay of the flow separation can be observed as in subsonic flows, the existence of a leading-edge vortex can not be proven in transonic flow.

For Mach 0.72, excitations up to $k_{Gust} = 2.0$ lead to dynamic overshoots, whereas for Mach 0.66, they occur only up to $k_{Gust} = 0.3$. The maximum lift overshoot is recorded with $\Delta C_L = 0.23$ above the steady maximum lift at Mach 0.72.

5.1.4 Unsteady Shock Motion

One of the prominent features of transonic airfoil flow is the occurrence of recompression shocks, which can be detected using the maximum gradient of the pressures on the surface of the airfoil. In one of the first extensive studies on transonic airfoil flow, Tijdeman describes three types of periodic shock motions [56, 123]. Two can also be found for the analyzed gust responses, see Figs. 5.16 to 5.18: "sinusoidal shock-wave motion" (shock motion type A) and "interrupted shock-wave motion" (shock motion type B).

Trends for the unsteady shock motion due to gust encounters are shown in Fig. 5.16 for two different gust lengths and various amplitudes. The maximum shock position per excitation period moves further downstream with increasing excitation amplitude. However, a certain saturation of the shock position seems to be reached slightly downstream of the steady maximum position. The shock motion from the steady shock position in the upstream direction is much larger than that in the downstream direction. Deviations from a sinusoidal shock motion start at an amplitude of about $\widehat{W}_G = 5$ m/s.

Minimum and maximum shock positions for Mach 0.66 and Mach 0.70 are summarized in Fig. 5.17. The previously mentioned saturation in the maximum downstream shock position occurs up to reduced frequencies of about $k_{Gust} = 0.5$ at Mach 0.70. There seems to be a specific characteristic in the flow field which prevents the shock from a further downstream motion. Note that the limit in the maximum unsteady shock position does not imply a limit in the maximum lift value that is obtained, compare Fig. 5.17(b) with Fig. 5.11.

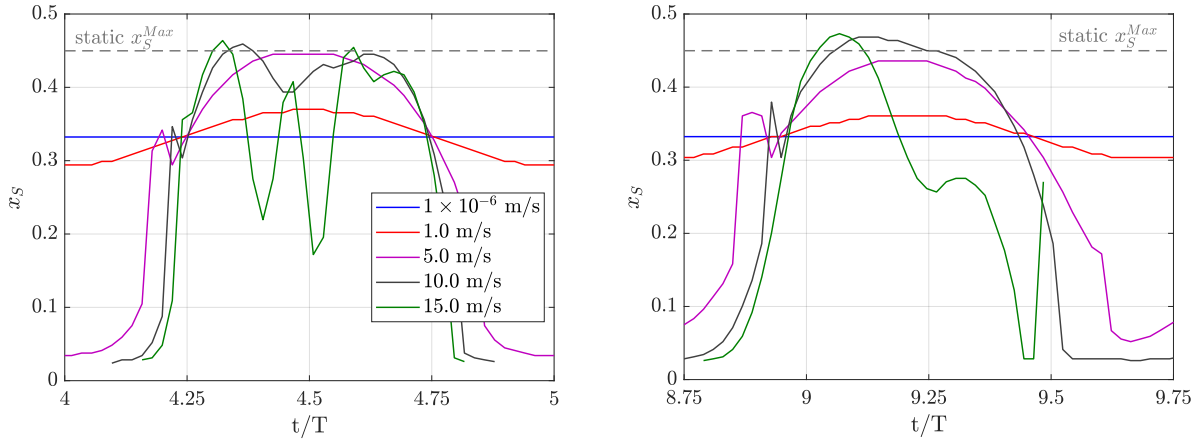

(a) $k_{Gust} = 0.05$ ($L_G = 125.5$ m) **(b)** $k_{Gust} = 0.20$ ($L_G = 31.5$ m)

Fig. 5.16: Shock motion for two gust lengths and various amplitudes at Mach 0.70

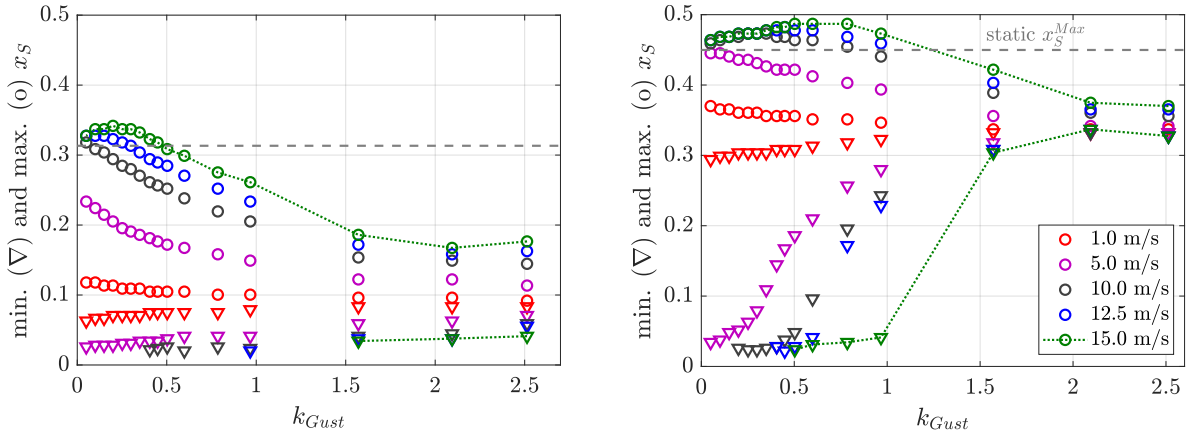

(a) Mach 0.66 **(b)** Mach 0.70

Fig. 5.17: Minimum and maximum x-coordinates for the shock position during one period of excitation. Missing points denote a vanishing of the shock.

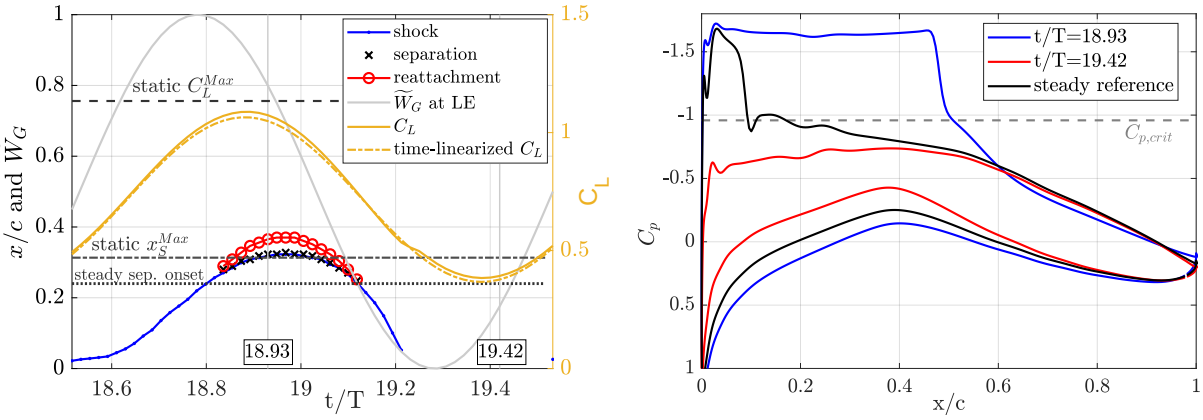

(a) Time histories **(b)** Pressure distributions

Fig. 5.18: Gust encounter at Ma 0.66, with $L_G = 15.5$ m ($k_{Gust} = 0.40$), $\widehat{W}_G = 15.0$ m/s; The normalized gust velocity is defined as $\widetilde{W}_G = 0.5\left(W_G/\widehat{W}_G + 1\right)$.

In general, maximum and minimum shock positions show significant frequency- and Mach-dependence. Whereas the shock moves by almost 50% over the airfoil chord at lower frequencies at Mach 0.70, the total shock motion is less than 10% for reduced frequencies as high as 2.0. Recalling from Chapter 5.1.1, that large shock motions induce high values for the lift curve slope, the high maximum lift values for lower excitation frequencies in Fig. 5.11 and Fig. 5.12 can be attributed to the observed large shock motions. However, it can not be observed in the data that a shock motion of 5% is a sufficient criterion to obtain a nonlinear response, as it is suggested by Dowell [57]. The shock motion can be much larger than 5% and still cause linear responses. The extent of the shock motion therefore does not appear to be a suitable criterion for identifying nonlinear responses.

For lower frequencies and medium to large amplitudes, the shock vanishes partly during one excitation period. The recompression shock disappears more often at the lower Mach number, see Fig. 5.17(a), as it is naturally closer to a subsonic flow condition. Fig. 5.18(a) shows an exemplary time history of such a flow: Local and global variables for a gust encounter at Mach 0.66 are depicted. On the one hand, the large amplitude of the gust causes transonic flow with shock-induced separation, and on the other hand, subsonic attached flow conditions. The diagram illustrates the relationship that is also relevant for the occurrence of ”dynamic overshoots”: during the gust response, the boundary layer separation is delayed compared to its quasi-steady reference. Separation sets in at a shock position that is about 5% chord further downstream than in the steady case. The shock reaches a position during the gust encounter that is further downstream than the maximum steady shock position. As already described above, the large shock motion leads to higher lift gradients in the nonlinear computation than is predicted by the time-linearized method. In consequence, the maximum lift obtained by the nonlinear method is higher than that obtained by the time-linearized method. As the gust continues to pass over the airfoil, the shock moves upstream again, and the flow reattaches until, at a certain point in time, the shock vanishes. This coincides with a kink in the lift response, and so even leads to a higher minimum lift value when the nonlinear method instead of the time-linearized method is used for the prediction. Since the time-linearized prediction is based on a steady transonic flow field, the assumed value for the lift curve slope is larger than the instantaneous value for subsonic flow. Hence, a lower minimum lift value is computed with the time-linearized method than with the nonlinear method. Summing up, significant changes in the topology of the flow field can be observed for this case, which can only be modeled using a nonlinear aerodynamic method.

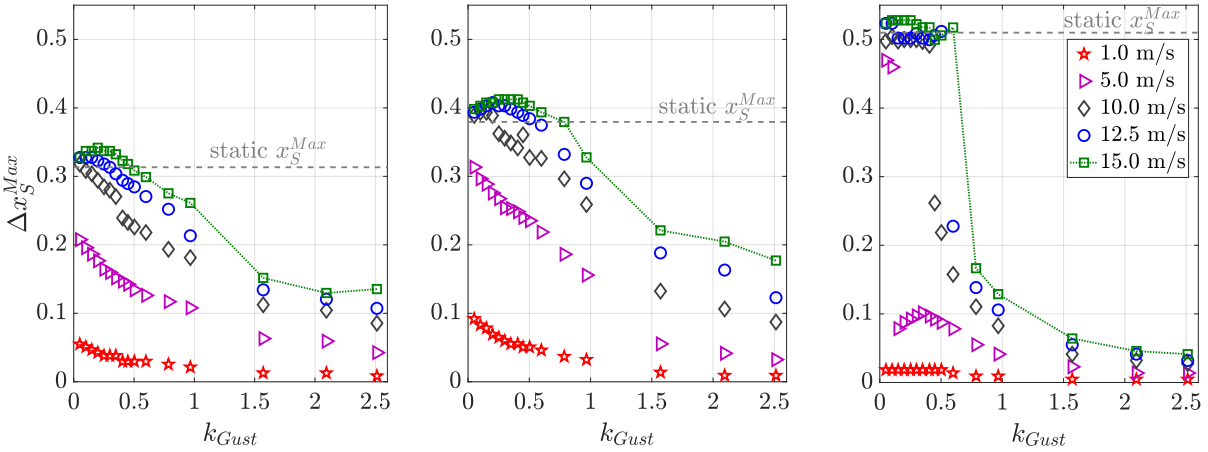

(a) Mach 0.66 **(b)** Mach 0.68 **(c)** Mach 0.72

Fig. 5.19: Maximum shock motion during one period of excitation;
$\Delta x_S^{Max} = max\,(x_S(t)) - min\,(x_S(t))$

From Fig. 5.19 is can be assumed that the static maximum shock position for each Mach number serves as a good indicator of the range of the maximum unsteady shock motion that might occur. Though the static value is not a hard limit, its value is overshot only by a few percent in any case. Note that the differences between the shock motion at lower and higher frequencies increase with increasing Mach number. However, the saturation in the shock motion that is observed for Mach 0.70 is also found in the data for the other Mach numbers and so seems to be a general effect.

5.1.5 Examples of Instantaneous Flow Fields

An impression of the flow field surrounding the airfoil is given in Fig. 5.20 for the test case at Mach 0.70 and $\alpha_0 = 3$ deg with $L_G = 125.5$ m and $\widehat{W}_G = 15.0$ m/s. For this long gust, the real-time for one period of oscillation amounts to 0.54 s. Time histories of shock position, lift, and gust velocity and the locations of the snapshots (a)–(g) are presented in Fig. 5.20(h).

The supersonic regions extend to almost 50% of the airfoil chord during the gust encounter, see snapshots (a)–(f), as could already be identified with the data from Fig. 5.20(h). For this specific case, lift and shock motion show three local maxima during one period of oscillation each, which might be an indicator of a beginning aerodynamic resonance, as already stated above. The snapshot couples (a)–(b) and (c)–(d) reveal a similar dynamic behavior for the first two maxima: just before the peaks, a large supersonic region and a separation bubble about mid-chord of the airfoil are found; see snapshots (a) and (c). The supersonic region then grows further, i.e., the shock moves downstream,

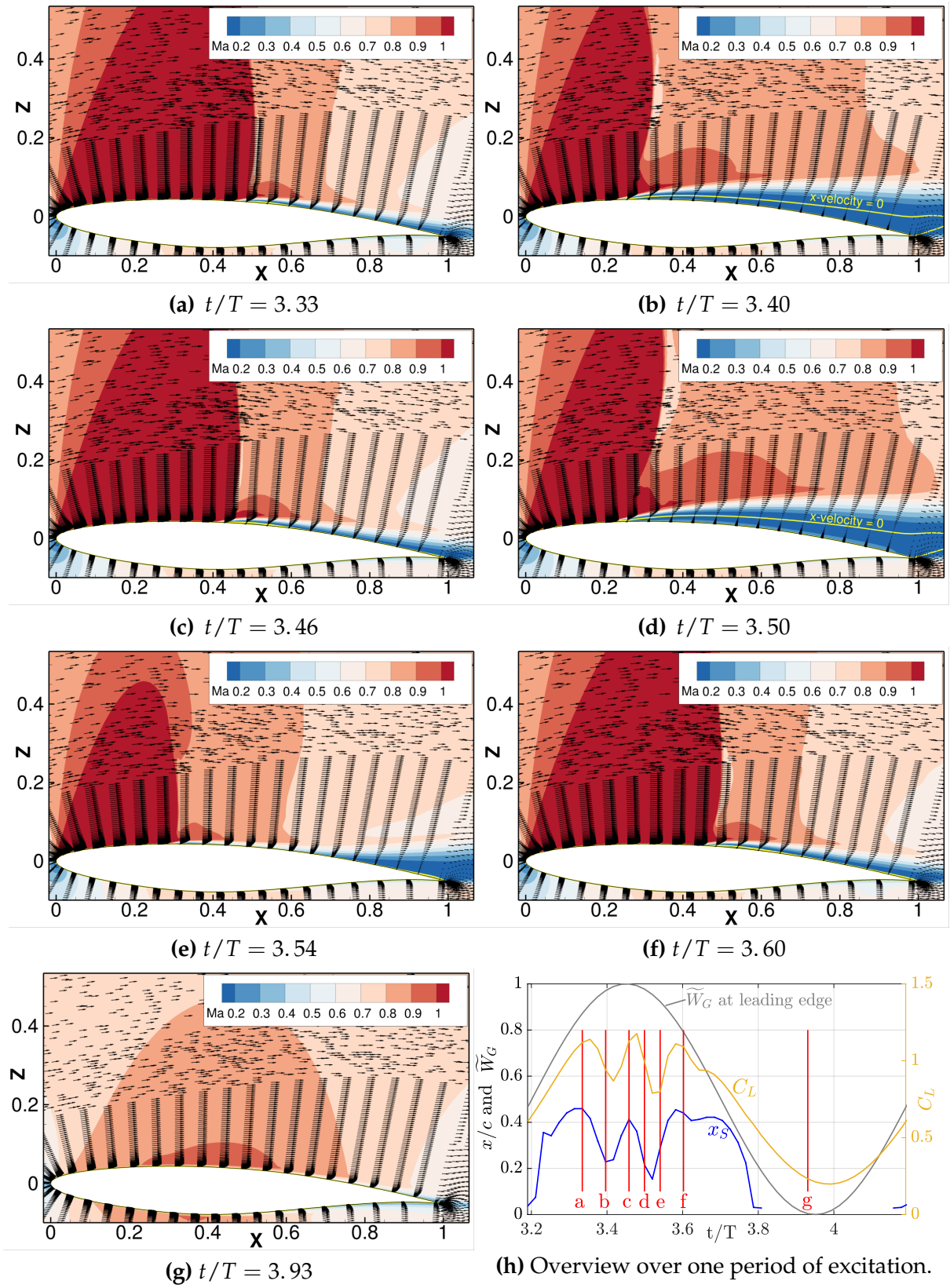

(a) $t/T = 3.33$ **(b)** $t/T = 3.40$

(c) $t/T = 3.46$ **(d)** $t/T = 3.50$

(e) $t/T = 3.54$ **(f)** $t/T = 3.60$

(g) $t/T = 3.93$ **(h)** Overview over one period of excitation.

Fig. 5.20: Gust encounter at Mach 0.70, $k_{Gust} = 0.05$ ($L_G = 125.5$ m) and $\widehat{W}_G = 15.0$ m/s: (**a**–**g**): Mach number contours, including velocity vectors. The yellow line in the field plots shows the contour for x-velocity = 0. (**h**): Lift, shock motion, and normalized gust velocity during one period of excitation

until, at some point, the shock eventually starts to move upstream together with an enlarging region of reversed flow; see snapshots (b) and (d). After snapshot (d), the flow attaches again shortly before snapshot (e) is reached. The third peak in the curves comes without such an extensive region of reversed flow and is probably limited by the now decreasing edge of the gust velocity. With the decrease of the excitation velocity down to $\widehat{W}_G = -15$ m/s, the flow reaches a purely subsonic state, see snapshot (g), which explains the interrupted shock motion curve in Fig. 5.20(h).

The significant flow separation that is observed during large portions of the excitation period leads to the early breakdown of the lift and hence stays below the time-linearized prediction of the maximum lift, compare with Fig. 5.11.

5.1.6 Influence of the Turbulence Model at Mach 0.70

Knowing that different RANS-based turbulence models compute quite similar solutions for attached flow conditions, but might lead to different results when flow separation is involved, this section should cover the effect of a different turbulence model on some of the results. For this airfoil configuration, the two-equation turbulence model Menter SST is used to re-compute some of the gust encounters with an otherwise unchanged set of parameters.

Fig. 5.21 reveals similar trends for the steady airfoil flow when computed with Menter SST instead of SAO, compare with Fig. 5.4(b) and Fig. 5.5(b): Subsonic flow corresponds to an almost constant lift curve slope, whereas transonic flow conditions introduce a nonlinear trend in the slope. The maximum value of the slope is encountered shortly before separation onset. Note, however, that the exact separation pattern is significantly different when

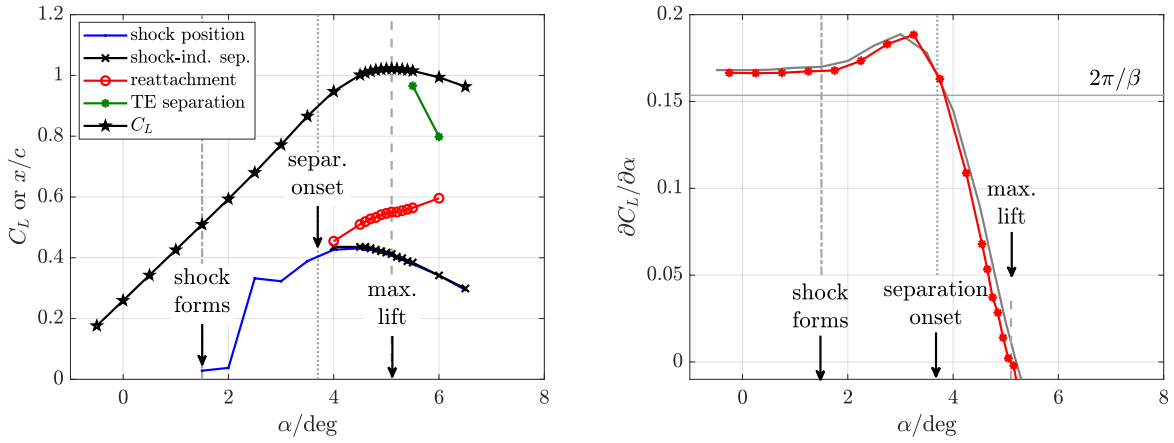

(a) Lift, shock position and separation **(b)** Lift curve slope (grey line: SAO reference)

Fig. 5.21: Steady trends at Mach 0.70 using Menter SST

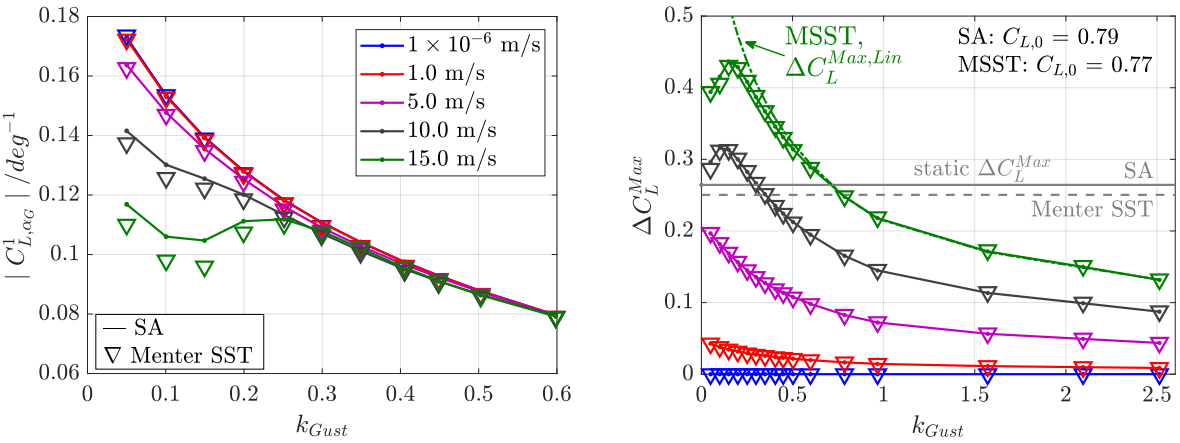

(a) First harmonic of the lift FRF. **(b)** Maximum lift.

Fig. 5.22: Global variables in comparison between Spalart-Allmaras (solid lines) and Menter SST (symbols) at Mach 0.70

compared to SAO: Trailing-edge separation starts with an offset of about $\alpha = +1.0$ deg when using Menter SST and the separation bubble behind the shock does not grow as strong as with SAO. The lift curve slopes are, however, almost identical for these two eddy-viscosity models.

The impact of the different modeling on the global gust response variables is displayed in Fig. 5.22. Most importantly, no previously described trend changes when changing the turbulence model. There are, however, slight differences between the quantitative values of the different models. The first harmonic response is more affected by the turbulence model than the incremental maximum lift coefficient, where the results of both models are almost identical. Note, however, that the steady lift coefficient between both turbulence models differ, though the freestream conditions are identical: the SA-model predicts a value of $C_L(\alpha_0 = 3\text{deg}) = 0.79$ and Menter SST predicts $C_L(\alpha_0 = 3\text{deg}) = 0.77$. Neglecting that steady difference, the unsteady increment of both turbulence models match nearly perfectly. Speaking about the first harmonic of the responses, the absolute deviations are more significant, probably because the first harmonic is more sensitive to the exact development of local flow features and incorporates the differences of the steady base flow. However, the observed deviations nearly vanish for small amplitudes or high frequencies.

The influence of the turbulence model increases when local variables are assessed, as shown in Fig. 5.23(a). The SA model predicts all shock positions further downstream than Menter SST. This trend is observed in several publications on transonic airfoil flows [96, 116, 124]. The agreement between the models is again better when incremental values are analyzed; see Fig. 5.23(b). However, the observed trends in shock motion from

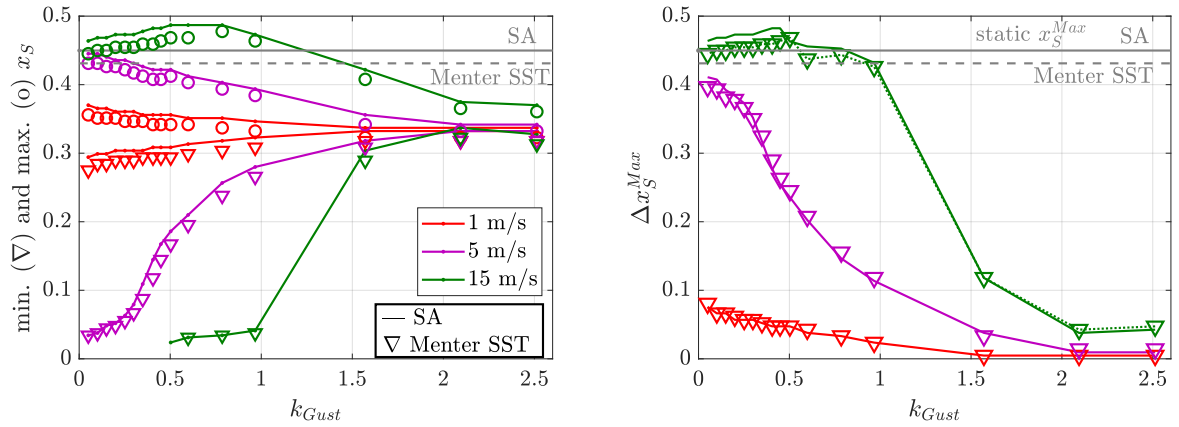

(a) Minimum and maximum x-coordinates for the shock position

(b) Maximum shock motion during one period of excitation

Fig. 5.23: Shock motion in comparison between Spalart-Allmaras (solid lines) and Menter SST (symbols) at Mach 0.70

Chapter 5.1.4 can also be found with Menter SST. The static maximum shock position is overshot in the unsteady responses and seems to be saturated in its maximum position for low excitation frequencies. Moreover, the shock vanishes during an excitation period if the excitation frequency is low and the excitation amplitude is rather large.

Summing up, the results obtained with the two-equation model Menter SST confirm the results of the one-equation model SAO concerning basic local and global trends for large-amplitude excitations in transonic flows.

5.2 Sinusoidal Gusts on the NASA Common Research Model

Gust encounters for this transport aircraft configuration are computed for three different steady base flows: the design case at Mach 0.85 and $C_L = 0.5$, which results in an angle of attack of $\alpha_0 = 2.02$ deg, and additional simulations for Mach 0.87 and Mach 0.83 at identical angle of attack. Note that all results in this chapter are computed for the (rigid) design geometry of the NASA Common Research Model.

5.2.1 Steady Lift Polars

The steady results reveal typical polar trends, see Fig. 5.24(a): increasing the Mach number increases the linear lift curve slope as long as the flow is attached. At higher angles of attack, separation sets in and leads to a decrease of the slope. The highest Mach number shows the narrowest linear range. None of the polars shows a distinct maximum value, contrary to results known from static airfoil flow.

The respective lift curve slopes of the aircraft configuration are depicted in Fig. 5.24(b). Though the configuration is geometrically more complex than the two-dimensional example in Chapter 5.1, similar trends can be observed: conditions with mainly shock-free flow over wide parts of the wing correspond to a range of almost constant lift curve slopes. With increasing transonic effects, i.e. increasing downstream shock position and increasing shock strength over wide areas of the wing, the lift curve slope increases. It decreases significantly if shock-induced separation is present and inverse shock motion can be observed at least in some parts of the wing. Fig. 5.25 – 5.27 illustrate some of the corresponding surface pressure distributions. Note that the gust encounter at the design point happens at an angle of attack that is slightly below the angle for the maximum lift

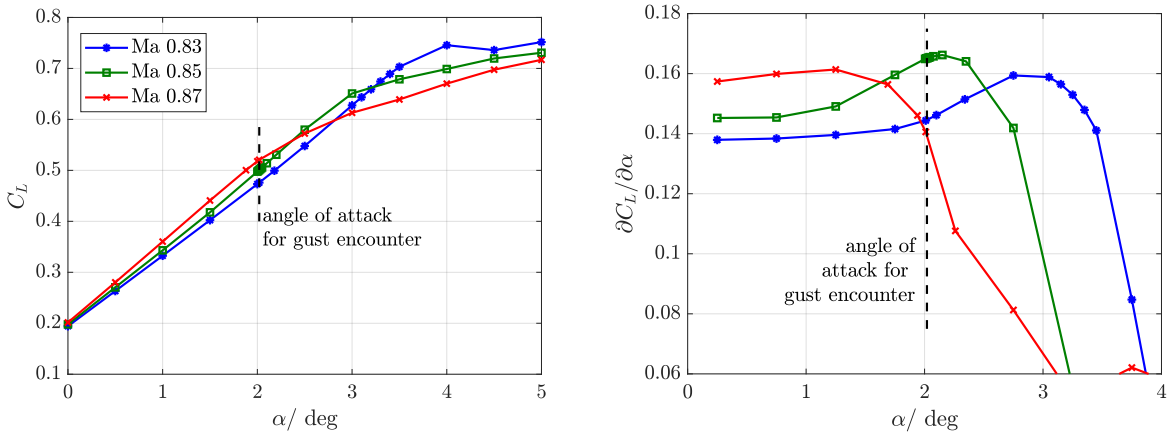

(a) Lift polars **(b)** Lift curve slopes

Fig. 5.24: Steady results for the design geometry of the NASA Common Research Model

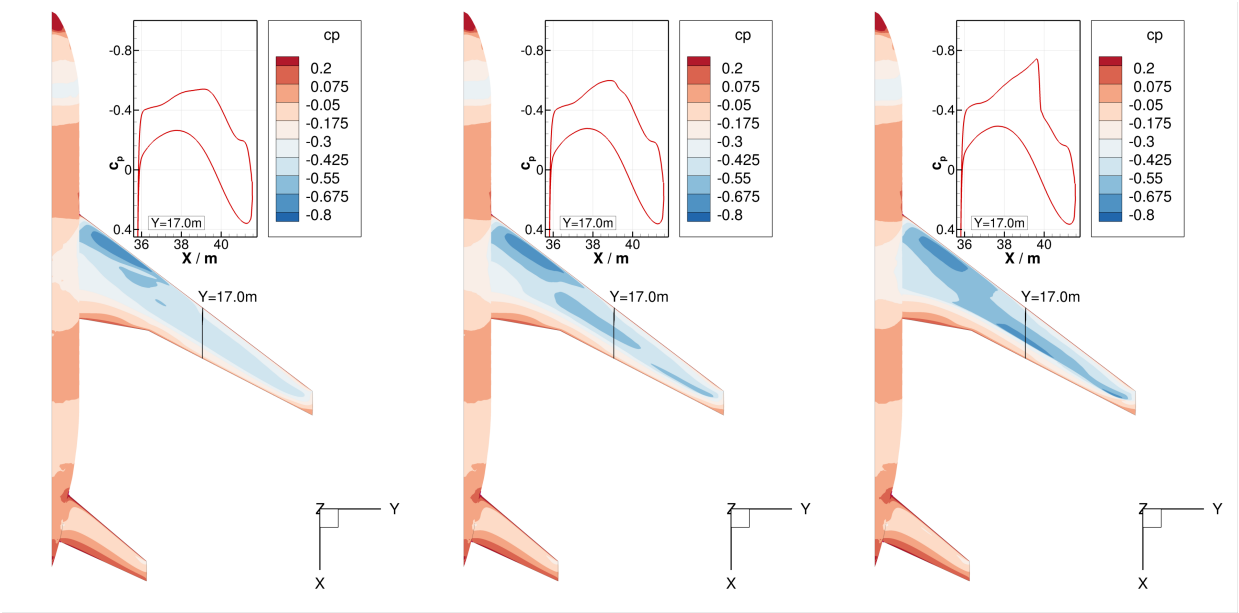

(a) Mach 0.83 **(b)** Mach 0.85 **(c)** Mach 0.87

Fig. 5.25: Steady pressure distributions at $\alpha_0 = 0.50$ deg

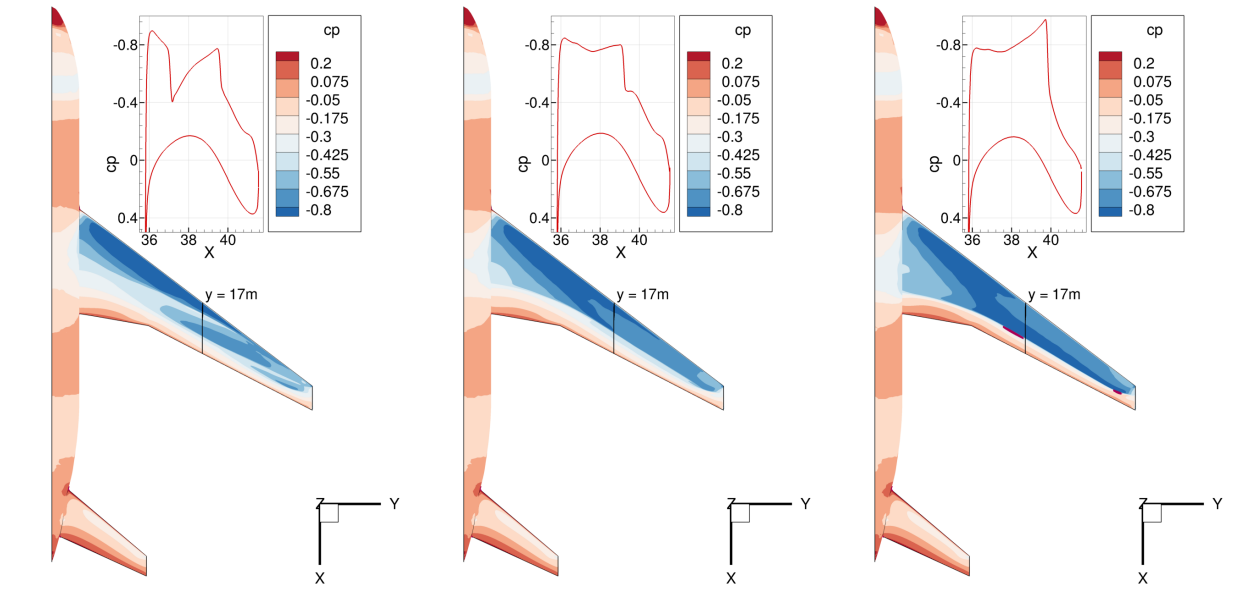

(a) Mach 0.83, $C_L = 0.48$ **(b)** Mach 0.85, $C_L = 0.50$ **(c)** Mach 0.87, $C_L = 0.52$

Fig. 5.26: Steady pressure distributions at $\alpha_0 = 2.02$ deg, which correspond to steady states for the gust encounters. (Magenta lines on the wing show the contour level $c_{fx} = 0$.)

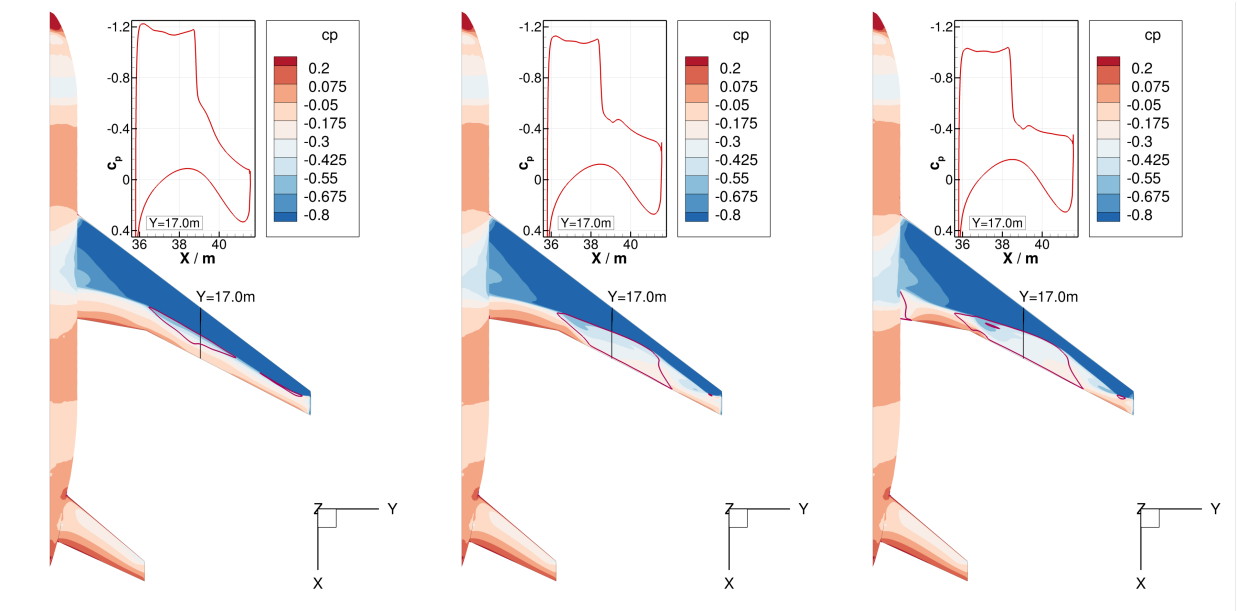

(a) Mach 0.83 **(b)** Mach 0.85 **(c)** Mach 0.87

Fig. 5.27: Steady pressure distributions at $\alpha_0 = 4.00$ deg. (Magenta lines on the wing show the contour level $c_{fx} = 0.$)

curve slope. Gust encounters at Mach 0.87 happen well beyond the maximum value, and gust encounters at Mach 0.83 well below.

5.2.2 Unsteady Nonlinear Lift Responses

Global trends

Time histories of lift responses at the design point of the aircraft are shown for reduced frequencies of $k_{Gust} = 0.1$ and $k_{Gust} = 0.2$ for different gust amplitudes in Fig. 5.28. With increasing excitation amplitude and decreasing excitation frequency, the responses deviate increasingly from a purely sinusoidal shape, which illustrates the impact of nonlinear modeling. The nonlinearities manifest in a premature breakdown of the lift due to an onset of shock-induced flow separation. A lower maximum lift value than for the time-linearized reference results are obtained. Note that also the minimum value of the gust response changes in the nonlinear responses, as well as the points in time when minimum and maximum values are reached. All nonlinear lift responses show rather smooth time histories, which are significantly smoother than those from similar airfoil simulations, see Fig. 5.6. Response peaks are not as sharp as in the two-dimensional studies, as the separation over the aircraft happens spatially more distributed, and some areas of the wing even stay fully attached during a complete cycle.

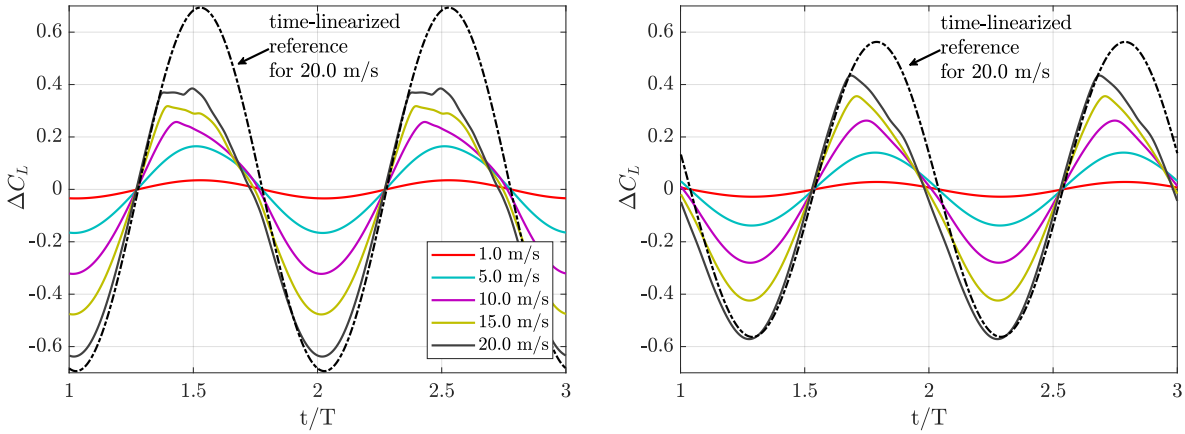

(a) $k_{Gust} = 0.10$ ($L_G = 440.0$ m) **(b)** $k_{Gust} = 0.20$ ($L_G = 220.0$ m)

Fig. 5.28: Increments of lift coefficients for two gust lengths and various amplitudes using SAO at Mach 0.85

Fig. 5.29 shows results for the maximum lift increments for several gust amplitudes and all frequencies computed at Mach 0.85. Linearly and nonlinearly computed results are in excellent agreement for small-amplitude responses where both show a monotonic trend with respect to the excitation frequency. For large-amplitude excitations, differences between the methods occur mainly in the range of low excitation frequencies: Exemplarily, for the case of $k_{Gust} = 0.10$ and $\widehat{W}_G = 15.0$ m/s, the nonlinearly computed maximum lift increment amounts to only 62% of the linearly computed value. Massive flow separation leads to lower maximum lift values in the nonlinear computations. Time-linearized predictions can neither capture a realistic shock motion [19] nor a reasonable flow sep-

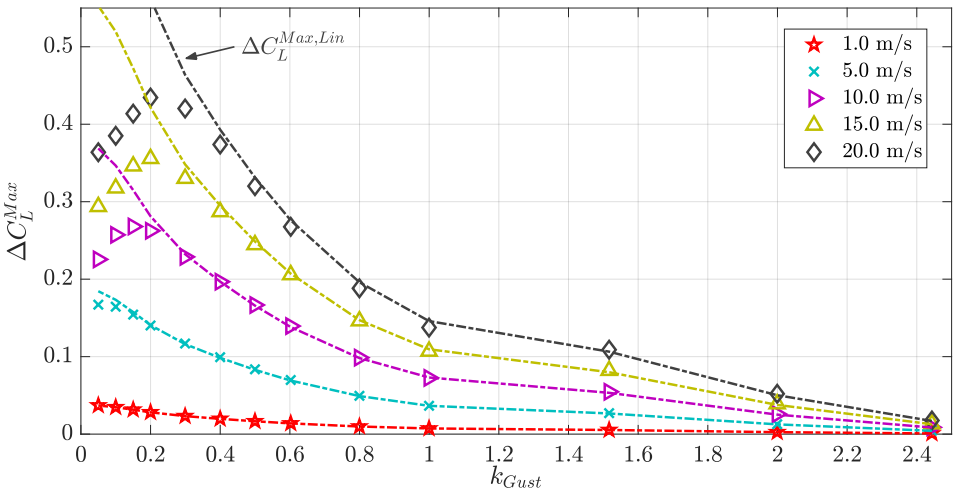

Fig. 5.29: Maximum linear and nonlinear increments of the lift coefficient for different gust amplitudes at Mach 0.85 for the NASA CRM

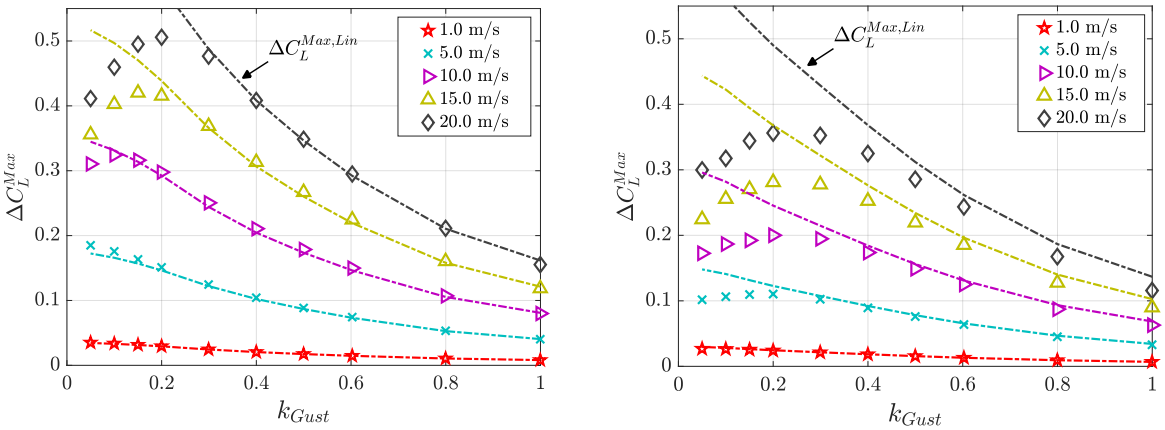

(a) Mach 0.83 **(b)** Mach 0.87

Fig. 5.30: Maximum linear and nonlinear increments of the lift coefficient for different gust amplitudes

aration. With increasing frequency, however, separation diminishes, and the differences between the methods are reduced. These findings are qualitatively identical to the airfoil investigations.

Fig. 5.30 summarizes the trends for the maximum incremental lift coefficient for the additional Mach numbers. Again, the same trends as for the airfoil configuration can be observed. The higher Mach number indicates amplitude effects for a broader range of frequencies and amplitudes. Flow separation leads to significantly reduced maximum values, when a nonlinear aerodynamic method instead of a time-linearized aerodynamic method is used. For the lowest Mach number of 0.83, additional nonlinear effects can be observed for the peak lift estimations: In the range of moderate amplitudes and at low frequencies, and in the range of medium to large amplitudes at mid-frequencies, the nonlinear computations show slightly higher maximum lift values compared to the time-linearized prediction. This suggests that the linear results are not conservative concerning aerodynamic peak load estimation in every case.

Analysis of Effective Slopes

It can be observed that gust encounters at a steady base flow with $\alpha_0 < \alpha\left((\partial C_L/\partial\alpha)^{Max}\right)$ might lead to higher nonlinear maximum lift values than the respective time-linearized computation, compare with Fig. 5.24(b). If the steady angle of attack is equal to or larger than the angle for the maximum lift curve slope, flow separation dominates the nonlinear solution and, hence, leads to lower maximum lift values.

This potential correlation is illustrated in Fig. 5.31 and Fig. 5.32 using a comparison of steady and effective lift slopes for Mach 0.83 and Mach 0.85. The unsteady, nonlinear

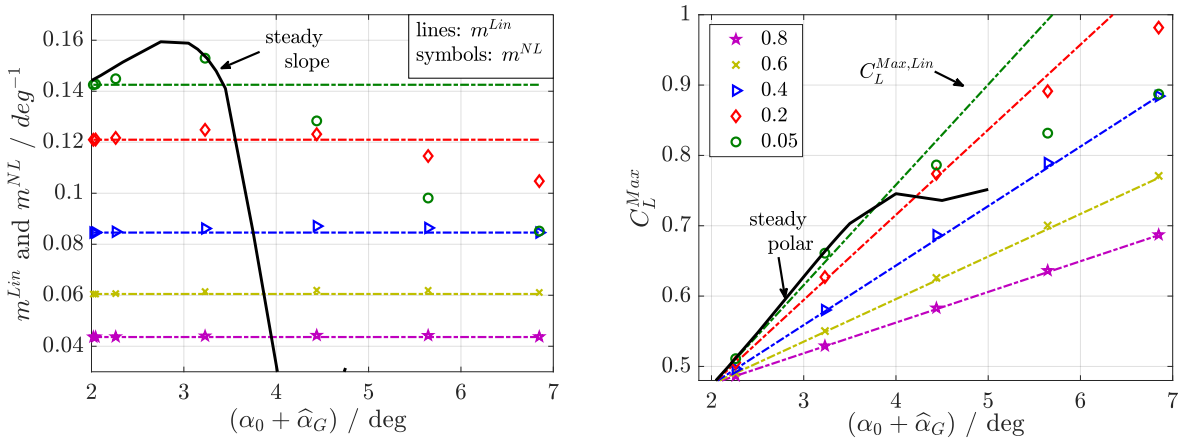

(a) Effective (linear and nonlinear) lift slopes **(b)** Maximum gust-induced lift as a function of total induced angle of attack

Fig. 5.31: Time-linearized and nonlinear results for different reduced gust frequencies at Mach 0.83 in comparison to steady data

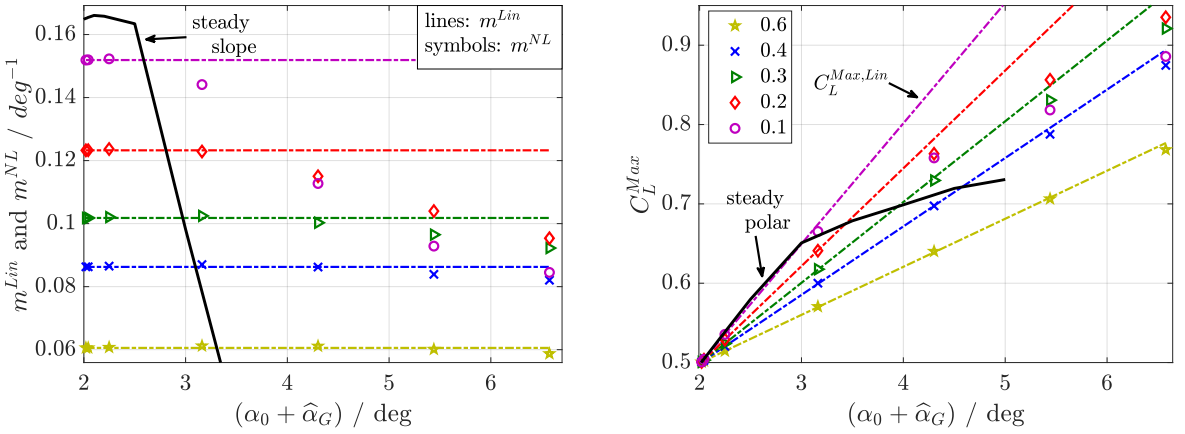

(a) Effective (linear and nonlinear) lift slopes **(b)** Maximum gust-induced lift as a function of total induced angle of attack

Fig. 5.32: Time-linearized and nonlinear results for different reduced gust frequencies at Mach 0.85 in comparison to steady data

computations result in the same trend for the slopes as the steady computations. The effective slopes are stretched along the x-axis, i. e., along the dimension of the induced angle of attack, when compared to the steady slope, whereby the stretching factor increases with increasing frequency.

The steady angle of attack for the gust encounter at Mach 0.83 is significantly below the angle of attack for the maximum steady lift curve slope, see Fig. 5.31(a). As a result, long gusts at medium amplitudes and medium-length to short gusts, especially at large amplitudes, result in higher maximum lift coefficients if nonlinear computations are used

instead of time-linearized ones, see Fig. 5.31(b). Significantly lower values for the maximum lift coefficient are only computed when the excitation amplitudes are large enough. The corresponding decrease in the effective lift slope can be attributed to the onset of significant flow separation.

The steady angle of attack for the gust encounter at Mach 0.85 is only minimal below the angle of attack for for the maximum steady lift curve slope, see Fig. 5.32(a). As a result, all gust encounters computed with the nonlinear method result in lower maximum values than with the time-linearized method. Flow separation is the dominant effect here. The same explanation holds for the responses at Mach 0.87.

The described relations are identical to those already identified on the RAE2822 airfoil in Chapter 5.1.3.

Details of the local pressure distributions

The following paragraphs illustrate three exemplary gust encounters at Mach 0.83 and $k_{Gust} = 0.4$, where different features of the nonlinear responses can be observed. Some details on the corresponding pressure distributions will be explained. Recalling Fig. 5.30(a) for the responses at $k_{Gust} = 0.4$, it can be observed that linear and nonlinear responses agree at an excitation amplitude of $\widehat{W}_G = 5.0$ m/s. When the amplitude is further increased to $\widehat{W}_G = 10.0$ m/s, the nonlinear maximum value slightly exceeds the time-linearized result. When the amplitude is further increased up to $\widehat{W}_G = 20.0$ m/s, both methods show identical maximum lift values again. However, the underlying physical mechanisms for these large-amplitude responses are totally different between the methods.

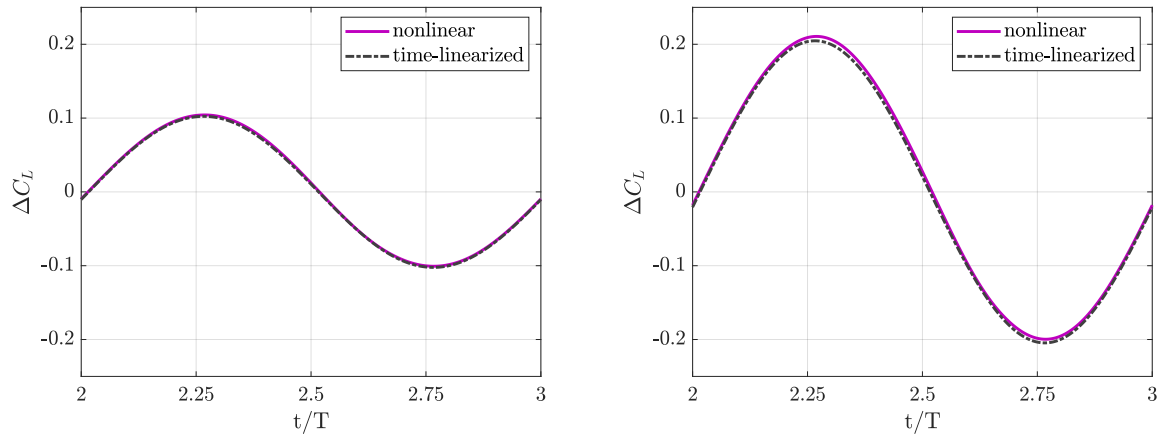

(a) $\widehat{W}_G = 5.0$ m/s **(b)** $\widehat{W}_G = 10.0$ m/s

Fig. 5.33: Time-domain lift responses at Mach 0.83 and $k_{Gust} = 0.4$

The time-domain histories of the incremental lift responses at $\widehat{W}_G = 5.0\,\mathrm{m/s}$ and $\widehat{W}_G = 10.0\,\mathrm{m/s}$ are depicted in Fig. 5.33. For the lower excitation amplitude, the results are almost on top of each other. For the higher excitation amplitude, a shift in the mean value can be observed for the nonlinear response. This leads to slightly higher maximum and minimum values when compared to the time-linearized prediction and will be explained in the following.

Recall from Fig. 5.26(a) that the steady base flow for Mach 0.83 shows a double-shock configuration at $y = 17.0\,\mathrm{m}$, which vanishes for higher angles of attack, see Fig. 5.27(a). The pressure distributions in Fig. 5.34 illustrate the corresponding unsteady shock motion at that specific spanwise position: for an amplitude of $\widehat{W}_G = 5.0\,\mathrm{m/s}$, the double shock moves but remains present over the complete response cycle, see Fig. 5.34(a). So linear and nonlinear results agree excellently, even though strong shock motion is observed. For the amplitude of $\widehat{W}_G = 10.0\,\mathrm{m/s}$, the double shock temporarily turns into a single shock, see Fig. 5.34(b). The effective lift curve slope is increased due to the change of the shock configuration and, hence, a higher maximum lift coefficient is obtained, compare with Fig. 5.31.

Increasing the gust amplitude up to $\widehat{W}_G = 20.0\,\mathrm{m/s}$ leads to identical linear and nonlinear maximum increments for the lift, Fig. 5.35(a), which might be rather unexpected from the above discussion. The reason for this is a compensation of different (nonlinear) effects, Fig. 5.35(b): on the one hand, the double shock turns into a single shock and increases the lift curve slope. On the other hand, this gust amplitude is large enough also to cause shock-induced flow separation ($t/T = 2.23, 2.36, 2.49$), which decreases the lift curve slope and limits the maximum lift value. Both effects superimpose during the re-

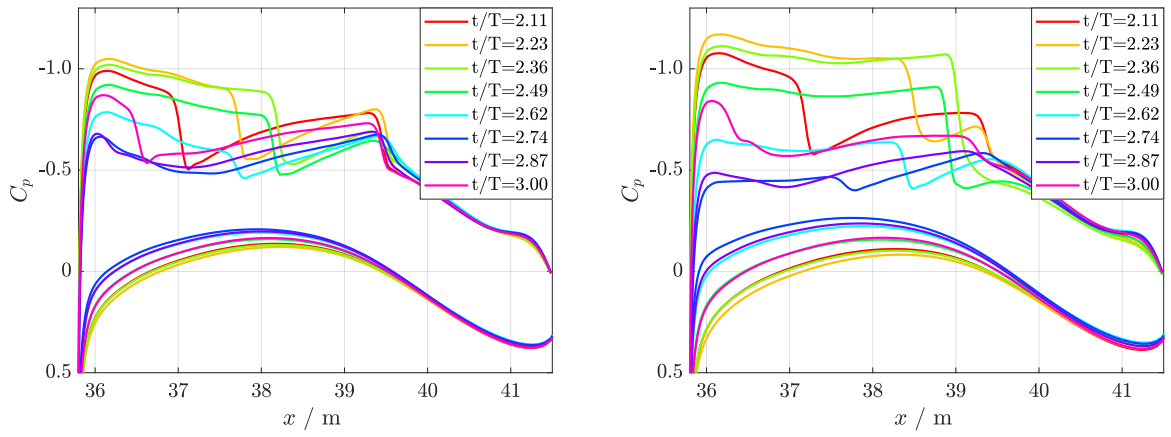

(a) $\widehat{W}_G = 5.0\,\mathrm{m/s}$ **(b)** $\widehat{W}_G = 10.0\,\mathrm{m/s}$

Fig. 5.34: Mach 0.83, $k_{Gust} = 0.4$: Time-series of surface pressures at $y = 17.0\,\mathrm{m}$, plotted every 0.039s for one response period

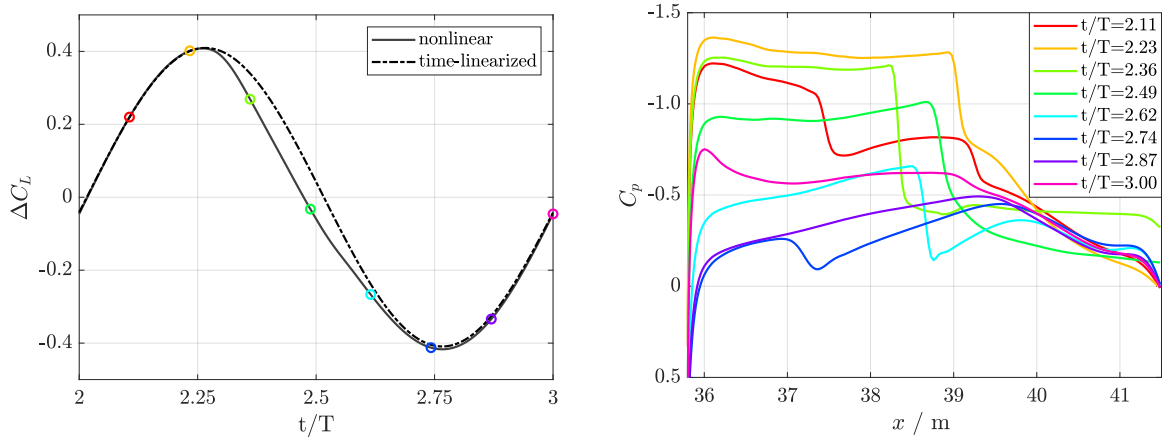

(a) Time-domain lift responses. Markers correspond to points in time for the pressure distributions

(b) Time-series of upper surface pressures at $y = 17.0$ m, plotted every 0.039s for one response period

Fig. 5.35: Mach 0.83, $k_{Gust} = 0.4$ and $\widehat{W}_G = 20.0$ m/s

sponse, and so the maximum lift of the linear and nonlinear solutions coincide in this case. Effective linear and nonlinear lift slopes are identical, see Fig. 5.31(a).

The exemplary trends described for the different responses at $k_{Gust} = 0.4$ also apply to other excitation frequencies at this Mach number. For lower excitation frequencies, these effects occur already at lower excitation amplitudes. For higher excitation frequencies, these effects occur at larger excitation amplitudes and only vanish at about $k_{Gust} = 0.8$. These findings correlate with the respective changes in the effective lift slope, which occur due to topological changes in the flow field in combination with the onset of flow separation.

5.2.3 Harmonic Responses of the Lift

The effect of the nonlinear modeling on the magnitude of the first and second harmonic of the lift coefficient at Mach 0.85 is analyzed using Fig. 5.36. Amplitude-independent results are observed for amplitudes as low as $\widehat{W}_G = 1 \times 10^{-6}$ m/s up to 1.0 m/s, compare also with Section B.3 . Nonlinear responses are characterized by a significant decrease in their first harmonic response and an increase of the second harmonic. First harmonic lift responses for $\widehat{W}_G = 15.0$ m/s and 20.0 m/s result in similar values, which might indicate a lower bound for the value of the first harmonic for high excitation amplitudes, as will be discussed below. Results for large-amplitude excitations for the first harmonic response at Mach 0.83 and Mach 0.87 mainly show similar trends as at Mach 0.85, see Fig. 5.37.

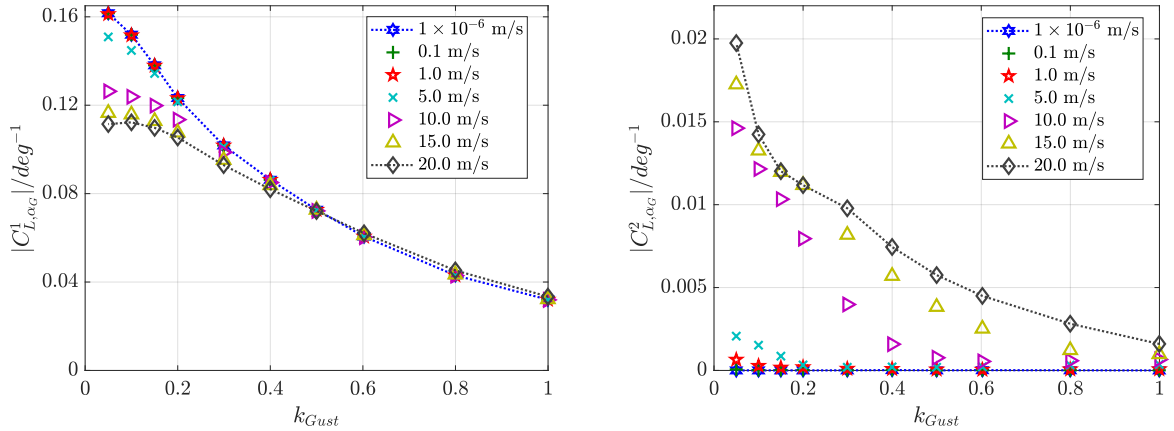

(a) First harmonic **(b)** Second harmonic

Fig. 5.36: Magnitude of the first and the second harmonic of the lift coefficient for different gust amplitudes at Mach 0.85

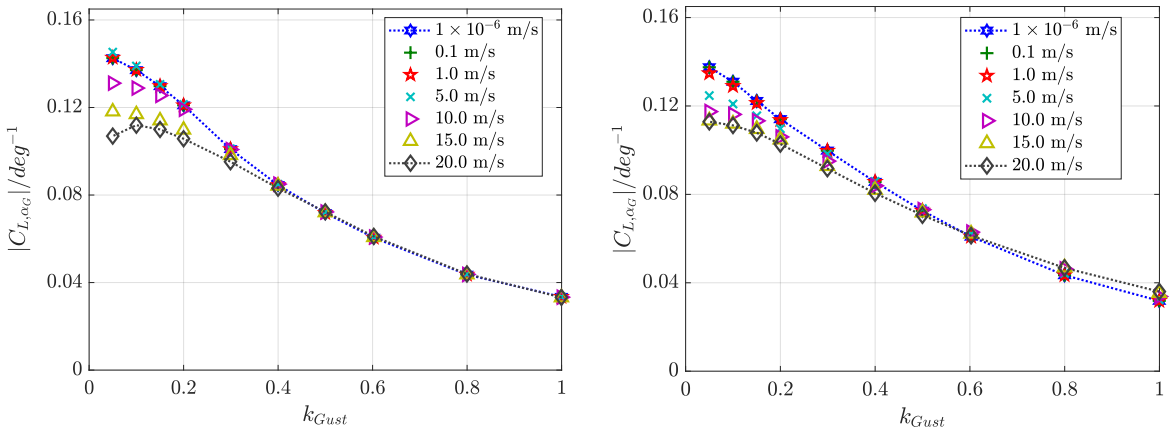

(a) Mach 0.83 **(b)** Mach 0.87

Fig. 5.37: Magnitude of the first harmonic of the lift coefficient

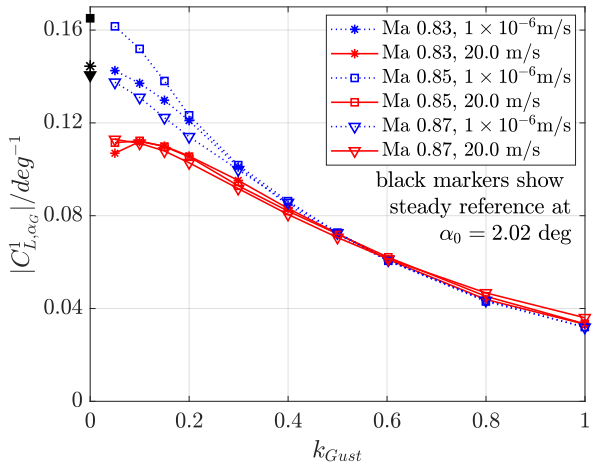

Fig. 5.38: Magnitude of the first harmonic of the lift coefficient.

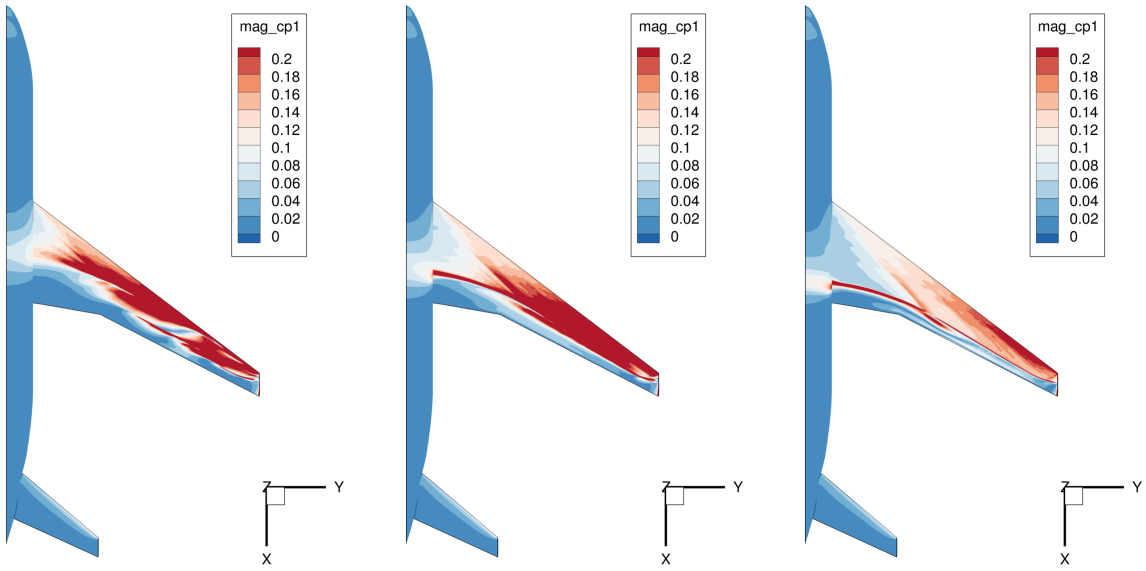

(a) Mach 0.83 **(b)** Mach 0.85 **(c)** Mach 0.87

Fig. 5.39: First harmonic magnitude of the upper surface pressure coefficient, $k_{Gust} = 0.1$ and $\widehat{W}_G = 1 \times 10^{-6}$ m/s

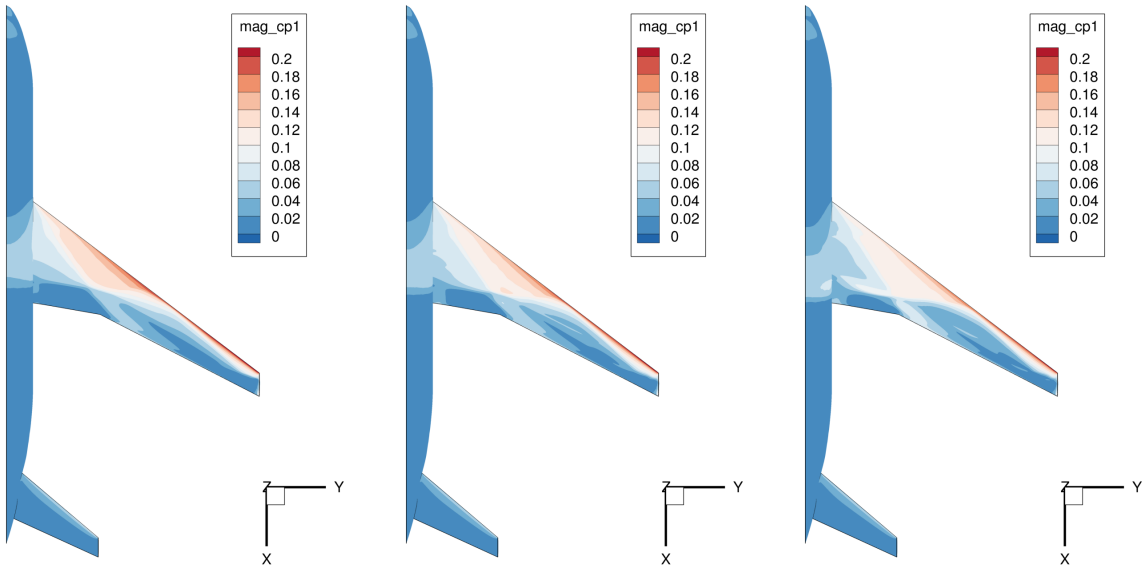

(a) Mach 0.83 **(b)** Mach 0.85 **(c)** Mach 0.87

Fig. 5.40: First harmonic magnitude of the upper surface pressure coefficient, $k_{Gust} = 0.1$ and $\widehat{W}_G = 20.0$ m/s.

The results in Fig. 5.38 suggest that the influence of the Mach number on the first harmonic is much larger for the linear responses than for the nonlinear ones. Fig. 5.39 and Fig. 5.40 illustrate corresponding details of the upper surface pressure of the aircraft. The small-amplitude responses shown in Fig. 5.39 are mainly influenced by their steady pressure distribution, which differs significantly between the different Mach numbers, recall Fig. 5.26.

During large-amplitude responses, however, the instantaneous pressure distributions deviate significantly from their corresponding steady states. Topological changes in the flow field due to shock motion and separation can be observed. The flow is dominated by the gust excitation and the steady state only plays a secondary role. The first harmonic response of the pressures is very similar between the different Mach numbers, see Fig. 5.40. Consequently, the first harmonic of the lift coefficient results in almost identical values even for different Mach numbers.

This effect could not be observed for the previous airfoil investigations, which might be caused by excitation amplitudes that are too low for the cases considered, compare with Chapter 5.1.2. A lower bound for the value of the first harmonic can not be observed in the airfoil data.

5.2.4 Influence of the Turbulence Model at Mach 0.85

Steady Polars

To quantify the influence of a different turbulence model, and hence, shock motion and separation behavior, on the results, the differential Reynolds-Stress model SSG/LRR in ln-omega-formulation [44] is used for additional computations. This model permits an anisotropy of the turbulent stresses and seems to predict more realistic results for the NASA Common Research Model configuration than SAO when compared to steady wind tunnel results [43]. However, for the settings used in this thesis, the computational time is almost doubled in comparison to unsteady computations based on SAO.

Steady lift polars for both turbulence models are almost identical up to an angle of attack of $\alpha_0 = 3.0$ deg, see Fig. 5.41. The lift curves start to deviate only when flow separation increases. The corresponding lift curve slopes are spot-on for attached flow cases and the trend of the slope computed with SAO is reproduced similarly using RSM. The computed drag is lower for SAO than RSM for the same lift value. Close to the design point of $C_L = 0.5$, both models exhibit their local maximum of the glide ratio C_L/C_D, as this geometry is optimized precisely for this condition. Computed steady angles of attack for each design point are slightly different for RSM ($\alpha_0 = 2.07$ deg) and SAO ($\alpha_0 = 2.02$ deg). Pressure distributions are almost identical and, therefore, not shown here, but the skin

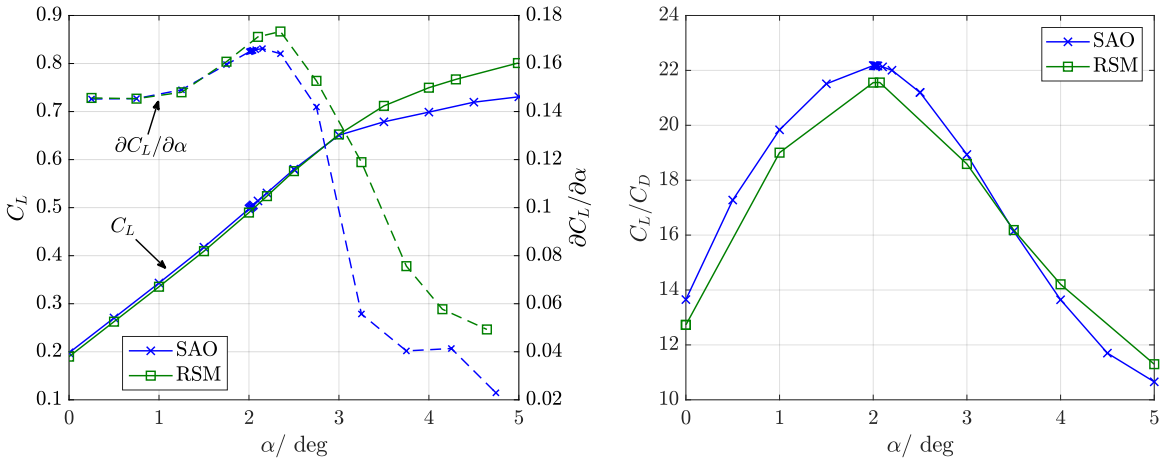

(a) Lift polar and lift curve slope **(b)** Glide ratio

Fig. 5.41: Steady results for SAO and RSM at Mach 0.85 and $Re = 40 \times 10^6$

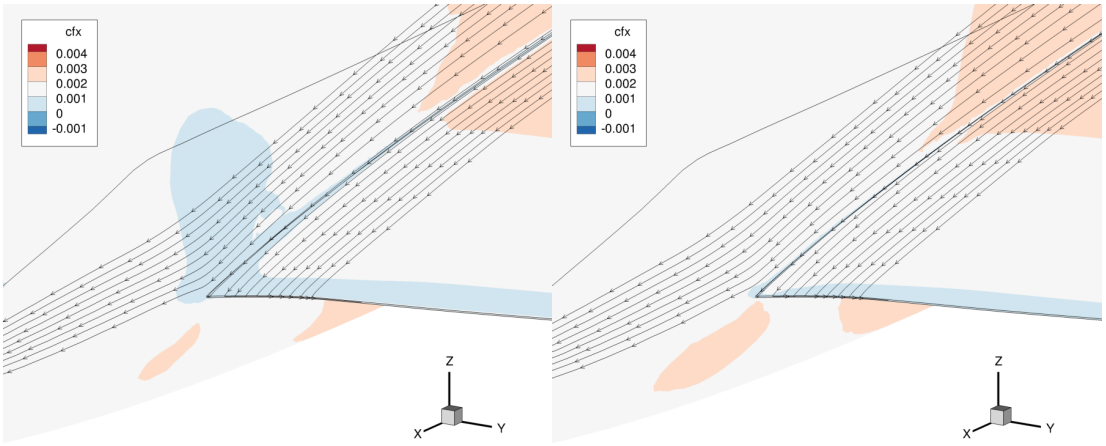

(a) SAO, $\alpha_0 = 2.02$ deg **(b)** RSM, $\alpha_0 = 2.07$ deg

Fig. 5.42: Steady skin friction distribution at design conditions for Mach 0.85, $Re = 40 \times 10^6$ and $C_L = 0.5$

friction distribution reveals slight differences in the region of the wing-fuselage juncture; see Fig. 5.42. SAO is already close to separation at the wing-fuselage junction, whereas RSM is not, which matches the findings in [43].

Lift Responses

Time-domain responses for the lift coefficient computed with RSM are shown in Fig. 5.43. Though this turbulence model additionally includes the anisotropy of the Reynolds stresses, the resulting qualitative trends are similar to SAO computations based on only one equation for turbulent closure: with increasing excitation amplitude, the deviation between linearly and nonlinearly computed results grow. The lift curves obtained with

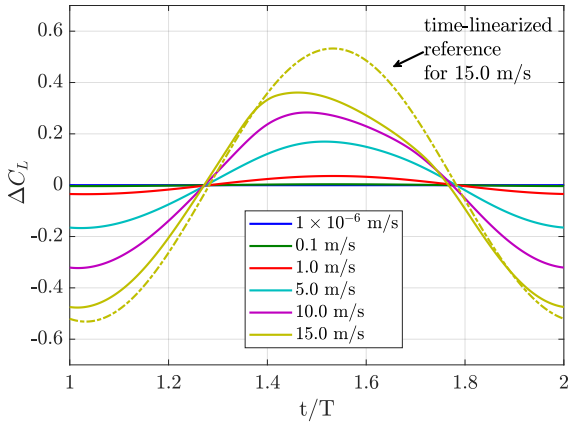

Fig. 5.43: Increments of lift coefficients for various amplitudes at $k_{Gust} = 0.1$ using RSM

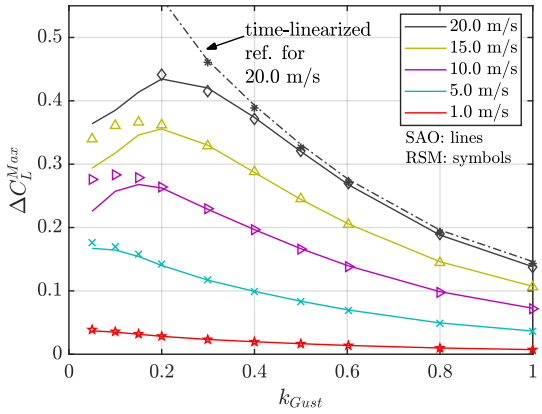

Fig. 5.44: Maximum nonlinear increments of the lift coefficient for SAO and RSM

RSM are smoother than the SAO results in Fig. 5.28, and nonlinear effects set in at higher amplitudes compared to SAO.

This becomes more obvious in Fig. 5.44, where the increments of the maximum lift values are shown for both turbulence models in a direct comparison. Note that it was not possible to obtain converged RSM results for the three lowest frequencies and a gust velocity of $\widehat{W}_G = 20.0$ m/s. The general trends found with SAO are confirmed with the Reynolds-stress model: Large amplitudes and low excitation frequencies lead to nonlinear lift responses. For reduced frequencies higher than $k_{Gust} = 0.2$, nonlinear results of SAO and RSM agree excellently. SAO leads to lower maximum lift values for lower frequencies than RSM, which can be attributed to a different separation behavior. Using RSM, the linear trend is kept over a broader range of frequencies than with SAO. The lift histories in Fig. 5.45(a) indicate a difference in the separation behavior of the models, which affects the maximum lift values. In consequence, the mean value between both models differs slightly, see Fig. 5.45(b). For harmonics higher than the third, SAO values

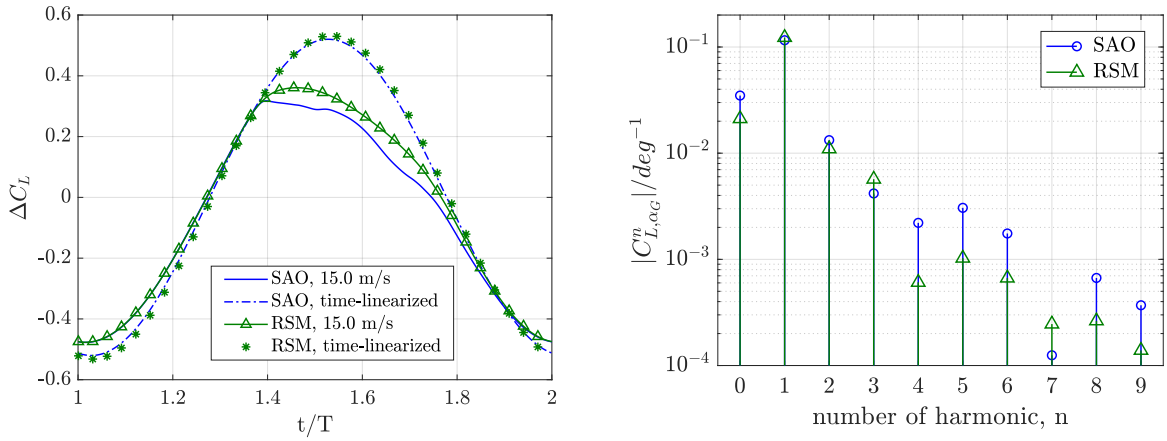

(a) Lift response (markers for RSM are only plotted for every 40th sample point)

(b) Frequency content of nonlinear responses

Fig. 5.45: SAO and RSM for $k_{Gust} = 0.1$ and $\widehat{W}_G = 15.0$ m/s

are about half of an order of magnitude larger than those of RSM, and imply a broader response spectrum for SAO results. However, as these higher harmonics result in very small values, they are not important in the prediction of the maximum lift values.

5.2.5 Examples of Instantaneous Surface Flow

Details of the pressure distribution on the surface of the wing are illustrated in Fig. 5.46 for SAO and in Fig. 5.47 for RSM. An additional contour line on the wing is plotted for $c_{fx} = 0$. The instantaneous gust velocity is marked by the green line in the diagrams. Note that the term "separation" is used for areas with $c_{fx} < 0$, though this might not be a sufficient criterion for an exact definition in an unsteady, three-dimensional flow [125, 126]. However, this criterion is easy to implement and serves as an approximation.

When the instantaneous gust velocity is at its minimum value of about $W_G = -15.0$ m/s, both turbulence models show similar, almost subsonic-type, pressure distributions and fully attached flow on the upper side of the wing, see Fig. 5.46(a) and Fig. 5.47(a). With increasing gust velocity, transonic flow develops with a recompression shock on the wing. First separation sets in just behind the shock at the outer wing for both models, though this happens at a lower instantaneous gust velocity for SAO than for RSM, compare Fig. 5.46(b) and Fig. 5.47(b). For SAO, the initially small separation bubble quickly grows and develops into a largely separated area behind the recompression shock (c), even before the maximum gust velocity is reached. This separated area grows in size until about half of the excitation period (d). With decreasing gust velocity, separation starts to recover first at the wing tip and shifts towards mid-wing (e). During all the time from

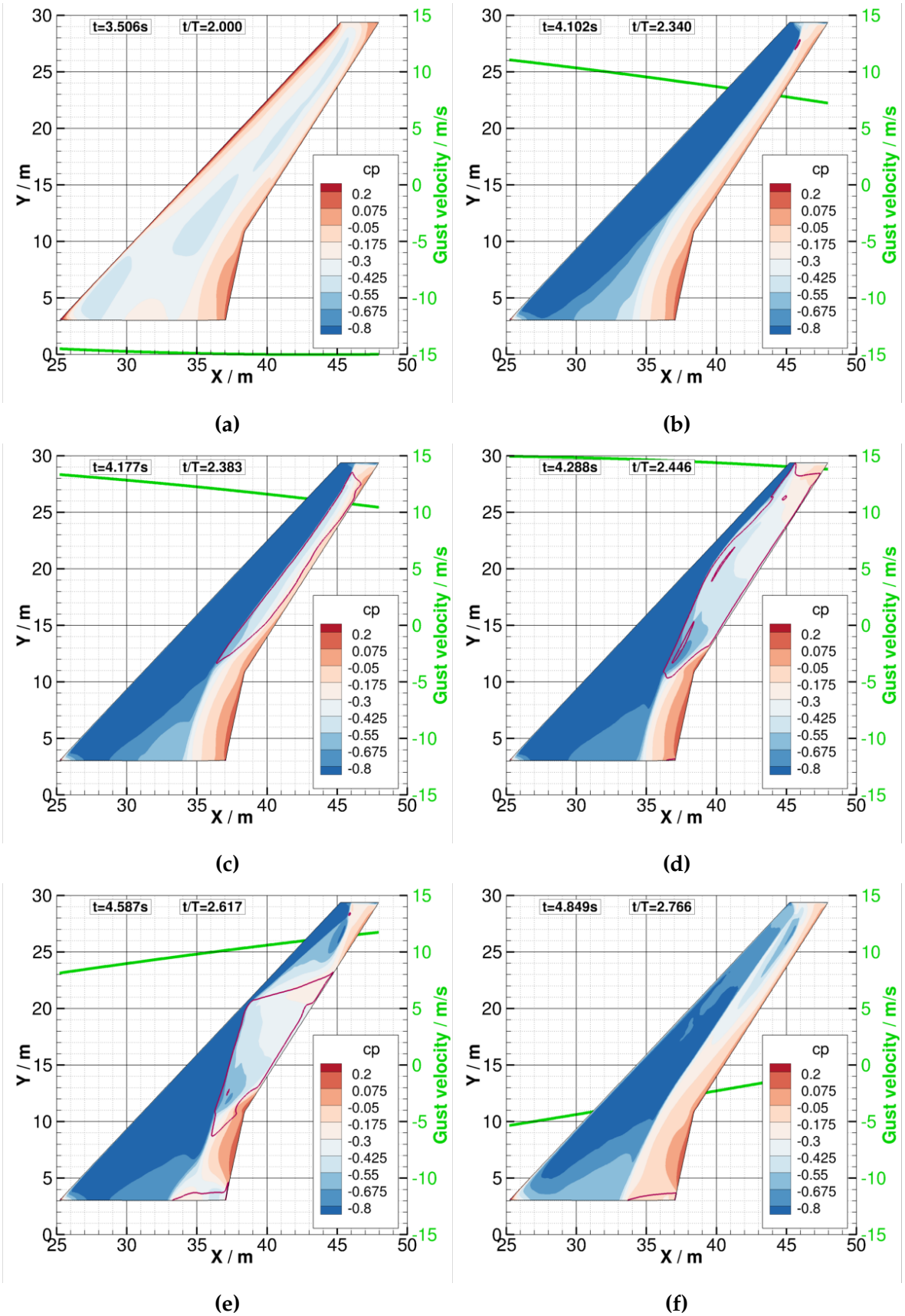

Fig. 5.46: Some highlights of the flow during one period of excitation using SAO, $k_{Gust} = 0.1$ ($L_G = 440.0$ m) and $\widehat{W}_G = 15.0$ m/s
(magenta line on the wing marks contour level $c_{fx} = 0$)

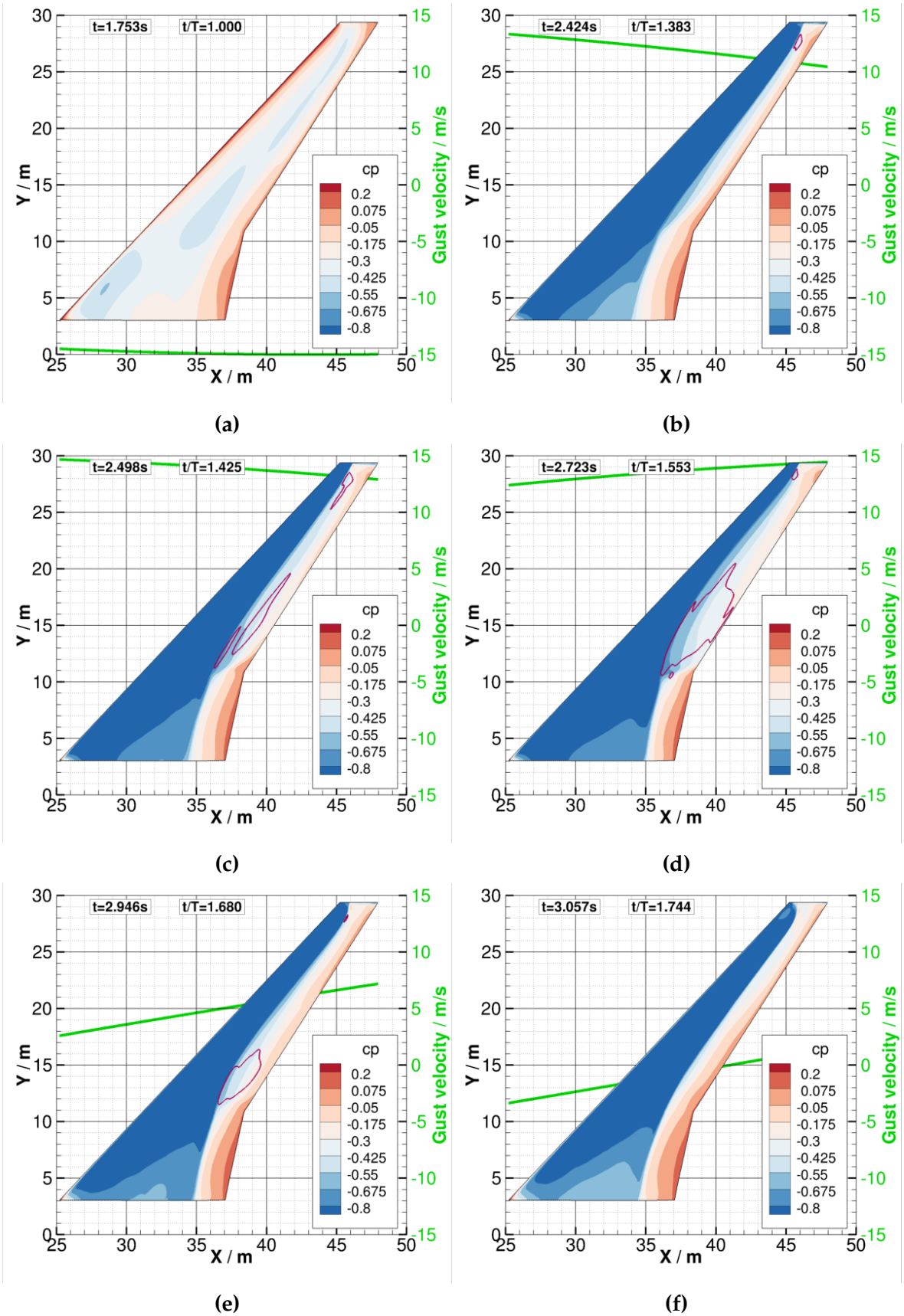

Fig. 5.47: Some highlights of the flow during one period of excitation using RSM, $k_{Gust} = 0.1$ ($L_G = 440.0$ m) and $\widehat{W}_G = 15.0$ m/s
(magenta line on the wing marks contour level $c_{fx} = 0$)

(c) to (e), an inverse shock motion takes place on the outer part of the wing, i.e., the shock moves upstream, which explains the loss in lift. Note that all separated regions are located just downstream of the shock front which emphasizes the superior role of the shock/boundary layer interaction in transonic dynamic stall as stated by Liiva [49] and Visbal [50]. It takes three-quarters of the excitation period until the flow has nearly recovered from separation; see (f). During the shrinking of the largely separated area over the main wing, a so-called side-of-body (SOB) separation [43] develops at the wing-body-junction, see (d), which first grows in size (e) and is still present when the flow on the main wing returns to the attached flow again; see (f).

Separation patterns are modeled completely different using the Reynolds-stress model; see Fig. 5.47. After separation onset at the wing tip (b), two separate zones of negative skin friction develop in the mid-wing region behind the recompression shock. These two zones then coalesce (d), stay spatially very limited, and rapidly decrease again in size (e). After three-quarters of the excitation period is over, the flow is fully attached again (f).

So, in general, the results with the RSM show a spatially more bounded separation over the main wing and a fundamentally different behavior at the wing root when compared to SAO. Similar findings are reported by Feldwisch [20]. Using SAO, a side-of-body separation develops at the trailing edge of the wing root for the second half of the excitation period. In contrast, with the RSM, the flow is fully attached to the wing root throughout the cycle. Recall that an earlier separation also applies to the steady flow solutions computed with SAO, see Fig. 5.41.

Although there are differences in the local quantities between the turbulence models, however, the analysis of the global lift and its maximum value show qualitatively identical trends. The further analyses, therefore, continue with the model SAO.

5.3 Discrete Gusts on the NASA Common Research Model

5.3.1 Unsteady Nonlinear Lift Responses

This chapter discusses amplitude effects and recurring stages in the time histories for discrete gust encounters, as the certification specifications require this gust shape. Differences and similarities to the results of the monofrequent gusts are investigated. Note that computations are carried out only at Mach 0.83 and Mach 0.85. Based on the findings of the sinusoidal gusts, it is assumed that there are no further new findings for Mach 0.87. Moreover, results in this section are preferably plotted using the gust length instead of the reduced gust frequency, as this variable is more intuitive for discrete gust encounters.

Note that the time scale in the following figures is plotted using the nondimensional time τ with

$$\tau = t \cdot U_\infty / l_{ref} = \Delta x / l_{ref}. \tag{5.1}$$

Analysis at Mach 0.83

Incremental lift coefficients of different gust responses at Mach 0.83 are shown in Fig. 5.48. Similar trends are observed as for the monofrequent gusts: Small gust amplitudes result in linear responses. Large gust amplitudes lead to an early breakdown of the lift compared to their time-linearized counterpart. It is also noted that responses to medium-size gust amplitudes show slightly higher maximum lift values than the linear prediction. Longer gusts are more affected by amplitude nonlinearities than shorter gusts, compare Fig. 5.48(a) and Fig. 5.48(b).

Time histories of the surface pressures reveal identical mechanisms as for monofrequent gusts for the different types of responses: for a medium-amplitude gust, see Fig. 5.49(a), the double shock transforms into a single shock during the gust encounter. Separation happens only in a very limited region, and for a short period. A gust encounter with the same gust length, but with a larger gust amplitude triggers significant shock-induced separation, see Fig. 5.49(b), and hence, results in a significant decrease in the predicted peak lift value. These findings agree with the trends observed in Chapter 5.2.2.

Fig. 5.50 shows time-linearized and nonlinear incremental maximum lift coefficients for all computed "1-cos" gust encounters. The qualitative findings are identical to those from monofrequent gusts, see Fig. 5.30(a): Large excitation amplitudes and low excitation frequencies tend to result in nonlinear responses, which lead to a significant reduction in the

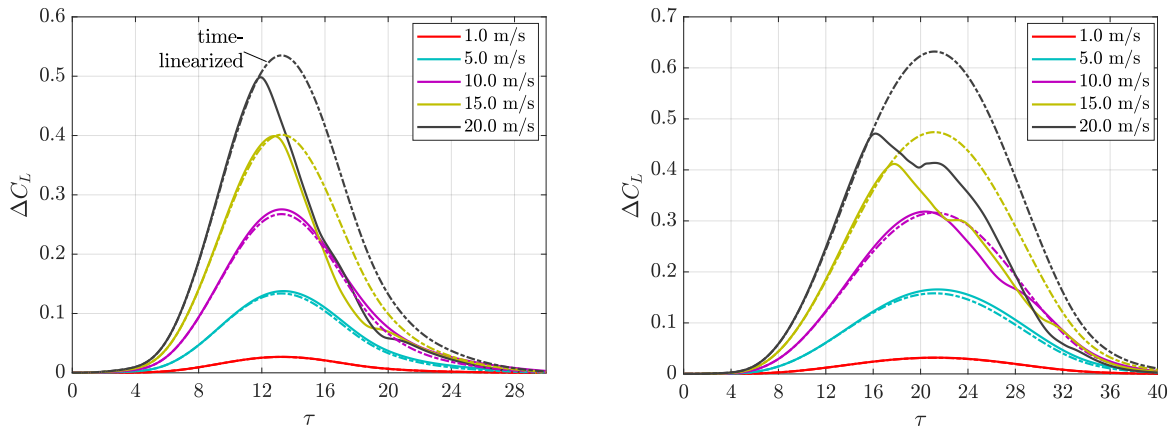

(a) $L_G = 105.0$ m **(b)** $L_G = 210.0$ m

Fig. 5.48: Increments of lift coefficients for two gust lengths and various amplitudes, Mach 0.83

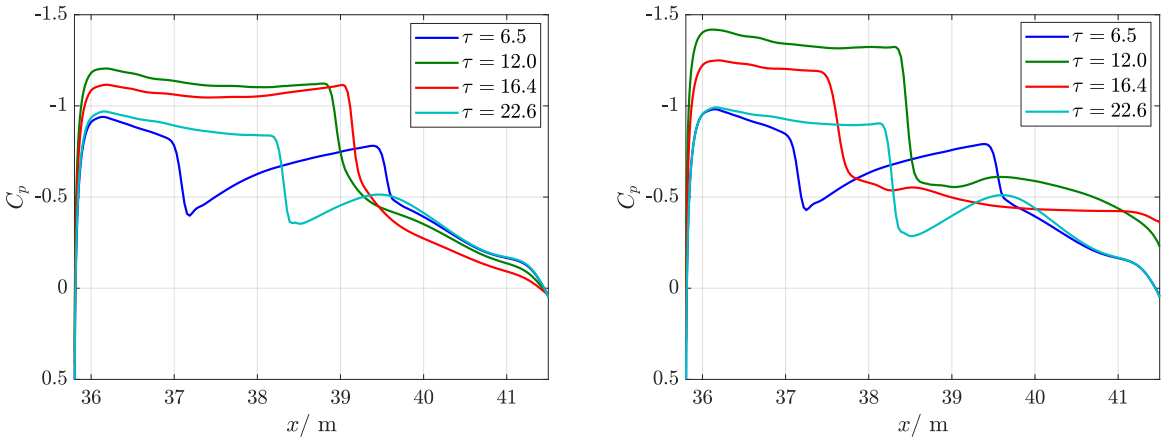

(a) $\widehat{W}_G = 10.0\,\mathrm{m/s}$ **(b)** $\widehat{W}_G = 20.0\,\mathrm{m/s}$

Fig. 5.49: Upper surface pressures at $y = 17.0$ m for $L_G = 105.0$ m at Ma 0.83

maximum lift coefficient. Medium-length and medium-amplitude gusts trigger a higher maximum lift values than the time-linearized prediction. Gust lengths and amplitudes in between impose almost identical time-linearized and nonlinear lift peaks.

A direct comparison of the nonlinearly computed incremental maximum lift coefficients from monofrequent and broadband gusts is shown in Fig. 5.51(a). Note that the results are plotted over the gust equivalent reduced frequency, k_{Gust}^{equiv}, for a proper comparison. For the sinusoidal gusts, $k_{Gust}^{equiv} = k_{Gust}$ applies. For "1-cos" gusts, the respective reduced frequency is halved, $k_{Gust}^{equiv} = k_{Gust}/2$, which corresponds to a factor of 0.5 for the effective gust length. Fig. 5.51(b) illustrates the scaling effect.

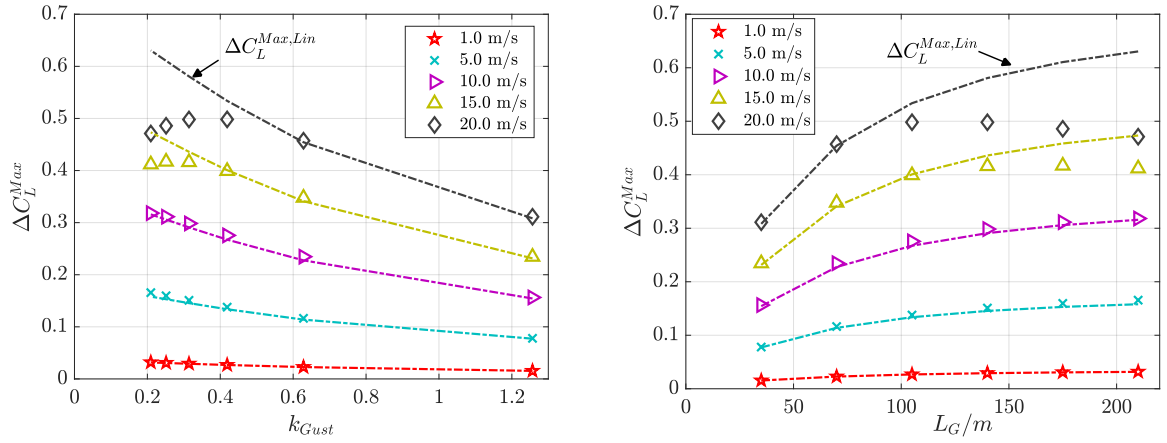

(a) In terms of reduced gust frequency **(b)** In terms of gust length

Fig. 5.50: Maximum linear and nonlinear increments of the lift coefficient for different discrete gust amplitudes at Mach 0.83

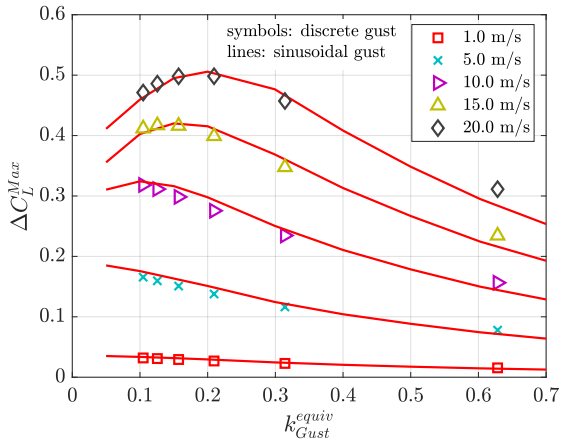

(a) Incremental maximum lift coefficients

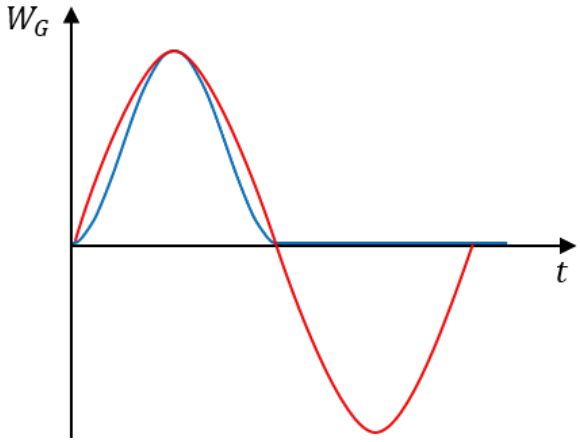

(b) Effective gust lengths for identical k_{Gust}^{equiv}

Fig. 5.51: Comparison of sinusoidal and "1-cos" gusts

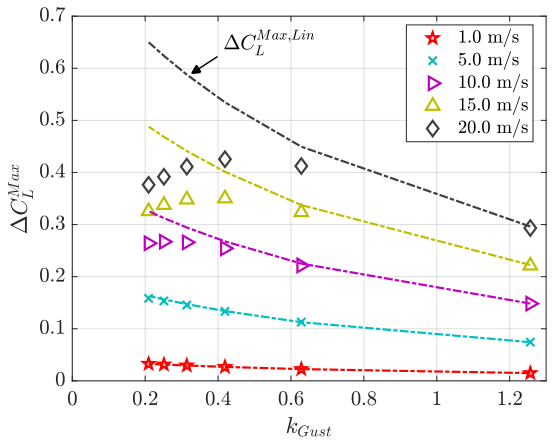

(a) In terms of reduced gust frequency

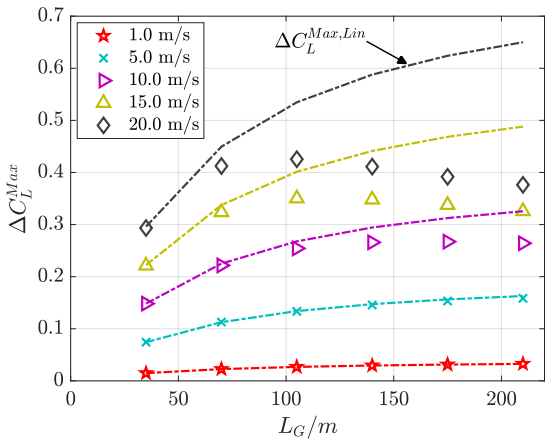

(b) In terms of gust length

Fig. 5.52: Maximum linear and nonlinear increments of the lift coefficient for different discrete gust amplitudes at Mach 0.85

Both types of gust excitation lead to very similar values for the maximum lift coefficient, especially for long gusts, i.e., low frequencies. Deviations increase with decreasing gust length: for short gusts, "1-cos" excitations always result in higher maximum values than sinusoidal excitations. It can be assumed from these results that the exact shape of the (gust) excitation is important in the prediction of responses to short gusts and does only play a minor role for excitations with long-wavelength gusts, which is an effect that is already reflected in the linear data.

Analysis at Mach 0.85

Maximum incremental lift coefficients for gust encounters at the design point of the configuration are shown in Fig. 5.52. Again, identical overall trends and similar absolute values as for the responses to monofrequent gusts are found. For this steady-state con-

figuration, nonlinear effects are governed by shock-induced flow separation and, hence, exclusively lead to lower nonlinear lift peaks than the time-linearized predictions.

Relative differences in maximum incremental lift

The relative differences in the maximum incremental lift, δC_L^{Max}, for the respective parameter spaces at Mach 0.83 and Mach 0.85 are depicted in Fig. 5.53. Three important aspects are emphasized again using these graphics:

- The exceeding of the time-linearized predicted maximum values by the nonlinear method can be observed at Mach 0.83, independently of the gust length. This increase is caused by a topological change in the flow field, which can already be observed in the steady state and only occurs with a lag in the unsteady responses.
- However, the effect mentioned occurs on a much smaller scale than nonlinear effects that arise due to separation and thus lead to a reduction in the nonlinear predicted maximum lift value in the lift. (Compare: +1% increase is opposed to a –20% reduction in lift)
- The underlying steady flow field determines which of the nonlinear effects mentioned occurs in the unsteady responses. Based on the steady lift curve slope, it seems predictable whether nonlinear aerodynamic methods result in conservative or nonconservative values for the maximum incremental lift coefficients.

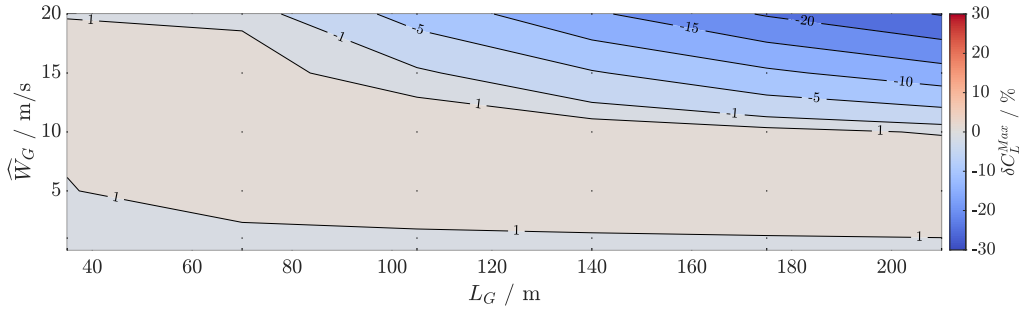

(a) Mach 0.83

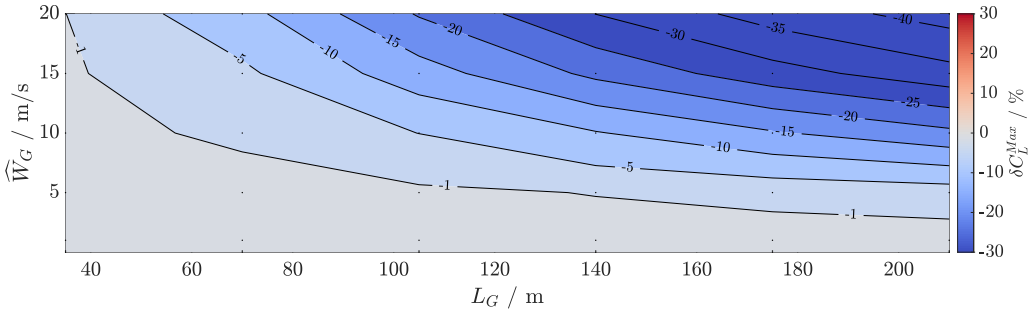

(b) Mach 0.85

Fig. 5.53: Relative difference between linear and nonlinear computations in the maximum incremental lift coefficient (black dots mark test case samples)

5.3.2 Chronology of a Discrete Gust Encounter

This section aims to identify a general chronology of events during a discrete gust encounter, as loads based on this type of gust are required by the regulation authorities. The time history of the lift response is analyzed for specific stages to better understand the sequence of events.

In the first step, distinct points in the gust excitation are identified, which are denoted by τ_G. They mainly relate to the encounter of the maximum gust velocity on specific

Table 5.1: Significant points in time during excitation with a discrete gust, τ_G. Examples for Mach 0.83.

Index	Location of maximum gust velocity	τ_G	τ for $L_G =$ 210.0 m	τ for $L_G =$ 70.0 m
1	Gust encounter starts, $W_G > 0$	τ_G^{Start}	0.0	0.0
2	$\widehat{W}_G$ at nose ($x = 2.75$ m)	τ_G^{Nose}	14.5	4.5
3	$\widehat{W}_G$ at wing root leading edge ($x = 24.9$ m)	τ_G^{LE}	17.8	7.8
4	$\widehat{W}_G$ at wing tip trailing edge ($x = 47.9$ m)	τ_G^{TE}	21.0	11.0
5	$\widehat{W}_G$ at HTP root leading edge ($x = 56.8$ m)	$\tau_G^{HTP,LE}$	22.3	12.3
6	$\widehat{W}_G$ at HTP tip trailing edge ($x = 66.7$ m)	$\tau_G^{HTP,TE}$	23.8	13.8
7	Gust leaves aircraft, $W_G = 0$	τ_G^{Stop}	38.7	18.7

Table 5.2: Significant points in time for the lift response due to a discrete gust, τ_L. Examples for Mach 0.83 and $\widehat{W}_G = 20.0$ m/s.

Trend in global lift coefficient	τ_L	τ for $L_G =$ 210.0 m	τ for $L_G =$ 70.0 m
lift increases	$\tau_{L,1}$	5.3	1.8
lift derivative exceeds time-linearized value	$\tau_{L,2}$	12.1	8.3
lift breaks down	$\tau_{L,3}$	16.2	10.3
lift increases slightly	$\tau_{L,4}$	19.9	–
lift decreases	$\tau_{L,5}$	21.3	–
lift decreases less	$\tau_{L,6}$	31.5	14.8
decay of the disturbance in lift	$\tau_{L,7}$	33.9	16.7
lift has reached steady-state value	$\tau_{L,8}$	42.7	26.0

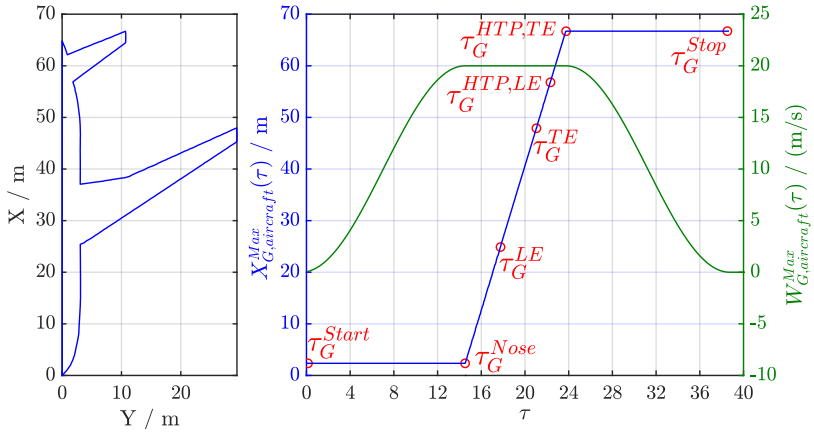

(a) $L_G = 210.0$ m

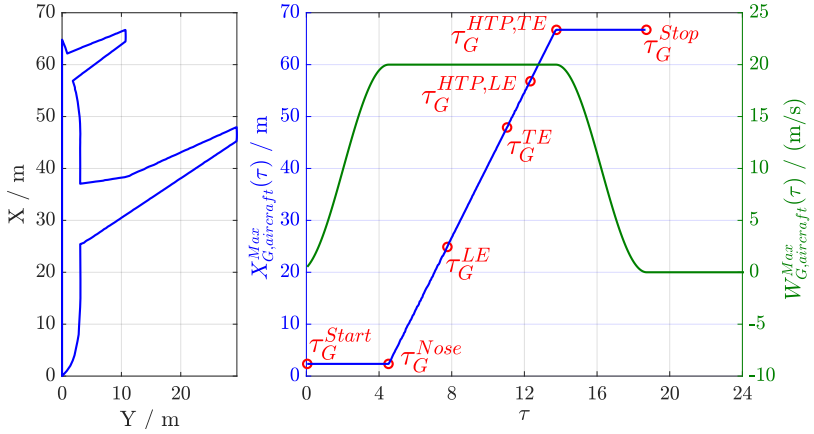

(b) $L_G = 70.0$ m

Fig. 5.54: Significant points in time during excitation with a discrete gust, τ_G

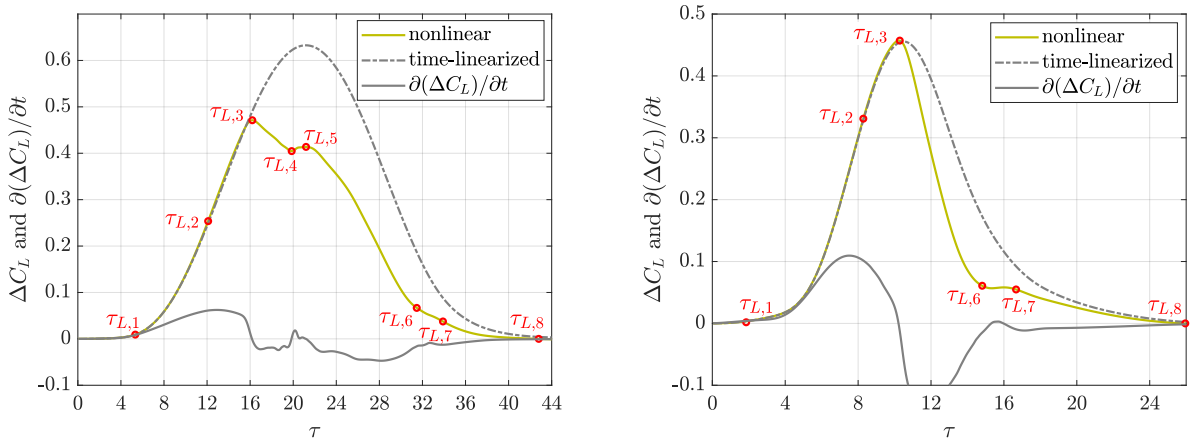

(a) $L_G = 210.0$ m, $\widehat{W}_G = 20.0$ m/s

(b) $L_G = 70.0$ m, $\widehat{W}_G = 20.0$ m/s

Fig. 5.55: Stages in lift history during a nonlinear gust encounter, τ_L, at Ma 0.83

components of the aircraft, see Table 5.1 and Fig. 5.54: Five distinct points are marked on the aircraft geometry: the nose of the aircraft, the wing root leading edge, the wing tip trailing edge, the HTP root leading edge, and the HTP tip trailing edge. The convecting maximum gust velocity hits all these points at different points in time, as displayed in the figure. The location of the instantaneous maximum gust velocity on the aircraft is labeled by $X^{Max}_{G,aircraft}$ and $W^{Max}_{G,aircraft}$ shows the corresponding the maximum gust velocity on the aircraft in Fig. 5.54. The total time for the gust encounter amounts to $\Delta\tau = 38.7$ for the longer gust, $L_G = 210.0$ m, and to $\Delta\tau = 18.7$ for the shorter gust, $L_G = 70.0$ m.

In the second step, the pressure distribution on the upper surface of the wing is analyzed for a correlation with significant points in time concerning the lift history. Since the qualitative trend of the lift response seems to be governed by the wing only, see Appendix B.5, this approach seems suitable. Table 5.2 lists eight distinct points in time, $\tau_{L,i}$, which can each be attributed to a changing trend in the lift's time history. These points in time are depicted in Fig. 5.55 for two different gust responses. Corresponding snapshots of the pressure distribution on the upper surface of the wing are shown in Fig. 5.56 and Fig. 5.57. The following section is intended to show the different relationships and mechanisms in the flow, between the convecting gust velocity, the global lift response, and the local pressure distributions.

Stages of the gust encounter with $L_G = 210.0$ m and $\widehat{W}_G = 20.0$ m/s are depicted in Fig. 5.56: the gust starts to convect over the aircraft at τ_G^{Start} and with a slight lag, the lift starts to increase around $\tau_{L,1}$. The double shock is present on the upper surface of the wing, Fig. 5.56(a). Before the maximum gust velocity even reaches the aircraft's nose (τ_G^{Nose}), the nonlinear lift derivative exceeds its time-linearized value due to the formation of a single recompression shock over the wing's span at $\tau_{L,2}$, Fig. 5.56(b). The lift increases until it reaches its maximum value at $\tau_{L,3}$, where the flow is largely separated behind the shock on mid- and outer wing, Fig. 5.56(c). Only then does the gust amplitude reach the wing root leading edge (τ_G^{LE}) and convects over the wing. During that time, the flow on the wing tip recovers, and the inverse shock motion at the wing tip changes into a regular shock motion at $\tau_{L,4}$, see Fig. 5.56(d). The overall lift increases slightly and then remains on a plateau due to the high gust velocity. Just after the maximum gust velocity leaves the wing tip trailing edge (τ_G^{TE}) the lift starts to finally decrease at $\tau_{L,5}$. The largely separated region on the mid-wing, which is visible in Fig. 5.56(e), reduces due to the falling edge of the gust velocity, which leads to the onset of a regular shock motion. At the same time, with the decreasing gust velocity, the shock on the outer wing starts to move upstream and reaches the leading edge at $\tau_{L,6}$, see Fig. 5.56(f). A single shock front is manifested again with only minor separated regions. This single-shock configuration

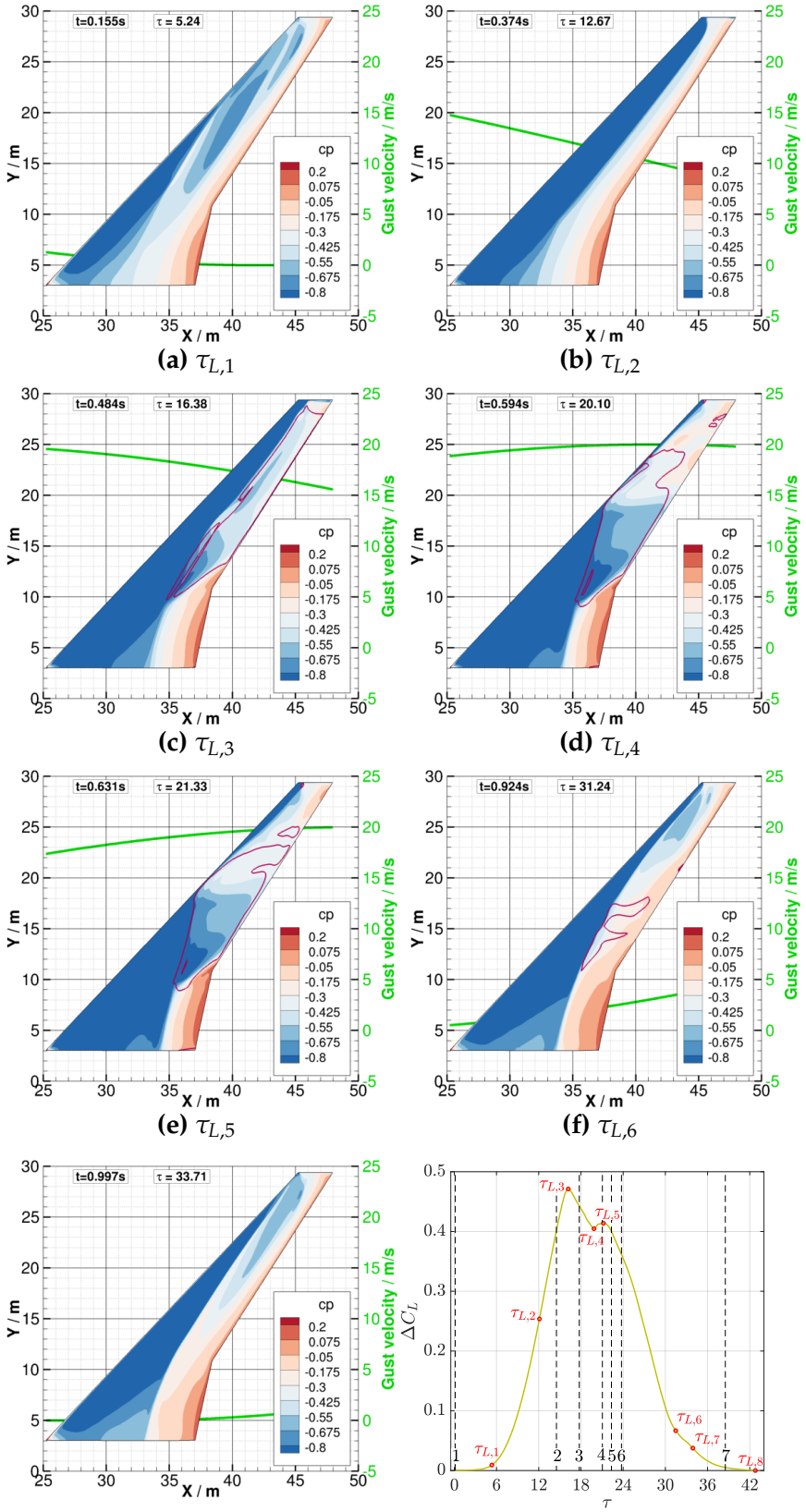

(a) $\tau_{L,1}$ **(b)** $\tau_{L,2}$ **(c)** $\tau_{L,3}$ **(d)** $\tau_{L,4}$ **(e)** $\tau_{L,5}$ **(f)** $\tau_{L,6}$ **(g)** $\tau_{L,7}$ **(h)** Global lift history. Vertical lines mark indices of τ_G.

Fig. 5.56: Surface pressures during a nonlinear gust encounter, Ma 0.83, $L_G = 210.0$ m, $\widehat{W}_G = 20.0$ m/s. (magenta line on the wing shows the contour level $c_{fx} = 0$)

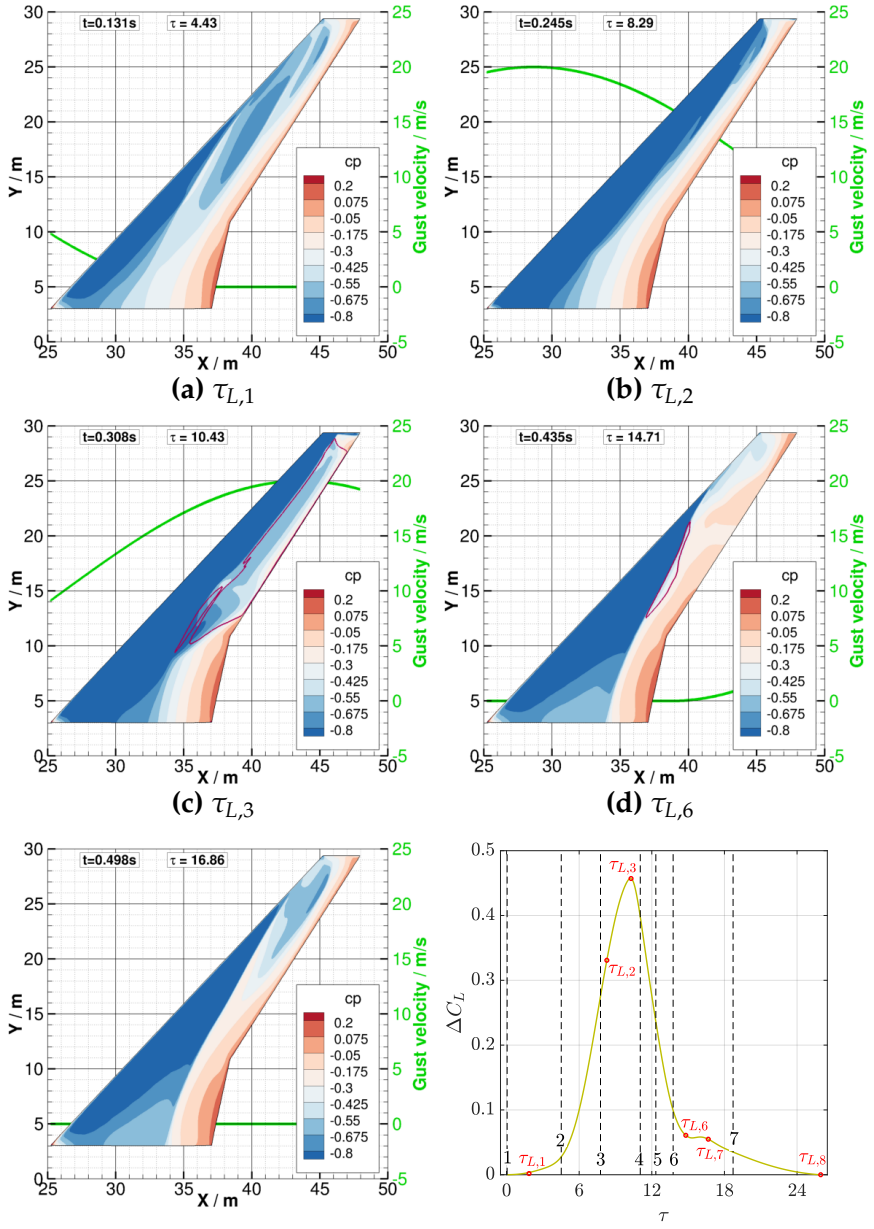

(a) $\tau_{L,1}$ **(b)** $\tau_{L,2}$ **(c)** $\tau_{L,3}$ **(d)** $\tau_{L,6}$ **(e)** $\tau_{L,7}$ **(f)** Global lift history. Vertical lines mark indices of τ_G.

Fig. 5.57: Surface pressures during a nonlinear gust encounter, Ma 0.83, $L_G = 70.0$ m, $\widehat{W}_G = 20.0$ m/s (magenta line on the wing shows the contour level $c_{fx} = 0$)

turns into a double-shock configuration between $\tau_{L,6}$ and $\tau_{L,7}$, which delays the decay of the disturbance in the lift. At $\tau_{L,7}$ the flow is fully attached again, see Fig. 5.56(g). The lift coefficient reaches its steady-state value at $\tau_{L,8}$, shortly after the gust leaves the aircraft (τ_G^{Stop}).

Distinct stages for the shorter gust with $L_G = 70.0$ m are summarized in Fig. 5.57 . The different points in time $\tau_{L,i}$ are associated with the same characteristics in the pressure

distribution and separation behavior as described above for $L_G = 210.0$ m. However, due to the smaller spatial extent of the gust, the sequence of events changes slightly, and also, two stages are missing, namely $\tau_{L,4}$ and $\tau_{L,5}$. For this gust length, the maximum gust velocity reaches the wing (τ_G^{LE}) even before the double-shock configuration turns into a single shock at $\tau_{L,2}$. Then, the peak lift value at $\tau_{L,3}$ is reached, and shortly afterward, the maximum gust velocity already leaves the wing tip trailing edge at τ_G^{TE}. The missing stages, $\tau_{L,4}$ and $\tau_{L,5}$, only seem to occur when the gust is long enough so that the flow condition at $\tau_{L,4}$ can occur *before* the maximum gust velocity leaves the wing at τ_G^{TE} and so triggers the final decay of the response at $\tau_{L,5}$.

At the design point of the aircraft, i.e., at Mach 0.85, there is only a single recompression shock on the wing's surface, recall Fig. 5.26(b). Consequently, stages $\tau_{L,2}$, $\tau_{L,6}$, and $\tau_{L,7}$ can not occur, as the change between single and double-shock configurations induces them.

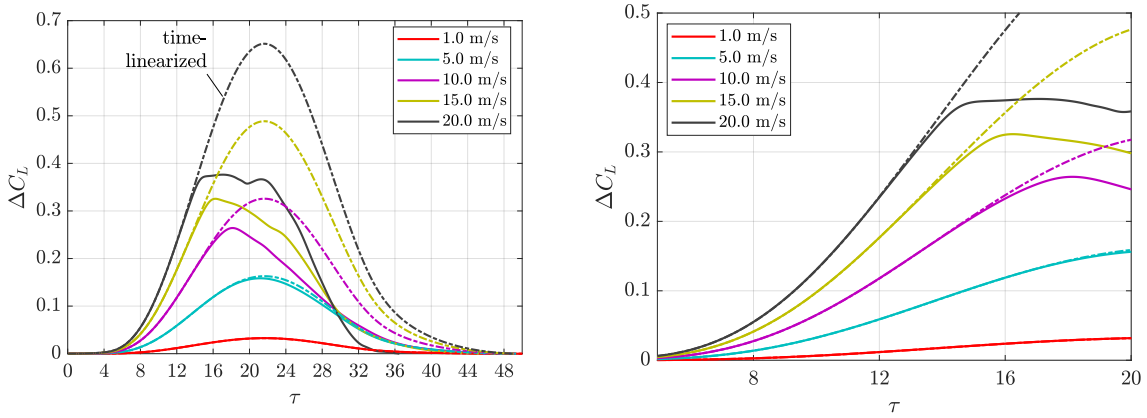

(a) Time-linearized and nonlinear responses

(b) Detailed view of rising edge

Fig. 5.58: Time histories of gust responses, Ma 0.85, $L_G = 210.0$ m

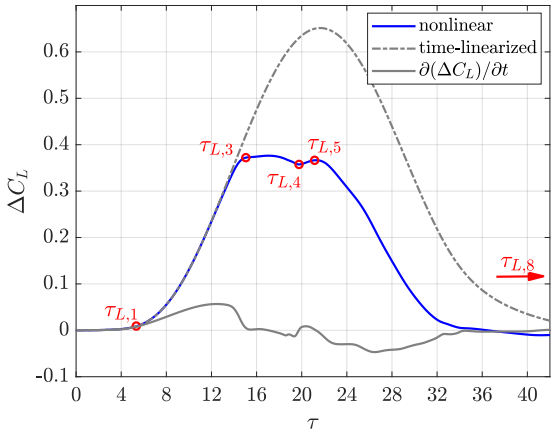

Fig. 5.59: Stages in lift history during a nonlinear gust encounter, $\tau_{L,i}$, at Ma 0.85 with $L_G = 210.0$ m, $\widehat{W}_G = 20.0$ m/s

Fig. 5.58(a) shows responses to different amplitudes for $L_G = 210.0$ m. The detailed view in Fig. 5.58(b) illustrates that there is no additional increase in the lift curve slope, since there is no significant change in the flow field, as was the case for Mach 0.83. The resulting stages in the lift history are then depicted in Fig. 5.59, highlighting the important points in time $\tau_{L,1}$, $\tau_{L,3}$, $\tau_{L,4}$, $\tau_{L,5}$, and $\tau_{L,8}$ for these flow conditions.

Summing up, up to eight characteristic stages in the nonlinear lift response of a transport aircraft configuration during a discrete gust encounter are identified. Each stage can be attributed to specific trends in the lift history. The occurrence of each of the stages depends on the steady state, gust amplitude, and length of the gust. Linear responses only

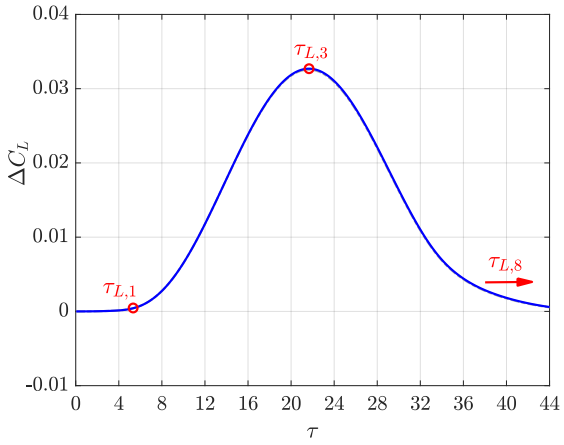

(a) $\tau_{L,1}$, $\tau_{L,3}$ and $\tau_{L,8}$ as observed, e.g., in a linear response

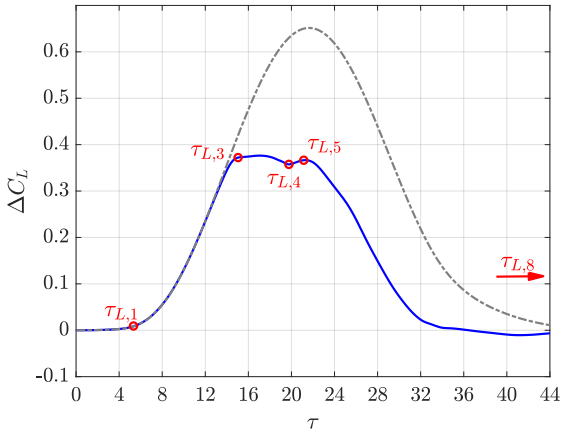

(b) addition of $\tau_{L,4}$ and $\tau_{L,5}$ for gusts with long wavelengths, and large amplitudes

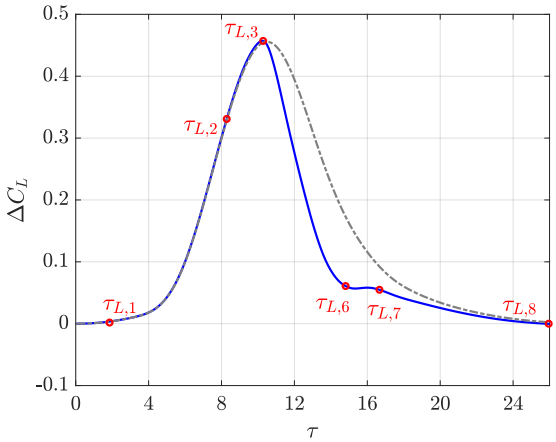

(c) addition of $\tau_{L,2}$, $\tau_{L,6}$ and $\tau_{L,7}$ for gusts inducing a significant topological change in the flow field

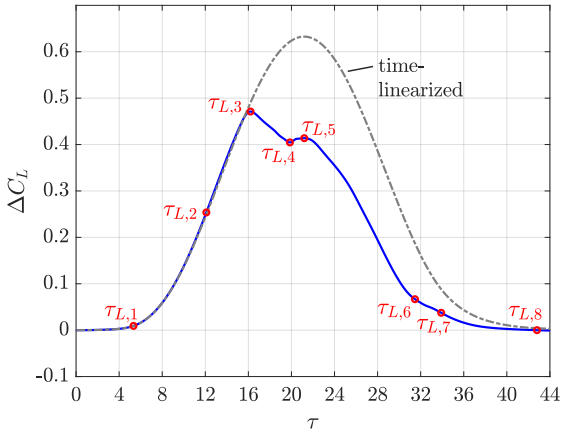

(d) $\tau_{L,1}$ to $\tau_{L,8}$ for gusts inducing a significant topological change in the flow field and significant shock-induced separation

Fig. 5.60: Up to eight stages $\tau_{L,1}$ to $\tau_{L,8}$ in an aerodynamic lift response during a discrete gust encounter for a transport aircraft configuration

include points $\tau_{L,1}$, $\tau_{L,3}$ and $\tau_{L,8}$, see Fig. 5.60(a). Additionally, stages $\tau_{L,4}$ and $\tau_{L,5}$ occur if the gust is long enough, see Fig. 5.60(b). If there is a significant topological change in the flow field, stages $\tau_{L,2}$ on the rising edge and $\tau_{L,6}$ and $\tau_{L,7}$ on the falling edge occur, see Fig. 5.60(c). A lift response to a long large-amplitude gust, which includes a significant topological change of the flow field and significant flow separation consequently contains all of the above mentioned stages $\tau_{L,1}$ to $\tau_{L,8}$, see Fig. 5.60(d).

5.4 Summary

5.4.1 Three Types of Nonlinear Lift Responses

The investigations in this Chapter 5 reveal three basic types of nonlinear lift responses in transonic flow that are summarized here.

- Nonlinear lift response type A: These responses are separation-driven and, hence, show a reduction in the nonlinear maximum lift coefficient compared to the corresponding time-linearized result. Shock-induced separation is the dominant feature of this type of flow. This effect can be observed for all underlying steady states as long as the gust amplitude is large enough to trigger a significant flow separation. It is reduced with decreasing wavelength of the gust.
- Nonlinear lift response type B: These responses are shock-topology-driven, i.e., the motion and the transformation of an existing shock configuration play a dominant role. Slight separation might occur, but it only plays a minor role. This effect can be observed only for some of the steady states investigated for long to medium-length gusts.
- Nonlinear lift response type C: These responses mark the transition between type A and type B and thus result from a combination of changes in the shock-topology and the onset of significant flow separation. These responses lead to a reasonable agreement of nonlinearly predicted and time-linearized peak lift values, though the underlying unsteady flow fields are fundamentally different.

5.4.2 The Influence of the Steady Flow Field

The results indicate that the trend of the steady base flow influences the types of nonlinear responses that occur. A closer look at the steady results shows a division of the lift curve slope for attached flow into two different regions, see Fig. 5.61. With the occurrence of recompression shocks and further downstream shock positions for increasing angles of attack, the lift curve slope deviates from its subsonic reference value. The recompression shock causes a stronger increase in lift, i.e., a steeper lift curve slope, compared

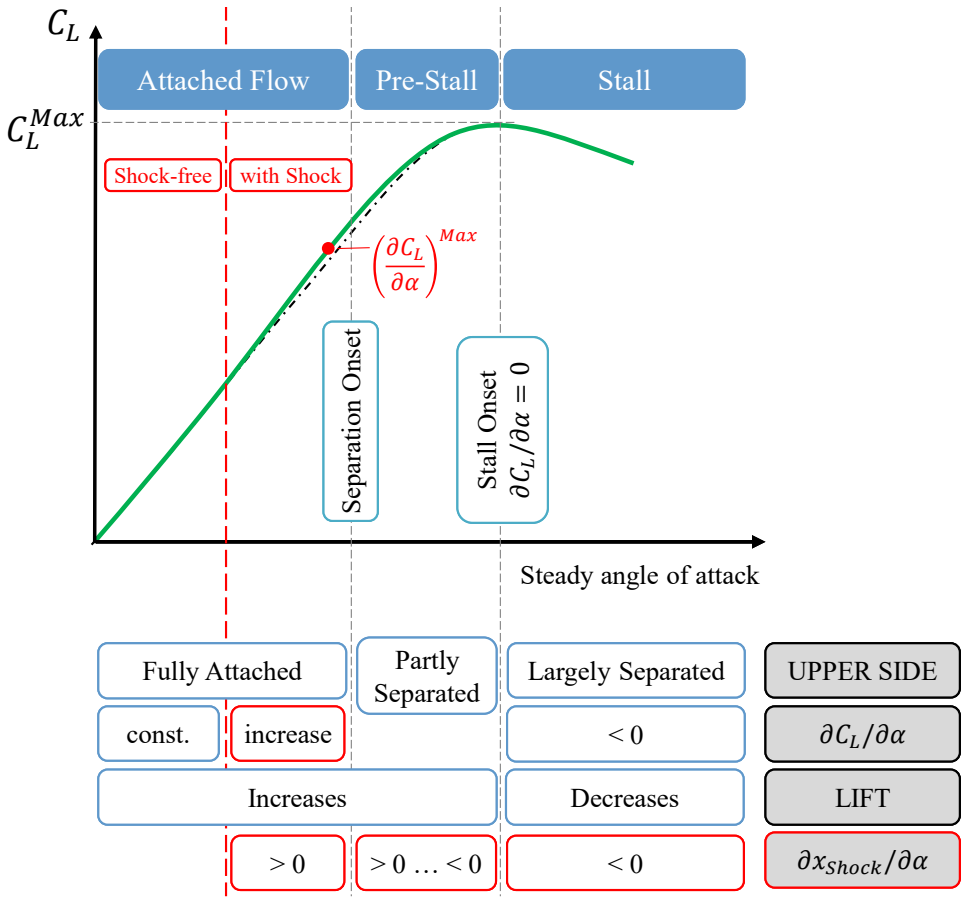

Fig. 5.61: Extended classification of steady airfoil flow

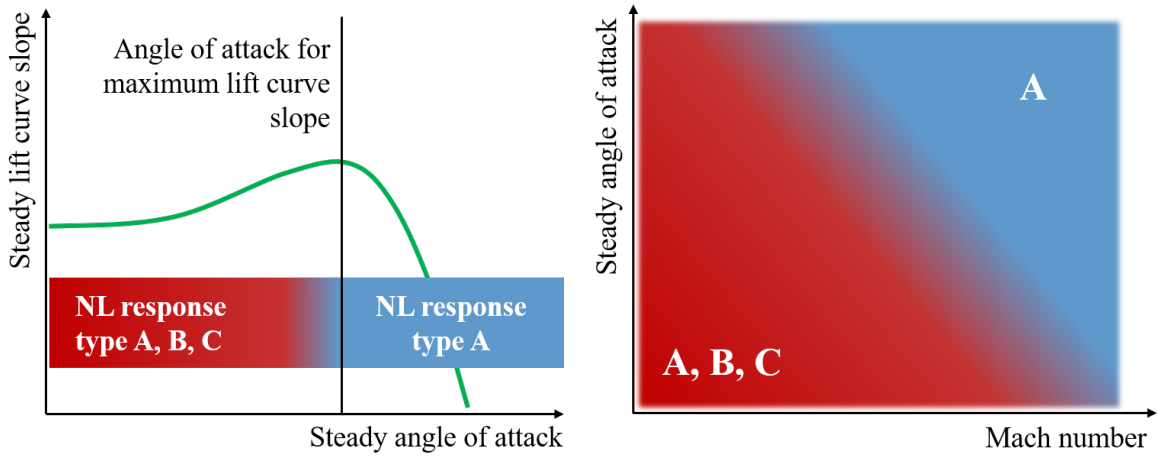

(a) Response types depending on the steady lift curve slope

(b) Response types in the Ma-α-plane

Fig. 5.62: Schematic representation of nonlinear lift response types for different steady conditions

the shock-free flow. The lift curve slope $\partial C_L/\partial\alpha$ increases until shortly before the onset of separation. These characteristic trends in the lift curve slopes were observed for both configurations, the airfoil and the transport aircraft, and are shown schematically in Fig. 5.62(a).

For low angles of attack and/or low Mach numbers, nonlinear response types A, B, or C can be expected. With increasing Mach number and increasing steady angle of attack the responses of type B and C tend to vanish, see Fig. 5.62(b), as the angle of attack for the maximum lift curve slope is encountered earlier.

Putting it in other words: As long as the angle of attack is low enough, i.e. $\alpha_0 < \alpha\left((\partial C_L/\partial\alpha)^{Max}\right)$, unsteady responses might result in type A, B, or C, depending on gust amplitude and gust length. It depends on the steady base flow in combination with the excitation parameters, if changes in the shock configuration and/or significant separation is triggered. For $\alpha_0 \geq \alpha\left((\partial C_L/\partial\alpha)^{Max}\right)$, only nonlinear responses of type A can be expected. Shock-induced separation is the dominant effect, causing a decrease in the maximum lift in the nonlinear computations when compared to the time-linearized results. With increasing Mach number, the maximum slope is encountered at lower angles of attack and so time-linearized computations at higher Mach numbers tend to be more conservative.

For a specific steady base flow field, the different nonlinear response types occur for different combinations of excitation amplitude and gust length, see Fig. 5.63. Nonlinear responses of type A can be observed for long gusts, i.e., low excitation frequencies and

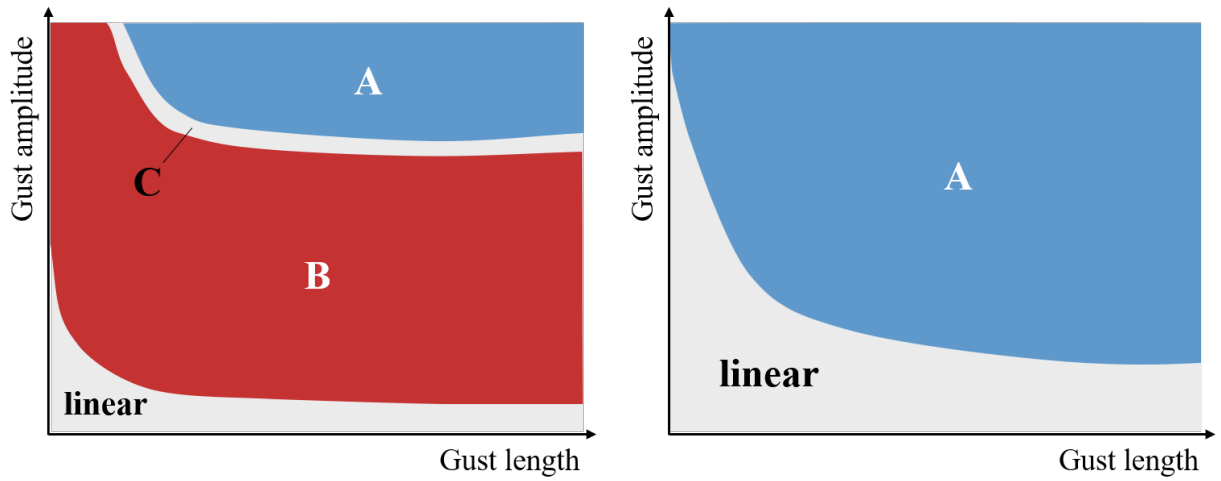

(a) $\alpha_0 < \alpha\left((\partial C_L/\partial\alpha)^{Max}\right)$ **(b)** $\alpha_0 \geq \alpha\left((\partial C_L/\partial\alpha)^{Max}\right)$

Fig. 5.63: Schematic representation of nonlinear lift response types for different excitation parameters

medium to large excitation amplitudes, as these trigger significant separation. The extent of the nonlinear response type A reduces for shorter gusts and lower excitation amplitudes. The prediction of higher lift values by the nonlinear method, i.e., nonlinear responses of type B, mainly occurs for medium-amplitude excitations, as long as there is no significant shock-induced flow separation. It can be observed for all gust lengths, i.e., excitation frequencies. However, the impact of this response type on the peak lift value is significantly less than that for nonlinear responses of type A, and it amounts to only a few percent.

Note that the classification into short, medium, or long gusts, as well as small, medium, or large gust amplitudes corresponds to different absolute values for each individual steady base flow field.

To summarize, the steady lift polar and the respective steady lift curve slope seem to be reliable indicators, to estimate whether the use of aerodynamically nonlinear methods in the gust simulations results in conservative or non-conservative maximum lift coefficients compared to the time-linearized method.

5.4.3 Stages in the Time-Domain History of a Nonlinear Lift Response

Discrete "1-cos" gust encounters need to be considered during aircraft design and, hence, a detailed understanding of the sequence of events during such an encounter is necessary. Table 5.3 summarizes the different stages for the different nonlinear response types A, B,

Table 5.3: Assignment of the different stages τ_L to the nonlinear lift response types A, B, and C; Symbols: X = occurs, – = does not occur, (X) = might occur (depending on the steady state)

NL response type Gust length	A long	A short	B any	C any	
$\tau_{L,1}$	X	X	X	X	increase in lift
$\tau_{L,2}$	(X)	(X)	X	X	increase in instantaneous lift curve slope
$\tau_{L,3}$	X	X	X	X	lift peak and decrease afterwards
$\tau_{L,4}$	X	–	–	–	slight increase in lift
$\tau_{L,5}$	X	–	–	–	final decrease in lift starts
$\tau_{L,6}$	(X)	(X)	X	X	decrease in instantaneous lift curve slope
$\tau_{L,7}$	(X)	(X)	X	X	decay of the lift response
$\tau_{L,8}$	X	X	X	X	lift reaches steady-state value

and C. Up to eight different stages in a nonlinear lift response can be identified. Influencing factors for the occurrence of the stages are the steady state, the gust amplitude, and the gust length.

In a purely linear response, only three stages can be observed: lift increases due to the gust, $\tau_{L,1}$, then the maximum value is reached, $\tau_{L,3}$, and the lift response decays until it reaches its steady-state value, $\tau_{L,8}$. If, e.g., the shock configuration changes during the gust encounter and induces a topology change in the flow, the instantaneous lift slope increases further during the rising edge of the excitation, and stage $\tau_{L,2}$ is added. On the falling edge of the excitation, the shock configuration changes back, inducing a slower decrease of the lift value, so stages $\tau_{L,6}$ and $\tau_{L,7}$ are added to the response. If the gust is long enough, stages $\tau_{L,4}$ and $\tau_{L,5}$ additionally occur in the lift response to account for an additional increase in lift after the separation-induced breakdown.

6 Aeroelastic Analysis of a Transport Aircraft Configuration

This chapter presents the results of aeroelastic computations for the NASA Common Research Model. The wing root bending moment is analyzed for nonlinear response effects and details of the corresponding fluid-structure interactions are studied. Moreover, amplitude-dependent critical gust lengths are identified and the lift responses of aerodynamic and aeroelastic simulations are compared. A summary of the nonlinear effects in the aeroelastic computations forms the last part of this chapter.

6.1 Analysis of the Wing Root Bending Moment

6.1.1 Unsteady Nonlinear Responses

The following section shows responses of the incremental wing root bending moment, $\Delta M_{x,root}$, when a nonlinear aerodynamic modeling is applied in the aeroelastic computations. For the calculation of this internal quantity, the reader is referred to Chapter 3.3. Applied models are described in Chapter 4.2.

Time-histories at Mach 0.83

Typical aeroelastic responses are displayed in Fig. 6.1. After a first load peak, the oscillating response decays. The additional oscillations compared to purely aerodynamic responses result from the involved structural mode shapes. Flow separation shows a significant impact, especially on the first minimum value that occurs, see $L_G = 210.0$ m with $\widehat{W}_G = 20.0$ m/s in Fig. 6.1(a). The negative peak between $\tau = 20 \ldots 40$ that can

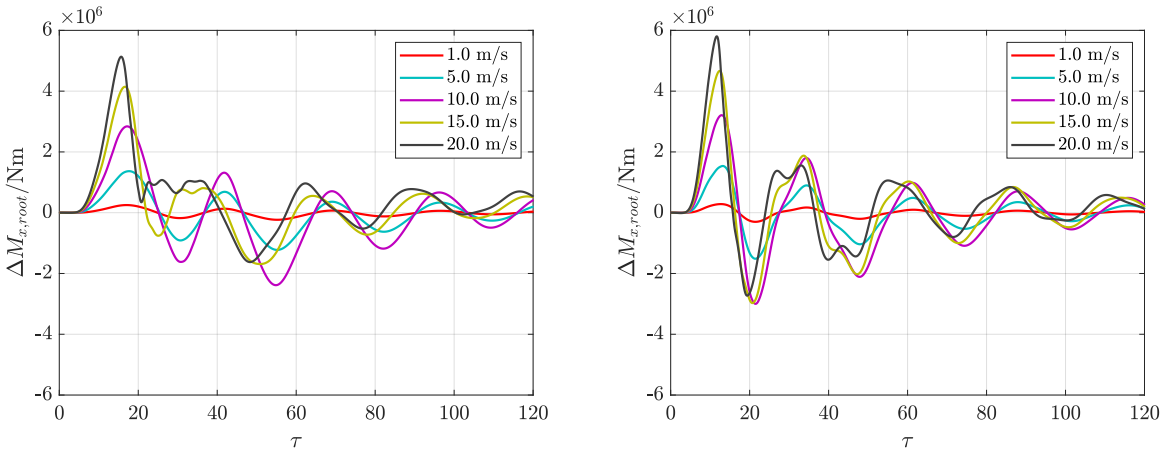

(a) $L_G = 210.0$ m **(b)** $L_G = 105.0$ m

Fig. 6.1: Time histories of the wing root bending moment, Mach 0.83

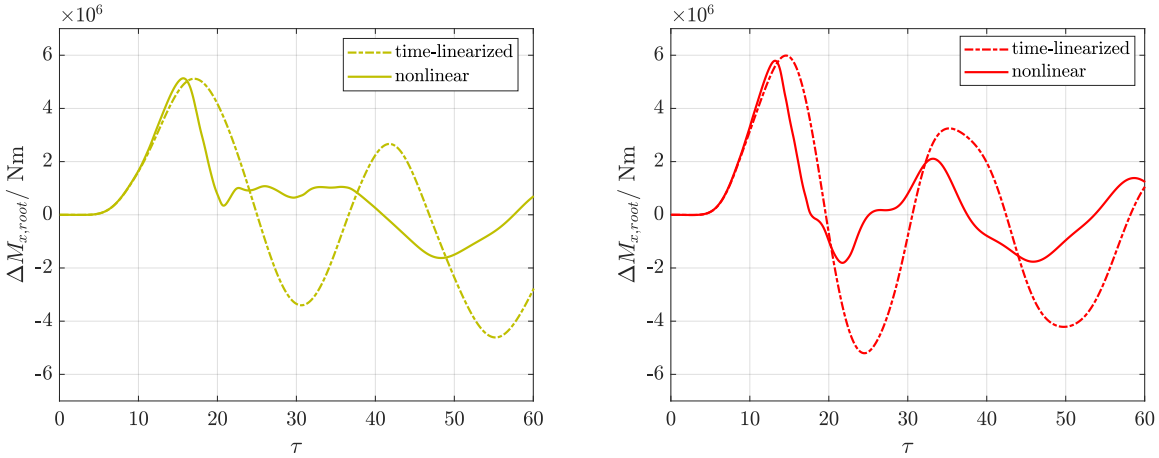

(a) $L_G = 210.0$ m, $\widehat{W}_G = 20.0$ m/s **(b)** $L_G = 140.0$ m, $\widehat{W}_G = 20.0$ m/s

Fig. 6.2: Linear and nonlinear predictions of the wing root bending moment, Mach 0.83

be observed for low-amplitude gusts vanishes for the largest amplitude. However, the decaying response at $\tau > 40$ still shows similar response amplitudes, but with a phase shift as compared to the low-amplitude responses. In all cases considered, the maximum bending moment is defined by the first positive peak of the response. However, the first or second negative peak defines the minimum bending moment.

The comparison between time-linearized and nonlinear responses in Fig. 6.2 indicate that similar mechanisms exist in the flow as in the purely aerodynamic investigations. An increase in the instantaneous slope can be observed in the aeroelastic responses. The same behavior is observed in the purely aerodynamic responses, compare with Fig. 5.55(a). This increasing slope can be attributed to a change in the shock topology. Moreover, the trends in Fig. 6.2 show the strong influence of the flow separation, which sets in at $\tau \approx 15$ and $\tau \approx 13$, respectively. The onset of flow separation alters the structural response and leads to totally different trends in the time histories of linear and nonlinear responses.

Contributions of Aerodynamic and Inertial Wing Root Bending Moment

As the aeroelastic response consists of an aerodynamic and an inertial contribution, a look at both components reveals more details, see Fig. 6.3. The trends for the aerodynamic bending moment show high similarity in the first part with the trends that can be observed for the nonlinear lift responses in Chapter 5.3.1. It is the inertial loads that bring the higher frequency oscillations into the total bending moment. The aerodynamic contribution seems to be more relevant for the maximum bending moment, and the inertial contribution tends to define the minimum bending moment. For the shorter gusts, inertial accelerations induce higher frequency oscillations in the responses which are not present for the responses to longer gusts.

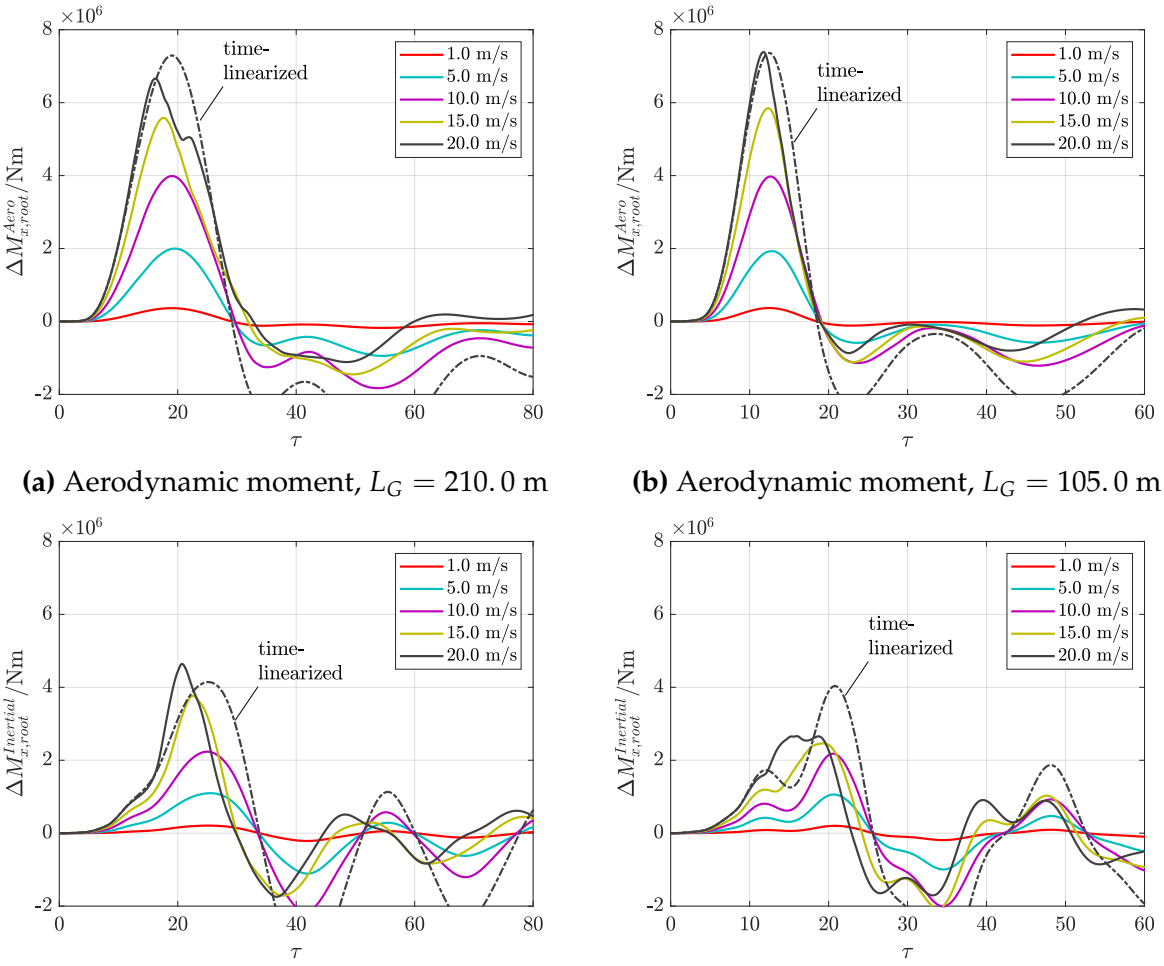

(a) Aerodynamic moment, $L_G = 210.0$ m

(b) Aerodynamic moment, $L_G = 105.0$ m

(c) Inertial moment, $L_G = 210.0$ m

(d) Inertial moment, $L_G = 105.0$ m

Fig. 6.3: Contributions of aerodynamic and inertial wing root bending moment, Mach 0.83

The division into aerodynamic and inertial loads makes it clear that both the changed shock topology and the flow separation on the wing lead to a different structural response than the time-linearized method. Both aerodynamic effects have a visible impact on the aerodynamic bending moment, for example, for $L_G = 210.0$ m and $\widehat{W}_G = 20.0$ m/s: the instantaneous slope in the response increases due to the changed flow topology (at approx. $\tau = 11$) and the subsequent strong flow separation induces a premature breakdown in the moment curve (at approx. $\tau = 16$). This breakdown in the aerodynamic response ultimately leads to a higher maximum in the inertial response, when nonlinear and time-linearized responses are compared.

Time-histories at Mach 0.85

At the design point of the aircraft at Mach 0.85, the onset of flow separation causes significantly different aerodynamic and inertial loads than the time-linearized computations, see Fig. 6.4. An overall lower maximum bending moment is obtained by the nonlinear aerodynamic modeling.

However, if the wavelength of the gust excitation is significantly longer, the dynamic response changes, and two local peaks can be observed in the response of the total wing bending moment with the nonlinear aerodynamic model, see Fig. 6.5(a). Splitting the total response into aerodynamic and inertial parts, see Fig. 6.5(b), further details are found: At about $\tau = 21.3$, the flow starts to separate on the wing, see Fig. 6.5(c), and typical transonic separated flow conditions can be observed. However, due to the still-increasing gust velocity on the wing up to about $\tau = 36.2$, the aerodynamic bending moment increases further, see Fig. 6.5(b), and the pressures, especially on the inner part of the wing reduce significantly, compare with Fig. 6.5(d) . The maximum gust velocity leaves the wing tip shortly after $\tau = 36.2$. Only then, the aerodynamic bending moment finally decreases. The inertial moment responds only with a single peak, namely shortly after the onset of flow separation, and it decays with some slight oscillations afterward. The separated flow over large parts of the wing does not induce any further significant structural reactions. Consequently, the high maximum value of the wing root bending moment is due to the long length of the gust in combination with the large amplitude, which together cause a strong acceleration of the flow on the inner wing and thus large aerodynamic loads, which are not counteracted by the inertial loads.

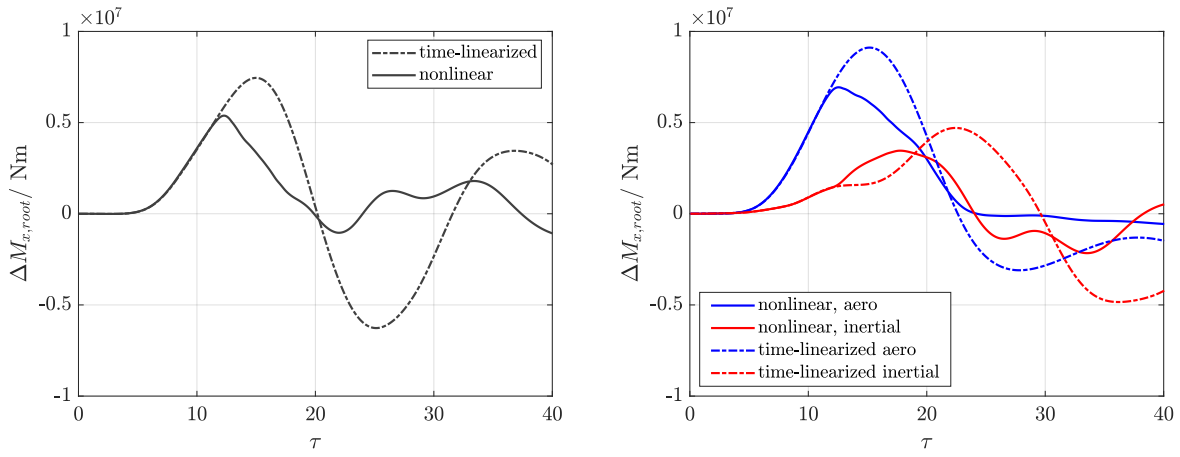

(a) Time-linearized and nonlinear responses **(b)** Aerodynamic and inertial responses

Fig. 6.4: Gust encounter with $L_G = 140.0$ m and $\widehat{W}_G = 20.0$ m/s, Mach 0.85

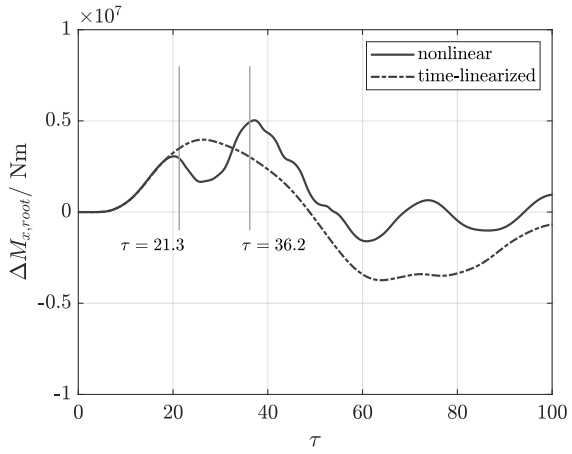

(a) Total responses

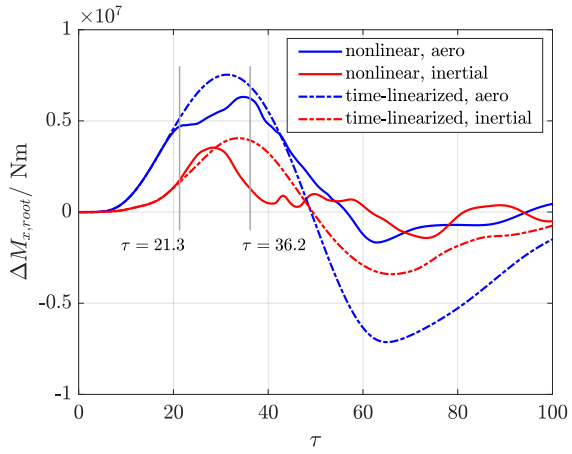

(b) Aerodynamic and inertial responses

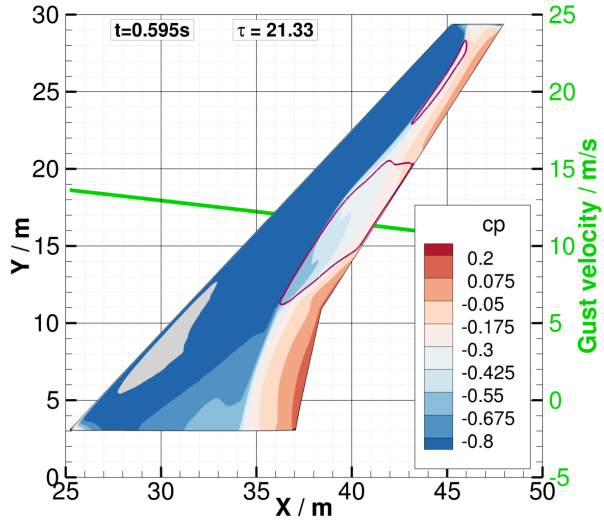

(c) Surface pressures at $\tau = 21.33$

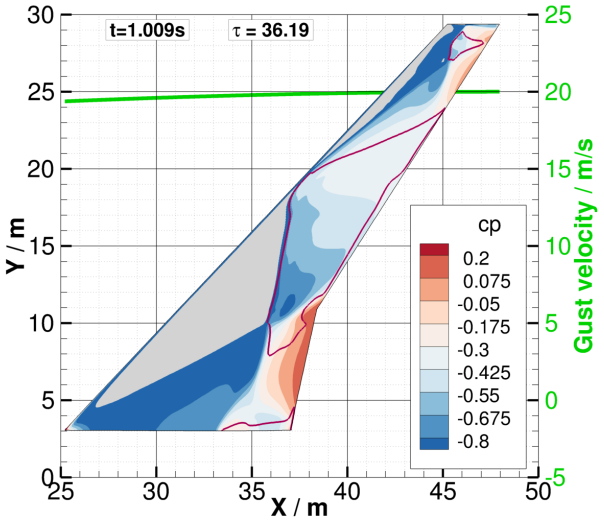

(d) Surface pressures at $\tau = 36.19$

Fig. 6.5: Gust encounter with $L_G = 420.0$ m and $\widehat{W}_G = 20.0$ m/s, Mach 0.85, with two exemplary snapshots of the wing's pressure distribution (magenta lines on the wing shows the contour level $c_{fx} = 0$; the grey areas correspond to $c_p < -1.2$)

6.1.2 Maximum and Minimum Bending Moments

As already described in the previous chapter, the coupling of aerodynamic and structural models leads to interaction effects, which can not be predicted straightforwardly, and especially maximum and minimum loads depend on the details of models and methods. The peak loads occurring with current models and methods are analyzed below.

Analysis at Mach 0.83

Typical trends from the purely time-linearized loads analysis can be confirmed by the current study, see Fig. 6.6. Minimum and maximum values for the wing root bending moment do not show monotonic trends with respect to the gust length but exhibit a maxi-

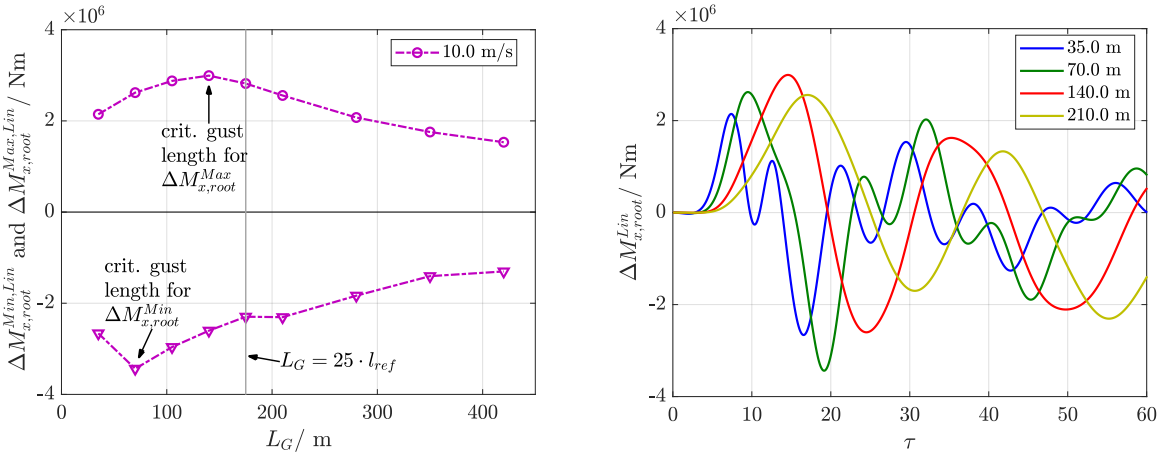

(a) Maximum and minimum values **(b)** Time histories for $\widehat{W}_G = 10.0$ m/s

Fig. 6.6: Time-linearized results for the wing root bending moment, Mach 0.83

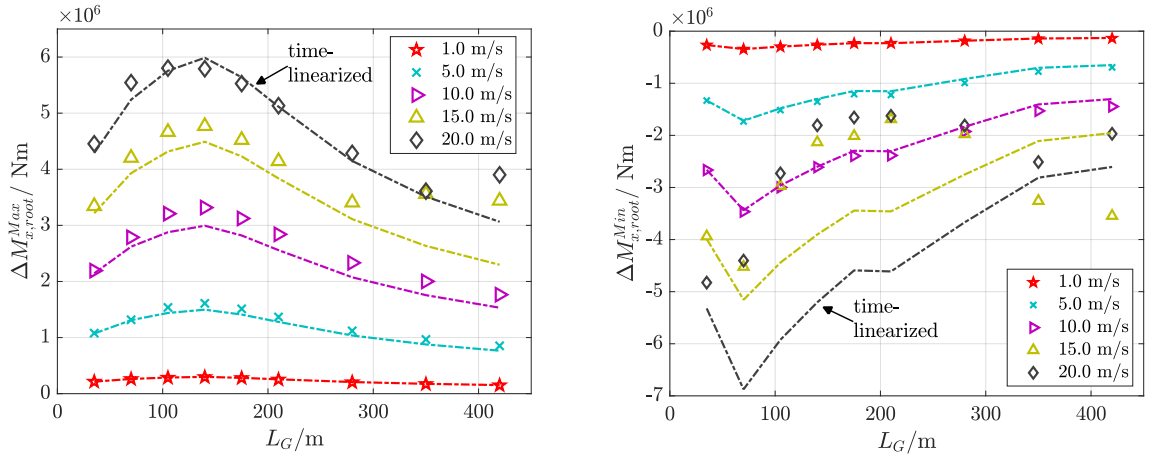

(a) Maximum values **(b)** Minimum values

Fig. 6.7: Wing root bending moments for linear and nonlinear responses, Mach 0.83

mum value in the range of medium-length gusts, which each correspond to the respective "critical gust length". The decrease of the maximum loads with increasing gust length is mainly caused by an increasing impact of the rigid-body modes. The time histories in Fig. 6.6(b) show the strong oscillatory content in the short-gust responses. Longer gusts induce low-frequency responses, and hence trigger mainly an interaction with the flight mechanics mode shapes.

A look at the maximum wing root bending moment as a function of the gust length shows, that the above-mentioned time-linearized trends are largely reflected by the nonlinear results, see Fig. 6.7(a). However, medium-amplitude gusts are stronger influenced by the change in shock topology and lead to larger values of the maximum incremental bending moment when a nonlinear aerodynamic method is applied, see the responses to $\widehat{W}_G = 10.0$ m/s and $\widehat{W}_G = 15.0$ m/s. For the case with a gust length of $L_G = 140.0$ m and

an amplitude of $\widehat{W}_G = 10.0$ m/s, an increase in the maximum incremental wing root bending moment of 10.8% is observed. With a further increase of the excitation amplitude to $\widehat{W}_G = 20.0$ m/s, separation dominates the response and leads to a reduction of the nonlinearly computed maximum value. Note that very long gusts ($L_G = 350.0$ m and $L_G = 420.0$ m), in combination with large-amplitude excitations lead to a significant increase of the maximum value, with the mechanisms as already discussed in Fig. 6.5.

Significant deviations from the linear trends occur for the minimum root bending moment due to large-amplitude excitations, see Fig. 6.7(b). The amount of the nonlinear minimum values is not as large as that of the time-linearized predictions. There is even a trend reversal for mid-length gusts, see, e.g., $L_G = 175.0$ m: with increasing excitation amplitude, the magnitude of the minimum bending moment decreases in the nonlinear computations due to the changing interaction of aerodynamic and structural responses, cf. Fig. 6.3. Note that the described trends for maximum and minimum wing root bending moment apply over the entire wing span. Monotonic trends with respect to wing span can be expected, as no additional structural components are attached to the wing.

The share of aerodynamic and inertial bending moments on the total maximum root bending moment is shown in Fig. 6.8. Recall that the internal loads L_c result from the difference between aerodynamic and inertial loads, $\Delta L_c = \Delta L_c^{Aero} - \Delta L_c^{Inertial}$, see also Section 3.3. The respective shares are extracted at that point in time when the total maximum root bending moment occurs. It is observed that the absolute value of the maximum root bending moment is essentially influenced by the aerodynamic contribution, for all

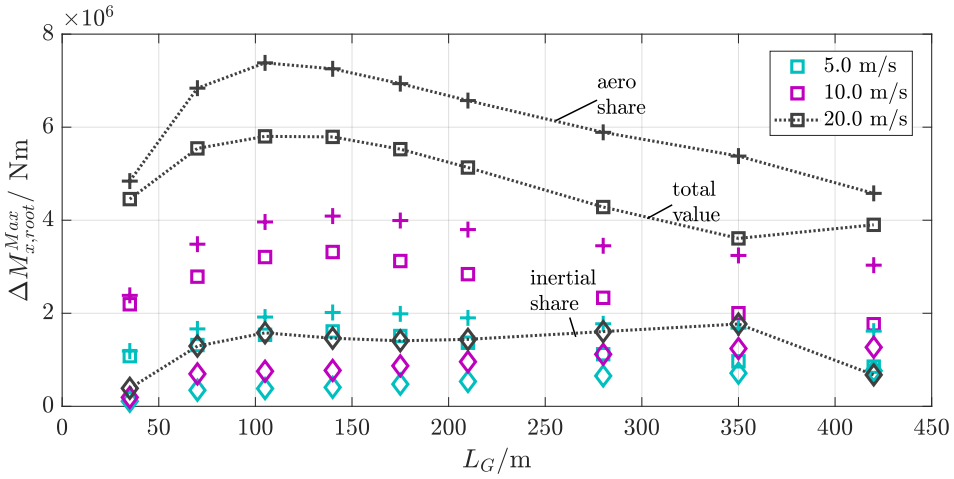

Fig. 6.8: Shares of aerodynamic and inertial moments on the maximum wing root bending moment at Mach 0.83 (Symbols: cross – aero share, diamond – inertial share, square – total value)

gust lengths and amplitudes considered. Absolute values of the counteracting inertial bending moment are significantly lower.

Analysis at Mach 0.85

The results for Mach 0.85 are depicted in Fig. 6.9 and correspond to the design point of the aircraft. The massive flow separation causes significantly reduced maximum values for large-amplitude excitations and short to medium-length gusts. Exemplarily, for the case with $L_G = 140.0$ m and $\widehat{W}_G = 20.0$ m/s, the nonlinear maximum root bending moment amounts to only 72% of its time-linearized counterpart, it is reduced from $\Delta M^{Max}_{x,root} = 7.5 \cdot 10^6$ Nm to $\Delta M^{Max}_{x,root} = 5.4 \cdot 10^6$ Nm. As already discussed with Fig. 6.4, the flow separation causes an early breakdown in the aerodynamic loads and leads to this decreased peak value. However, with increasing gust length, the trend changes and so for the longest gust with $L_G = 420.0$ m, it is the other way around: the nonlinear response increases the predicted incremental maximum root bending moment by 25% compared to the time-linearized computation. Though this gust amplitude leads to separated flow conditions, the aerodynamic peak load occurs only after the maximum gust velocity has completely convected over the wing. The peak inertial response, however, is encountered significantly earlier, namely directly after the onset of separation, and so alters the overall response. The database indicates this trend for all large-amplitude excitations and long-wavelength gusts.

Note that the computation of such long-wavelength gusts is not demanded by the certification specifications. The acceptable means of compliance (CS 25.341, "Gust and turbulence loads") would demand the computation of gust gradients up to $H = L_G/2 = 107.0$ m for this aircraft configuration. So the very long gusts with, e.g., $L_G = 420.0$ m are clearly out of range for the current certification standards. Looking at

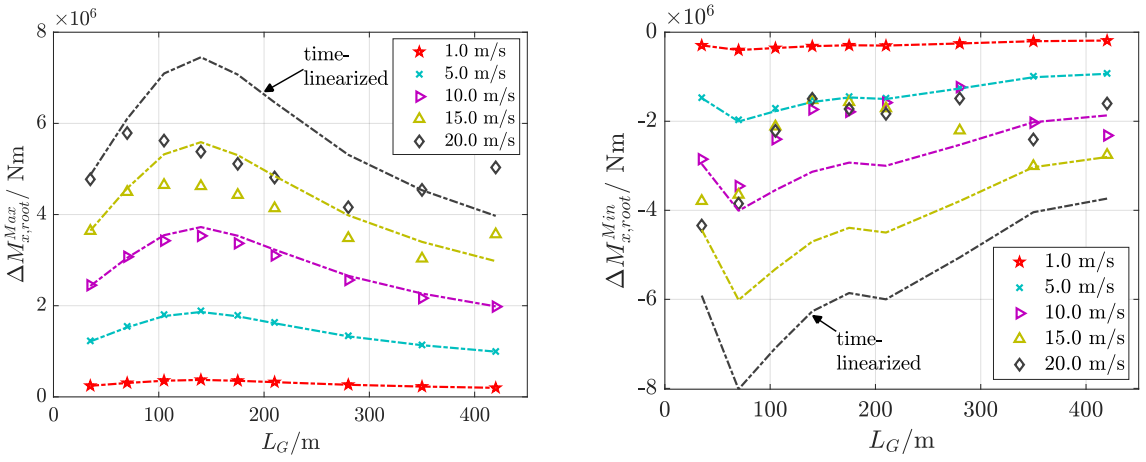

(a) Maximum values **(b)** Minimum values

Fig. 6.9: Wing root bending moments for linear and nonlinear responses, Mach 0.85

the data, this approach seems reasonable as long as time-linearized methods are used, as the predicted time-linearized loads exclusively decrease with increasing gust lengths, see Fig. 6.7 and Fig. 6.9. However, looking at the nonlinearly computed results, a careful assessment of the certification gust lengths seems necessary, if nonlinear methods are to be included in the calculations.

In general, the minimum peak values of the wing root bending moment are even more affected by the nonlinear effects than the occurring maximum values, see Fig. 6.9(b). Not only does the critical gust length change, but the amounts of the loads are significantly reduced, as could already be observed for the cases at Mach 0.83. Flow separation, in combination with the different structural interaction are the reason for these changes.

6.1.3 Points in Time for Peak Loads

For load calculations in the context of aircraft design, not only the absolute values of the expected peak loads are relevant, but also the points in time at which these occur [86].

The points in time for the occurrence of maximum and minimum wing root bending moments at Mach 0.83 are summarized in Fig. 6.10. Short gusts each encounter their maximum or minimum values at the same point in time, independently of the excitation amplitude. Mid-length gusts with medium to large amplitudes induce responses where the maximum bending moment is encountered slightly earlier than for low-amplitude excitations. The separation-induced early breakdown in the loads corresponds to these earlier points in time, as the maximum bending moment is mainly influenced by aerodynamics. For the two longest gusts with $L_G = 350.0$ m and $L_G = 420.0$ m, the trend is not as monotonic anymore due to the changing interactions between flow separation and the structural response.

Whereas the maximum bending moment always increases with increasing excitation amplitude, the magnitude of the minimum bending moment might decrease despite an increasing excitation amplitude, as discussed in Fig. 6.7(b). For all cases considered here, this decrease in the magnitude of the minimum bending moment is associated with an earlier appearance of the minimum value, see Fig. 6.10(b). The sharp turning point in the curves can be attributed to the observed phase shift of the nonlinear responses, compare the curve for $L_G = 210.0$ m with the corresponding time histories in Fig. 6.1(a).

Trends for Mach 0.85 are largely similar to those at Mach 0.83, see Fig. 6.11. However, note that the minimum bending moment is not exclusively encountered at an earlier point in time with increasing excitation amplitude, see the curve for $L_G = 140.0$ m in Fig. 6.11(b). Nonlinear effects at the design point can also lead to a later occurrence of the minimum

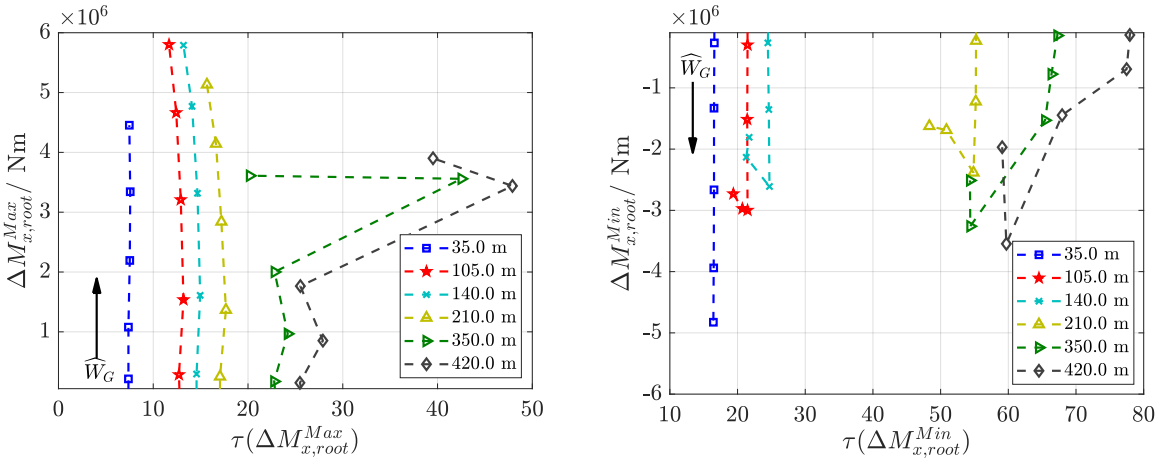

(a) Maximum wing root bending moment **(b)** Minimum wing root bending moment

Fig. 6.10: Points in time for maximum and minimum wing root bending moment, Mach 0.83 (Results are colored by gust lengths.)

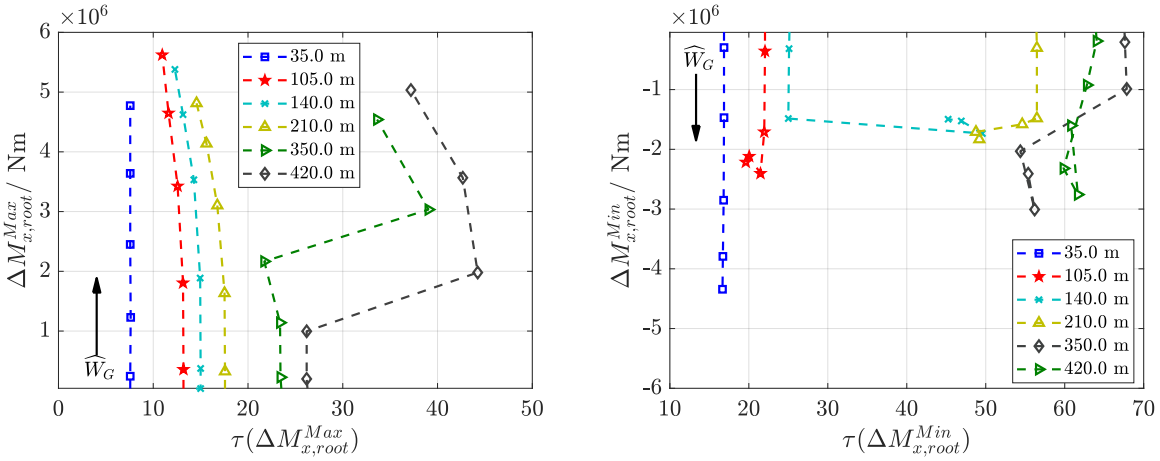

(a) Maximum wing root bending moment **(b)** Minimum wing root bending moment

Fig. 6.11: Points in time for maximum and minimum wing root bending moment, Mach 0.85 (Results are colored by gust lengths.)

value due to an attenuated inertial response which is caused by the onset of flow separation, compare with Fig. 6.4.

6.1.4 Critical Gust Lengths

As explained in Chapter 2.4, the critical gust length is a key parameter in the identification of maximum and minimum loads. Due to the complex interaction of aerodynamics and structural dynamics, a prediction of that value is not straightforward. This section investigates the effect of the nonlinear aerodynamic modeling on the critical gust length. The values are taken out of the respective diagrams in Fig. 6.7 and Fig. 6.9.

One of the biggest differences compared to a time-linearized analysis is the fact that a nonlinear method leads to amplitude-dependent values for the critical gust length. In the cases considered here, responses at Mach 0.83 and Mach 0.85 result in identical time-linearized values for the critical gust lengths, see Fig. 6.12. When a nonlinear aerodynamic modeling is applied, the critical gust length shifts to shorter wavelengths, for the maximum, as well as for the minimum bending moments, due to the above-described onset of significant flow separation which reduces the peak moments for longer gust lengths. Note that all results are well below Pratt's reference value for the critical gust length of $L_G = 25 \cdot c_{MAC} = 175.0\,\text{m}$.

For deeper analysis of the different critical gust lengths, a different representation of the time scale seems to be more intuitive, see Fig. 6.13. In these diagrams, all time signals are shifted so that the zero point of the x-axis corresponds to that point in time when the maximum gust velocity reaches the wing root leading edge at τ_G^{LE}. Moreover, the grey shaded area marks the period that the gust amplitude convects over the wing. See Section 5.3.2 for an explanation of the different points in time, τ_G. Note that, for more clarity in the diagrams, the results for the gust lengths of $L_G = 350.0\,\text{m}$ and $L_G = 420.0\,\text{m}$ are left out in these figures.

The gust velocities in Fig. 6.13(a) show, that the gust gradient of the shortest gust with $H = L_G/2 = 17.5\,\text{m}$ is shorter than the extension of the wing in x-direction, i.e. $L_G/(2 \cdot c_{MAC}) < (\tau_G^{TE} - \tau_G^{LE})$. Consequently, this gust length is not capable of causing large loads on the aircraft.

The critical gust length for the maximum time-linearized wing bending moment is found

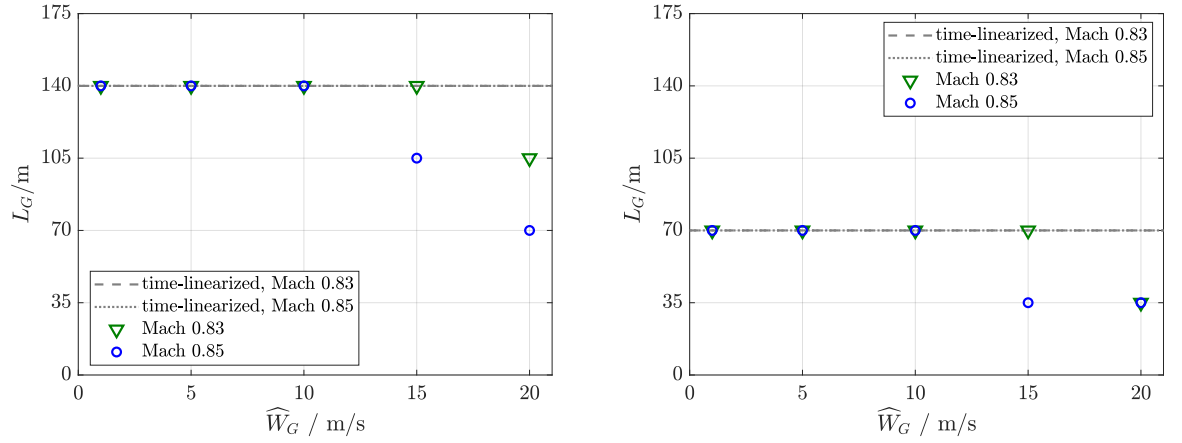

(a) Maximum wing root bending moment **(b)** Minimum wing root bending moment

Fig. 6.12: Critical gust lengths for different excitation amplitudes,
Pratt reference: $L_G = 25 \cdot c_{MAC} = 175.0\,\text{m}$

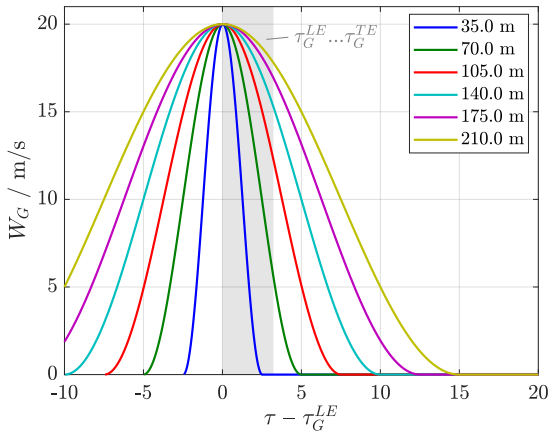

(a) Gust velocities

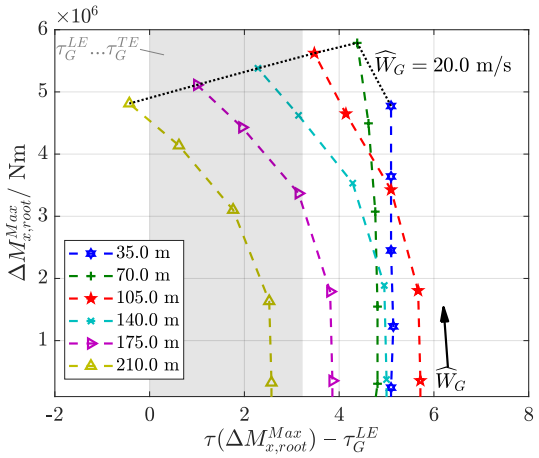

(b) Points in time for maximum nonlinear wing root bending moments

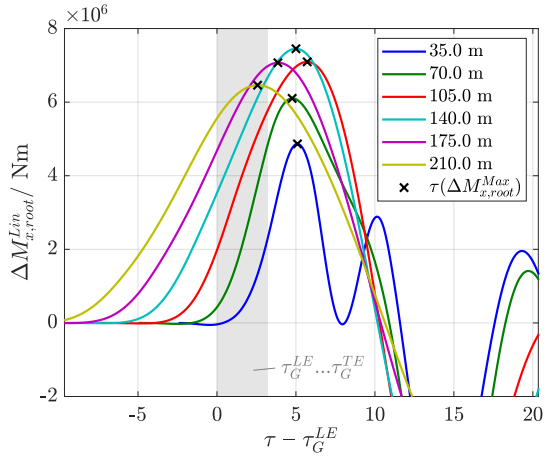

(c) Time-linearized responses for $\widehat{W}_G = 20\,\mathrm{m/s}$

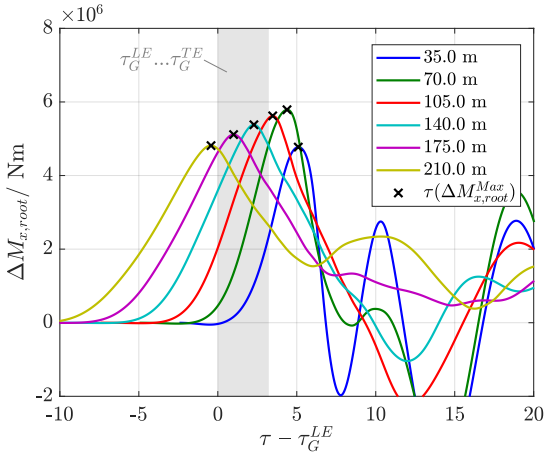

(d) Nonlinear responses for $\widehat{W}_G = 20\,\mathrm{m/s}$

Fig. 6.13: Aeroelastic gust responses at Mach 0.85

at $L_G = 140.0$ m ($H = 10\,c_{MAC}$), see Fig. 6.13(c). Up to this gust length, the time-linearized maximum values occur in a very narrow time range, at around $\tau \approx 5$. This indicates that the interaction between aerodynamic and structural dynamics with respect to the maximum bending moment does not change as long as the gust is short enough and mainly triggers the elastic mode shapes. However, once the critical gust length is reached, the interaction with the rigid-body modes first of all leads to a reduction in the maximum bending moment, and secondly, to a significantly earlier occurrence with respect to the specific gust encounter. For the gust with $L_G = 210.0$ m, the maximum value is already reached before the maximum gust velocity has finished convecting over the aircraft's wing.

For the nonlinear responses in Fig. 6.13(d), the response dynamics, and hence, the critical gust length change in comparison to the time-linearized results. At this large gust

amplitude the flow separation constantly causes an earlier maximum value, in relation to the respective $\tau_G^{LE}(L_G)$. Ultimately, the combination of flow separation and counteracting effect of the rigid-body modes leads to the effect that the maximum bending moment for the gust with $L_G = 210.0$ m is already reached even before the maximum gust velocity has hit the root leading edge of the wing. Therefore, the critical gust length for the maximum wing bending moment at $\widehat{W}_G = 20.0$ m/s is already found at $L_G = 70.0$ m ($H = 5\,c_{MAC}$).

Fig. 6.13(b) again summarizes the trends over time for the gust encounters studied, compare also with Fig. 6.11(a).

6.2 Analysis of the Lift Coefficient

This chapter is intended to build on some of the analysis from the aerodynamics chapter. Differences and similarities in the lift response of time-linearized and nonlinear computations are studied and compared to the purely aerodynamic results.

6.2.1 Unsteady Nonlinear Lift Responses

Typical aeroelastic responses of the lift coefficient are displayed in Fig. 6.14 for Mach 0.83. Whereas the first part of the responses results in similar trends as observed in the aerodynamic gust responses, compare Fig. 6.14(a) with Fig. 5.48, the decaying part is completely different due to oscillations triggered by the involved structural mode shapes. As for the nonlinear aerodynamic responses, the maximum peak lift coefficient for large-amplitude excitations occurs for medium-length gusts, see Fig. 6.14(b). These first results already

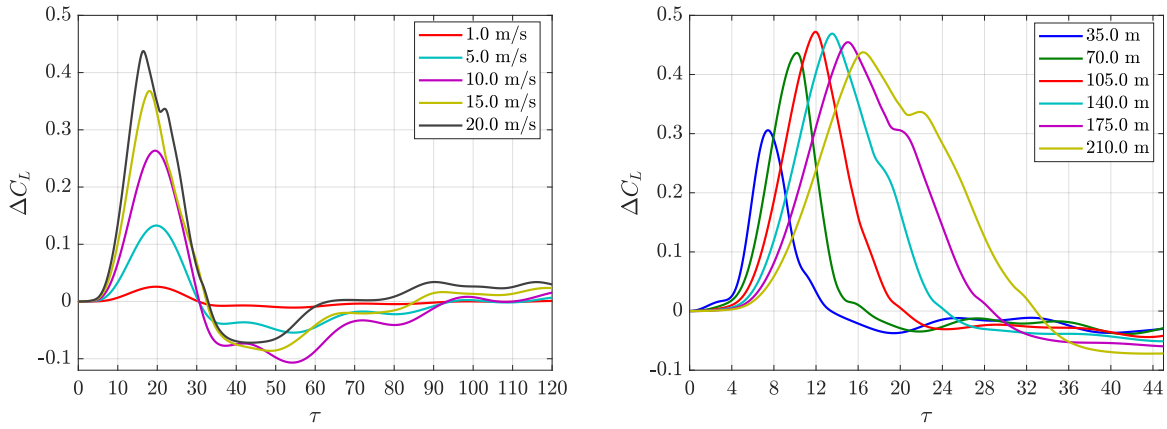

(a) $L_G = 210.0$ m **(b)** $\widehat{W}_G = 20.0$ m/s

Fig. 6.14: Time histories of aeroelastic gust responses, Mach 0.83

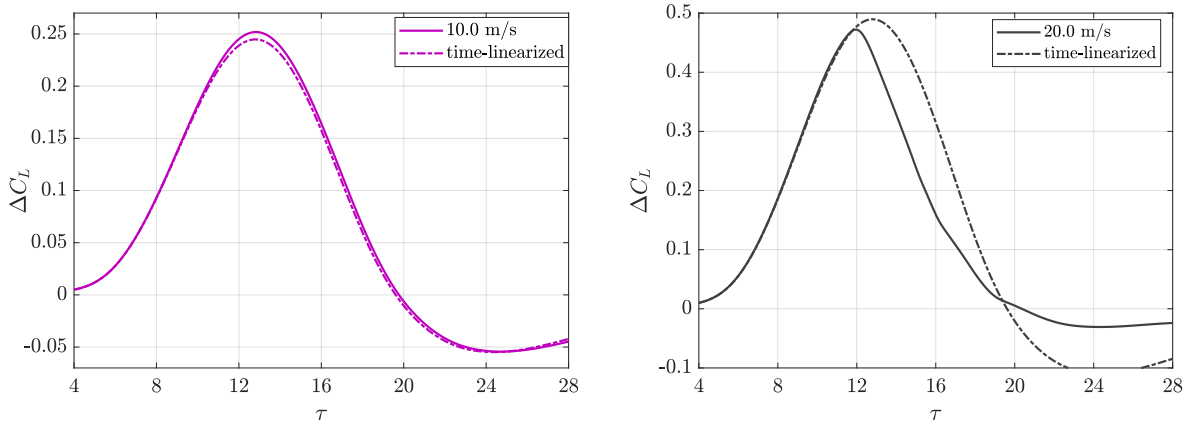

(a) $\widehat{W}_G = 10.0\,\mathrm{m/s}$, Nonlinear lift response type B

(b) $\widehat{W}_G = 20.0\,\mathrm{m/s}$, Nonlinear lift response type A

Fig. 6.15: Time histories of aeroelastic gust responses for $L_G = 105.0\,\mathrm{m}$ at Mach 0.83

indicate that the structural coupling only does not change overall trends of the maximum lift coefficient.

A detailed look at the time histories reveals identical trends and mechanisms as for the nonlinear aerodynamic results, compare Fig. 6.15 with Fig. 5.48(a). The change between double-shock and single-shock configuration at Mach 0.83 is still present also in the aeroelastic response. Moreover, it dominates the response for medium-amplitude gusts and leads to an increase in the instantaneous lift curve slope and finally to a higher nonlinear lift peak, when compared to the time-linearized result, see Fig. 6.15(a). When the amplitude is increased further, the shock-induced flow separation dominates the response and, hence, the nonlinear maximum lift value is lower than the time-linearized prediction, see Fig. 6.15(b).

Consequently, maximum increments of the lift coefficient reveal similar trends as already observed in the aerodynamic computations, with an exception for the very long gusts, see Fig. 6.16. Results at Mach 0.83 show conservative and non-conservative nonlinear responses as described in Chapter 5.4.1. The nonlinear responses at Mach 0.85 are exclusively influenced by the shock-induced flow separation and so the maximum lift values are significantly reduced by up to 30% for the largest excitation amplitude. Note, however, that the nonlinear maximum lift increases again for the two longest gusts, $L_G = 350.0\,\mathrm{m}$ and $L_G = 420.0\,\mathrm{m}$, at the largest excitation amplitude, $\widehat{W}_G = 20.0\,\mathrm{m/s}$. That last case was already discussed in Fig. 6.5 for the wing root bending moment. The analysis revealed that shock-induced flow separation is present, but that the aerodynamic loads continue to increase until the maximum gust velocity leaves the wing tip. The same explanation holds true for the lift coefficient: Due to the long wavelength of the gust in

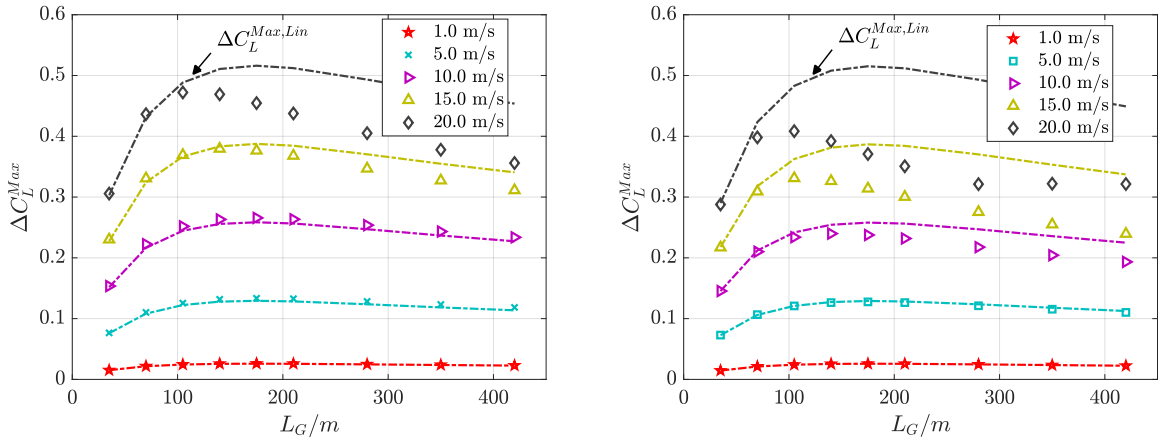

(a) Mach 0.83 **(b)** Mach 0.85

Fig. 6.16: Maximum increments of the lift coefficient for the aeroelastic configuration

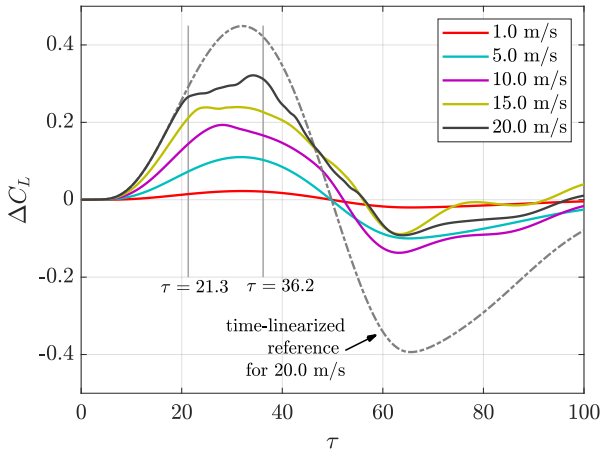

Fig. 6.17: Incremental lift coefficients for $L_G = 420.0$ m, for instantaneous snapshots of the pressure distributions see Fig. 6.5 and Fig. 6.18

combination with the large excitation amplitude, a large low-pressure region develops on the inner wing and causes this increase in lift. Note that such a large and late load peak does not occur for amplitudes lower than $\widehat{W}_G = 20.0$ m/s at $L_G = 420.0$ m, see Fig. 6.17. The amount of the induced pressures especially on the inner wing is significantly lower for the lower amplitudes, compare Fig. 6.18 with Fig. 6.5. Consequently, the peak lift coefficient does not increase further.

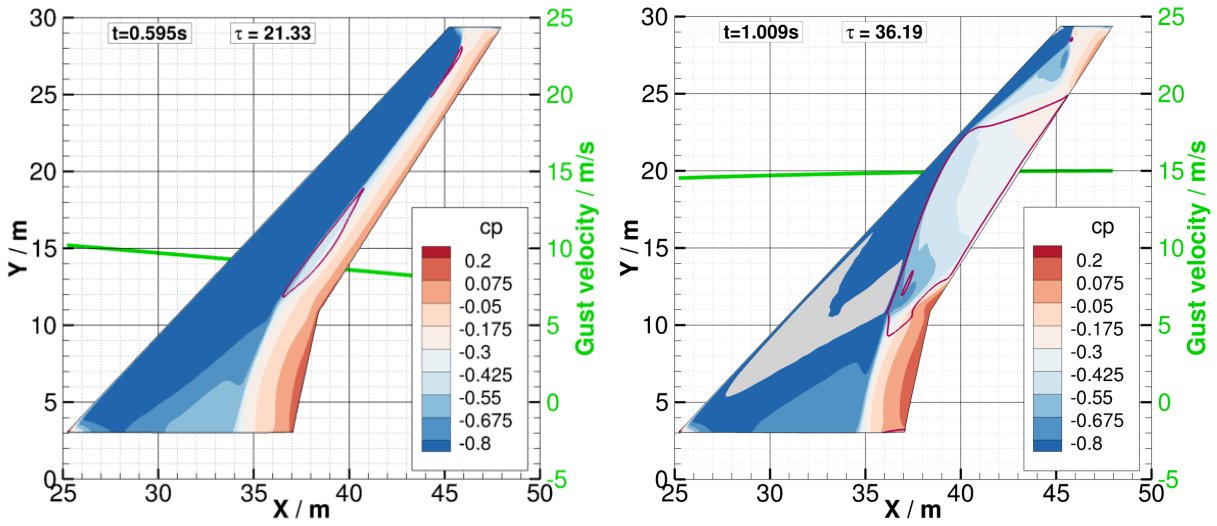

(a) Surface pressures at $\tau = 21.33$ **(b)** Surface pressures at $\tau = 36.19$

Fig. 6.18: Gust encounter with $L_G = 420.0$ m and $\widehat{W}_G = 15.0$ m/s, Mach 0.85, with two exemplary snapshots of the wing's pressure distribution (magenta lines on the wing shows the contour level $c_{fx} = 0$; the grey areas correspond to $c_p < -1.2$)

6.2.2 Comparison to Aerodynamic Results

In this section, aerodynamic and aeroelastic results for the lift coefficient are presented and compared side-by-side. For all cases considered here, the aeroelastic computations result in lower lift values throughout the complete time histories when compared to purely aerodynamic computations. This is depicted exemplarily for three test cases in Fig. 6.19(a). Taking the structural model into account in the computations has a mitigating effect on the increase of the lift coefficient and also leads to lower peak lift values. This effect seems to be caused mainly by the response of the rigid-body modes to the excitation. Fig. 6.19(b) depicts the resulting angle of attack when heave and pitch motions are evaluated. The corresponding angles of attack are defined by their modal coordinates, q_3 and q_5, see Chapter 3.3, and more specifically

$$\alpha_{Pitch} = q_5 \tag{6.1}$$

$$\alpha_{Heave} = \text{atand}(-q_3/U_\infty) \tag{6.2}$$

$$\alpha_{total} = \alpha_{Heave} + \alpha_{Pitch} \tag{6.3}$$

The resulting total induced angle of attack has a negative sign and, hence, corresponds to the slower increase of the lift coefficient when aeroelastic and aerodynamic responses are compared. It is mainly the large heave motion that induces this effect, i.e., the upward motion of the aircraft in response to the gust causes the reduction in lift.

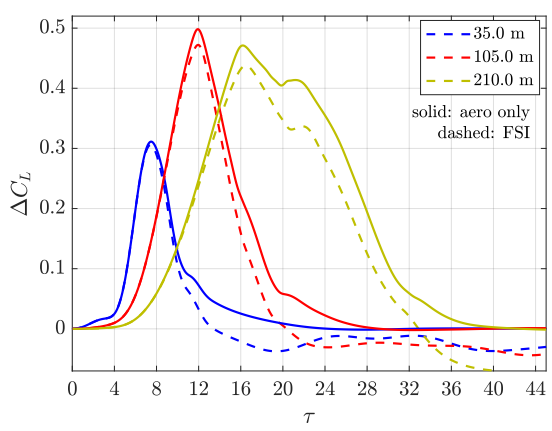

(a) Incremental lift coefficient for $\widehat{W}_G = 20.0$ m/s

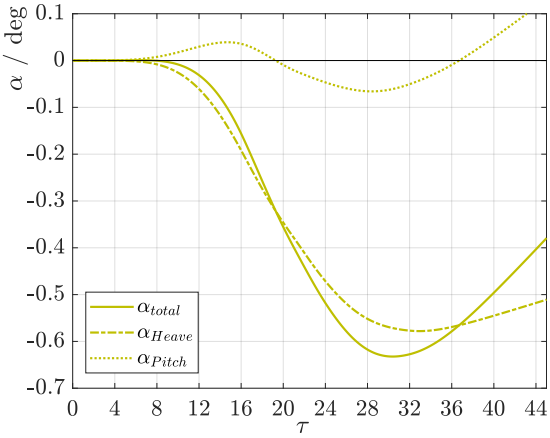

(b) Instantaneous induced angles of attack by rigid-body modes for test case with $L_G = 210.0$ m and $\widehat{W}_G = 20.0$ m/s

Fig. 6.19: Time histories for aerodynamic and aeroelastic gust encounters at Mach 0.83

Therefore, the aeroelastic computations result in lower nonlinear maximum lift values than the purely aerodynamic simulations for all cases considered, see Fig. 6.20, which is also reported by different studies [21]. An increasing gust length leads to an increasing difference between aeroelastic and aerodynamic results. Long gusts lead to larger heave motions and reduce the effective angle of attack, as described above.

Note further that the described aerodynamic stages during a discrete gust encounter, see Chapter 5.3.2, are also observed for the aeroelastic setup, compare the stages in Fig. 5.55(a)

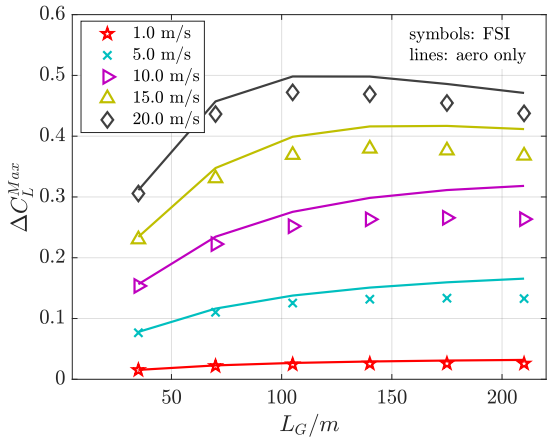

(a) Mach 0.83

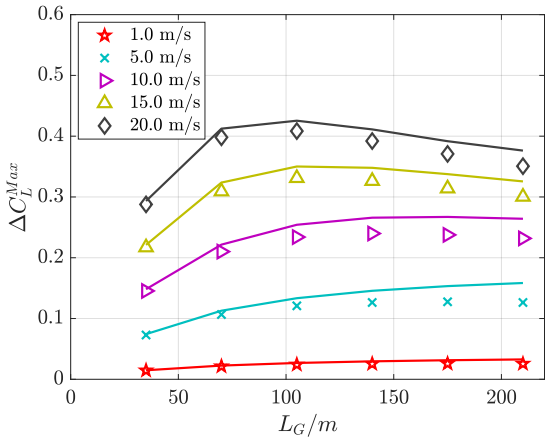

(b) Mach 0.85

Fig. 6.20: Incremental maximum lift in comparison between aeroelastic and aerodynamic simulations

with Fig. 6.19(a). Though the stages happen at later points in time, the previously identified trends can also be found in the aeroelastic responses.

Finally, Fig. 6.21 shows the impact of a nonlinear aerodynamic modeling for purely aerodynamic computations in a direct comparison to aeroelastic computations. Time-linearized FSI responses lead to lower maximum lift values than the time-linearized aerodynamic responses in any case considered due to the response of the rigid-body modes. The nonlinear aerodynamic modeling might additionally reduce the lift values, which mainly happens for large-amplitude gusts that yield the nonlinear response type A; see results for $\widehat{W}_G = 20.0\,\mathrm{m/s}$. Mid-amplitude gusts at Mach 0.83 might trigger the nonlinear response type B and so exceed the respective computed time-linearized maxima for aerodynamic and aeroelastic systems. In this direct comparison, it can be observed that the nonlinear response type B gets even stronger when fluid-structure coupled simulations instead of purely aerodynamic simulations are involved; see results for $\widehat{W}_G = 10.0\,\mathrm{m/s}$ in Fig. 6.21(a). The increase in flow separation with increasing Mach number leads to greater absolute differences between linear and nonlinear modeling for the higher Mach number, regardless of whether an aerodynamic or aeroelastic system is considered.

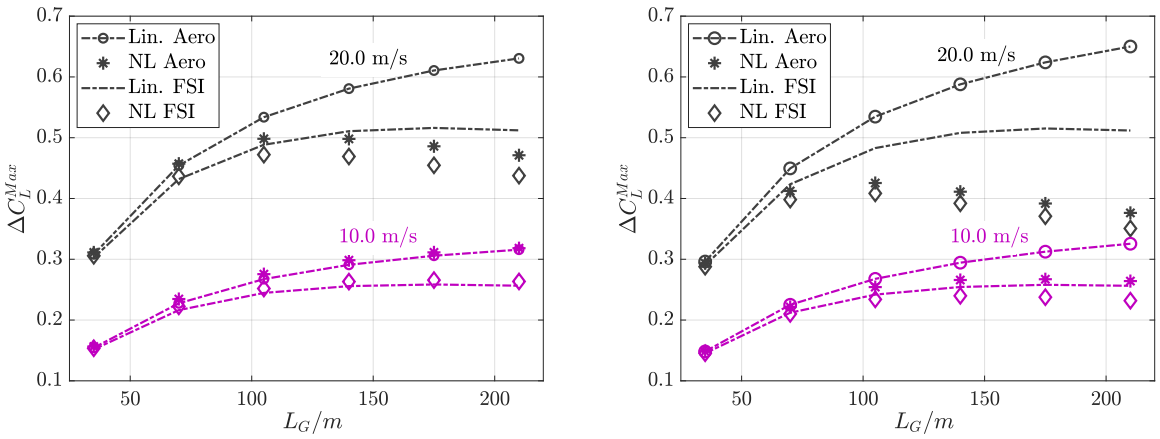

(a) Mach 0.83 **(b)** Mach 0.85

Fig. 6.21: Incremental maximum lift values: time-linearized and nonlinear responses for aerodynamic and aeroelastic gust encounters

6.3 Summary

6.3.1 Little Impact of the Elastic Modeling on Aerodynamic Nonlinearities

It is found that the consequences of a nonlinear aerodynamic modeling in an aeroelastic simulation are comparable to those found in purely aerodynamic simulations. The peak values of the bending moment histories are significantly influenced by the onset of shock-induced flow separation and/or a change in shock topology. Therefore, the comparison between time-linearized and nonlinear peak values of the aeroelastic bending moment and the corresponding lift coefficient leads to identical trends as those observed for the aerodynamic lift coefficient in Chapter 5: Significant flow separation leads to lower nonlinear maximum values, and a change in the shock topology leads to higher nonlinear maximum values as compared to the time-linearized results. The latter scenario only occurs for the lower Mach number, as was already the case in the aerodynamic computations. However, the data suggest that using the flexible instead of the rigid aircraft model amplifies a non-conservative peak lift prediction. Whereas the maximum value of the analyzed loads variable is essentially determined by the aerodynamics, the minimum value is significantly more influenced by the inertial response. Therefore, the above-mentioned trends do not apply to the investigated minimum loads, i.e., the minimum wing root bending moment. Instead, it is found that a nonlinear aerodynamic modeling leads to a decrease in the absolute value of the minimum wing root bending moment for large-amplitude gusts in any case.

6.3.2 Critical Gust at Shorter Gust Length

In a time-linearized analysis, the critical gust length mainly depends on the response of the rigid-body modes to the gust excitation. Its value depends on the variable studied, but it is constant for different excitation amplitudes. The results in this work additionally reveal a dependence of the critical gust length on the gust amplitude if a nonlinear aerodynamic modeling is applied. It is the effect of the unsteady flow separation that leads to a load reduction mainly for long-wavelength gusts. Consequently, the highest peak loads are encountered for shorter gusts when the excitation amplitude is increased. This trend is observed for the maximum wing bending moment for both Mach numbers studied.

Moreover, maximum and minimum peak loads occur at earlier points in time with increasing excitation amplitude. On the one hand, the gust length for the critical gust needs to be long enough so that the loads have enough time to grow. The maximum value in the loads may only be reached after the maximum gust velocity has already passed com-

pletely over the wing. And on the other hand, the gust length for the critical gust must not become too long in order to prevent premature separation of the flow.

7 Summary and Discussion

The current thesis analyzes the effects of an increase in aerodynamic modeling fidelity for large-amplitude gust encounters in transonic flow. Computations are based on the unsteady nonlinear RANS equations, which are solved in the time domain. The results are compared to time-linearized responses which are obtained using small-amplitude excitations. Analyzes are conducted for different transonic steady base flows for a 2D airfoil configuration, as well as for a transport aircraft configuration for a rigid and flexible aircraft model.

The data suggest that there are three basic types of nonlinear lift responses, which are either triggered by shock-induced separation, by a change in flow topology or by a combination of both. The nonlinear responses can therefore lead to lower or higher lift values than the time-linearized computations, depending on the steady base flow and the excitation parameters. It seems that the steady lift polar, and more specifically, the steady lift derivative can be used as an indicator for the occurrence of the different response types.

During a discrete gust encounter of a transport aircraft configuration, up to eight different stages are found in the time-domain history of the lift response. These stages, again, depend on the steady base flow, gust amplitude, and gust length and can also be assigned to the different response types.

The reported nonlinear effects from purely aerodynamic simulations for the peak lift coefficient also apply for the wing bending moment and the lift coefficient resulting from aeroelastic simulations. The critical gust length for load analysis shifts to shorter gust lengths when the excitation amplitude is increased.

Summing up, the recompression shock, its motion, and a possibly following separation of the flow can be identified as the main drivers for all observed nonlinear effects in transonic flows, both for rigid and flexible aircraft models. Therefore, the **main hypothesis of this work** only partly holds true and so needs to be extended: It is not only the shock-induced flow separation, but also the topology of the shock that develops during the gust encounter, which is responsible for the occurrence of nonlinear effects. The nonlinearly computed lift might, therefore, become lower or higher, than the corresponding time-linearized value. The **additional hypotheses** are responded in the following:

- **A.** Unsteady nonlinear effects get stronger with increasing Mach number and decreasing excitation frequency. $\Longrightarrow$ It can be confirmed that unsteady nonlinear effects get stronger with decreasing excitation frequency. However, only separation-induced nonlinear effects get stronger with increasing Mach number. Flows at lower Mach numbers might result in additional nonlinear effects.

- **B.** Similar basic nonlinear aerodynamic effects can be observed for a two-dimensional airfoil and also for a transport aircraft configuration. $\Longrightarrow$ This hypothesis can be confirmed. Three different nonlinear response types are identified.
- **C.** Specific aerodynamic stages for the response of the lift coefficient over time can be identified for a discrete gust encounter of a transport aircraft configuration. $\Longrightarrow$ This hypothesis can be confirmed. Nonlinear lift responses to discrete gusts consist of up to eight stages.
- **D.** For a large-amplitude gust encounter of a two-dimensional airfoil in transonic flow, the maximum dynamic lift might result in larger values than the maximum static lift, implying a dynamic overshoot. $\Longrightarrow$ This hypothesis can be confirmed. Dynamic overshoots also exist in transonic flows.
- **E.** The difference between time-linearized and nonlinear peak lift response is larger for purely aerodynamic simulations than for fluid-structure coupled simulations. $\Longrightarrow$ This hypothesis can be confirmed. The interaction of aerodynamics and structure mitigates the response and leads to significantly lower time-linearized peak lift values than the purely aerodynamic simulation. If a nonlinear aerodynamic method is used, the maximum lift coefficients of aerodynamic and aeroelastic simulations are very similar.
- **F.** The "critical gust length" depends on the excitation amplitude. $\Longrightarrow$ This hypothesis can be confirmed. An increasing excitation amplitude leads to shorter gust lengths for the critical gust.

Results are numerically robust concerning spatial and temporal discretization and the number of structural mode shapes involved in the flexible aircraft configuration. The main features in the global responses are identical between different turbulence models. However, specific details concerning absolute values and local separation effects differ between them.

Discussion: Aerodynamic Analysis

Though nonlinear effects due to shock-induced flow separation and the corresponding breakdown in lift are already reported in the literature, e.g. in [19, 20, 76], unsteady nonlinear effects due to a significant topological change of the recompression shock are first reported in this work. In the 1980s, it was assumed that the extent of the shock motion is the crucial aspect for the nonlinearity of a response [57, 58]. In the 2010s, computations indicated an inappropriate physical modeling of the shock motion for large amplitude disturbances using a linear frequency domain solver [19, 59]. In this work, it could be shown that the extent of the shock motion is less important for the occurrence of non-

linearities. Rather, changes in the shock topology itself are causing nonlinear response effects, regardless of the extent of the shock motion.

The different response types in this work are identified for different Mach numbers at a constant angle of attack. It should be noted that the same categorization can also be expected for a constant Mach number when the angle of attack is varied. It is not the inflow velocity but the shock and separation behavior on the specific configuration, which triggers the different effects. An increase in the steady Mach number causes similar effects as an increase in the steady angle of attack in terms of shock position and separation behavior.

It is emphasized here that the observed effect of an increase in the steady lift curve slope with the onset of transonic flow is not yet discussed in the literature, though indications for this trend are found also for different airfoils as, e.g., for the supercritical airfoil OAT15A [30]. Further insight into this steady trend and influencing variables seems necessary.

Closely related to this is the observation that the changing topology of the recompression shock contributes to the increase in the lift derivative. The conditions under which these observations and the associated nonlinear effects can be generalized need to be investigated and understood in more detail. Further studies on different configurations are essential.

Compared to subsonic large-amplitude responses, one of the major differences in transonic flows seems to be the absence of a leading-edge vortex. The presence of the recompression shock in transonic flow changes the overall physics and does not seem to permit a formation of such a vortex on the airfoil's leading edge as it is, e.g., recently described for a subsonic airfoil flow in [22]. Instead, the shock motion and a possibly following separation of the flow seem to be the main drivers for the observed nonlinear effects in transonic flows. The results therefore support the early assumptions from Liiva [49] and Visbal [50].

In this work, unsteady nonlinear transonic effects exclusively result out of gust excitations. It can be expected that qualitatively similar trends might occur for different mode shapes of excitation, e.g., a pitching excitation. When the responses are compared for the same excitation amplitude, gust responses are milder than those for a pitching motion [127]. The reason is that gusts do not excite the complete airfoil simultaneously but are gradually moving over the airfoil's chord.

Though the numerical results are consistent throughout this thesis, one of the deficiencies of this work certainly is the lack of experimental validation data for the observed effects.

Corresponding wind tunnel data or even flight test data do not seem to be available at the time of writing. The numerical studies in this thesis were carefully designed, especially concerning spatial and temporal convergence. Additionally, it was confirmed that different turbulence models yielded the same qualitative results. It can not be completely excluded, however, that URANS-based turbulence models might miss some specific effects that occur during large-amplitude excitations in transonic flows. Though the applied turbulence models show reasonable results for small-disturbance transonic flows, as well as for large-amplitude subsonic flows, a validation for large disturbances in transonic flows is missing.

All findings can be helpful for the design of further studies aiming at an improved understanding of unsteady nonlinear transonic flows. Moreover, the data can be used to identify and develop suitable and robust physics-based aerodynamic or aeroelastic reduced-order models that could be applied in a future industrial aircraft design process.

Discussion: Aeroelastic Analysis

The increase in aerodynamic modeling fidelity also affects the prediction of peak internal loads such as the wing root bending moment. Reductions as well as enlargements, each in the order of 25%, are found when the results of the time-linearized and the nonlinear computations are compared for the incremental loads. Similar studies on the NASA CRM result in reductions of the maximum incremental root bending moment of 24% and 29%, respectively, depending on the turbulence model that is used [20]. In the case that these gust loads are sizing-relevant, the results show on the one hand a great potential for savings in the structural weight, but on the other hand also indicate that additional structural weight might be necessary to ensure the specific safety factors. However, since there are several 100 sizing load cases (gust, maneuver, ground, etc.), the share of the critical *gust* loads finally depends on the configuration and the specific aircraft component.

From this individual study it is difficult to estimate under which assumptions the present results can be generalized. In particular, the combination of aerodynamic and inertial responses might lead to different total loads if a different set of mode shapes determines the structural design.

Taking into account that the level of model fidelity increases, considerable care should also be taken to the specific load cases that are required by the certification specifications. A more realistic model might also demand more realistic load cases in order to strive for optimal structural sizing.

In any case, critical gust lengths shift to shorter gusts, with increasing excitation amplitude, which is in agreement to previous studies in subsonic and transonic flows [19, 22].

8 Conclusion

The design of new energy-efficient aircraft reduces the climate impact and helps in paving the way for more sustainable aviation. The fuel consumption of an aircraft can directly be reduced if, e.g., more lightweight structures are designed. Therefore, accurate knowledge of peak loads is necessary for all load cases that are demanded by the certification specifications as these peak loads lead to the sizing of an aircraft's components. However, standard design practices are mainly based on time-linearized aerodynamics and are therefore not accurate for the prediction of nonlinear loads due to large-amplitude excitations.

The findings from this work imply a consequent application of an unsteady nonlinear aerodynamic method in an aircraft's design process, as it shows a diverse impact on the loads in a broad parameter range. Moreover, with an increasing level of aerodynamic model fidelity, considerable care should also be taken to the specific load cases that are required by the certification specifications. Existing standards might need to be reworked as nonlinear methods might change overall trends, e.g., with respect to the maximum gust length that is required for the load assessment.

Three main topics are recommended for further studies:

- First of all, wind tunnel tests for large-amplitude excitations in transonic flows are necessary in order to obtain reliable validation data for the observed nonlinear effects in the numerical studies.
- Secondly, additional numerical studies are helpful for potentially generalizing or delimiting the described effects. Different airfoils and transport aircraft configurations should be investigated. Possible correlations between steady and unsteady flows need to be analyzed in more detail as such findings could serve a more fundamental understanding of transonic flows.
- Lastly, the interaction between the nonlinear aerodynamic modeling and the structural modeling needs to be addressed more deeply in future investigations. Various aircraft configurations with different structural models should be analyzed to investigate the impact of aerodynamic nonlinear effects on industrially relevant loads. Due to the superposition of aerodynamic and inertial loads, changes in the inertial response might lead to different trends in the peak values of the total loads.

Finally, note that complex numerical studies are necessary, especially for a better understanding of complex processes, but a comparison to actual flight test data will always be required, to align computer-based research with real-world data. Therefore, this thesis is closed with the words from J. R. Fuller, a former manager of loads and flutter research at

the Boeing Commercial Airplane Group, who commented already in the 1990s [83]: ”All things considered, we are, no doubt, fooling ourselves with analytical oversophistication, therefore, periodic checks of actual flight test results against dynamic analysis results will continue to be required to properly scope design analyses efforts [...].”

References

[1] European Commission: A European Green Deal - Striving to be the first climate-neutral continent (2019). URL https://commission.europa.eu/strategy-and-policy/priorities-2019-2024/european-green-deal_en. Retrieved on 04 January 2022

[2] DLR: Towards Zero-Emission Aviation (2021). URL https://www.dlr.de/content/en/articles/news/2021/04/20211215_towards-zero-emission-aviation.html. Retrieved on 04 January 2022

[3] Schuster, D.M., Liu, D.D., Huttsell, L.J.: Computational Aeroelasticity: Success, Progress, Challenge. Journal of Aircraft **40**(5), pp. 843–856 (2003). doi:10.2514/2.6875

[4] European Aviation Safety Agency (EASA): Certification Specifications and Acceptable Means of Compliance for Large Aeroplanes CS-25, Amendment 27 (2021)

[5] Hoblit, Frederic M: Gust Loads on Aircraft: Concepts and Applications. American Institute of Aeronautics and Astronautics, Inc. (1988). doi:10.2514/4.861888. ISBN: 978-0-930403-45-4

[6] Streitenberger, K.M., Feldwisch, J.M.: Cfd-based aeroelastic maneuver and gust loads analysis for a high aspect ratio wing configuration. In: AIAA SCITECH 2025 Forum (2025). doi:10.2514/6.2025-1663

[7] Albano, E., Rodden, W.P.: A doublet-lattice method for calculating lift distributions on oscillating surfaces in subsonic flows. AIAA Journal **7**(2), pp. 279–285 (1969). doi:10.2514/6.1968-73

[8] Giesing, J.P., Kalman, T.P., Rodden, W.P.: Correction factor techniques for improving aerodynamic prediction methods. Tech. rep., McDonnell Douglas Corporation & NASA (1976). NACA-CR-144967

[9] Brink-Spalink, J., Bruns, J.M.: Correction of unsteady aerodynamic influence coefficients using experimental or CFD data. In: International Forum on Aeroelasticity and Structural Dynamics (2001). IFASD-2001-034

[10] Palacios, R., Climent, H., Karlsson, A., Winzell, B.: Assessment of strategies for correcting linear unsteady aerodynamics using CFD or experimental results. In: Haase, Selmin, Winzell (eds.) Progress in Computational Flow-Structure Interaction, pp. 209–224. Springer Verlag (2003)

[11] Thormann, R., Dimitrov, D.: Correction of aerodynamic influence matrices for transonic flow. CEAS Aeronautical Journal **5**(4), pp. 435–446 (2014). doi:10.1007/s13272-014-0114-3

[12] Banavara, N.K., Dimitrov, D.: Prediction of Transonic Flutter Behavior of a Supercritical Airfoil Using Reduced Order Methods. In: New Results in Numerical and Experimental Fluid Mechanics IX, *Notes on Numerical Fluid Mechanics and Multidisciplinary Design*, vol. 124, pp. pp. 365–373. Springer International Publishing (2014). doi:10.1007/978-3-319-03158-3_37

[13] Quero-Martin, D.: An aeroelastic reduced order model for dynamic response prediction to gust encounters. Ph.D. thesis, TU Berlin (2017). doi:10.14279/depositonce-6014

[14] Katzenmeier, L., Vidy, C., Breitsamter, C.: Correction Technique for Quality Improvement of Doublet Lattice Unsteady Loads by Introducing CFD Small Disturbance Aerodynamics. Journal of Aeroelasticity and Structural Dynamics **5**(1), pp. 17–40 (2017). doi:10.3293/asdj.2017.42

[15] Kaiser, C., Friedewald, D.: Aeroelastic AIC-Based Reduced Order Model with CFD-Corrections for Gust Encounter Simulations, pp. pp. 55–74. Springer International Publishing (2024). doi:10.1007/978-3-031-69425-7_4

[16] Thormann, R., Widhalm, M.: Linear-Frequency-domain predictions of Dynamic-Response data for viscous transonic flows. AIAA Journal **51**(11), pp. 2540–2557 (2013). doi:10.2514/1.J051896

[17] Weigold, W., Stickan, B., Travieso-Alvarez, I., Kaiser, C., Teufel, P.: Linearized Unsteady CFD for Gust Loads with TAU. In: International Forum on Aeroelasticity and Structural Dynamics (2017). IFASD-2017-187

[18] Bekemeyer, P., Thormann, R., Timme, S.: Frequency-domain gust response simulation using computational fluid dynamics. AIAA Journal **55**(7), pp. 2174–2185 (2017). doi:10.2514/1.J055373

[19] Kaiser, C., Quero, D., Nitzsche, J.: Quantification of Nonlinear Effects in Gust Load Prediction. In: International Forum on Aeroelasticity and Structural Dynamics (2019). IFASD-2019-054

[20] Feldwisch, J.: Effect of Flow Separation on Discrete Gust Loads for a Free-Flying Elastic Aircraft. In: International Forum on Aeroelasticity and Structural Dynamics (2024). IFASD-2024-193

[21] Reimer, L., Ritter, M., Heinrich, R., Krüger, W.: CFD-based Gust Load Analysis for a Free-flying Flexible Passenger Aircraft in Comparison to a DLM-based Approach. In: 22nd AIAA Computational Fluid Dynamics Conference (2015). doi:10.2514/6.2015-2455. AIAA 2015-2455

[22] Mallik, W., Raveh, D.E.: Gust response at high angles of attack. AIAA Journal **57**(8), pp. pp. 3250–3260 (2019). doi:10.2514/1.J057546

[23] Friedewald, D., Thormann, R., Kaiser, C., Nitzsche, J.: Quasi-steady doublet-lattice correction for aerodynamic gust response prediction in attached and separated transonic flow. CEAS Aeronautical Journal **9**(1), pp. 53–66 (2018). doi:10.1007/s13272-017-0273-0

[24] Friedewald, D.: Numerical Simulations on Unsteady Nonlinear Transonic Airfoil Flow. Aerospace **8**(1) (2021). doi:10.3390/aerospace8010007

[25] Friedewald, D.: Large-Amplitude Gusts on the NASA Common Research Model. Journal of Aircraft **60**(6), pp. 1901–1916 (2023). doi:10.2514/1.C037198

[26] Anderson, J.D.: Fundamentals of Aerodynamics. McGraw Hill Higher Education, 4. Edition, New York (2006). ISBN: 978-1259129919

[27] Leishman, J.G.: Principles of Helicopter Aerodynamics. Cambridge Aerospace Series. Cambridge University Press (2000). ISBN: 0-521-66060-2

[28] Vos, R., Farokhi, S.: Introduction to Transonic Aerodynamics. Springer Dordrecht (2015). doi:10.1007/978-94-017-9747-4. ISBN: 978-94-017-9746-7

[29] Glauert, H., Taylor, G.I.: The effect of compressibility on the lift of an aerofoil. Proceedings of the Royal Society of London. Series A, Containing Papers of a Mathematical and Physical Character **118**(779), pp. 113–119 (1928). doi:10.1098/rspa.1928.0039

[30] Nitzsche, J., Ringel, L.M., Kaiser, C., Hennings, H.: Fluid-Mode Flutter in Plane Transonic Flows. In: International Forum on Aeroelasticity and Structural Dynamics (2019). IFASD-2019-006

[31] Gault, D.E.: A correlation of low-speed, airfoil-section stalling characteristics with Reynolds number and airfoil geometry. Tech. Rep. NACA-TN-3963, NACA (1957)

[32] McCroskey, W.J., McAlister, K.W., Carr, L.W., Pucci, S.L., Lambert, O., Indergrand, R.F.: Dynamic Stall on Advanced Airfoil Sections. Journal of the American Helicopter Society **26**(3), pp. 40–50 (1981). doi:10.4050/JAHS.26.40

[33] Pearcey, H.H.: Some effects of shock-induced separation of turbulent boundary layers in transonic flow past aerofoils. Tech. Rep. R. and M. No. 3108, Ministry of Aviation, Aeronautical Reserach Council (1959)

[34] McDevitt, J.B., Okuno, A.F.: Static and Dynamic Pressure Measurements on a NACA0012 Airfoil in the Ames high Reynolds number facility. Tech. rep., NASA Ames Research Center, USA (1985). NASA-TP-2485

[35] Crouch, J.D., Garbaruk, A., Magidov, D., Travin, A.: Origin of transonic buffet on aerofoils. Journal of Fluid Mechanics **628**, pp. 357–369 (2009). doi:10.1017/S0022112009006673

[36] Giannelis, N.F., Vio, G.A., Levinski, O.: A review of recent developments in the understanding of transonic shock buffet. Progress in Aerospace Sciences **92**, pp. 39 – 84 (2017). doi:10.1016/j.paerosci.2017.05.004

[37] Iovnovich, M., Raveh, D.: Transonic Unsteady Aerodynamics in the Vicinity of Shock-Buffet Instability. Journal of Fluids and Structures **29**, pp. 131 – 142 (2012). doi:10.1016/j.jfluidstructs.2011.12.015

[38] Tinoco, E.N., Brodersen, O.P., Keye, S., Laflin, K.R., Feltrop, E., Vassberg, J.C., Mani, M., Rider, B., Wahls, R.A., Morrison, J.H., Hue, D., Roy, C.J., Mavriplis, D.J., Murayama, M.: Summary Data from the Sixth AIAA CFD Drag Prediction Workshop: CRM Cases. Journal of Aircraft **55**(4), pp. 1352–1379 (2018). doi:10.2514/1.C034409

[39] Tinoco, E.N.: An Evaluation and Recommendations for Further CFD Research Based on the NASA Common Research Model (CRM) Analysis from the AIAA Drag Prediction Workshop (DPW) Series. Tech. Rep. NASA/CR-2019-220284, NASA (2019)

[40] Abbas-Bayoumi, A., Becker, K.: An industrial view on numerical simulation for aircraft aerodynamic design. Journal of Mathematics in Industry **1**, pp. 1–14 (2011). doi:10.1186/2190-5983-1-10

[41] Slotnick, J., Heller, G.: Emerging opportunities for predictive CFD for off-design commercial airplane flight characteristics. In: 54th 3AF International Conference on Applied Aerodynamics, Paris (2019)

[42] Brodersen, O., Crippa, S., Eisfeld, B., Keye, S., Geisbauer, S.: DLR Results from the Fourth AIAA Computational Fluid Dynamics Drag Prediction Workshop. Journal of Aircraft **51**(4), pp. 1135–1148 (2014). doi:10.2514/1.C031533

[43] Togiti, V., Eisfeld, B., Brodersen, O.: Turbulence Model Study for the Flow Around the NASA Common Research Model. Journal of Aircraft **51**(4), pp. 1331–1343 (2014). doi:10.2514/1.C032609

[44] Eisfeld, B., Rumsey, C.L., Togiti, V., Braun, S., Stürmer, A.: Reynolds-Stress Model Computations of NASA Juncture Flow Experiment. AIAA Journal **60**(3), pp. 1643–1662 (2022). doi:10.2514/1.J060510

[45] Keye, S., Brodersen, O.P., Melber-Wilkending, S., Friedewald, D., Fehrs, M., Jägersküpper, J.: Summary of DLR Results for the Seventh AIAA Computational Fluid Dynamics Drag Prediction Workshop. In: AIAA AVIATION 2023 Forum (2023). doi:10.2514/6.2023-4120

[46] Gardner, A.D., Jones, A.R., Mulleners, K., Naughton, J.W., Smith, M.J.: Review of rotating wing dynamic stall: Experiments and flow control. Progress in Aerospace Sciences **137**, pp. 100,887 (2023). doi:10.1016/j.paerosci.2023.100887

[47] Choudhry, A., Leknys, R., Arjomandi, M., Kelso, R.: An Insight into the Dynamic Stall Lift Characteristics. Experimental Thermal and Fluid Science **58**(0), pp. 188 – 208 (2014). doi:https://doi.org/10.1016/j.expthermflusci.2014.07.006

[48] Ericsson, L., Reding, J.: Dynamic stall overshoot of static airfoil characteristics. In: 12th Atmospheric Flight Mechanics Conference (1985). doi:10.2514/6.1985-1773

[49] Liiva, J.: Unsteady aerodynamic and stall effects on helicopter rotor blade airfoil sections. Journal of Aircraft **6**(1), pp. 46–51 (1969). doi:10.2514/3.44000

[50] Visbal, M.R.: Dynamic stall of a constant-rate pitching airfoil. Journal of Aircraft **27**(5), pp. 400–407 (1990). doi:10.2514/3.25289

[51] Corke, T.C., Thomas, F.O.: Dynamic stall in pitching airfoils: Aerodynamic damping and compressibility effects. Annual Review of Fluid Mechanics **47**(1), pp. 479–505 (2015). doi:10.1146/annurev-fluid-010814-013632

[52] Harper, P.W., Flanigan, R.E.: The effect of rate of change of angle of attack in the maximum lift of a small model. Tech. Rep. NACA Technical Note 2061 (1950). NACA TN 2061

[53] Leishman, J.G., Beddoes, T.S.: A generalised model for airfoil unsteady aerodynamic behaviour and dynamic stall using the indicial method. In: American Helicopter Society (AHS) Annual Forum (1986)

[54] Reddy, T.S.R., Kaza, K.R.V.: Comparative Study of some Dynamic Stall Models. Tech. Rep. NASA-TM-88917, NASA (1987)

[55] Goman, M., Khrabrov, A.: State-space representation of aerodynamic characteristics of an aircraft at high angles of attack. Journal of Aircraft **31**(5), pp. 1109–1115 (1994). doi:10.2514/3.46618

[56] Tijdeman, H.: Investigations of the Transonic Flow around Oscillating Airfoils. Ph.D. thesis, TU Delft (1977)

[57] Dowell, E.H., Williams, M.H., Bland, S.R.: Linear/Nonlinear Behavior in Unsteady Transonic Aerodynamics. AIAA Journal **21**(1), pp. 38–46 (1983). doi:10.2514/3.8025

[58] McCroskey, W.J.: Unsteady Airfoils. Annual Review of Fluid Mechanics **14**(1), pp. 285–311 (1982). doi:10.1146/annurev.fl.14.010182.001441

[59] Bekemeyer, P., Ripepi, M., Heinrich, R., Görtz, S.: Nonlinear Unsteady Reduced-Order Modeling for Gust-Load Predictions. AIAA Journal **57**(5), pp. 1839–1850 (2019). doi:10.2514/1.j057804

[60] Huebner, A., Reimer, L.: Gust Encounter Simulations of a Generic Transport Aircraft and Analysis of Load Alleviation Potentials by Control Surface Deflections Using a RANS-CFD-based Multidisciplinary Simulation Environment. In: AIAA Aviation 2019 Forum (2019). doi:10.2514/6.2019-3198

[61] Lancelot, P., Sodja, J., Breuker, R.D.: Investigation of the unsteady flow over a wing under gust excitation. In: International Forum on Aeroelasticity and Structural Dynamics (2017). IFASD-2017-185

[62] Lepage, A., Paletta, N., Russo, S., Ricci, S., Rantet, E., Barnique, A.: Wind tunnel tests for gust load investigation in transonic flows – Part 1 : Development of an innovative test rig. In: International Forum on Aeroelasticity and Structural Dynamics (2024). IFASD-2024-231

[63] Theodorsen, T., Mutchler, W.: General theory of aerodynamic instability and the mechanism of flutter. Tech. Rep. NACA-TR-496, National Advisory Committee for Aeronautics (1935)

[64] Wagner, H.: Über die entstehung des dynamischen auftriebes von tragflügeln. ZAMM - Journal of Applied Mathematics and Mechanics / Zeitschrift für Angewandte Mathematik und Mechanik **5**(1), pp. 17–35 (1925). doi:10.1002/zamm.19250050103

[65] Küssner, H.G.: Zusammenfassender Bericht über den instationären Auftrieb von Flügeln. In: Luftfahrtforschung, Band 13, vol. 12 (1936)

[66] Sears, W.R.: A systematic presentation of the theory of thin airfoils in non-uniform motion. Ph.D. thesis, California Institute of Technology (1938)

[67] Sears, W.R.: Some aspects of non-stationary airfoil theory and its practical application. Journal of the Aeronautical Sciences (Institute of the Aeronautical Sciences) **8**(3), pp. 104–108 (1941)

[68] Blair, M.: A Compilation of the Mathematics Leading to the Doublet Lattice Method. Tech. Rep. WL-TR-92-3028, Wright Laboratory (1992)

[69] AIAA: Recommended Practice: When Flight Modelling Is Used to Reduce Flight Testing Supporting Aircraft Certification. Tech. Rep. AIAA R-154-2021, AIAA (2021). doi:10.2514/4.106231.001

[70] Sartor, F., Timme, S.: Delayed Detached–Eddy Simulation of Shock Buffet on Half Wing–Body Configuration. AIAA Journal **55**(4), pp. 1230–1240 (2017). doi:10.2514/1.J055186

[71] Streitenberger, K., Nitzsche, J.: Investigation of Vortex-induced Vibrations to compare Reynolds-Average Navier-Stokes and Detached-Eddy Simulations. In: International Forum on Aeroelasticity and Structural Dynamics (2024). IFASD-2024-214

[72] Spalart, P., Allmaras, S.: A One-Equation Turbulence Model for Aerodynamic Flows. In: 30th Aerospace Sciences Meeting and Exhibit (1992). doi:10.2514/6.1992-439. AIAA-92-0439

[73] Neumann, J., Mai, H.: Gust response: Simulation of an aeroelastic experiment by a fluid–structure interaction method. Journal of Fluids and Structures **38**, pp. 290 – 302 (2013). doi:10.1016/j.jfluidstructs.2012.12.007

[74] Thormann, R.: Accurate and efficient, time-linearized flutter analysis of transport aircraft. Ph.D. thesis, TU Braunschweig (2018)

[75] Kaiser, C., Thormann, R., Dimitrov, D., Nitzsche, J.: Time-Linearized Analysis of Motion-induced and Gust-induced Airloads with the DLR TAU Code. In: Deutscher Luft- und Raumfahrtkongress (2015)

[76] Bekemeyer, P.: Rapid computational aerodynamics for aircraft gust response analysis. Ph.D. thesis, University of Liverpool (2018). doi:10.17638/03027827

[77] Wilson, E.B.W.: Theory of an Aeroplane Encountering Gusts. Tech. Rep. No. 1, Part 2, NACA (1915)

[78] Donely, P.: Summary of Information relating to Gust Loads on Airplanes. Tech. Rep. No. 997, NACA (1949)

[79] Houbolt, J.C.: Atmospheric turbulence. AIAA Journal **11**(4), pp. 421–437 (1973). doi:10.2514/6.1972-219

[80] Etkin, B.: Turbulent wind and its effect on flight. Journal of Aircraft **18**(5), pp. 327–345 (1981). doi:10.2514/3.57498

[81] Murrow, H., Pratt, K., Houbolt, J.: NACA/NASA Research related to Evolution of U.S. Gust Design Criteria. In: 30th Structures, Structural Dynamics and Materials Conference (1989). doi:10.2514/6.1989-1373

[82] Barnes, T.J.: Harmonization of U.S. and European Gust Criteria for Transport Airplanes. In: International Council of the Aeronautical Sciences, ICAS-90-1.4.1 (1990)

[83] Fuller, J.R.: Evolution of Airplane Gust Loads Design Requirements. Journal of Aircraft **32**(2), pp. 235–246 (1995). doi:10.2514/3.46709

[84] Fuller, J.R.: Evolution and future development of airplane gust loads design requirements. In: World Aviation Congress (1997). doi:10.2514/6.1997-5577

[85] Brockhaus, R., Alles, W., Luckner, R.: Flugregelung. Springer-Verlag Berlin Heidelberg (2011). doi:10.1007/978-3-642-01443-7

[86] Handojo, V.: Contribution to load alleviation in aircraft pre-design and its influence on structural mass and fatigue. Doctoral thesis, Technische Universität Berlin, Berlin (2020). doi:10.14279/depositonce-10986

[87] Jenkinson, L., Rhodes, D., Simpkin, P.: Civil Jet Aircraft Design. AIAA Education Series. Arnold (1999). ISBN: 978-0340741528

[88] Khodaparast, H.H., Cooper, J.E.: Rapid Prediction of Worst-Case Gust Loads Following Structural Modification. AIAA Journal **52**(2), pp. 242–254 (2014). doi:10.2514/1.J052031

[89] Chiozzotto, G., Handojo, V.: Tuned gust analysis methods. In: Luftfahrttechnisches Handbuch (2017). LTH-Beitragsnummer BM 41 200-03

[90] Knoblach, A., Looye, G.: Efficient Determination of Worst-Case Gust Loads Using System Norms. Journal of Aircraft **54**(3), pp. 1205–1210 (2017). doi:10.2514/1.C033919

[91] Pratt, K.G.: A Revised Formula for the Calculation of Gust Loads. Tech. Rep. NACA-TN-2964, NACA (1953)

[92] European Aviation Safety Agency (EASA): Certification Specifications and Acceptable Means of Compliance for Large Aeroplanes CS-23, Amendment 4 (2018)

[93] Flomenhoft, H.I.: Brief history of gust models for aircraft design. Journal of Aircraft **31**(5), pp. 1225–1227 (1994). doi:10.2514/3.46637

[94] Blazek, J.: Computational Fluid Dynamics: Principles and Applications. Elsevier, Oxford (2001). doi:10.1016/B978-0-08-044506-9.X5000-0. ISBN: 978-0-08-044506-9

[95] Ferziger, J.H., Peric, M.: Numerische Strömungsmechanik. Springer-Verlag, Berlin Heidelberg (2008). doi:10.1007/978-3-662-46544-8. ISBN: 978-3-662-46543-1

[96] Bardina, J.E., Huang, P.G., Coakley, T.J.: Turbulence modeling validation, testing and development. Tech. Rep. NASA Technical Memorandum 110446, NASA (1997)

[97] Menter, F.R.: Two-Equation Eddy-Viscosity Turbulence Models for Engineering Applications. AIAA Journal **8**(32), pp. 1598–1605 (1994). doi:10.2514/3.12149

[98] Eisfeld, B., Brodersen, O.: Advanced Turbulence Modelling and Stress Analysis for the DLR-F6 configuration. In: 23rd AIAA Applied Aerodynamics Conference (2005). doi:10.2514/6.2005-4727

[99] Pototzky, A.S., Perry, B.: New and existing techniques for dynamic loads analyses of flexible airplanes. Journal of Aircraft **23**(4), pp. 340–347 (1986). doi:10.2514/3.45309

[100] Gerhold, T., Galle, M., Friedrich, O., Evans, J.: Calculation of complex three-dimensional configurations employing the DLR-TAU-code. In: 35th Aerospace Sciences Meeting and Exhibit (1997). doi:10.2514/6.1997-167

[101] Schwamborn, D., Gerhold, T., Heinrich, R.: The DLR TAU-Code: Recent Applications in Research and Industry. In: P. Wesseling, E. Onate, J. Periaux (ed.) European Conference on Computational Fluid Dynamics (ECCOMAS) (2006)

[102] Jameson, A., Schmidt, W., Turkel, E.: Numerical Solutions of the Euler Equations by the Finite Volume Methods Using Runge Kutta Time Stepping Schemes. In: 14th Fluid and Plasma Dynamics Conference (1981). doi:10.2514/6.1981-1259. AIAA 81-1259

[103] Jameson, A.: Time Dependent Calculations using Multigrid, with Applications to Unsteady Flows past Airfoils and Wings. In: 10th Computational Fluid Dynamics Conference (1991). doi:10.2514/6.1991-1596. AlAA 91-1596

[104] Hirt, C., Amsden, A., Cook, J.: An arbitrary Lagrangian-Eulerian computing method for all flow speeds. Journal of Computational Physics **14**(3), pp. 227–253 (1974). doi:10.1016/0021-9991(74)90051-5

[105] Meinel, M., Einarsson, G.O.: The FlowSimulator framework for massively parallel CFD applications. In: PARA 2010, Paper-44 (2010)

[106] Parameswaran, V., Baeder, J.D.: Indicial Aerodynamics in Compressible Flow - Direct Computational Fluid Dynamic Calculations. Journal of Aircraft **34**(1), pp. 131–133 (1997). doi:10.2514/2.2146

[107] Singh, R., Baeder, J.D.: The direct calculation of indicial lift response of a wing using computational fluid dynamics. In: AIAA Applied Aerodynamics Conference (1996). doi:10.2514/2.2214

[108] Heinrich, R., Reimer, L.: Comparison of Different Approaches for Gust Modeling in the CFD Code TAU. In: International Forum on Aeroelasticity and Structural Dynamics (2013)

[109] Heinrich, R.: Simulation of Interaction of Aircraft and Gust Using the TAU-Code. In: New Results in Numerical and Experimental Fluid Mechanics IX, *Notes on Numerical Fluid Mechanics and Multidisciplinary Design*, vol. 124, pp. 503–511. Springer International Publishing (2014). doi:10.1007/978-3-319-03158-3_51

[110] Huvelin, F., Girodroux-Lavigne, P., Blondeau, C.: High fidelity numerical simulations for gust response analysis. In: International Forum on Aeroelasticity and Structural Dynamics (2013). IFASD-2013-24B

[111] Zaide, A., Raveh, D.: Numerical simulation and reduced-order modeling of airfoil gust response. AIAA Jounal **44**(8), pp. 1826–1834 (2006). doi:10.2514/1.16995

[112] Newmark, N.M.: A Method of Computation for Structural Dynamics. Journal of the Engineering Mechanics Division **85**(3), pp. 67–94 (1959). doi:10.1061/JMCEA3.0000098

[113] de Boer, A., van der Schoot, M., Bijl, H.: Mesh deformation based on radial basis function interpolation. Computers and Structures **85**(11), pp. 784–795 (2007). doi:10.1016/j.compstruc.2007.01.013

[114] Cook, P.H., McDonald, M.A., Firmin, M.C.P.: Aerofoil RAE 2822: pressure distributions, and boundary layer and wake measurements. Tech. Rep. AGARD-AR-138, AGARD, North Atlantic Treaty Organization (1979)

[115] Hellström, T., Davidson, L., Rizzi, A.: Reynolds stress transport modelling of transonic flow around the RAE2822 airfoil. In: 32nd Aerospace Sciences Meeting and Exhibit (1994). doi:10.2514/6.1994-309

[116] Knopp, T.: Validation of the Turbulence Models in the DLR TAU Code for Transonic Flows - A Best Practice Guide. Forschungsbericht 2006-01, Institut für Aerodynamik und Strömungsmechanik, DLR Göttingen (2006)

[117] Vassberg, J., Dehaan, M., Rivers, M., Wahls, R.: Development of a Common Research Model for Applied CFD Validation Studies. In: 26th AIAA Applied Aerodynamics Conference. American Institute of Aeronautics and Astronautics (2008). doi:10.2514/6.2008-6919

[118] Vassberg, J.C., DeHaan, M.A., Rivers, M.S., Wahls, R.A.: Retrospective on the Common Research Model for Computational Fluid Dynamics Validation Studies. Journal of Aircraft **55**(4), pp. 1325–1337 (2018). doi:10.2514/1.C034906

[119] Tinoco, E.: Summary Data from the Seventh AIAA CFD Drag Prediction Workshop. In: AIAA AVIATION 2023 Forum (2023). doi:10.2514/6.2023-3492

[120] CentaurSoft: CENTAUR Grid Generator. URL `https://home.centaursoft.com/`. Retrieved on 19 January 2025

[121] Klimmek, T.: Parametric set-up of a structural model for fermat configuration for aeroelastic and loads analysis. Journal of Aeroelasticity and Structural Dynamics **3**(2), pp. 31–49 (2014)

[122] Nitzsche, J.: A numerical study on aerodynamic resonance in transonic separated flow. In: International Forum on Aeroelasticity and Structural Dynamics (2009). IFASD-2009-126

[123] Tijdeman, H., Seebass, R.: Transonic flow past oscillating airfoils. Annual Review of Fluid Mechanics **12**(1), pp. 181–222 (1980). doi:10.1146/annurev.fl.12.010180.001145

[124] Dimitrov, D.: Unsteady aerodynamics of wings with an oscillating flap in transonic flow. In: 8th PEGASUS-AIAA Student Conference (2012)

[125] Haller, G.: Exact theory of unsteady separation for two-dimensional flows. Journal of Fluid Mechanics **512**, pp. 257–311 (2004). doi:10.1017/S0022112004009929

[126] Sears, W.R., Telionis, D.P.: Boundary-Layer Separation in Unsteady Flow. SIAM Journal on Applied Mathematics **28**(1), pp. 215–235 (1975). doi:10.1137/0128018

[127] Mallik, W., Raveh, D.E.: Kriging-Based Aeroelastic Gust Response Analysis at High Angles of Attack. AIAA Journal **58**(9), pp. 3777–3787 (2020). doi:10.2514/1.J059332

A RAE2822 airfoil

A.1 Grid Sensitivity Study

In order to check the spatial convergence of gust responses on the RAE2822 airfoil, some of the results are reproduced using a significantly finer mesh with a total of about 980.000 nodes and 700 cells on the upper and lower surfaces each. This mesh is denoted as ”fine” in the following, whereas the mesh used in the main part of the paper is denoted as ”medium”, see Chapter 4.1. Additionally, a ”very fine” mesh is tested, with about 2.9 million nodes in total and 1350 cells on the upper and lower surface each.

The results for the different meshes are presented in Fig. A.1. Note that the whole parameter space is computed for the fine mesh, but only three reduced frequencies are computed for the very fine mesh, due to computational cost. The findings for the mesh convergence study are similar to the ones for the turbulence model study in Section 5.1.6. Overall trends do not change when using the finer meshes and the first harmonic is more influenced by the mesh than the maximum lift coefficient. The two finer meshes shift the values for the magnitude of the first harmonic up to slightly higher values and also predict a slightly higher maximum lift. Due to the very similar results on all three grids, the medium grid is chosen for all computations shown in the main part of the paper.

A.2 Time Step Study

Five different time step sizes are used to compute responses to the lowest and the highest frequency considered, each for the maximum gust amplitude. The results

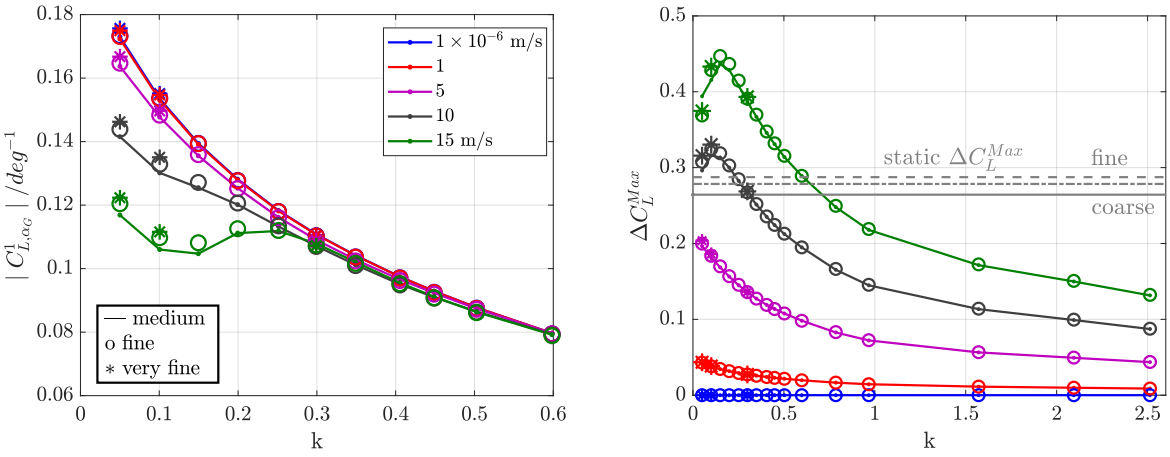

(a) First harmonic of the lift FRF **(b)** Maximum lift

Fig. A.1: Comparison of three CFD meshes at Mach 0.70.

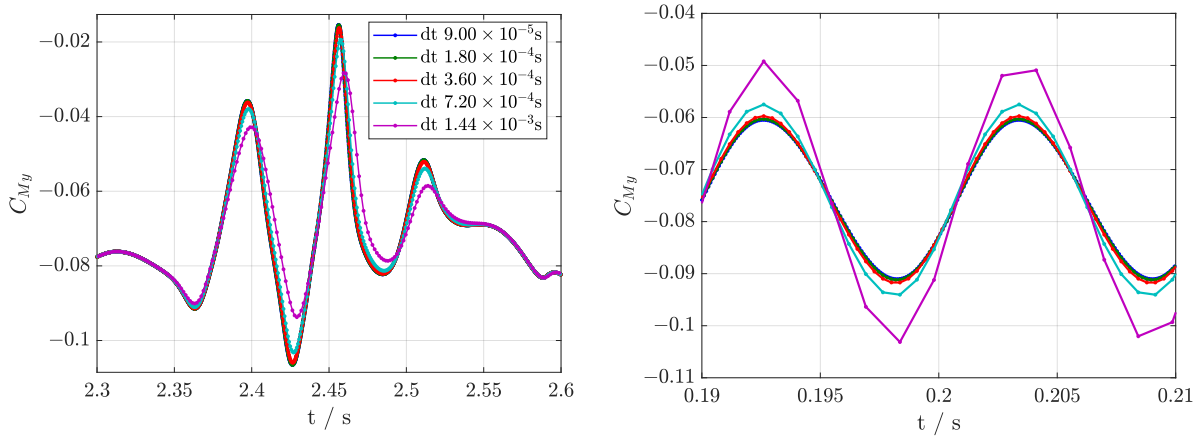

(a) $L_G = 125.5$ m ($k_{Gust} = 0.05$) **(b)** $L_G = 2.50$ m ($k_{Gust} = 2.50$)

Fig. A.2: Comparison of different time step sizes at Mach 0.70

for the pitching moment coefficient are compared in Fig. A.2. Time step sizes of $\mathrm{dt} = \{1/48, 1/24, 1/12, 1/6, 1/3\} \cdot U_\infty^{-1}$ are tested. Though the results for both gust lengths show an influence of the time step size, the shorter gust results are more severely affected. For time steps smaller than $\mathrm{dt} = 1/12 \cdot U_\infty^{-1}$ the results are converged. So, for the computations at Mach 0.70 in the main part of the paper, a time step size of $\mathrm{dt} = 1/24 \cdot U_\infty^{-1} = 1.8 \cdot 10^{-4}$ s is chosen, see Section 4.1.

A.3 Verification of Linearity for Low-Amplitude Results

It is stated above that the results for the lowest excitation amplitude can be taken as linear reference values, which is verified by the data in Fig. A.3: The first harmonic response of the lift draws a horizontal line between the results at $\widehat{W}_G = 10^{-6}$ m/s and $\widehat{W}_G = 0.1$ m/s That shows that the response is independent of the excitation amplitude and, therefore,

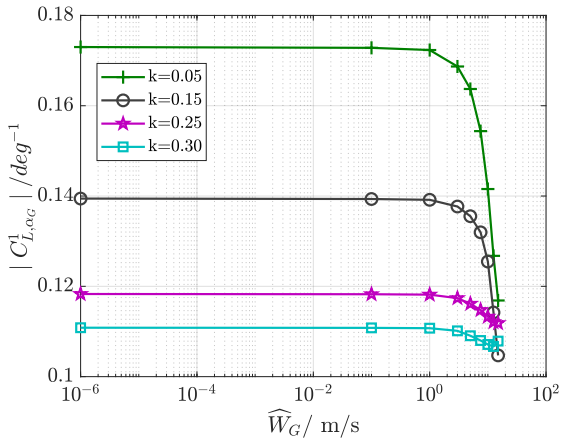

Fig. A.3: Verification of linearity for low-amplitude results at Mach 0.70.

corresponds to the definition of a linear system. The same derivative values for the first harmonic could be computed using a RANS-based linear frequency domain approach, such as the TAU-LFD solver [16], see e.g. [75] for a detailed comparison.

A.4 Static Airfoil Flow at Mach 0.68 and Mach 0.72

The following figures complement the results from Chapter 5.1.1 for two additional Mach numbers, Mach 0.68 and Mach 0.72. They reveal identical trends as could already be observed for Mach 0.66 and Mach 0.70.

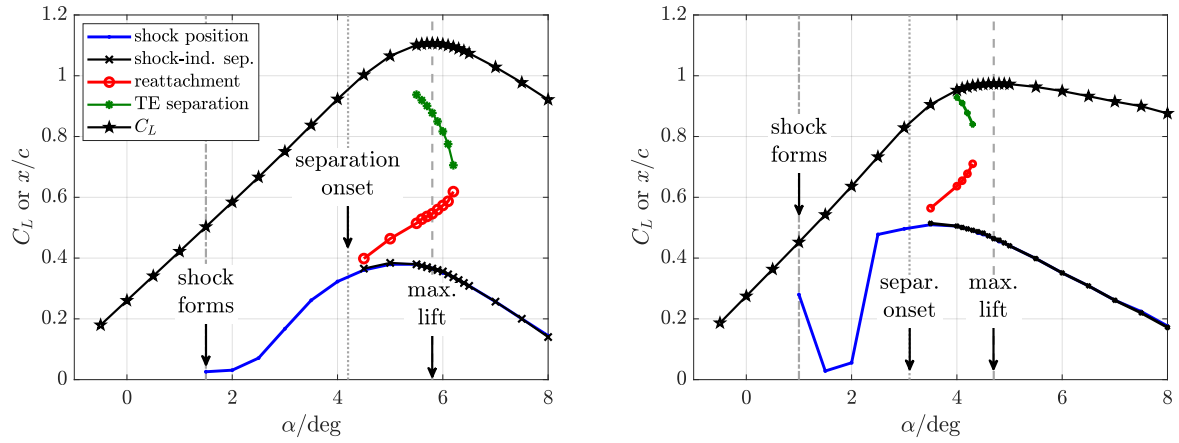

(a) Mach 0.68 **(b)** Mach 0.72

Fig. A.4: Characteristics of static airfoil flow

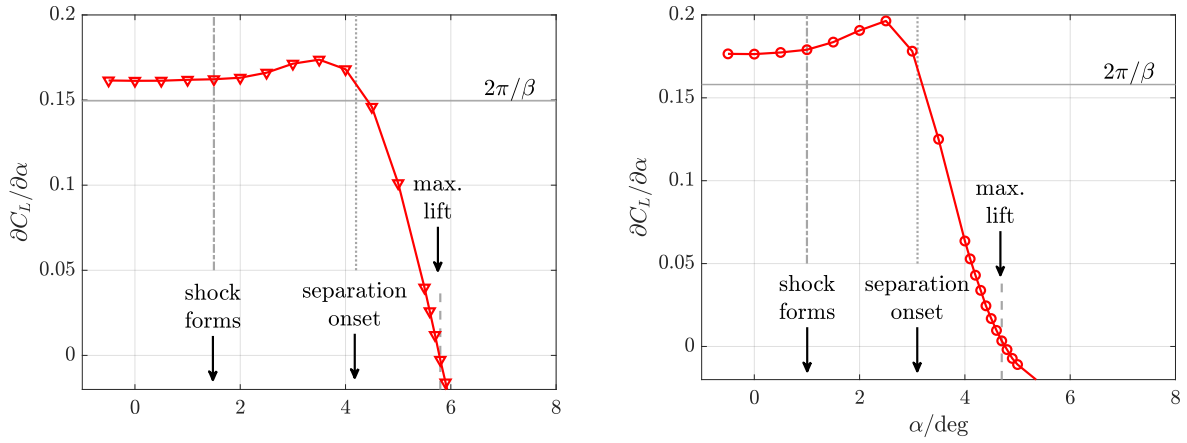

(a) Mach 0.68 **(b)** Mach 0.72

Fig. A.5: Lift curve slopes

B NASA Common Research Model

B.1 Grid Sensitivity Study

Results in this section provide information on the numerical robustness concerning the numerical mesh used for the NASA Common Research Model configuration. Three different grid levels are applied, which are listed in Table B.1. Though slight differences can be observed in the maximum lift coefficient, see Fig. B.1, all flow features that are relevant for the maximum lift coefficient seem to be adequately captured even with the coarsest mesh. The results shown throughout the paper are all computed with the medium-level mesh.

Table B.1: Grid levels used for the sensitivity study (Nx: number of points in chordwise direction).

Grid level	Nx, wing	Nx, HTP	total nr. of surface nodes	total nr. of nodes
coarse	100	75	3.6×10^5	5.5×10^6
medium	200	150	6.0×10^5	11.0×10^6
fine	400	300	1.15×10^6	24.5×10^6

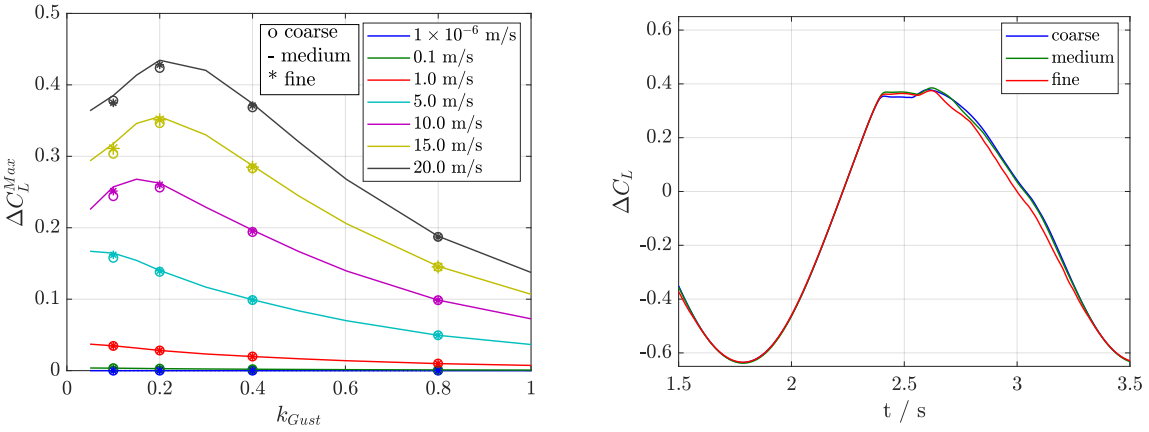

(a) Maximum increments of the lift coefficient **(b)** Time histories, $k_{Gust} = 0.1$, $\widehat{W}_G = 20.0\,\mathrm{m/s}$

Fig. B.1: Influence of the spatial discretization on the lift coefficient at Mach 0.85

B.2 Sensitivity to Number of Mode Shapes in FSI Simulations

The coupled simulations require a structural model which contains a sufficient number of elastic mode shapes in order to capture the relevant interaction with the aerodynamics.

The sensitivity study comprises three different sets of mode shapes:

- 3 modes: heave + pitch + first bending (1.065 Hz)
- 7 modes: heave + pitch + first five symmetric modes (up to 3.58 Hz)
- 24 modes: heave + pitch + 22 symmetric modes (up to 28.6 Hz)

Results are evaluated for different gust lengths and amplitudes. Responses for two different gust lengths at $\widehat{W}_G = 20.0$ m/s are plotted in Fig. B.2 and Fig. B.3. Overall, the moment coefficient prediction is more affected by the different number of mode shapes than the lift coefficient. As expected, the resulting response spectrum for both lift and moment coefficients gets broader when higher modes are included in the coupled simulations. A recent study by Feldwisch [20] shows that the separation patterns, especially from the SA turbulence model, trigger higher frequencies in the aeroelastic responses.

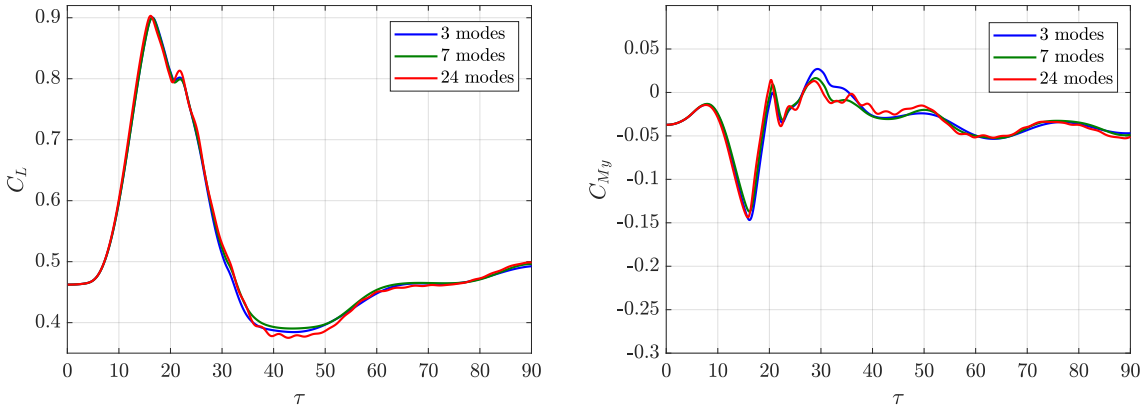

(a) Lift coefficient **(b)** Moment coefficient

Fig. B.2: Influence of the number of mode shapes for $L_G = 210.0$ m and $\widehat{W}_G = 20.0$ m/s

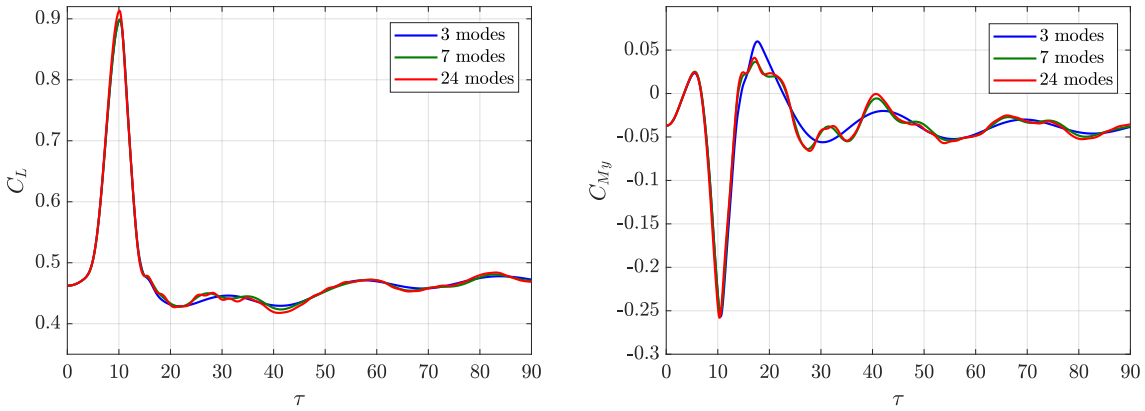

(a) Lift coefficient **(b)** Moment coefficient

Fig. B.3: Influence of the number of mode shapes for $L_G = 70.0$ m and $\widehat{W}_G = 20.0$ m/s at Mach 0.85

However, the relevant trends for the peak lift prediction are captured sufficiently accurate using seven mode shapes in the structural model and are therefore applied in the main part of this thesis.

B.3 Verification of Linearity for Low-Amplitude Results

It is stated above that the results for the lowest excitation amplitude of $\widehat{W}_G = 1 \times 10^{-6}$ m/s can be regarded as time-linearized reference solutions, which is verified by the data in Fig. B.4. By definition, the derivative of a linear system is independent of the excitation amplitude. Fig. B.4(a) shows the trends of the first harmonic response with increasing excitation amplitude. It is found that the aerodynamic system can be regarded as linear for excitation amplitudes up to $\widehat{W}_G = 1.0$ m/s as the corresponding relative error $\delta C^1_{L,\alpha_G}(k_{Gust},\widehat{W}_G)$ reveals a deviation from the linear of less than 1% for all excitation frequencies, see Fig. B.4(b). The relative error is defined as $\delta C^1_{L,\alpha_G}(k_{Gust},\widehat{W}_G) = \left(|C^1_{L,\alpha_G}(k_{Gust},\widehat{W}_G)| - |C^{Lin}_{L,\alpha_G}(k_{Gust})|\right) / \left(|C^{Lin}_{L,\alpha_G}(k_{Gust})|\right) \cdot 100\%$.

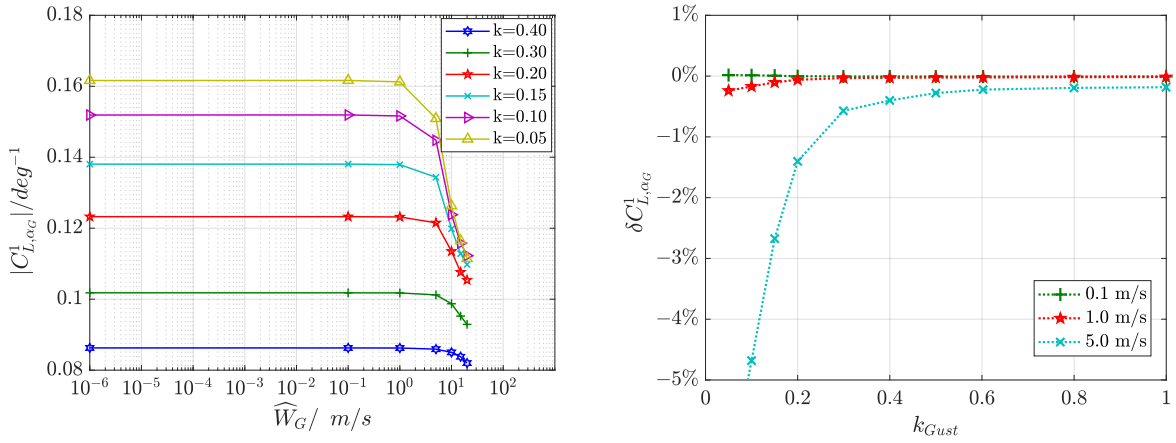

(a) First harmonic of the lift response

(b) Relative error of the first harmonic lift coefficient magnitude

Fig. B.4: Verification of linearity for low-amplitude results at Mach 0.85

B.4 Time Step Study

The influence of the time step size is shown in Fig. B.5. All computations in the main part of the paper are carried out with 100 inner iterations and the time step size of $dt = 1.3 \times 10^{-3}$ s, which corresponds to the nondimensional time step size of $\Delta\tau = dt/\left(l_{ref}/U_\infty\right) = 0.0466$. Though, there is still a difference between the results for the two smallest time step sizes, the general trend seems to be captured sufficiently accurately by $dt = 0.0013$ s.

With the chosen time step settings, the total computational time for the lowest reduced frequency $k_{Gust} = 0.05$ on the medium-level mesh using 3 sinusoidal excitation periods and the turbulence model of Spalart-Allmaras took about 197 hours on 320 CPU on the DLR-HPC cluster CARA[2]. The highest reduced frequency $k_{Gust} = 2.50$ was simulated for 8 excitation periods, which took about 11 hours of computation.

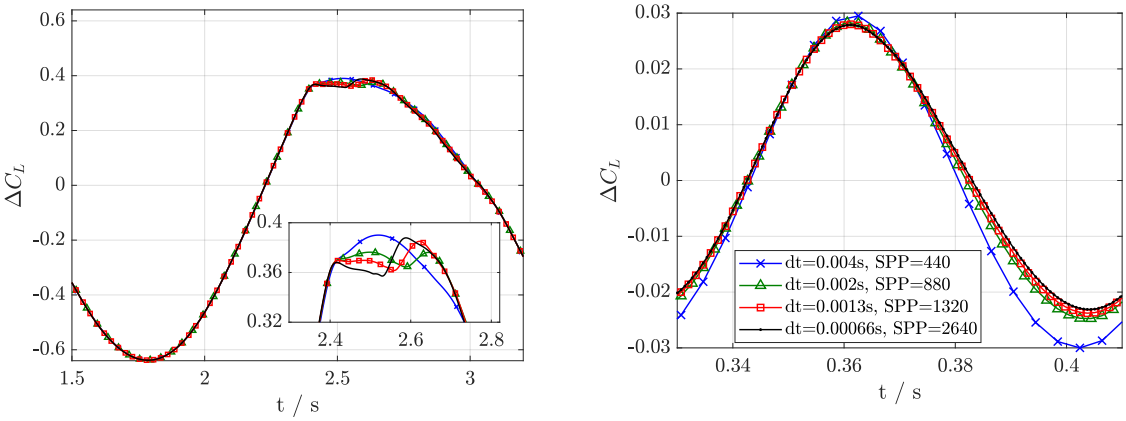

(a) $k_{Gust} = 0.1$ (markers show every 20th time step)

(b) $k_{Gust} = 2.5$

Fig. B.5: Influence of the time step size on the lift coefficient using $\widehat{W}_G = 20.0$ m/s at Mach 0.85

[2]Cluster for Advanced Research in Aerospace

B.5 Componentwise Contributions to Global Lift Response

Fig. B.6 displays the lift coefficient for different aircraft components in relation to the defined points in time τ_G^i from Chapter 5.3.2. The figures show that the qualitative trend of the total lift is mainly governed by the flow physics on the aircraft's wing. The HTP has only a minor effect on the lift coefficient, which is noticeable mainly during the decay of the response. The fuselage only introduces an almost constant offset onto the wing's lift.

It can be observed that the long gust induces a noticeable increase in the lift coefficient even before the maximum gust velocity reaches the wing's leading edge at τ_G^{LE}. The same observation can be made for the increase in the lift coefficient of the HTP with respect to $\tau_G^{HTP,LE}$, which marks the point in time when the maximum gust velocity hits the HTP leading edge. For the shorter gust, these lags are reduced.

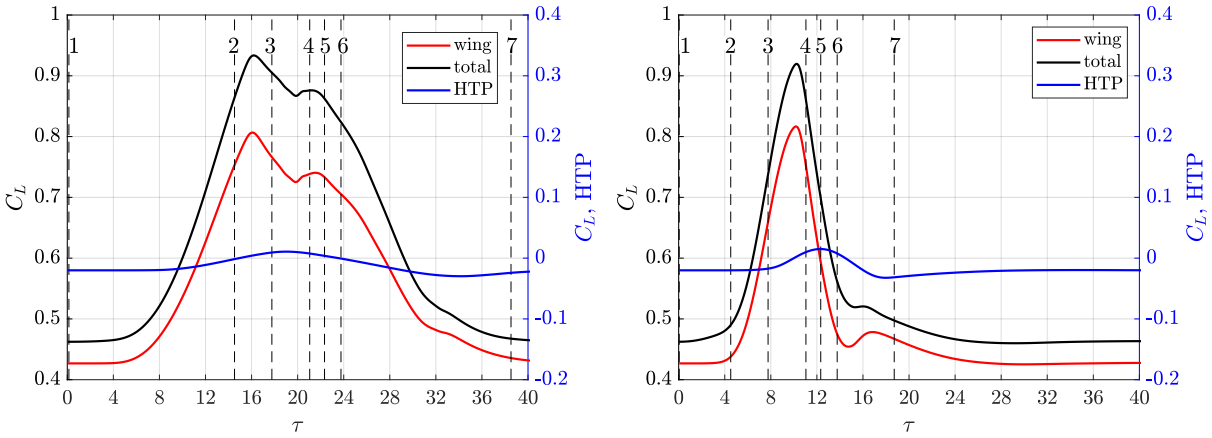

(a) $L_G = 210.0$ m. **(b)** $L_G = 70.0$ m

Fig. B.6: Contributions to total lift at Mach 0.83 for $\widehat{W}_G = 20.0$ m/s. Vertical lines mark τ_G^i (labels for i are 1:*Start*, 2:*Nose*, 3:*LE*, 4:*TE*, 5:*HTP,LE*, 6:*HTP,TE*, 7:*Stop*)

List of Figures

List of Tables